Development of MRI techniques for the assessment of Chronic Kidney Disease

Charlotte E. Buchanan, MMath&Phys.

Thesis submitted to the University of Nottingham for the degree of Doctor of Philosophy

March 2016

Abstract

It is well established that patients with Chronic Kidney Disease (CKD) are more susceptible to develop cardiovascular disease in comparison to the healthy population. This thesis aims to develop and apply MRI techniques to assess the human heart and kidney in patients with chronic kidney disease (CKD).

Magnetic resonance imaging (MRI) can be used to inform on structure, function, perfusion and blood flow, without the need for ionizing radiation. In order to assess blood flow using MRI, gadolinium based contrast agents are often used. Patients with compromised kidney function are contraindicated to these contrast agents and so it is necessary to develop imaging techniques that can be used without a contrast agent.

Arterial spin labelling (ASL) is an MRI technique that provides a non-contrast enhanced method to assess tissue perfusion using the intrinsic signal from the water in the body. ASL is now becoming a well-established technique in the brain, however applications of ASL in the body are currently limited. In this work, a cardiac ASL technique is developed using a modified Look-Locker scheme to study the myocardium of the heart. This technique is then applied in patients with CKD Stage 3 and age-matched healthy control subjects to assess the changes in myocardial perfusion during a handgrip exercise challenge.

MRI measurements of cardiac index and stroke volume index, global and regional contractile function (myocardial strain), coronary artery flow and myocardial perfusion using ASL are applied to assess changes in cardiac function in CKD Stage 5 patients during dialysis treatment. The measures are

performed in a randomised design to assess the cardiovascular effects in patients undergoing both haemodialysis and haemodiafiltration.

Finally, a comparison of 2D readout schemes for renal ASL is performed. Gradient and spin echo based readout schemes for multi-slice ASL of the kidney at 3 T are evaluated and directly compared in terms of temporal SNR, image SNR, spatial coverage, perfusion quantification and variability across slices/subjects. This work aims to determine the optimal readout scheme for pulsed ASL (PASL) of the kidneys at 3 T in healthy volunteers with normal renal function. In future work this could be applied to patients with compromised renal function where a robust imaging technique is needed.

Finally, a summary of the key findings of this thesis and an outline of the potential future directions of this work is provided.

Table of Contents

Acknowledgements

There are a few people that I would like to thank for their help in producing this work and for their support throughout my PhD.

Firstly, and most importantly, I have to thank Prof Sue Francis who has supervised this project and whose knowledge and enthusiasm for the work has resulted in a project that I have thoroughly enjoyed and a body of work that I am very proud of.

Secondly, I must thank Dr Eleanor Cox who has been a great mentor and friend throughout my PhD. She has put up with endless stupid questions and entertained me through many long scan days!

I would also like to acknowledge Prof Maarten Taal, Dr Nick Selby, Prof Chris McIntyre, Dr Claire Grant, Dr Huda Mahmood, Dr Azhar Mohammed who have helped me try to understand the medical knowledge needed and who have provided the clinical questions that motivated a lot of this work.

I would also like to thank the dialysis nurses from the Royal Derby hospital; who attended every dialysis study day and who helped the days run very smoothly and provided a lot of entertainment during the long study days.

Very importantly I have to thank all of the staff at the SPMIC. It is a brilliant place to work and I feel very fortunate to have you all as colleagues and friends!

I would like to thank all my housemates for being so much fun over the past few years, especially Bissie, Paula and Laura. Thanks to Rich for being generally great, accompanying me on many tea breaks and keeping me very cheerful throughout the whole write up process. Finally, I think this is the perfect time to thank my family for being the amazing people they are; my grandad who would be so proud if he could have seen me finish my PhD and most importantly my dad for being my best friend and my biggest support.

Glossary

2DE: 2D echocardiography

3DE: 3D echocardiography

AKI: Acute kidney injury

ASL: Arterial Spin Labelling

bFFE: Balanced fast field echo

BFR: Blood flow rate

bpMBF: Blood pool MBF

BSA: Body surface area

CAD: Coronary artery disease

CASL: Continuous ASL

CE: Contrast enhanced

CI: Cardiac index

CKD: Chronic Kidney Disease

CoV: Coefficient of variance

CPT: Cold pressor test

CSPAMM: Complimentary modulation of magnetisation

CVD: Cardiovascular disease

DBP: Diastolic blood pressure

DCE: Dynamic contrast enhanced

DWI: Diffusion weighted imaging

EDV: End diastolic volume

EPI: Echo planar imaging

EPISTAR: Echo planar imaging and signal targeting with alternative radiofrequency

ESRD: End stage renal disease

ESV: End systolic volume

ETL: Echo train length

FAIR: Flow sensitive alternating inversion recovery

FLASH: Fast low angle shot

FOCI: Frequency offset corrected inversion

FOV: Field of view

GE: Gradient-echo

GFR: Glomerular filtration rate

GRASE: Gradient and spin echo

HC: Healthy control

HD: Haemodialysis

HDF: Haemodiafiltration

HR: Heart rate

IDH: Intradialytic hypotension

IR: Inversion recovery

IVC: Inferior vena cava

LL: Look-Locker

LV: Left ventricular

MBF: Myocardial blood flow

MOLLI: Modified Look-Locker inversion recovery

MRA: Magnetic resonance angiography

MRI: Magnetic resonance imaging

MT: Magnetisation transfer

NMR: Nuclear magnetic resonance

NS: Non-selective

NSF: Nephrogenic systemic fibrosis

PASL: Pulsed ASL

pCASL: Pseudo-continuous ASL

PC-MRI: Phase contrast MRI

PET: Positron emission tomography

PLD: Post-label delay

PPE: Pulse programming environment

PW: Perfusion weighted

PW-SNR: Perfusion weighted signal-to-noise ratio

RF: Radiofrequency

ROI: Region of interest

SA: Sinoatrial

SAR: Specific absorption rate

SBP: Systolic blood pressre

SE: Spin-echo

SEL: Selective

SENSE: Sensitivity encoding

SNR: Signal-to-noise ratio

SPAMM: Spatial modulation of magnetisation

SPECT: Single positron emission computed tomography

SVI: Stroke volume index

TD: Trigger delay

TE: Echo time

TI: Inversion time

TR: Repetition time

TSE: Turbo spin echo

tSNR: Temporal signal-to-noise ratio

VCG: Vector cardiogram

WET: Water suppression enhanced through T_1 effects

1. Introduction: context of thesis

The primary aim of this thesis is to develop MRI haemodynamic measures of blood flow and perfusion for the assessment of cardiac and kidney function in people with Chronic Kidney Disease (CKD).

This chapter provides an introduction to the methods and clinical conditions studied in this thesis. Firstly, the structure and function of the kidney and heart are outlined. The deficits that occur in these organs in CKD are described and the use of dialysis treatment in CKD is then explained. Finally, this chapter provides an evaluation of the current methods used to assess blood flow and perfusion of the heart and kidney. Firstly, the methods of ultrasound, positron emission tomography (PET) and single positron emission computed tomography (SPECT) are outlined. This is followed by an overview of the MR methods that can be used. Specifically, a focus is provided on the use of arterial spin labelling (ASL) for the measurement of perfusion and its application in the heart and kidneys, to address the primary aim of using these methods in the study of people with CKD.

1.1. Anatomy

The following sections provide an outline of the anatomy of the human heart and kidney.

1.1.1. Heart structure and function

The human heart comprises 4 chambers; the right atrium and the right ventricle and the left atrium and left ventricle. The left and right sides of the heart are separated by a wall of muscle called the septum. The basic anatomy of the heart is shown in the schematic in Figure 1.1-1. The external wall of the heart contains three layers; the epicardium, which is the outer most layer, the myocardium, which contains the muscle that contracts, and the endocardium which is the inner wall. The atria and ventricles are separated by the atrioventricular valves; the tricuspid valve on the right side and the mitral valve on the left. The pulmonary semi-lunar valve separates the right ventricle from the pulmonary artery, and the left ventricle and aorta are separated by the aortic valve.

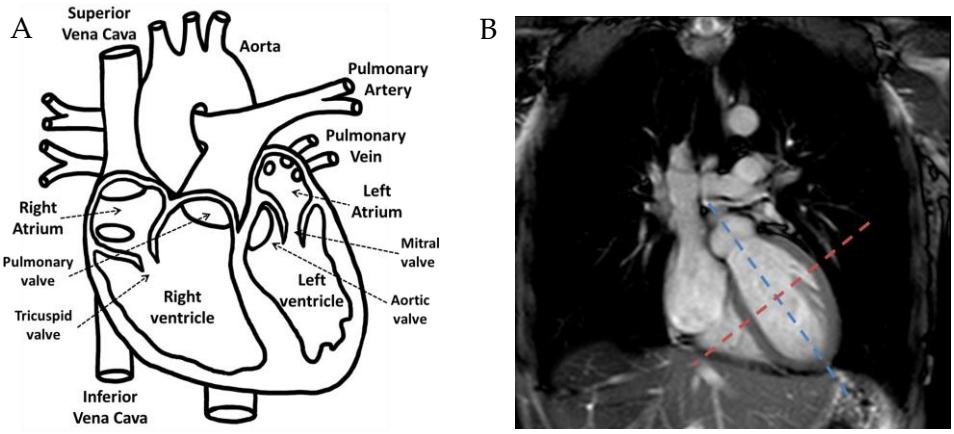

Figure 1.1-1: *A) Schematic showing the basic anatomy of the human heart adapted from* (1) *and B) a coronal MR image through the heart collected using a bFFE localizer scheme. The red dotted line shows the short axis and the blue dotted line shows the long axis of the left ventricle.*

Blood circulates around the body via the pulmonary circuit and the systemic circuit. In the pulmonary circuit, deoxygenated blood leaves the right ventricle of the heart through the pulmonary artery and travels to the lungs. This blood is then oxygenated in the lungs and returns to the left atrium via the pulmonary veins. In the systemic circuit, oxygenated blood leaves the heart via the left ventricle to the aorta. It then supplies the body's organs with oxygen through the arteries and capillaries. Once this blood has been deoxygenated it returns to the heart's right atrium via the superior and inferior vena cava.

The cardiac cycle describes the series of events that occur when the heart beats. The RR-wave defines the spacing between two consecutive peaks in the cardiac cycle, typically around 1 s in humans. The cardiac cycle consists of two phases: the diastolic phase and the systolic phase as shown in Figure 1.1-2.

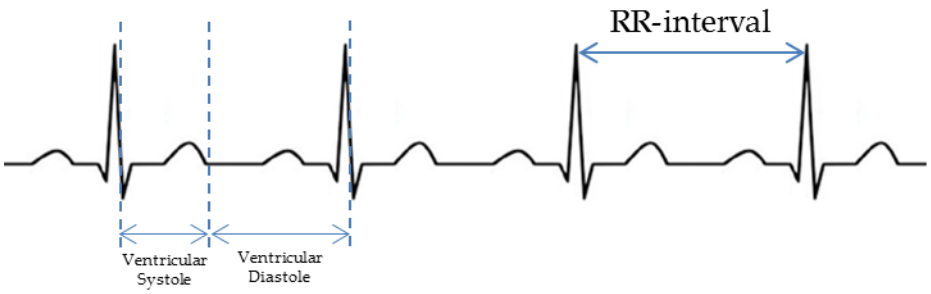

Figure 1.1-2: *Schematic of an electrocardiogram trace indicating ventricular systole and diastole in an RR-interval.*

During the diastolic phase, the atria and ventricles are fully relaxed and the atrioventricular valves are open. Deoxygenated blood enters the right atrium via the superior and inferior vena cavae. The open atrioventricular valves allow blood to move into the ventricles. The sinoatrial (SA) node acts as the heart's natural pacemaker and is situated in the upper part of the wall of the right atrium. Here electrical impulses are generated which trigger the atria to contract and then blood in the right atrium moves into the right ventricle. The tricuspid valve prevents blood from moving back into the right atrium.

Simultaneously, blood from the pulmonary veins fills the left atrium. When the atria contract, the contents of the left atrium are moved into the left ventricle, the mitral valve then stops oxygenated blood from moving back into the left atrium.

In the systolic phase, the ventricles contract and the atrioventricular valves close whilst the aortic and pulmonary valves open. Deoxygenated blood then travels from the right ventricle into the pulmonary artery and is prevented from flowing back into the right ventricle by the pulmonary valve. The pulmonary artery carries deoxygenated blood to the lungs where it becomes oxygenated and returns to the left atrium via the pulmonary veins. At the same time, the left ventricle contracts and oxygenated blood moves to the aorta to circulate the body, whilst the aortic valve prevents blood from travelling back into the left ventricle. Oxygenated blood then circulates in the body.

The heart muscle, myocardium, is perfused by the left and right coronary artery, as shown in Figure 1.1-3A. The average tissue perfusion of the myocardium is approximately 1 ml/g/min.

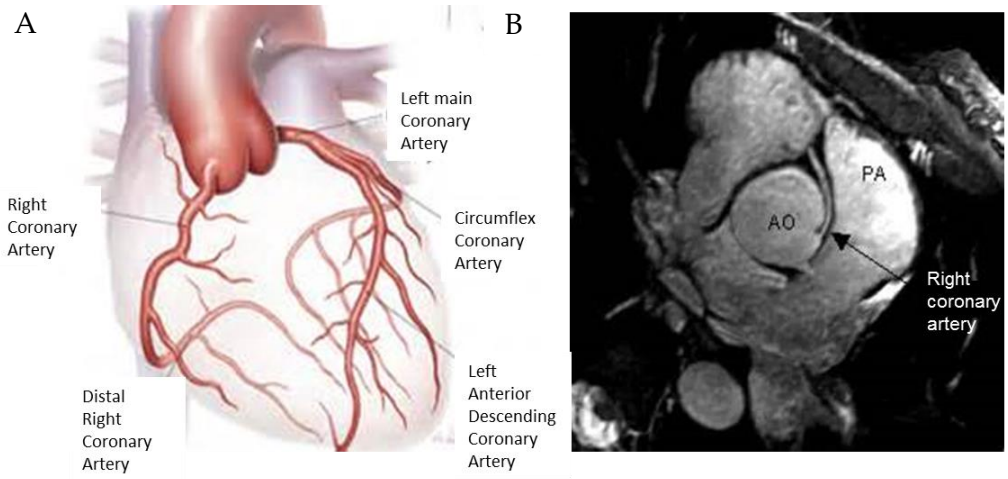

Figure 1.1-3: *A) A schematic showing left and right coronary artery, adapted from* (2) *and B) an MR image showing the right coronary artery acquired using an axial bFFE localizer scheme.*

The left main coronary artery branches into the left anterior descending artery and the left circumflex artery. The right coronary artery branches on the right side of the aorta into the distal right coronary artery. The coronary arteries are approximately 3 mm in diameter with a blood flow rate of approximately 10 ml/s.

1.1.2. Kidney structure and function

The kidneys (Figure 1.1-4) are two intra-abdominal organs whose purpose is to filter the blood. The kidneys remove waste metabolites, control the body's fluid balance and regulate the balance of electrolytes.

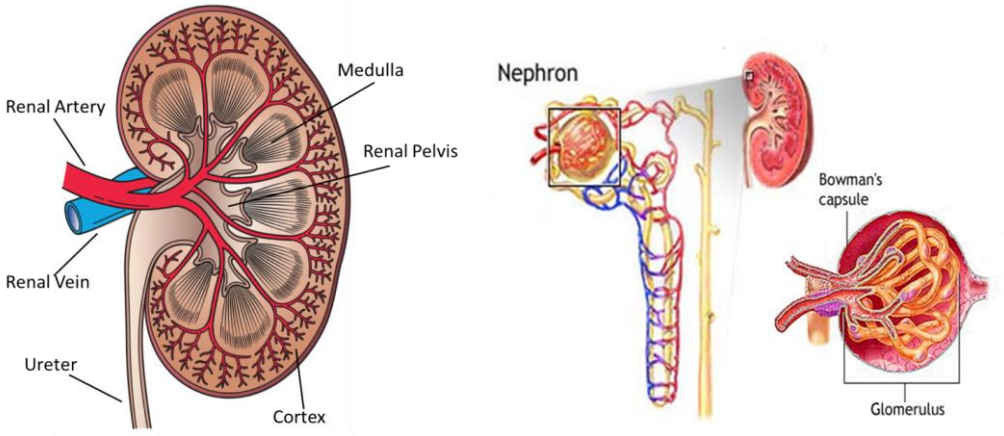

Figure 1.1-4: *Basic kidney anatomy, highlighting a nephron with the Bowman's capsule and glomerulus, adapted from* (3).

The basic functional component of the kidney is the nephron; this is where blood is filtered to produce fluid which then undergoes multiple reabsorption and secretion processes to produce urine which drains into the renal pelvis. There are around one million nephrons in each human kidney. Each nephron is composed of a filtering component known as the renal corpuscle (composed of a glomerulus surrounded by the Bowman's capsule) and the renal tubule for reabsorption and secretion. The renal corpuscle filters solutes from the

blood and then delivers water and small solutes to the renal tubule. Each nephron starts in the cortex where there is a knot of capillaries known as the glomerulus. In these glomeruli, blood is filtered so that waste metabolites and excess water are removed from the blood. Greater resistance in the efferent versus afferent arteriole increases local hydraulic pressure in the glomerulus, which results in fluid being squeezed out of the capillaries. This fluid is collected in the Bowman's capsule which surrounds the glomerulus. The fluid moves from the Bowman's capsule into the tubule. The process of moving the fluid from the glomerulus into the Bowman's capsule is known as ultrafiltration. In ultrafiltration, large molecules such as proteins and blood cells are kept in the blood whereas smaller molecules, such as sodium, pass into the Bowman's capsule. The renal tubule transports fluid which has been filtered through the glomerulus to the collecting duct system. During the passage through the renal tubule a large number of substances are reabsorbed from the tubular fluid and others are secreted into it.

The kidney can be separated into the renal cortex and renal medulla. The renal cortex is the outer portion of the kidney which contains the renal corpuscles and the renal tubules, as well as blood vessels and the cortical collecting ducts. It is in the renal cortex that the ultrafiltration process occurs. The renal medulla is the inner most part of the kidney and is split into a number of sections called the renal pyramids. The interstitium (tissue between the tubules) in the renal medulla contains the renal tubules and those parts of the nephrons responsible for maintaining salt and water balance within the blood. The renal medulla is hypertonic to the filtrate in the nephron and so aids in the reabsorption of water. Despite being only 0.2 % of the body weight, the kidneys receive around 20 % of the cardiac output via the renal artery (with a flow of approximately 20 ml/s) which branches from the abdominal aorta. The blood flow to the renal cortex is much higher than that to the renal medulla with the cortex receiving approximately 80 % of the total blood flow to the

kidneys. The approximate perfusion of the kidney is 300 ml/100g/min to the cortex and 60 ml/100g/min to the medulla.

The renal arteries divide into smaller arteries in the kidneys which eventually lead to afferent arterioles that supply blood to the glomeruli. After passing through the glomeruli, blood recollects in efferent arterioles which lead to peritubular capillaries that descend into the renal medulla and merge to form veins which later meet to become the large renal vein. The renal vein exits the kidney to join the inferior vena cava from which blood is carried to the heart.

1.2. Chronic Kidney Disease

1.2.1. Aetiology of CKD

Chronic Kidney Disease (CKD) is a condition characterised by gradual loss of kidney function over time. CKD is described in five stages, each representing a worsening disease state of the kidney, as outlined in Table 1.2-1. Clinically, the stage of kidney disease is determined by the glomerular filtration rate (GFR) which provides an estimate of how much filtrate is produced by the glomeruli each minute. GFR is calculated mathematically from serum creatinine levels in blood taking into account a person's size, age, sex and race.

Stage	GFR	Description	Treatment
1	90+	Normal kidney function but indications of kidney disease such as structural abnormalities, urine findings or a genetic trait	Observation and control of blood pressure
2	60-89	Small reduction in kidney function and other findings which suggest kidney disease	Observation, control of blood pressure and other risk factors
3A 3B	45-59 30-44	Moderately reduced kidney function	Observation, control of blood pressure and other risk factors
4	15-29	Severely reduced kidney function	Begin planning for end stage renal failure
5	<15	Very severe reduced kidney function or end stage renal failure	Transplant or dialysis

Table 1.2-1: *Stages of Chronic Kidney Disease with corresponding GFR values, description of disease and typical treatment* (4).

CKD is characterised by a GFR < 60 ml/min/1.73m^2 that persists for more than 3 months. In CKD, it is thought that renal tissue hypoxia (oxygen deficiency) plays an important role. This is complex and can be influenced by multiple factors. It may be related to altered renal blood flow and perfusion or altered renal oxygen consumption. Thus measures to assess these parameters are important in understanding CKD progression.

Patients with CKD have a very high risk of developing cardiovascular disease (CVD) (5). The pathophysiology and mechanics underlying the increased incidence of CVD in CKD remain incompletely understood (6), but disease of one organ causes dysfunction in the other, ultimately leading to organ failure in both. These factors are well recognized in advanced kidney disease but the increased risk of mortality from heart disease begins to occur at an early stage of CKD. CKD Stage 3 is the most commonly diagnosed stage of the disease. Even at this relatively early stage patients are prone to changes in blood pressure and other risk factors that could lead to compromised cardiovascular function. Chapter 3 of this thesis assesses blood flow and perfusion of the heart in patients with CKD Stage 3.

When the GFR falls below 15, CKD Stage 5 is diagnosed and at this point patients have end stage renal disease (ESRD). Most patients then either undergo a kidney transplant or begin preparation for dialysis treatment. The effect of haemodialysis on the cardiac function in CKD Stage 5 patients is assessed in Chapter 4 of this thesis.

1.2.2. Dialysis in end-stage renal disease (ESRD) patients

Dialysis is the procedure that is used to perform many of the normal excretory functions of the kidney, such as the removal of waste products and excess fluid from the blood. Dialysis works by the principal of diffusion, removing solutes from the blood through a concentration gradient across a semi-permeable membrane. This semi-permeable membrane ensures that larger

proteins and blood cells are not removed from the blood. There are two main dialysis modalities: peritoneal dialysis and haemodialysis.

In peritoneal dialysis (7), a catheter is implanted in the peritoneal cavity, a space between the parietal peritoneum and visceral peritoneum in the abdominal cavity, and anchored in the subcutaneous tissues. Dialysate fluid flows through the catheter into the peritoneum where it remains for several hours. In that time, dialysis is performed as waste products and excess fluid diffuse across the semi-permeable peritoneal membrane. Excess fluid is removed by osmosis as the dialysate fluid is hypertonic compared to plasma. When this process is completed the remaining dialysis fluid and waste products are drained from the abdomen and the process is repeated. Peritoneal dialysis is preferable for patients who wish to maintain an active lifestyle as it can be performed at home and so removes the need for regular hospital trips. Peritoneal dialysis is performed up to 4 times a day and takes around 30 minutes per exchange. It can also be performed during the night by a machine that performs automated exchanges during a 10-12 hour dialysis session.

Haemodialysis (8) works by moving the patients' blood through an extracorporeal system which contains a semi-permeable membrane with blood moving down one side and dialysate (dialysis fluid) flowing along the other side in the opposite direction. This counter-current flow maintains a concentration gradient across the membrane which increases the efficiency of the dialysis treatment. Waste products are free to move through the membrane, but the holes are only large enough to let small molecules through and so proteins and blood cells remain in the blood. By altering the hydrostatic pressure of the dialysate fluid, ultrafiltration (fluid removal) is achieved as excess fluids are removed from the blood when free water and some dissolved solutes move across the membrane along the created pressure gradient. Haemodialysis is usually performed three times a week and each

session takes approximately 4 hours; however more frequent, shorter schedules (including nocturnal haemodialysis) are becoming more common with an increasing drive to support home therapies.

Haemodiafiltration (HDF) is a modified form of haemodialysis that increases clearance of larger uremic toxins via convection, in this procedure ultrafiltration volumes are higher and coupled with greater fluid replacement. Water and solutes move from the blood to the dialysate at a much higher rate and solutes of both large and small molecular weights are removed. Replacement fluid is infused into the patient to ensure enough fluid is in the body.

It is well established that patients on dialysis treatment display a greatly elevated rate of mortality due to an excess of cardiovascular complications (9). This increase in all-cause mortality is over 30 times greater than that of age matched controls (Figure 1.2-1)

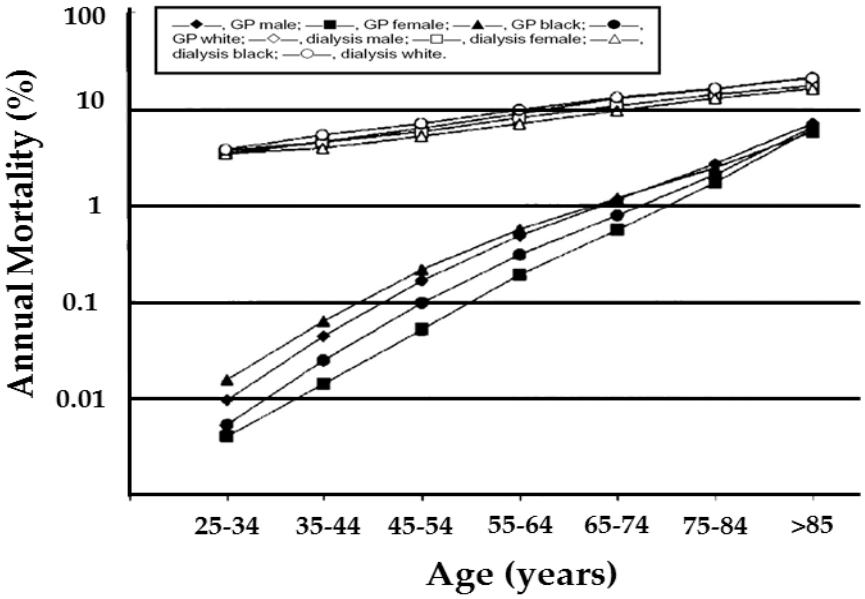

Figure 1.2-1: *All-cause mortality in general population and ESRD patients on dialysis, figure adapted from (4). This figure shows the general healthy population (black markers), and dialysis patients (white markers).*

The high levels of CVD in patients on dialysis is in part due to traditional risk factors for cardiac disease that are more prevalent in CKD patients. However, the treatment of these risk factors in dialysis patients has not been shown to significantly decrease the number of cardiovascular related deaths. For example, no benefit was observed with cholesterol lowering in diabetic haemodialysis patients (10). The mechanisms for such an extreme increase in mortality rates is not fully understood. However, it has been shown that the circulatory stress of dialysis treatment itself can result in ischemia of the heart muscle in vulnerable vascular beds. Myocardial ischemia can lead to left ventricular dysfunction which may not recover once normal perfusion is returned following dialysis. This effect is known as myocardial stunning (11). Studies have shown that repeated ischemic episodes can lead to prolonged left ventricular dysfunction. As such myocardial stunning is thought to be a causative mechanism for heart failure in dialysis patients (11). Since dialysis patients receive treatment multiple times per week they are subjected to frequent ischemic episodes which can lead to chronic cardiac damage. Chapter 4 of this thesis aims to perform intradialytic MR measures, and compares cardiac function in response to haemodialysis and haemodiafiltration as assessed by MRI.

1.3. Assessment of blood flow and tissue perfusion

Blood flow is the continuous circulation of blood in the cardiovascular system and can be used to assess delivery of blood to a given organ in ml/min. Perfusion describes the volume of blood that passes through the capillary bed per unit time to deliver nutrients to the tissue. It is typically measured in units of millilitres per gram per minute (ml/g/min), to provide a measure of the number of millilitres of blood that is delivered to each gram of tissue in a minute. Blood flow and perfusion measurements can potentially inform on tissue function, disease progression and therapy efficacy. A robust technique for measurement of absolute blood flow and perfusion in the kidney and

myocardium of the heart is important. The following section describes methods for such assessment, which is the main aim of this thesis.

1.3.1. Methods to Measure Blood Flow and Perfusion

There are a number of techniques used for the measurement of blood flow and perfusion. To acquire information about the structure and function of the heart, an echocardiogram is generally used. Electrocardiographic imaging measures the reflection of sound waves from the structure of the heart and movement of blood in the heart. Doppler ultrasound measures the direction of blood and speed of blood flow through the heart. An echocardiogram can be used to assess ventricular mass. Previously, myocardial perfusion was measured using microspheres labelled with radioactive isotopes. These radioactively labelled particles were injected into the patient and the radioactivity of the tissue of interest was then measured to determine how much blood had travelled into the tissue (12). Perfusion can also be measured using positron emission tomography (PET) (13) and single positron emission computed tomography (SPECT) (14), where radiopharmaceuticals are injected into the body and PET or SPECT scanners are used to visualise where the radioactively labelled blood has travelled to. There has previously been work using PET in patients with CKD Stage 5 to assess myocardial perfusion in response to dialysis (15). However, there are a number of limitations to the use of PET and SPECT, including a lower signal in comparison to MRI, limited spatial resolution and also exposure to ionising radiation, which prevents PET and SPECT studies being repeated multiple times.

Magnetic Resonance imaging (MRI) allows assessment of blood flow and voxel-by-voxel assessment of perfusion. Blood flow can be measured using phase contrast MRI (see Chapter 2). Perfusion assessment with MRI is classically performed using dynamic contrast-enhanced MRI (DCE-MRI) which uses the administration of a contrast agent, typically gadolinium (DTPA) (16). However, in patients with compromised kidney function,

gadolinium-based contrast agents can lead to side-effects including Nephrogenic Systemic Fibrosis (NSF) (17), highlighting the need for the development of reliable non-invasive techniques to assess perfusion. Arterial spin labelling (ASL) provides an alternative to DCE-MRI for the non-invasive quantitative assessment of tissue perfusion. ASL does not require injection of a contrast agent, but instead uses the magnetisation of endogenous labelled blood as a contrast agent. Development of ASL methods in the heart and kidney are the focus of Chapters 3 and 5. The following sections provide an overview of the current status of these methods in the literature.

1.3.2. Arterial Spin Labelling

Arterial Spin Labelling (ASL) is a non-invasive technique for the measurement of perfusion (18–24). The first studies using ASL were published over 15 years ago (18), and since then there has been a wide development of techniques for both brain and body applications, including those for the assessment of kidney and cardiac perfusion.

ASL uses magnetically labelled water protons as an endogenous tracer. An ASL image is formed from the difference between a label and control image. The label image of the tissue is collected under the condition of the inflowing arterial blood being inverted or saturated, whilst for the control image the longitudinal magnetisation of the inflowing blood is fully recovered. There are 3 variants of the labelling techniques for ASL; pulsed ASL (PASL), continuous ASL (CASL) and pseudo-continuous ASL (pCASL). These techniques are described in Chapter 2 and PASL is used in Chapters 3-5 of this thesis.

To date the majority of ASL studies have been carried out in the brain. However, the number of studies performed in other organs in the body has increased in recent years. In particular, a number of studies have used ASL to assess perfusion of the kidneys (25–33), lungs (34), skeletal muscle (35,36) and the heart (37–42). Since CKD leads to both changes in cardiac and renal

function, the ability to measure myocardial and renal tissue perfusion with the development of ASL methods is of great importance.

1.3.2.1. Cardiac ASL

There are a number of challenges associated with cardiac ASL. Firstly, due to the motion of the heart during the cardiac cycle, the scans must be synchronised to a fixed point in the cardiac cycle (typically end-diastole is chosen). This can be achieved using cardiac gating which matches the scan acquisition to the heartbeat using the signal from a vector cardiogram (VCG) thus minimising motion artefacts. In addition to the motion of the heart, cardiac MRI has to overcome the movement of the diaphragm during the respiratory cycle. There are a number of techniques that can be used to overcome respiratory motion including triggering scans on both the cardiac and respiratory cycle, using respiratory bellows, asking the subject to perform a breath hold during the scan, using a navigator scan or retrospective motion correction or sorting of the data.

There has recently been a small number of studies published using ASL techniques to assess myocardial perfusion in both animals (43–45) and humans (38,42,46–49). A number of papers have validated the measurement of myocardial perfusion values using a stress test, such as an injection of adenosine (48) or the use of an exercise challenge (37). Myocardial ASL is developed and discussed in more depth in Chapter 3 of this thesis, and a stress test using a handgrip task is used to assess the validity of the developed cardiac ASL technique. In Chapter 4, myocardial ASL is applied to the study of perfusion of the heart during dialysis.

1.3.2.2. Renal ASL

Typically, renal function is assessed via serum creatinine concentration and glomerular filtration rate (GFR) measures (50) or a renal biopsy. However, these methods are not highly specific or sensitive at an early stage of disease,

and changes in these parameters may arise only later in the development of CKD. As such, more sensitive measures are needed and MRI provides a method for voxel-by-voxel quantification of renal perfusion. In patients with advanced renal insufficiency, the administration of contrast agents should be avoided due to the risk of nephrogenic systemic fibrosis (NSF) (17). This has led to the drive for the development of ASL methods to quantify perfusion of the kidney.

The main challenge associated with ASL of the kidney is the need to overcome respiratory motion. If there is movement between the acquisition of the label and control image, this results in the subtraction images being poorly aligned leading to an error in quantified perfusion. This can be overcome with a breath hold strategy (28), but this places a constraint on acquisition time and may not be feasible for all patients. Also, since ASL relies on averaging over multiple repeats of label and control pairs, this would necessitate multiple breath holds, with the subject holding their breath such that their diaphragm is in the same position for each breath hold. An alternative to breath-holding is to acquire data using respiratory bellows which monitor the breathing cycle and trigger each ASL label and control image at the same point in the respiratory cycle (27), typically end expiration. Alternatively, post-processing approaches can be applied to overcome kidney movement (32).

To date, there have been a number of papers using a variety of ASL techniques for measurement of kidney perfusion. ASL has been applied in the kidney for the assessment of kidney transplants (29), renal masses (33,51) and acute kidney injury (AKI) (26). Chapter 5 of this thesis aims to develop robust renal perfusion measures by evaluating the optimal 2D readout scheme for respiratory triggered renal ASL.

1.4. Thesis Structure

The following lists the material covered in the remainder of this thesis.

Chapter 2 describes the origin of the NMR signal and MRI theory. This includes a more detailed description of the haemodynamic measures of blood flow and perfusion using the MR methods of phase contrast (PC) MRI and Arterial Spin Labelling (ASL) which are developed throughout this thesis.

Chapter 3 describes the development of cardiac ASL. First the method is developed and optimised in healthy volunteers. The technique is then applied to CKD Stage 3 patients and age-matched volunteers to assess changes in cardiac perfusion in response to a handgrip stress challenge. This work was presented at the International Society for Magnetic Resonance in Medicine (ISMRM) as an oral presentation (p0538) and a poster (p2749) in 2015.

Chapter 4 studies CKD Stage 5 patients by performing MRI during haemodialysis to determine the cardiac stress this places on the patient. Intradialytic MRI measures of cardiac function and structure (including assessment of cardiac output, stroke volume, myocardial tagging, and myocardial perfusion as measured using the ASL technique developed in Chapter 3) are assessed. This work will be presented at the International Society for Magnetic Resonance in Medicine (ISMRM) as an oral presentation (p146) in 2016.

Chapter 5 aims to develop renal ASL measures for future studies of Chronic Kidney Disease (CKD) and Acute Kidney Injury (AKI) patients. Renal ASL measures are acquired in healthy subjects using a pulsed ASL scheme and the optimal readout scheme for quantification of renal perfusion is assessed. This work was presented at the International Society for Magnetic Resonance in Medicine (ISMRM) as an oral presentation (p0256) in 2015.

Chapter 6 concludes with an overview of the findings of this thesis. An outline of the future direction in which these developed MRI methods can be applied

in improving the understanding of the pathophysiology of CKD and AKI, and the study of the consequences of dialysis is provided.

1.5. References

1. Anon. File:Heart labelled large.png - Wikimedia Commons.

2. https://www.bcm.edu/healthcare/care-centers/cardiothoracic/procedures/coronary-artery-disease-coronary-bypass. Coronary Artery Disease and Coronary Bypass Surgery.

3.http://www.pennmedicine.org/health_info/body_guide/reftext/html/urin_sys_fin.html. Urinary System Information.

4. Nice. Chronic kidney disease in adults: assessment and management: CG182. 2014.

5. Sarnak MJ. Kidney Disease as a Risk Factor for Development of Cardiovascular Disease: A Statement From the American Heart Association Councils on Kidney in Cardiovascular Disease, High Blood Pressure Research, Clinical Cardiology, and Epidemiology and Prevention. Circulation 2003;108:2154–2169. doi: 10.1161/01.CIR.0000095676.90936.80.

6. Liu M, Li X-C, Lu L, Cao Y, Sun R-R, Chen S, Zhang P-Y. Cardiovascular disease and its relationship with chronic kidney disease. Eur. Rev. Med. Pharmacol. Sci. 2014;18:2918–26.

7. Bargman JM. Advances in Peritoneal Dialysis: A Review. Semin. Dial. 2012;25:545–549. doi: 10.1111/j.1525-139X.2012.01124.x.

8. Himmelfarb J, Alp Ikizler T. Haemodialysis. 2013;1:178–182. doi: 10.1097/SHK.0000000000000058.

9. Foley RN, Parfrey PS, Sarnak MJ. Epidemiology of cardiovascular disease in chronic renal disease. J. Am. Soc. Nephrol. 1998;9:S16–S23.

10. Wanner C, Krane V, März W, Olschewski M, Mann JFE, Ruf G, Ritz E. Atorvastatin in patients with type 2 diabetes mellitus undergoing hemodialysis. N. Engl. J. Med. 2005;353:238–248. doi: 10.1056/NEJMoa043545.

11. Braunwald E, Kloner RA. The stunned myocardium: prolonged, postischemic ventricular dysfunction. Circulation 1982;66:1146–1149. doi: 10.1161/01.CIR.66.6.1146.

12. Anon. microsphere perfusion.pdf.

13. Nakazato R, Berman DS, Alexanderson E, Slomka P. Myocardial perfusion imaging with PET. Imaging Med. 2013;5:35–46. doi: 10.2217/iim.13.1.

14. Bourque JM, Beller G a. Stress Myocardial Perfusion Imaging for Assessing Prognosis: An Update. JACC Cardiovasc. Imaging 2011;4:1305–1319. doi: 10.1016/j.jcmg.2011.10.003.

15. McIntyre CW, Burton JO, Selby NM, Leccisotti L, Korsheed S, Baker CSR, Camici PG. Hemodialysis-induced cardiac dysfunction is associated with an acute reduction in global and segmental myocardial blood flow. Clin. J. Am. Soc. Nephrol. 2008;3:19–26. doi: 10.2215/CJN.03170707.

16. O'Connor JPB, Tofts PS, Miles K a, Parkes LM, Thompson G, Jackson a. Dynamic contrast-enhanced imaging techniques: CT and MRI. Br. J. Radiol. 2011;84:S112–S120. doi: 10.1259/bjr/55166688.

17. Issa N, Poggio ED, Fatica RA, Patel R, Ruggieri PM, Heyka RJ. Nephrogenic systemic fibrosis and its association with gadolinium exposure during MRI. Cleve. Clin. J. Med. 2008;75:95–111. doi: 10.3949/ccjm.75.2.95.

18. Detre JA, Zhang W, Roberts DA, Silva AC, Williams DS, Grandis DJ, Koretsky AP, Leigh JS. Tissue specific perfusion imaging using arterial spin labeling. NMR Biomed. 1994;7:75–82. doi: 10.1002/nbm.1940070112.

19. Detre J. Perfusion Imaging. Magn. Reson. Med. 1992;23:37–45. doi: 10.1002/jmri.24382.

20. Wong EC. An introduction to ASL labeling techniques. J. Magn. Reson. Imaging 2014;40:1–10. doi: 10.1002/jmri.24565.

21. Gunther M, Bock M, Schad LR. Arterial spin labeling in combination with a look-locker sampling strategy: Inflow turbo-sampling EPI-FAIR (ITS-FAIR). Magn. Reson. Med. 2001;46:974–984. doi: 10.1002/mrm.1284.

22. Alsop DC, Detre J a., Golay X, et al. Recommended implementation of arterial spin-labeled perfusion MRI for clinical applications: A consensus of the ISMRM perfusion study group and the european consortium for ASL in dementia. Magn. Reson. Med. 2014;00. doi: 10.1002/mrm.25197.

23. Osch M Van. Basics of Quantification of ASL Matthias van Osch. 2013:1–22.

24. Buxton RB, Frank LR, Wong EC, Siewert B, Warach S, Edelman RR. A general kinetic model for quantitative perfusion imaging with arterial spin labeling. Magn. Reson. Med. 1998;40:383–396. doi: 10.1002/mrm.1910400308.

25. Cutajar M, Thomas DL, Hales PW, Banks T, Clark C a., Gordon I. Comparison of ASL and DCE MRI for the non-invasive measurement of renal blood flow: Quantification and reproducibility. Eur. Radiol. 2014;24:1300–1308. doi: 10.1007/s00330-014-3130-0.

26. Dong J, Yang L, Su T, Yang X, Chen B, Zhang J, Wang X, Jiang X. Quantitative assessment of acute kidney injury by noninvasive arterial spin labeling perfusion MRI: a pilot study. Sci. China. Life Sci. 2013;56:745–50. doi: 10.1007/s11427-013-4503-3.

27. Gardener AG, Francis ST. Multislice perfusion of the kidneys using parallel imaging: Image acquisition and analysis strategies. Magn. Reson. Med. 2010;63:1627–1636. doi: 10.1002/mrm.22387.

28. Gillis K a, McComb C, Foster JE, et al. Inter-study reproducibility of arterial spin labelling magnetic resonance imaging for measurement of renal perfusion in healthy volunteers at 3 Tesla. BMC Nephrol. 2014;15:23. doi: 10.1186/1471-2369-15-23.

29. Heusch P, Wittsack HJ, Blondin D, et al. Functional evaluation of transplanted kidneys using arterial spin labeling MRI. J. Magn. Reson. Imaging 2014;40:84–89. doi: 10.1002/jmri.24336.

30. Park SH, Wang DJJ, Duong TQ. Balanced steady state free precession for arterial spin labeling MRI: Initial experience for blood flow mapping in human brain, retina, and kidney. Magn. Reson. Imaging 2013;31:1044–1050. doi: 10.1016/j.mri.2013.03.024.

31. Martirosian P, Klose U, Mader I, Schick F. FAIR True-FISP Perfusion Imaging of the Kidneys. Magn. Reson. Med. 2004;51:353–361. doi: 10.1002/mrm.10709.

32. Robson PM, Madhuranthakam AJ, Dai W, Pedrosa I, Rofsky NM, Alsop DC. Strategies for reducing respiratory motion artifacts in renal perfusion imaging with arterial spin labeling. Magn. Reson. Med. 2009;61:1374–1387. doi: 10.1002/mrm.21960.

33. Pedrosa I, Rafatzand K, Robson P, Wagner A a., Atkins MB, Rofsky NM, Alsop DC. Arterial spin labeling MR imaging for characterisation of renal masses in patients with impaired renal function: Initial experience. Eur. Radiol. 2012;22:484–492. doi: 10.1007/s00330-011-2250-z.

34. Henderson AC, Prisk GK, Levin DL, Hopkins SR, Buxton RB. Characterizing pulmonary blood flow distribution measured using arterial spin labeling. NMR Biomed. 2009;22:1025–1035. doi: 10.1002/nbm.1407.

35. Raynaud JS, Duteil S, Vaughan JT, Hennel F, Wary C, Leroy-Willig A, Carlier PG. Determination of skeletal muscle perfusion using arterial spin labeling NMRI: Validation by comparison with venous occlusion plethysmography. Magn. Reson. Med. 2001;46:305–311. doi: 10.1002/mrm.1192.

36. Frank LR, Wong EC, Haseler LJ, Buxton RB. Dynamic imaging of perfusion in human skeletal muscle during exercise with arterial spin labeling. Magn. Reson. Med. 1999;42:258–267. doi: 10.1002/(SICI)1522-2594(199908)42:2<258::AID-MRM7>3.0.CO;2-E [pii].

37. Zun Z, Wong EC, Nayak KS. Assessment of myocardial blood flow (MBF) in humans using arterial spin labeling (ASL): feasibility and noise analysis. Magn Reson Med 2009;62:975–983. doi: 10.1002/mrm.22088.

38. Wang DJJ, Bi X, Avants BB, Meng T, Zuehlsdorff S, Detre JA. Estimation of perfusion and arterial transit time in myocardium using free-breathing myocardial arterial spin labeling with navigator-echo. Magn. Reson. Med. 2010;64:1289–1295. doi: 10.1002/mrm.22630.

39. Do HP, Jao TR, Nayak KS. Myocardial arterial spin labeling perfusion imaging with improved sensitivity. J. Cardiovasc. Magn. Reson. 2014;16:15. doi: 10.1186/1532-429X-16-15.

40. Kampf T, Helluy X, Gutjahr FT, Winter P, Meyer CB, Jakob PM, Bauer WR, Ziener CH. Myocardial perfusion quantification using the T1-based FAIR-ASL

method: The influence of heart anatomy, cardiopulmonary blood flow and look-locker readout. Magn. Reson. Med. 2014;71:1784–1797. doi: 10.1002/mrm.24843.

41. Epstein FH, Meyer CH. Myocardial perfusion using arterial spin labeling CMR: Promise and challenges. JACC Cardiovasc. Imaging 2011;4:1262–1264. doi: 10.1016/j.jcmg.2011.08.015.

42. Northrup BE, McCommis KS, Zhang H, Ray S, Woodard PK, Gropler RJ, Zheng J. Resting myocardial perfusion quantification with CMR arterial spin labeling at 1.5 T and 3.0 T. J. Cardiovasc. Magn. Reson. 2008;10:53. doi: 10.1186/1532-429X-10-53.

43. Campbell-Washburn AE, Price AN, Wells J a., Thomas DL, Ordidge RJ, Lythgoe MF. Cardiac arterial spin labeling using segmented ECG-gated Look-Locker FAIR: Variability and repeatability in preclinical studies. Magn. Reson. Med. 2013;69:238–247. doi: 10.1002/mrm.24243.

44. Campbell-Washburn AE, Zhang H, Siow BM, Price AN, Lythgoe MF, Ordidge RJ, Thomas DL. Multislice cardiac arterial spin labeling using improved myocardial perfusion quantification with simultaneously measured blood pool input function. Magn. Reson. Med. 2013;70:1125–1136. doi: 10.1002/mrm.24545.

45. Belle V, Kahler E, Waller C, Rommel E, Voll S, Hiller KH, Bauer WR, Haase a. In vivo quantitative mapping of cardiac perfusion in rats using a noninvasive MR spin-labeling method. J. Magn. Reson. Imaging 8:1240–1245. doi: 10.1002/jmri.1880080610.

46. Poncelet BP, Koelling TM, Schmidt CJ, Kwong KK, Reese TG, Ledden P, Kantor HL, Brady TJ, Weisskoff RM. Measurement of human myocardial perfusion by double-gated flow alternating inversion recovery EPI. Magn. Reson. Med. 1999;41:510–519. doi: 10.1002/(SICI)1522-2594(199903)41:3<510::AID-MRM13>3.0.CO;2-G.

47. Wacker CM, Fidler F, Dueren C, Hirn S, Jakob PM, Ertl G, Haase a, Bauer WR. Quantitative assessment of myocardial perfusion with a spin-labeling technique: preliminary results in patients with coronary artery disease. J Magn Reson Imaging 2003;18:555–560. doi: 10.1002/jmri.10386.

48. Zun Z, Varadarajan P, Pai RG, Wong EC, Nayak KS. Arterial spin labeled CMR detects clinically relevant increase in myocardial blood flow with vasodilation. JACC Cardiovasc. Imaging 2011;4:1253–1261. doi: 10.1016/j.jcmg.2011.06.023.

49. Zun Z, Wong EC, Nayak KS. Assessment of myocardial blood flow (MBF) in humans using arterial spin labeling (ASL): feasibility and noise analysis. Magn. Reson. Med. 2009;62:975–983. doi: 10.1002/mrm.22088.

50. Stevens L a., Levey AS. Measurement of kidney function. Med. Clin. North Am. 2005;89:457–473. doi: 10.1016/j.mcna.2004.11.009.

51. Lanzman RS, Robson PM, Sun MR, Patel a. D, Mentore K, Wagner a. a., Genega EM, Rofsky NM, Alsop DC, Pedrosa I. Arterial Spin-labeling MR Imaging of Renal Masses: Correlation with Histopathologic Findings. Radiology 2012;265:799–808. doi: 10.1148/radiol.12112260.

2 Principles of MRI

This chapter provides an overview to nuclear magnetic resonance (NMR) and the magnetic resonance imaging (MRI) techniques necessary to understand the work presented in this thesis. This chapter begins with an overview of the origins of the NMR signal, the specific physics of MRI, and how image contrast is formed. MRI techniques developed and used in this thesis to assess blood flow and tissue perfusion using phase contrast MRI (PC-MRI) and arterial spin labelling (ASL) are then described and subsequently applied in Chapters 3-5. Finally, the method of cardiac tagging is outlined which is then implemented in Chapter 4.

2.1 Origin of NMR signal

A nucleus has three fundamental properties: mass (m), electronic charge (q) and spin (I). Magnetic resonance is based on the interaction between a nucleus that possesses spin and an applied magnetic field ($B = B_0\boldsymbol{k}$). Since nuclei are charged they also possess a magnetic moment $\boldsymbol{\mu}$, and as they have mass this generates spin angular moment, $\boldsymbol{P}$, where:

$$\boldsymbol{\mu} = \gamma \boldsymbol{P} \qquad 2\text{-}1$$

and γ is the gyromagnetic ratio which is a property specific to each nucleus; $\gamma = 267.5\ x\ 10^6\ rads^{-1}\ T^{-1}$ for the hydrogen nucleus. Table 2.1-1 shows the spin and gyromagnetic ratio of common nuclei.

Isotope	Nuclear Spin (I)	Gyromagnetic Ratio (γ) ($rads^{-1}T^{-1}$)
^{1}H	$^{1}/_{2}$	267.522
^{2}H	1	41.066
^{13}C	$^{1}/_{2}$	67.283
^{14}N	1	19.338
^{15}N	$^{1}/_{2}$	-27.126
^{17}O	$^{5}/_{2}$	-36.281
^{19}F	$^{1}/_{2}$	251.815
^{23}Na	$^{3}/_{2}$	70.808
^{31}P	$^{1}/_{2}$	108.394

Table 2.1-1: *Table of common isotopes and their nuclear spin (I) and gyromagnetic ratio (γ).*

Nuclear spin is an intrinsic quantum mechanical property of the nucleus. When a nuclei consists of multiple protons and neutrons, the spins combine to result in a net nuclear spin (I). Unlike macroscopic angular momentum, nuclear spin can only take integer or half integer values ($0, {}^{1}/_{2}, 1, {}^{3}/_{2}$ etc..).

In non-relativistic quantum mechanics, the magnitude of the spin angular momentum vector $\boldsymbol{P}$ of a nucleus with spin I is

$$\boldsymbol{P} = \hbar\sqrt{I(I+1)} \qquad 2\text{-}2$$

where $\hbar = h/2\pi$ and h is Planck's constant. For nuclei with spin I, there are $2I+1$ spin states (or eigenstates) given by the quantum number m_I, where $m_I = I, (I-1), (I-2), \ldots, {}^1/_2 \ldots - {}^1/_2, \ldots, -I$.

The z-component of the spin angular momentum of a spin state m_I is defined as

$$P_z = \hbar m_I \qquad 2\text{-}3$$

The orientation of P_z is shown in Figure 2.1-1 for a nuclei with spin ${}^1/_2$.

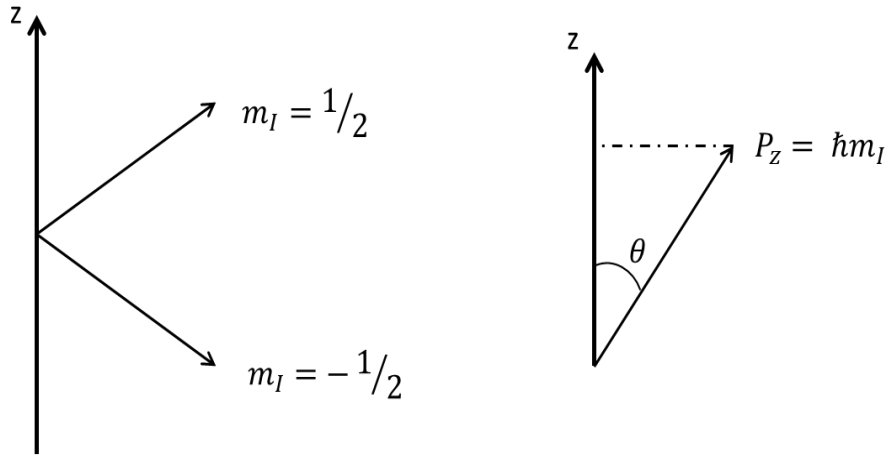

Figure 2.1-1: *The relationship between the z-component of spin angular momentum* $\boldsymbol{P_z}$ *and quantum number* $\boldsymbol{m_I}$.

An NMR signal can be detected from any nuclei with spin, but MRI is most often tuned to the signal from hydrogen nuclei contained in water, as this is the most abundant nucleus in the human body. Protons have spin $I = {}^1/_2$ and

spin states of $m_I = +{}^1/_2$ or $-{}^1/_2$. In the absence of a magnetic field, magnetic moments align in various directions. When the magnetic moments are placed in an external magnetic field, $B = B_o\boldsymbol{k}$, they align in parallel or anti-parallel to the external field as illustrated in Figure 2.1-2.

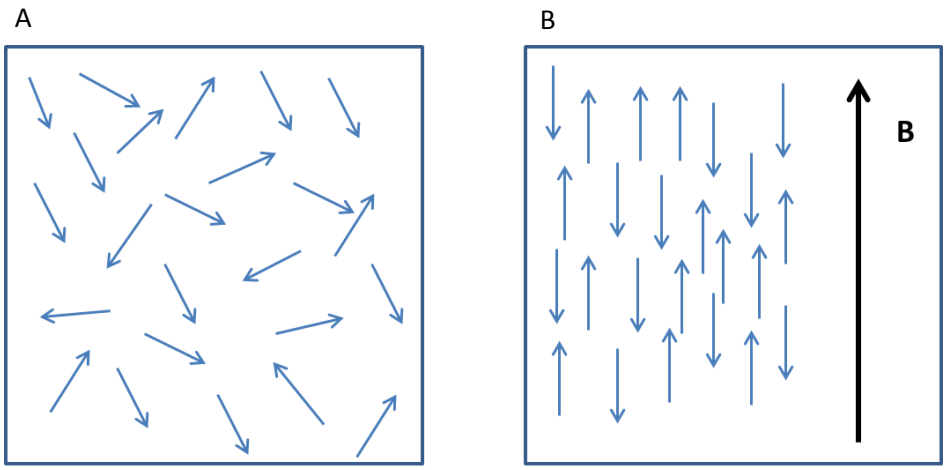

Figure 2.1-2: *Illustration showing (A) in the absence of a magnetic field, the magnetic moments (shown by arrows) align in various directions. (B) In the presence of a magnetic field, the magnetic moments align either parallel or anti-parallel with the applied field.*

When a nucleus with magnetic moment $\boldsymbol{\mu}$ is placed inside a magnetic field, $\boldsymbol{B}$, the associated energy, E, is given by

$$E = -\boldsymbol{\mu}.\boldsymbol{B} \qquad 2\text{-}4$$

Combining this expression with Equation 2-1, gives

$$E = -\gamma \boldsymbol{P}.\boldsymbol{B} \qquad 2\text{-}5$$

Since the main magnetic field, B_z, is defined to be along the z-axis, $\boldsymbol{B} = B_z\boldsymbol{k}$, this gives

$$E = -\gamma\hbar B_z m_I \qquad 2\text{-}6$$

For a proton, with spin $I = {}^{1}/_{2}$, $m_I = \pm {}^{1}/_{2}$ and so the energy difference between the two spin states in an external magnetic field B_z is

$$\Delta E = \gamma \hbar B_z. \qquad 2\text{-}7$$

This separation in energy levels is known as Zeeman splitting, as illustrated in Figure 2.1-3.

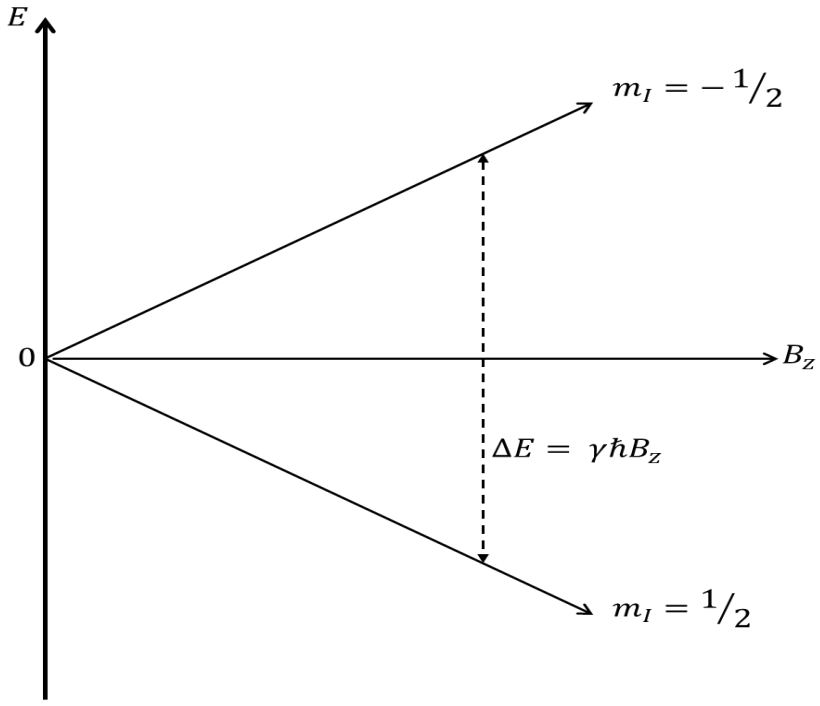

Figure 2.1-3: *Zeeman splitting illustrating the energy difference between protons in the higher and lower energy states as a function of applied magnetic field* $\boldsymbol{B_z}$.

When a single spin, $\boldsymbol{\mu}$, is placed in a magnetic field, $\boldsymbol{B}$, its magnetic moment will experience a torque which can be equated to the change in spin angular momentum,

$$\frac{d\boldsymbol{P}}{dt} = \boldsymbol{\mu} \times \boldsymbol{B} \qquad 2\text{-}8$$

Using Equation 2-1,

$$\frac{d\boldsymbol{\mu}}{dt} = \gamma \boldsymbol{\mu} \times \boldsymbol{B} \qquad 2\text{-}9$$

which is the equation of precession of motion. Solving this equation in the x, y and z directions, whilst assuming the applied magnetic field B_z is along the z axis, gives

$$\begin{aligned} \mu_x(t) &= \mu_x(0)\cos(\gamma B_z t) + \mu_y(0)\sin(\gamma B_z t) \\ \mu_y(t) &= -\mu_x(0)\sin(\gamma B_z t) + \mu_y(0)\cos(\gamma B_z t) \\ \mu_z &= 0 \end{aligned} \qquad 2\text{-}10$$

These equations describe the precession of the magnetic moment about the z-axis with an angular frequency, ω, of γB_z. This rate of precession is known as the Larmor frequency. For protons in a 3 Tesla MR system, the Larmor frequency of a proton is -128 MHz. Most nuclei have a positive gyromagnetic ratio resulting in a negative Larmor frequency which indicates that the spins precess clockwise about the z-axis, as illustrated in Figure 2.1-4.

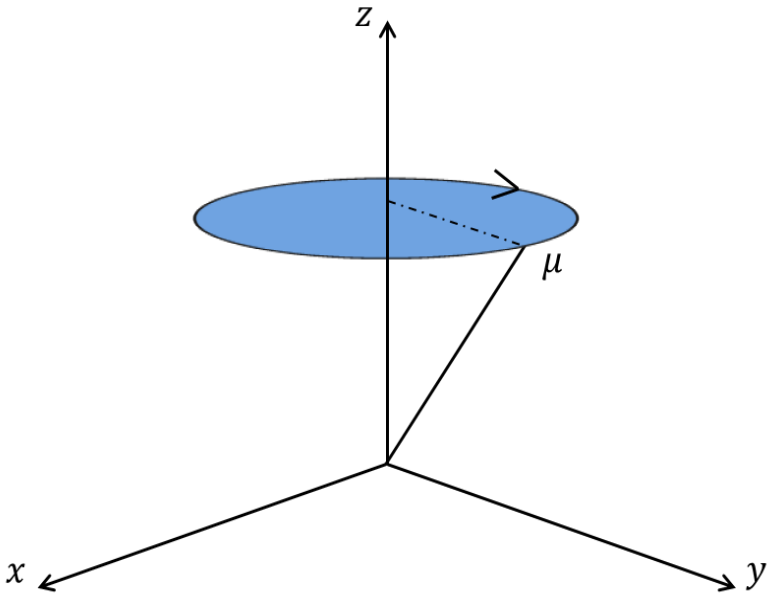

Figure 2.1-4: *Precession of a spin, μ, about the z-axis inside a magnetic field of* $\boldsymbol{B} = \boldsymbol{B_z k}$.

In NMR, an oscillating, time dependent, magnetic field $\boldsymbol{B_1}(t)$ of frequency ω is then applied perpendicular to the z-axis,

$$\boldsymbol{B_1}(t) = 2B_1 \cos(\omega t)\, \boldsymbol{i} \qquad 2\text{-}11$$

$\boldsymbol{B_1}(t)$ is linearly polarised along the x-axis, and so can be resolved into circular components rotating in the clockwise and anti-clockwise directions at Larmor frequency, ω.

$$\boldsymbol{B_a}(t) = B_1[\cos(\omega t)\, \boldsymbol{i} + \sin(\omega t)\, \boldsymbol{j}] \qquad 2\text{-}12$$
$$\boldsymbol{B_c}(t) = B_1[\cos(\omega t)\, \boldsymbol{i} - \sin(\omega t)\, \boldsymbol{j}]$$

where $\boldsymbol{B_a}(t)$ denotes the anti-clockwise component and $\boldsymbol{B_c}(t)$ is the clockwise component. If ω is matched to the Larmor frequency, ω_L, the contribution from B_a is negligible as it rotates at a frequency of $-2\omega_L$, far off-resonance. In contrast, $\boldsymbol{B_c}(t)$ rotates at the Larmor frequency, ω_L, and is on-resonance. This leads to a constant torque due to $\boldsymbol{B_c}(t)$ on the magnetic moment which perturbs the motion of magnetic moment, such that

$$\frac{d\boldsymbol{\mu}}{dt} = \gamma \boldsymbol{\mu}\, \mathbf{x}\, [\boldsymbol{B} + \boldsymbol{B_c}(\boldsymbol{t})] \qquad 2\text{-}13$$

This additional rotation about the x-axis causes a change in the precessional angle of the magnetic moment.

To understand the effect of the applied radiofrequency pulse, $\boldsymbol{B_c}(t)$, it is simpler to move into a rotating frame of reference. In a frame of reference rotating around the z-axis at the Larmor frequency, $\boldsymbol{B_1}(t)$ is stationary along the x-axis as shown in Figure 2.1-5.

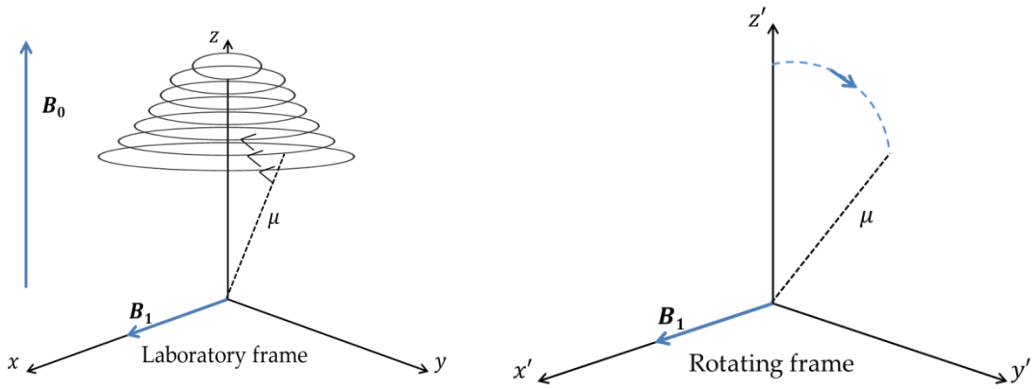

Figure 2.1-5: *Laboratory frame of reference showing the precession of a spin about the x- and z-axis and the corresponding rotating frame of reference with μ rotating about the x′ axis.*

In the rotating frame, the unit vectors can be written as ($\boldsymbol{i}'$, $\boldsymbol{j}'$, $\boldsymbol{k}$) within an axis system (x', y', z) and the time dependency of $\boldsymbol{B_1}(t)$ is removed such that the $\boldsymbol{B_1}$ field can be described by

$$\boldsymbol{B_1}(t) = B_1\boldsymbol{i}' \tag{2-14}$$

This results in the equation of motion of the magnetic moment in the rotating frame of

$$\left(\frac{d\boldsymbol{\mu}}{dt}\right)_{x',y',z} = \gamma\boldsymbol{\mu}\,\mathbf{x}\left(B_1\boldsymbol{i}' + \left(B_z - \frac{\omega}{\gamma}\right)\boldsymbol{k}\right) \tag{2-15}$$

which can be simplified to

$$\left(\frac{d\boldsymbol{\mu}}{dt}\right)_{x',y',z} = \gamma\boldsymbol{\mu}\,\mathbf{x}\boldsymbol{B_{eff}} \tag{2-16}$$

where

$$\boldsymbol{B_{eff}} = B_1\boldsymbol{i}' + \left(B_z - \frac{\omega}{\gamma}\right)\boldsymbol{k} \tag{2-17}$$

This equation shows that in the rotating frame of reference, the magnetic moment, $\boldsymbol{\mu}$, rotates about $\boldsymbol{B_{eff}}$ at a precessional frequency, $\omega_{eff} = \gamma B_{eff}$. When $\boldsymbol{B_1(t)}$ is applied on resonance, $\boldsymbol{B_{eff}} = \boldsymbol{B_1 i'}$, and the magnetic moment will rotate in the $y'z$ plane at a frequency $\omega = \gamma B_1$.

If a radiofrequency pulse with frequency ω_L is applied to a system for a time t_w, the magnetic moment will tip through a precessional angle θ given by

$$\omega = \frac{d\theta}{dt} = \gamma B_1 \quad \therefore \quad \theta = \gamma B_1 t_w \tag{2-18}$$

which corresponds to inducing transitions from the lower to higher energy state of the system.

So far only a single spin with magnetic moment, $\boldsymbol{\mu}$, has been considered. However, in a single voxel in MRI there will be of the order 10^{20} protons. The bulk magnetisation, $\boldsymbol{M}$, is calculated as the sum of the individual magnetic moments in the system per unit volume, V.

$$\boldsymbol{M} = \frac{1}{V} \sum_{\substack{number\ of \\ protons\ in\ V}} \boldsymbol{\mu_i} \tag{2-19}$$

In an ensemble of spins, such as the human body, most of the magnetic moments will cancel out due to the parallel/anti-parallel alignment. However, a net spin will result in the lower energy state (Figure 2.1-6); with the distribution of spins across the two energy states being determined by the Maxwell-Boltzmann distribution:

$$\frac{N_-}{N_+} = e^{\frac{-\Delta E}{k_B T}} = e^{\frac{-\hbar \gamma B_z}{k_B T}} \tag{2-20}$$

where N_+ denotes the number of spins in the lower energy state ($m_I = {}^1/_2$) and N_- is the number of anti-parallel spins, in the higher energy state ($m_I = -{}^1/_2$). k_B is the Boltzmann constant, T is the temperature in Kelvin, and ΔE is

the energy difference between the two energy states caused by Zeeman splitting.

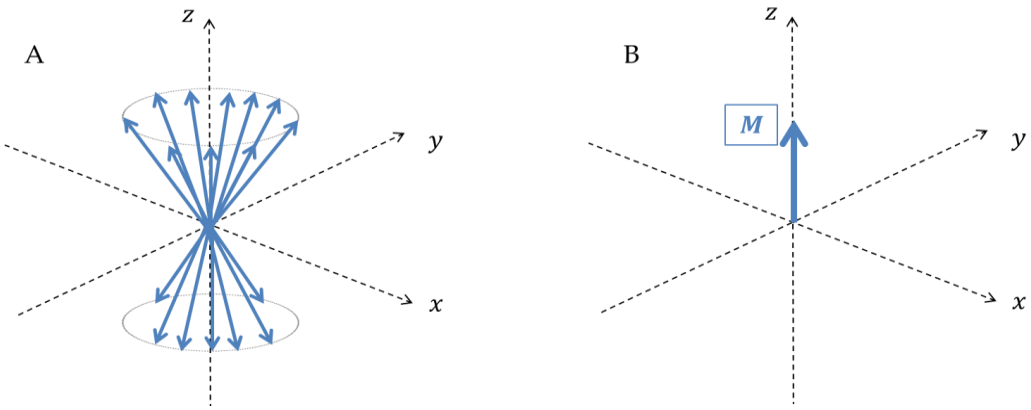

Figure 2.1-6: *(A) Protons move in either the positive or negative direction. (B) There are more protons in the positive direction resulting in a non-zero net magnetisation* ***M*** *in the positive direction parallel to* $\boldsymbol{B_0}$.

In the high temperature limit, $k_B T \gg \Delta E$. Equation 2-20 can be written as

$$\frac{N_-}{N_+} = 1 - \frac{\hbar \gamma B_z}{kT} \qquad 2\text{-}21$$

The population difference, n, between the lower and higher energy state can then be approximated as

$$n = N_+ - N_- = \frac{N_+ \hbar \gamma B_z}{kT} \qquad 2\text{-}22$$

As $N_+ \approx N_-$, the population difference between the lower and higher energy states is given by

$$n = \frac{N \hbar \gamma B_z}{2kT} \qquad 2\text{-}23$$

where $N = N_+ + N_- = 2N_-$, the total number of spins. The bulk magnetisation is then given by

$$\boldsymbol{M} = n\boldsymbol{\mu} = \frac{1}{4}\frac{N(\hbar\gamma)^2 B_z}{k_B T} \qquad 2\text{-}24$$

and is proportional to the applied magnetic field B_z and inversely proportional to the temperature of the system, T. This bulk magnetisation, $\boldsymbol{M}$, obeys the same classical equation of motion as a single spin and can be described by the Bloch equation

$$\frac{d\boldsymbol{M}}{dt} = \gamma \boldsymbol{M} \times \boldsymbol{B} \qquad 2\text{-}25$$

The radiofrequency pulses that are most often used in MRI pulse sequences include an excitation pulse where the flip angle θ is 90^o, or an inversion pulse for which the flip angle is 180^o. A radiofrequency pulse with flip angle θ of 90^o results in net magnetisation M_0 in the xy′- plane and zero in the z plane. When $\theta = 180^o$, the magnetisation is tipped along the negative z-axis and there is no component in the xy′ plane. The effect of an excitation and inversion pulse is shown in Figure 2.1-7. Refocusing pulses can also be applied which act to bring the magnetisation back into phase (see section 2.5.2).

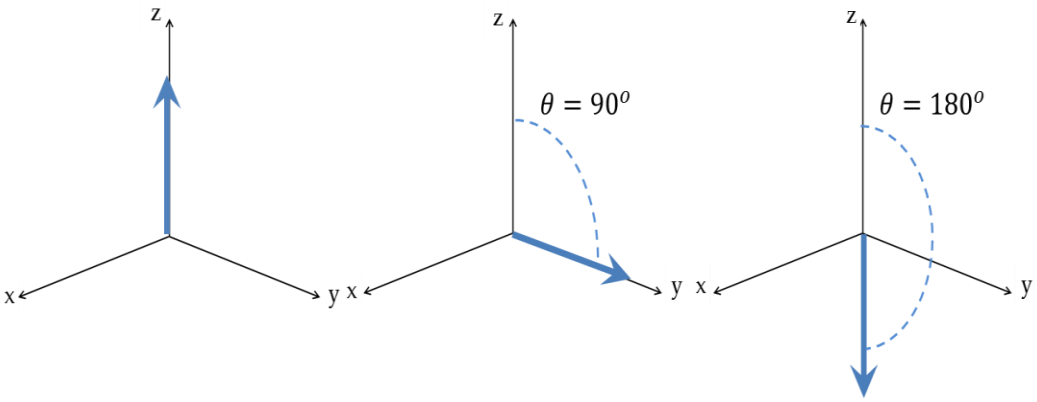

Figure 2.1-7: *Effect of a* $\mathbf{90^o}$ *and* $\mathbf{180^o}$ *pulse where the blue arrow shows the magnetisation* $\boldsymbol{M_z}$.

2.2 Relaxation

The spin system is classified in thermal equilibrium such that longitudinal magnetisation $M_z = M_0$ and transverse magnetisation $M_x = M_y = 0$.

When a radiofrequency $\boldsymbol{B_1(t)}$ pulse is applied, the magnetisation $\boldsymbol{M}$ is tipped away from the z-axis, and will gain phase coherence whilst precessing in the xy' plane. A 90° pulse results in equalisation of spin states with no component of $\boldsymbol{M}$ remaining in the z direction, and M_{xy} takes a finite quantity. On cessation of the radiofrequency pulse, the spins return to their lowest energy state and dephase to regain equilibrium. There are two modes of relaxation to return to equilibrium: longitudinal (T_1) relaxation is the process whereby longitudinal spin populations return to equilibrium. Transverse (T_2 or T_2^*) relaxation is the process of the decay of spin coherence. These are two independent relaxation processes, typically T_2 relaxation is a faster process than T_1relaxation with T_1 in the abdomen being around 1000 ms at 3T and T_2 approximately 70 ms.

2.2.1 Longitudinal (T_1) Relaxation

Longitudinal (T_1) relaxation is the process by which the net longitudinal magnetisation returns to the equilibrium Boltzmann distribution. As the longitudinal component of the magnetisation returns towards M_0 the energy of the spin system decreases with the spin system moving from a high to low energy state. Energy leaves the spin system with heat being transferred into nearby nuclei via collisions, rotations or electromagnetic interactions. This energy is very small compared to typical molecular kinetic energies. The T_1 relaxation time differs between biological materials depending on the efficiency of the energy transfer between protons and the surrounding lattice. T_1 relaxation time values are longer for water and tissue as the energy transfer is inefficient due to their natural motional frequency being much greater than the Larmor frequency. In contrast, fat has a short efficient T_1 relaxation since the natural motional frequency is equal to the Larmor frequency. Recently, T_1

relaxation time values have been suggested to indicate areas of fibrosis, as the T_1 relaxation time increases with an increased composition of oedema and pooling of water molecules (1). This is discussed further in Chapter 4.

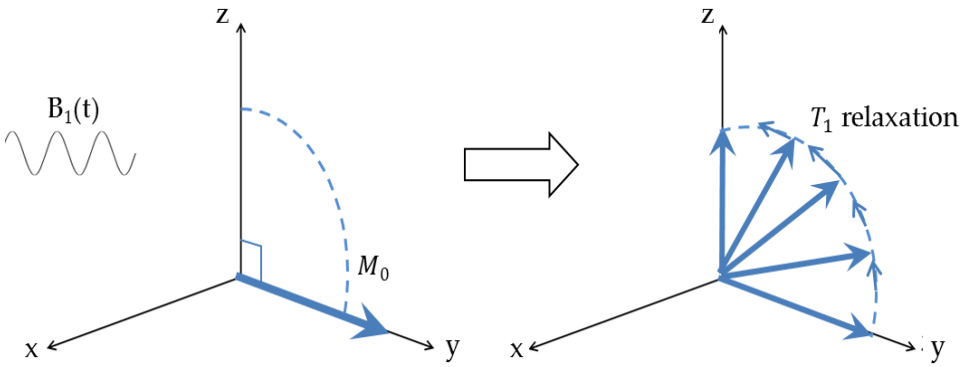

Figure 2.2-1: ***T_1*** *relaxation. The magnetisation M_0 (blue line) is knocked into the xy-plane by a 90° pulse. Following the RF pulse, the magnetisation then returns to equilibrium with the recovery governed by the T_1 relaxation time.*

2.2.2 Quantification of Longitudinal relaxation time (T_1)

The simplest and most commonly used pulse sequence for accurate quantification of T_1 values is the inversion recovery scheme.

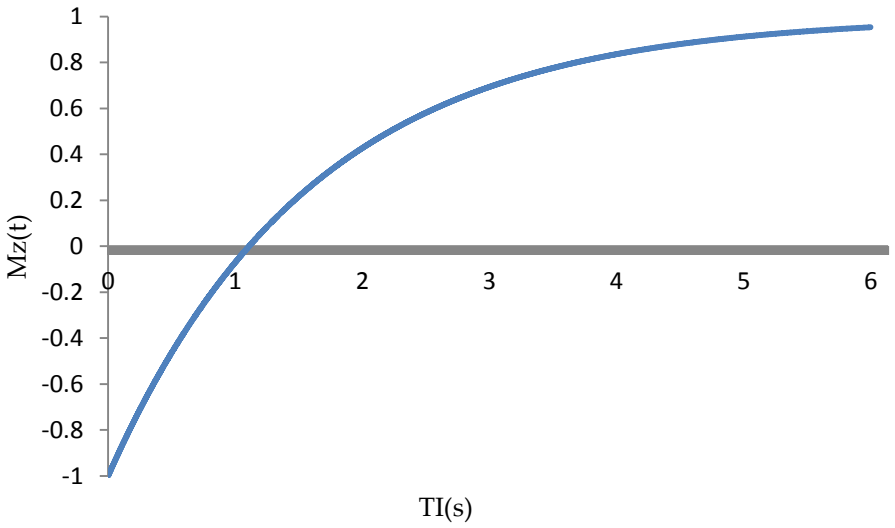

Figure 2.2-2: *Inversion recovery curve for a sample with T_1 of 1.6 s.*

In an inversion recovery scheme, a 180° RF pulse is applied to invert the magnetisation. This is followed at a given inversion time (*TI*) by a 90° RF pulse which rotates the residual magnetisation into the transverse plane where it can be detected by the RF coil. By repeating the experiment for multiple *TI* values, (Figure 2.2-2) data can be fit to the solution of the Bloch equation:

$$\frac{dM_z}{dt} = \frac{M_0 - M_z}{T_1}, \qquad 2\text{-}26$$

to estimate T_1. Integrating between the limits of $-M_0$ to $M_z(t)$ from time $t = 0$ to t = *TI* results in the equation

$$M_z(t) = M_0(1 - 2e^{-TI/T_1}) \qquad 2\text{-}27$$

It is important that the magnetisation is fully recovered between each 180° pulse, so a repetition time (TR) of greater than 5 times T_1 is left between repeats. This can result in a very time consuming acquisition to sample a number of *TI* values over the inversion recovery curve.

2.2.3 Look Locker (LL) readout scheme

To speed up the acquisition of multi-time point T_1 imaging, the Look-Locker (LL) T_1 mapping scheme was introduced (2). A Look-Locker readout scheme allows multiple low flip angle readouts to be acquired at different *TI*s following a single inversion pulse in a reduced scan time, as shown in Figure 2.2-3, to sample the T_1 recovery.

Low flip angle (α) readouts which are equally temporally spaced (TI_2) result in an apparent T_1 being measured, as the magnetisation is partially saturated by the Look-Locker readout pulses, this is known as $T_{1,LL}$. The true T_1 value can then be calculated using the equation

$$\frac{1}{T_{1,LL}} = \frac{1}{T_1} - \frac{\ln(cos\alpha)}{TI_2} \qquad 2\text{-}28$$

Alternatively, T_1 can be quantified by iteratively modelling the Look-Locker recovery curve. The first time point after the inversion pulse follows a standard inversion recovery (Equation 2-27), with the longitudinal magnetisation at this time point being given by $M_z = M_i \sin\alpha$ and the transverse magnetisation, $M_{xy} = M_i \cos\alpha$. For subsequent time points the transverse magnetisation is iteratively fit from the magnetisation of the *(i-1)* time point such that

2-29

$$M_i = M_0\left(1 - e^{-\frac{TI(i)-TI(i-1)}{T_1}}\right) + M_z(i-1)e^{\frac{TI(i)-TI(i-1)}{T_1}}$$

where i denotes the current time point. By iteratively fitting to these equations an estimate of the T1 can be obtained.

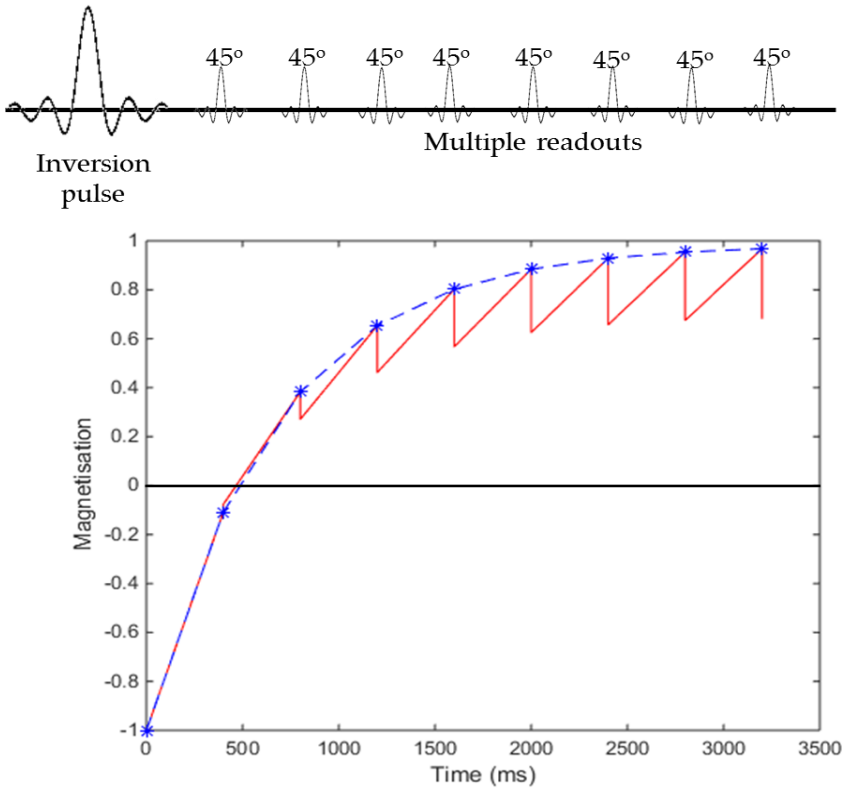

Figure 2.2-3: *Look locker readout scheme and resulting recovery curve simulated for a T1 of tissue of 1600ms, flip angle of 45° and readout spacing of 400ms.*

For T_1 mapping of the heart, an adaptation of a Look-Locker scheme, known as a modified Look-Locker inversion recovery (MOLLI), can be used (3). In cardiac imaging, the readouts must be synchronised to the cardiac cycle in order to eliminate motion of the heart. This results in a readout temporal spacing of approximately one second. For such a scheme there would only be enough time to acquire approximately three readouts before the signal has fully recovered (~3 s). To overcome this, the MOLLI scheme acquires multiple Look-Locker datasets, each with a different initial post-label delay, and then combines these datasets to span the T_1 recovery curve. This technique is described further in Chapter 3.

2.2.4 Transverse Relaxation

Transverse (T_2) relaxation is the process by which the transverse component of the magnetisation M_{xy} dephases. Immediately after a radiofrequency pulse is applied, all the spins are in phase and precess at approximately the same frequency. On cessation of the RF pulse, the spins de-phase over time, Figure 2.2-4, and the M_{xy} component of the magnetisation decreases exponentially as a function of T_2 (Figure 2.2-4).

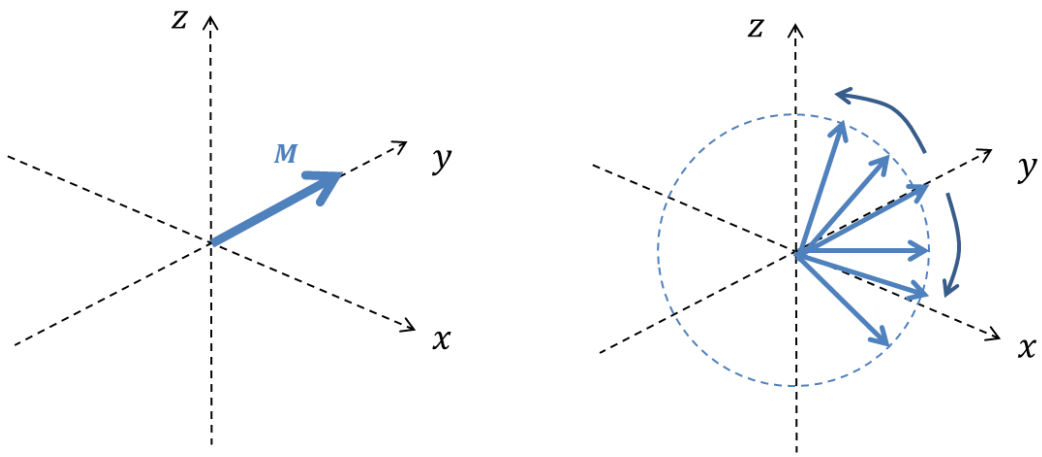

Figure 2.2-4: T_2 *relaxation (a) Magnetisation immediately after a 90° pulse and (b) dephasing of spins in the rotating frame of reference.*

The T_2 relaxation time is long in pure water ($\sim 3-4$ seconds), as water molecules move faster that the Larmor frequency, but is much shorter in other fluids and tissues.

The T_2 relaxation time can be derived from solving the coupled Bloch equations

$$\frac{dM_x}{dt} = -\frac{M_x}{T_2} + \gamma M_y B_z,$$
$$\frac{dM_y}{dt} = -\frac{M_y}{T_2} - \gamma M_x B_z, \qquad 2\text{-}30$$

Following a 90° pulse, this can be integrated with the limits M_0 to $M_{xy}(t)$ and $t = 0$ to echo time, TE, giving

$$M_{xy}(t) = M_0 e^{-TE/T_2} \qquad 2\text{-}31$$

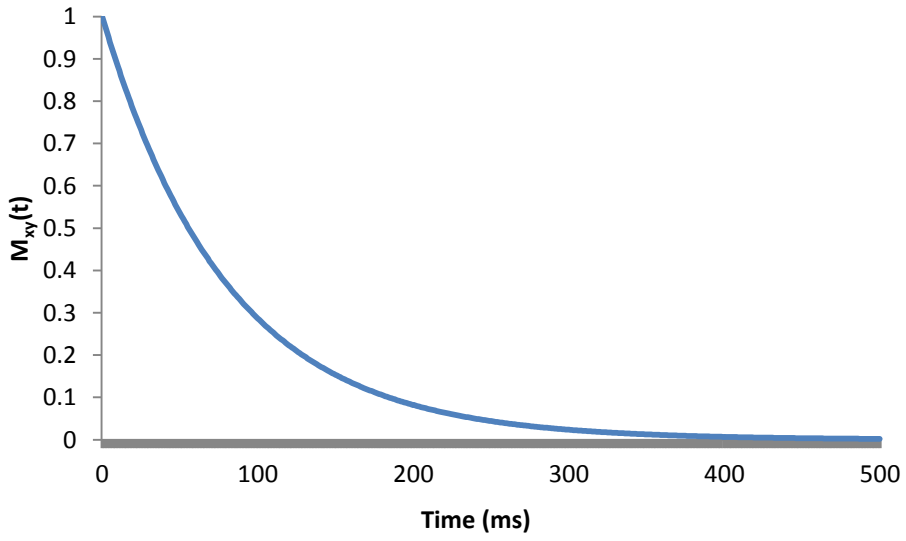

Figure 2.2-5: *T_2 decay curve for a T_2 of 80ms.*

In practice, the transverse magnetisation decays faster than the T_2 relaxation time as it also depends on the external magnetic field inhomogeneities (e.g. due to hardware problems or magnetic susceptibility differences) and

interactions between the samples which can lead to a T_2' relaxation term. This results in a T_2^* relaxation rate which is given by

$$\frac{1}{T_2^*} = \frac{1}{T_2} + \frac{1}{T_2'} \qquad 2\text{-}32$$

The received decaying MR signal is known as the free induction decay (FID).

2.3 Contrast

Image contrast can be broadly classified from a gradient echo or spin echo based scheme.

2.3.1 Gradient echo scheme

A gradient-echo (GE) is produced by a single radio-frequency pulse followed by a gradient reversal, as shown by Figure 2.3-1.

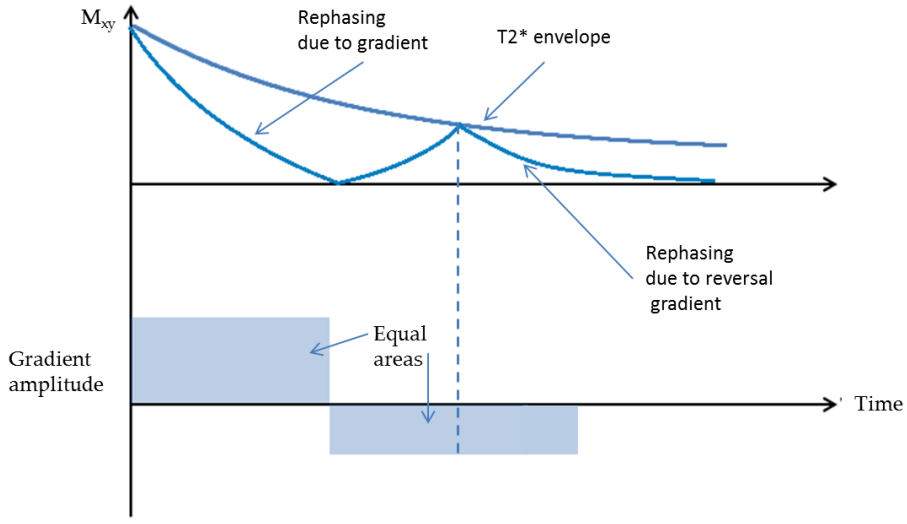

Figure 2.3-1: *Gradient-echo scheme showing refocussing of signal at the centre of the gradient reversal.*

The magnetisation dephases in the transverse plane under a negative read-out gradient which causes the spins to dephase faster. The readout gradient is then reversed which cause the spins to refocus and create an echo at the centre of the gradient. The echo time is defined as the time between the excitation pulse and the echo. Field homogeneity is important for GE imaging as the gradient reversal only refocuses spins that had been dephased by the gradient itself, and so phase shifts resulting from field inhomogeneities, static tissue susceptibility gradients and chemical shifts are not corrected.

2.3.2 Spin echo

In a spin-echo (SE) pulse sequence (Figure 2.3-2), a 180° RF pulse is used to refocus the magnetisation in the transverse plane. Spins are first excited using a 90° pulse. Due to the local inhomogeneity, some spins may precess faster relative to others and so spread out across the transverse plane. A 180° pulse is then applied which flips the magnetisation about the y-plane causing the spins to refocus. When the spins refocus, an echo occurs at a time twice the time between the 90° and 180° pulse. The time between the application of the 90° pulse and the peak of the echo signal is known as the echo time (TE).

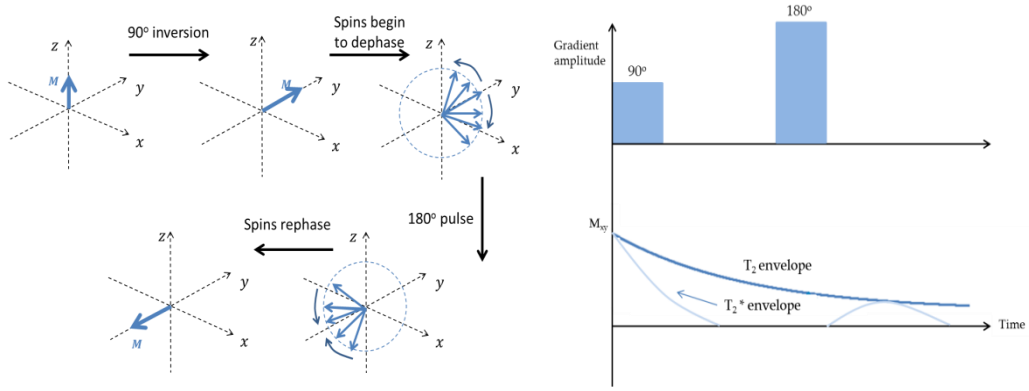

Figure 2.3-2: *Spin-echo scheme shown in the rotating frame A) A 90° pulse is applied to tip the magnetisation into the xy-plane then the spins begin to dephase. A 180° pulse is applied causing the spins to rephase in the xy plane at time TE. B) The 90° and 180° gradients applied during the SE-EPI sequence and resulting MR signal.*

2.4 Image formation

The following section describes techniques for image formation.

2.4.1 Slice selection

Applying an on-resonance radiofrequency pulse to a sample in a uniform magnetic field will excite the entire volume, which is not medically useful. In order to be selective about which area is excited, slice selection can be used.

If a field gradient G_z is applied, spins will experience a magnetic field,

$$B = B_0 + G_z z, \tag{2-33}$$

at a given position z. This results in the sample's resonant frequency being dependent on the spins position along the z-axis

$$\omega = \gamma(B_0 + G_z z), \tag{2-34}$$

Use of a frequency selective radiofrequency pulse will therefore excite a slice containing nuclei with the same bandwidth in resonant frequency. The thickness of this slice can be changed by adjusting the magnitude of the field gradient, G_z, and the bandwidth of the RF pulse, $\Delta\omega$.

$$\Delta z = \frac{\Delta\omega}{\gamma G_z} \tag{2-35}$$

Generally, a rectangular slice profile is desired. To achieve a rectangular slice profile in the Fourier domain, a sinc RF pulse is used. In practice, RF pulses are truncated to limit the duration of the excitation pulse, leading to some imperfections in the pulse profile. Since the gradient applied in combination with the RF pulse will result in the dephasing of the spins, a gradient of opposite polarity and half the magnitude of the original gradient is applied to re-establish the original phase of the spins.

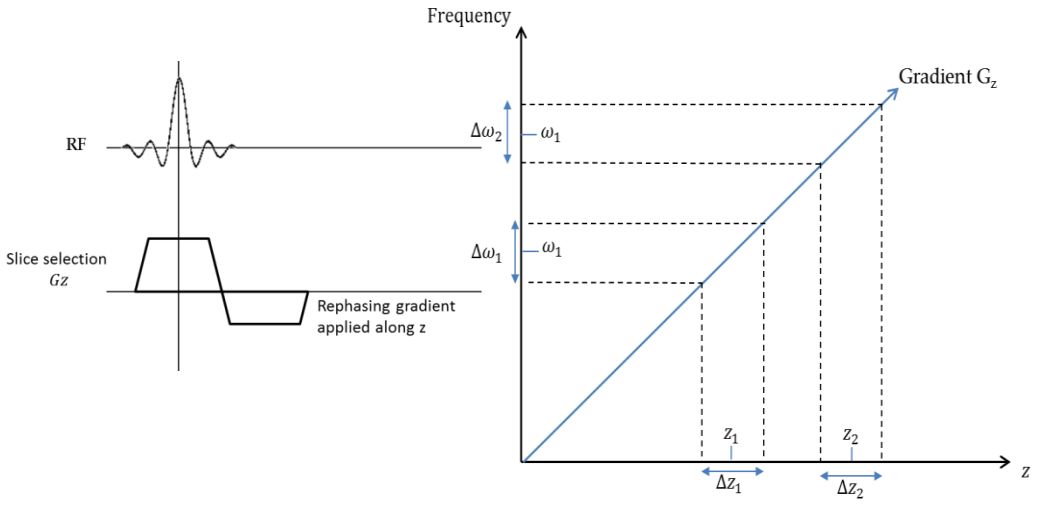

Figure 2.4-1: *Slice selection showing RF pulses with central frequency* $\boldsymbol{\omega_1}$ *and* $\boldsymbol{\omega_2}$ *of bandwidth* $\boldsymbol{\Delta\omega_1}$ *and* $\boldsymbol{\Delta\omega_2}$. *In combination with a gradient* $\boldsymbol{G_z}$ *this results in slice thicknesses* $\boldsymbol{\Delta z_1}$ *and* $\boldsymbol{\Delta z_2}$ *centred at position* $\boldsymbol{z_1}$ *and* $\boldsymbol{z_2}$.

2.4.2 Phase and frequency encoding

Information from the excited slice is then encoded to an image using phase and frequency encoding. A phase encoding pulse is applied in the y-direction prior to sampling the data. This results in nuclei precessing at different rates according to their position in the y-direction. After a time t, the phase shift is given by

$$\Delta\phi = \gamma G_y y t \qquad 2\text{-}36$$

and proportional to the y-coordinate, gradient strength, G_y, and the amount of time the gradient was applied for, t. In order to sample the whole of k-space, the phase encoding gradient amplitude changes with every repetition, as shown in Figure 2.4-2.

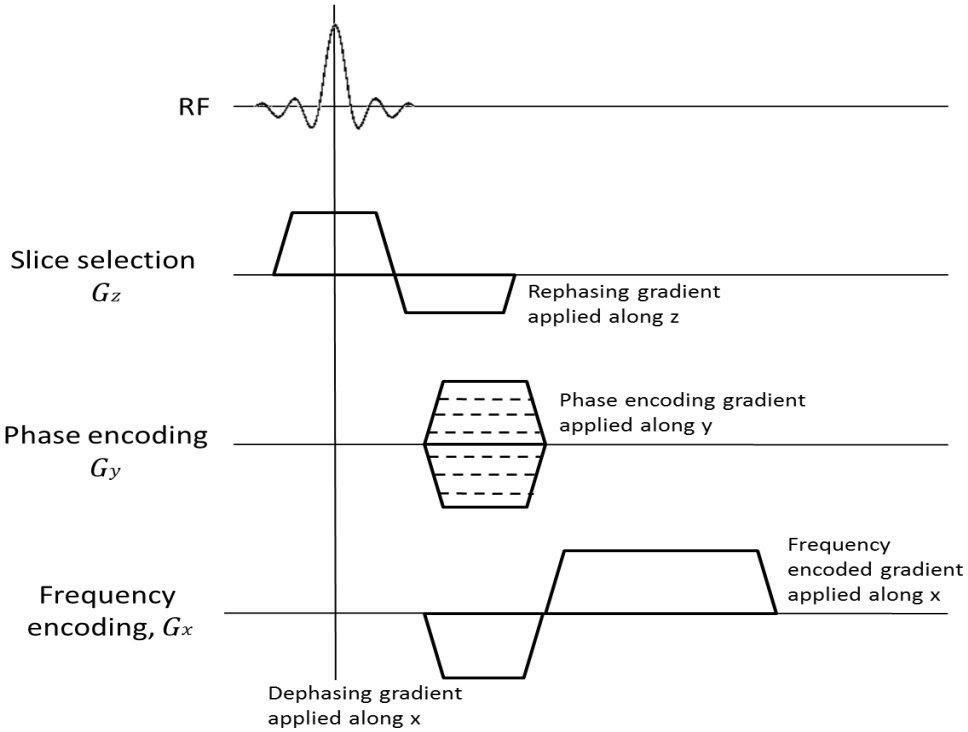

Figure 2.4-2: *Phase and frequency encoding gradients used to form a 2D image. Dashed lines represent the different phase encoding steps.*

A frequency encoding then follows phase encoding. By applying a linear gradient (also known as the read-out gradient) during image acquisition. The gradient in the frequency-encoding direction results in a spatial dependency on the frequency. These frequencies are then read out by summing the signal amplitude across the frequency encoding direction to result in a single line of k-space. When the whole of k-space has been filled, a Fourier transform is applied to the frequency data to form an image.

2.4.3 k-space

MRI images are spatially encoded in k-space, a two dimensional array (k_x, k_y) of spatial frequencies which contains raw data. k_x corresponds to time points in the readout direction and k_y to points in the phase encoding direction. Each (k_x, k_y) coordinate gives a signal influenced by a combination of readout and phase encoding points

$$k_x = \gamma G_x t_x \quad \text{2-37}$$

$$k_y = \gamma G_y t_y \quad \text{2-38}$$

where G_x and G_y are gradients in the readout and phase encoding directions respectively, and t_x and t_y are the duration of the readout and the phase encoding gradients. The change in k in each direction (Δk_x, Δk_y) is inversely related to the field of view (FOV), the distance over which the image is acquired, in that direction whilst the extent of k-space is proportional to the spatial resolution of the image. Data in the centre of k-space provides information on image contrast whereas the edge of k-space informs on high definition in the image. To achieve artefact free MR data, k-space needs to be well sampled, and is often sampled with a Cartesian configuration using uniform spacing in Δk_x and Δk_y.

2.5 Imaging Sequences

A number of different imaging schemes can be applied. The following sections overview those used in this thesis.

2.5.1 Echo planar imaging

Echo-planar imaging (EPI) is a fast imaging technique that was developed to speed up image acquisition time, thus motion related artefacts can be eliminated and fast changing physiological processes can be imaged. EPI samples all of k-space following a single excitation pulse. A train of gradient echoes are created by alternating the frequency encoding gradient from G_x to $-G_x$. The first line of k-space is acquired by traversing from $-k_x$ to k_x. After one line of k-space is sampled, a blipped phase encoding gradient (G_y) is applied, so the next line of k-space in the k_y direction is filled. The next

frequency echo gradient is then applied with opposite polarity to the first so that the next line of k-space is acquired in the k_x direction by traversing from k_x to $-k_x$. This technique is then repeated until all of k space is filled (Figure 2.5-1). An EPI scheme can be acquired using either a gradient echo (GE-EPI) or a spin echo (SE-EPI) sequence. The echo time of the EPI acquisition is governed by the time from the excitation pulse to the centre of k-space.

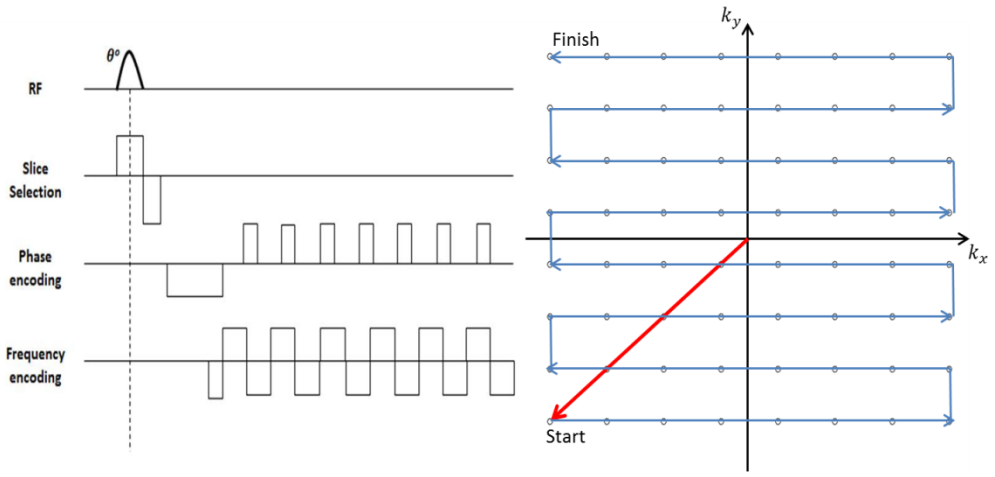

Figure 2.5-1: *EPI pulse sequence and corresponding k-space diagram. The first line of k-space is acquired by traversing from $-k_x$ to k_x, a blipped phase encoding gradient is then applied so the next line of k-space in the k_y direction is filled and a frequency echo gradient then again applied. This is repeated until all of k-space is filled.*

2.5.2 Fast imaging in the steady state

When RF pulses are applied repeatedly to a spin system, the magnetisation approaches a steady state. The number of pulses it takes to reach the steady state depends on the T_1 and T_2 of the tissue and the flip angle of the applied RF pulse. Steady state imaging can be divided into coherent and incoherent pulse sequences. In steady state incoherent pulse sequences, any residual transverse magnetisation is spoilt before the application of the next RF pulse. In steady state coherent sequences, the transverse magnetisation is not spoilt but contributes to the signal along with the longitudinal magnetisation. The

following section outlines the incoherent fast low angle shot (FLASH) sequence and coherent balanced fast field echo (bFFE) sequence.

2.5.2.1 Fast Low Angle Shot (FLASH)

In a fast low flip angle shot (FLASH) scheme, RF excitation pulses are applied with low flip angles of approximately 10° which are followed by gradient reversals to produce a gradient echo signal. The low flip angle creates an equilibrium of longitudinal magnetisation and spoiler gradients are applied to eliminate transverse magnetisation. A FLASH pulse sequence is shown in Figure 2.5-2. The magnetisation after the first RF pulse with flip angle θ is:

$$M_z = M_0 \cos\theta \qquad M_{xy} = M_0 sin\theta \tag{2-39}$$

Between the first and second RF pulse, the longitudinal magnetisation recovers towards M_0 and the transverse magnetisation decays. This process repeats with every RF pulse until a steady state is reached. If TR >> T_2 then the sequence is naturally spoilt since the system has enough time for the transverse magnetisation to decay. The magnetisation, M_{SS}, of the longitudinal steady state signal is

$$M_{SS} = \frac{M_0(1 - e^{-TR/T_1})}{1 - e^{-TR/T_1}\cos\theta} \tag{2-40}$$

and the transverse magnetisation decays as

$$M_{xy} = M_{SS}\sin(\theta)\, e^{-t/T_2} \tag{2-41}$$

The maximum signal will occur at the Ernst angle θ_E

$$\theta_E = cos^{-1}\left(e^{-TR/T_1}\right) \tag{2-42}$$

For TR << T_1, this can be simplified to

$$\theta_E = \sqrt{\frac{2TR}{T_1}} \qquad 2\text{-}43$$

The FLASH sequence is T_2 weighted at a short TR.

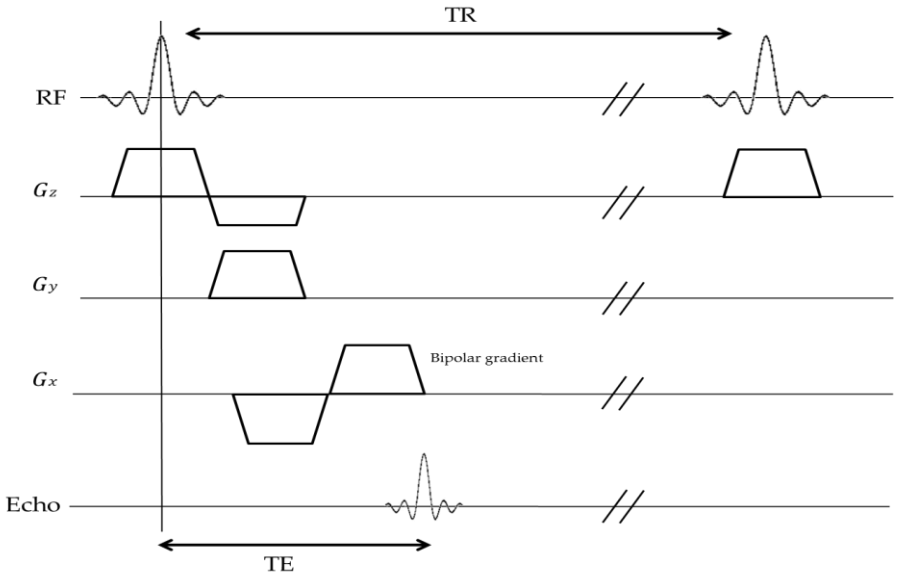

Figure 2.5-2: *FLASH pulse sequence.*

2.5.2.2 Balanced fast field echo (bFFE)

An alternative gradient echo based readout technique is balanced fast field echo (bFFE), also known as true fast imaging with steady state precession (TrueFISP). The image contrast from a bFFE image is determined by T_2/T_1. If the residual magnetisation is not eliminated and TR ≤ T_2, the signal moves towards the steady state and is dependent on the initial magnetisation, the flip angle, θ, TR, T_1 and T_2. The magnetisation also depends on the phase angle β through which the spins precess between each RF pulse. When the gradients are balanced, the transverse spin is preserved and all spins evolve under the same free precession conditions over each TR period without being affected by the phase and frequency encoding gradients.

For TR << T_2, and T_1 and $\beta = \pi$, the transverse magnetisation components are given as

$$M_x = 0 \qquad 2\text{-}44$$

$$M_y \approx \frac{M_0 \sin\theta}{\left(\frac{T_1}{T_2}+1\right) - \cos\theta\left(\frac{T_1}{T_2}-1\right)} \qquad 2\text{-}45$$

and so the contrast is T_2/T_1 weighted. The optimal signal will occur at the flip angle θ_{opt} where

$$\cos(\theta_{opt}) = \frac{T_1/T_2 - 1}{T_1/T_2 + 1} \qquad 2\text{-}46$$

For short TR, the peak signal can be simplified to:

$$M_y \approx \frac{1}{2} M_0 \sqrt{\frac{T_2}{T_1}} \qquad 2\text{-}47$$

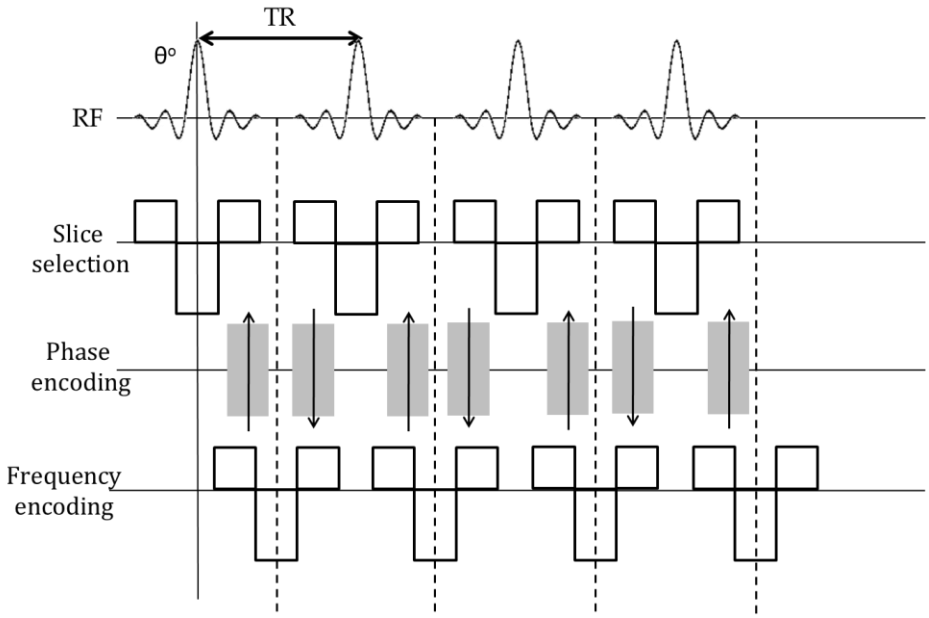

Figure 2.5-3: *bFFE pulse sequence diagram.*

For a long TR, FLASH and bFFE sequences have similar properties for a given TE and flip angle. In a bFFE scheme, the echo is typically recorded at the

middle of the interval between two RF pulses and TE is half TR. In a bFFE scheme the number of TFE factors controls the number of phase encodings applied during each shot.

2.5.3 Turbo spin echo

The turbo spin echo (TSE) scheme is an extension of a basic spin echo sequence, using a series of 180° refocusing pulses after a single 90° to generate an echo train, as shown in Figure 2.5-4. Echoes in the centre of k-space providing information on image contrast and the edge of k-space determine the spatial resolution. The phase encoding gradient changes for each of the echoes resulting in multiple lines of k-space being acquired in one TR. The number of echoes in one TR is called the turbo factor or the echo train length (ETL), the effective echo time (TE_{eff}) is the time from the 90° pulse to the centre of k-space (i.e. where the phase encoding gradients are zero). This significantly decreases scan time compared to a standard spin echo scheme.

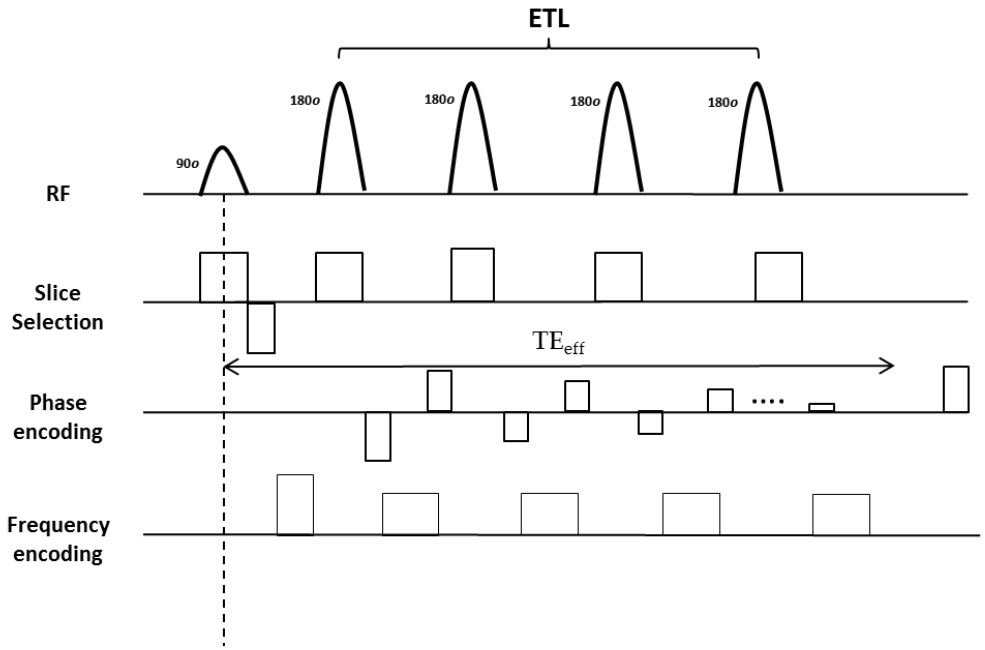

Figure 2.5-4: *TSE pulse sequence diagram showing the echo train length (ETL).*

2.5.4 Partial Fourier Imaging

One technique to decrease the scan time needed to acquire an image is partial Fourier imaging, in which only select lines of k-space are sampled. The real and imaginary components of the Fourier transform are respectively symmetric and asymmetric about the centre of k-space, and so images can be reconstructed from under-sampled k-space. Theoretically, only half of k-space needs to be acquired to reconstruct a full image, however in practice a few extra lines in the un-sampled half of k-space are collected to create an image. To decrease the echo time, a partial Fourier technique can be employed in the frequency encoding direction and to reduce scan time, the technique is applied in the phase encoding direction. Partial Fourier imaging however reduces SNR and introduce image artefacts if large half scan factors are employed.

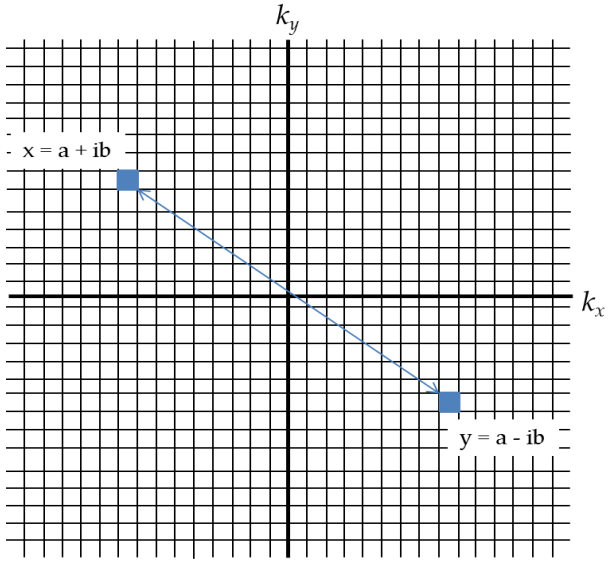

Figure 2.5-5: *Partial Fourier imaging. Two positions mirrored in k-space (shown in blue) have identical amplitude with opposite phases. If the data at x is the complex number a + bi then the data at y is its complex conjugate a – bi.*

2.5.5 Sensitivity Encoding (SENSE)

Most MRI scanners use radiofrequency coils that have multiple receive channels. All data in this thesis was collected with an XL Torso body coil with

16 receive channels. SENSE (sensitivity encoding) (4) is a technique that uses these parallel receive channels to reduce scan time. Since the signal received is dependent upon its position relative to the receive coil, by knowing the sensitivity of each receive coil, information about the origin of the signal can be used to construct an image. SENSE involves creating an aliased image for each element in the receiver array using a Fourier transform. These images can then be used to reconstruct an image of the entire field of view. A reference scan must be performed to provide a sensitivity map of each of the receiver coils which can then be used to unfold the signal superposition. The SENSE factor refers to the factor by which the amount of k-space is under-sampled, with the maximum SENSE factor determined by the number of receiver coils. Applying a SENSE factor results in a decrease in scan time, but reduces signal-to-noise ratio (SNR), so these factors need to be balanced to achieve an image with sufficient SNR within an acceptable scan time.

2.5.6 Multi-transmit

Multi-transmit divides the RF coil into separate independently powered and controlled elements that each have their own B_1. The sum of each separate B_1 field constitutes the new B_1 field experienced by the tissue being imaged. Using multi-transmit; it is possible to increase the homogeneity of the RF excitation, and minimise RF-energy deposition in tissues. This technique was used for all data collected in this thesis.

2.6 Using MRI techniques to measure blood flow and perfusion

The following sections provide an outline of the pulse sequences used to measure blood flow and tissue perfusion.

2.6.1 Phase Contrast (PC) MRI

Magnetic resonance angiography (MRA) uses the motion sensitivity of MRI to measure blood flow in vessels. In this thesis, phase contrast (PC) MRI is used to assess blood flow to the kidney and heart.

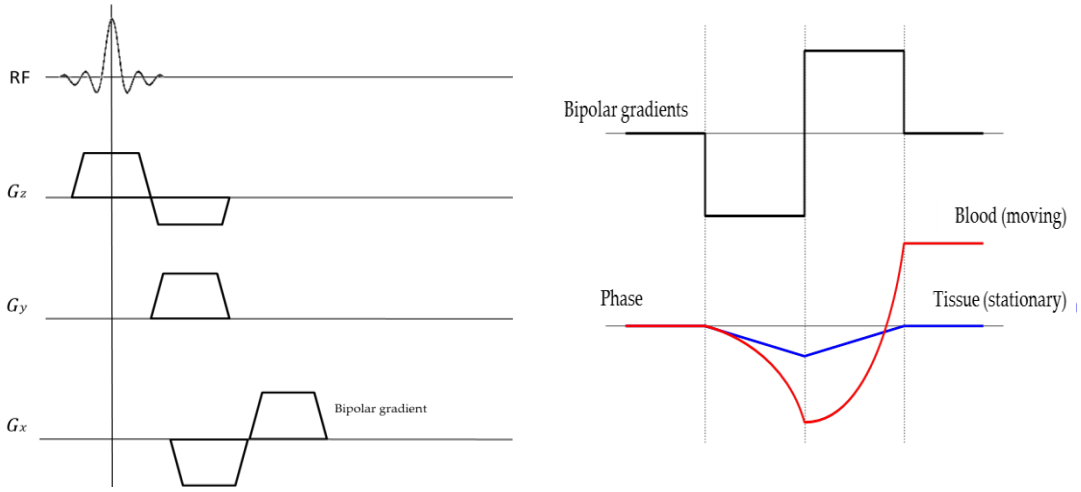

Figure 2.6-1: *A) Pulse sequence for PC-MRI showing slice selection, G_z, phase encoding, G_y and frequency encoding, G_x. B) Effect of bipolar gradients on the phase of moving and stationary spins.*

PC-MRI takes advantage of the velocity-induced phase changes resulting from blood flow. Protons moving along the direction of a magnetic field gradient will experience a phase shift proportional to their velocity. To perform PC-MRI sequence a bipolar gradient of two gradient pulses with the same magnitude but opposite direction is applied to sequentially de-phase and then re-phase spins. This gradient will result in a zero phase shift for stationary spins and non-zero phase shift for non-stationary spins. This is shown in Figure 2.6-1.

The relationship between velocity and phase is adjusted by setting the velocity encoding value, known as the V_{ENC}. This is the maximum velocity that will be encoded correctly by the scanner. If the velocity of the blood exceeds the V_{ENC} value then aliasing can occur.

To calculate the velocity of blood flow from the induced phase shift, the following equations are used. The phase shift (ϕ) is given by the time integral of the Larmor frequency

$$\phi = \int \omega \, dt \tag{2-48}$$

In a magnetic field gradient G_x, this can be written as

$$\phi = \gamma \int (B_0 + G_x x) \, dt \tag{2-49}$$

For spins moving at a constant velocity v in the x direction, the phase shift is

$$\phi = \gamma \int (B_0 + G_x(x + vt)) \, dt \tag{2-50}$$

For a single gradient pulse of amplitude *G* and duration *T*, the phase shift will be

$$\phi = \gamma \int_0^T Gvt \, dt = \left[\frac{1}{2}\gamma v G t^2\right]_0^T = \frac{1}{2}\gamma v G T^2 \tag{2-51}$$

The product GT^2 is known as the 'first moment' of the gradient, M_1, so

$$\phi = \frac{1}{2}\gamma v M_1 \tag{2-52}$$

If a second gradient of the same duration (*T*) but opposite amplitude (-G) is applied, this bipolar gradient will result in a total phase shift of

$$\phi = -\gamma v M_1 \tag{2-53}$$

If this acquisition is then repeated with the polarity of the bipolar pulse reversed and the phases subtracted, then the phase difference in the moments ΔM_1 of the two bipolar pulses is

$$\Delta\phi = \gamma v \Delta M_1 \qquad 2\text{-}54$$

The V_{ENC} is defined as the velocity that produces a phase shift $\Delta\phi$ of π or 180°

$$\pi = \gamma v_{ENC}\, \Delta M_1 \qquad 2\text{-}55$$

Therefore,

$$v_{ENC} = \frac{\pi}{\gamma \Delta M_1} \qquad 2\text{-}56$$

PC-MRI is sensitive to the direction of the flow of blood. Only blood moving in the same direction of a bipolar flow encoding gradient will result in a phase shift. For blood flowing in different directions, a bipolar gradient pair must be applied in each direction resulting in six acquisitions. In practise this can be reduced to four acquisitions by using no velocity sensitizing in one direction.

Two-dimensional (2D) PC-MRI images flow through a single thick slice. Since the blood vessels will only occupy a small volume of the slice, an extra de-phasing gradient is applied in the slice-selective direction to reduce the signal from stationary tissue. Secondly, instead of subtracting the phase angles, vector subtraction is used. For quantitative measurement of flow the slice plane must be perpendicular to the direction of flow. A flow velocity curve is then obtained as a function of time. PC-MRI is applied in Chapters 3 and 4.

2.6.2 Arterial Spin Labelling

Arterial Spin Labelling (ASL) (5) is a non-invasive technique for the quantification of tissue perfusion. Perfusion provides an estimate of the volume of blood that passes through the capillary bed per unit time to deliver nutrients to the tissue, typically expressed in units of ml g^{-1} min^{-1}. ASL uses magnetically labelled water protons as an endogenous tracer. During an ASL scan, label and control images are acquired and then subtracted to form a perfusion weighted (PW) image.

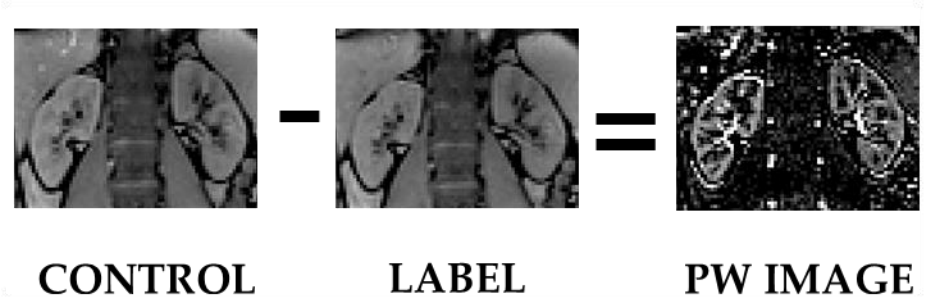

Figure 2.6-2: *Control, label and perfusion (PW) difference image for a coronal oblique slice through the kidneys.*

The label image of the tissue is collected under the condition of the inflowing arterial blood being labelled, typically inverted by inverting the water molecules of the blood supplying the imaging region using an off-resonance single adiabatic radiofrequency pulse. The control image is collected for fully recovered inflowing blood. A PW image is then created showing labelled blood that has perfused into the tissue by subtracting the label image from the control image. A typical ASL signal curve is shown in Figure 2.6-3, in which the arrival time of the blood in the capillary bed, Δc, can be seen, after which the signal begins to increase from zero.

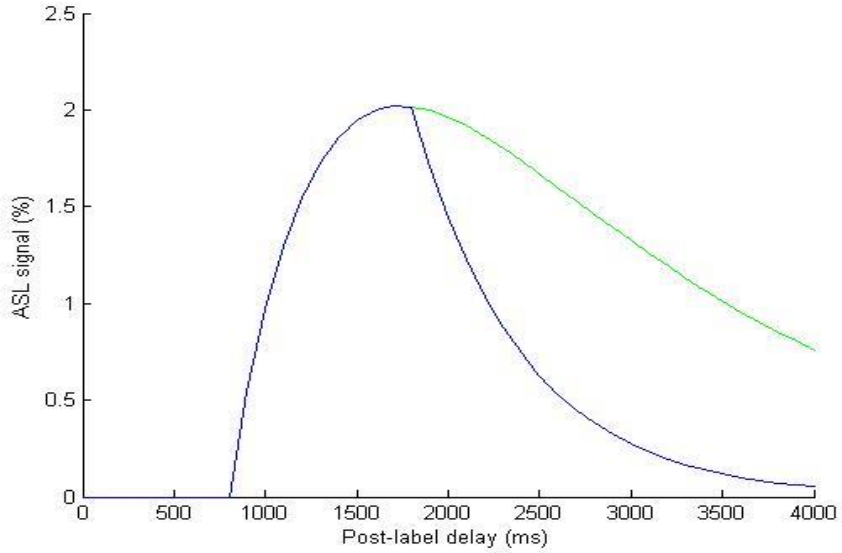

Figure 2.6-3: *Example of an ASL signal curve for arrival time (**Δc**) of 800ms, T_1 of 600 ms and perfusion of 60 ml/100g/min. The blue curve shows the ASL signal when the label has bolus duration of 1000ms whereas the green shows the signal following a label of infinite thickness and thus infinite bolus width.*

A post-label delay (PLD) is left between the labelling module and the imaging module to allow time for the labelled blood to travel from the labelling plane to imaging slice.

2.6.3 Pre and post saturation pulses

In order to ensure the signal in the imaging plane is in the same state at the beginning of each TR period, pre and post saturation pulses are used to null the signal in the imaging plane. Pre-saturation pulses are applied prior to the labelling and post-saturation follow the labelling pulse as shown in Figure 2.6-4.

Pre-saturation pulses typically use a WET (water suppression enhanced through T_1 effects) scheme whilst post-saturation uses a single sinc pulse. These pre and post saturations ensure there is no offset between the label and control conditions which could cause an artificial ASL signal. However, the use of additional RF pulses leads to increased SAR.

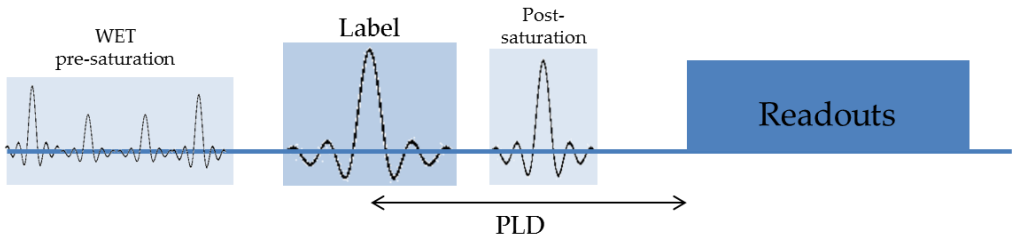

Figure 2.6-4: *ASL pulse sequence showing pre- and post-saturation pulses placed around the labelling pulse. This is followed by the readouts after a post label delay (PLD) time.*

2.6.4 Magnetisation Transfer

Magnetisation transfer causes magnetisation of stationary tissue to be present in the imaging slice in ASL. Protons that are bound to macromolecules have a much larger frequency range than free water molecules, as illustrated in Figure 2.8-5. When an ASL labelling pulse is applied off-resonance to the imaging slice this can affect both water-bound protons and macromolecule-bound protons from an exchange of magnetisation between the free protons and the bound protons via spin-spin interactions or water diffusion. To compensate for these effects, magnetisation transfer must be matched between the label and control conditions in ASL.

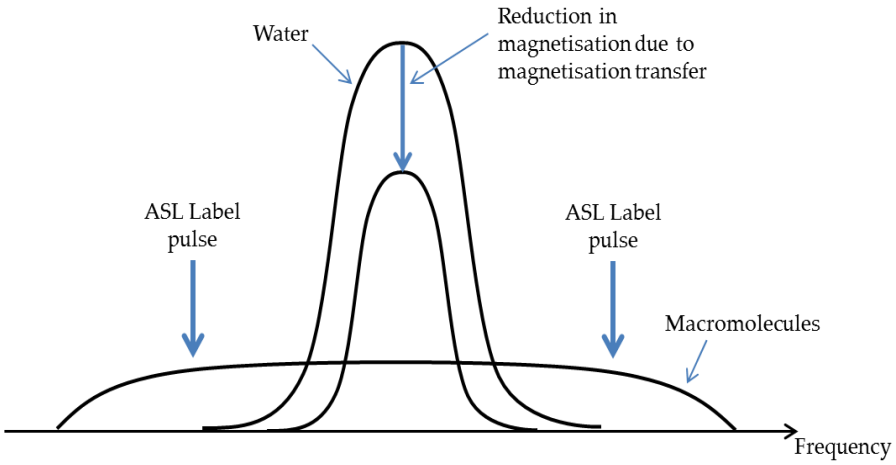

Figure 2.6-5: *The reduction in magnetisation in tissue due to magnetisation transfer for water and macromolecules.*

2.6.5 Variants of ASL

There are distinct ASL variants of continuous arterial spin labelling (CASL) (5), pulsed arterial spin labelling (PASL) (6–8) and pseudo-continuous ASL (pCASL) (11), an intermediate method between CASL and PASL. PASL, CASL and pCASL schemes are shown in Figure 2.6-6.

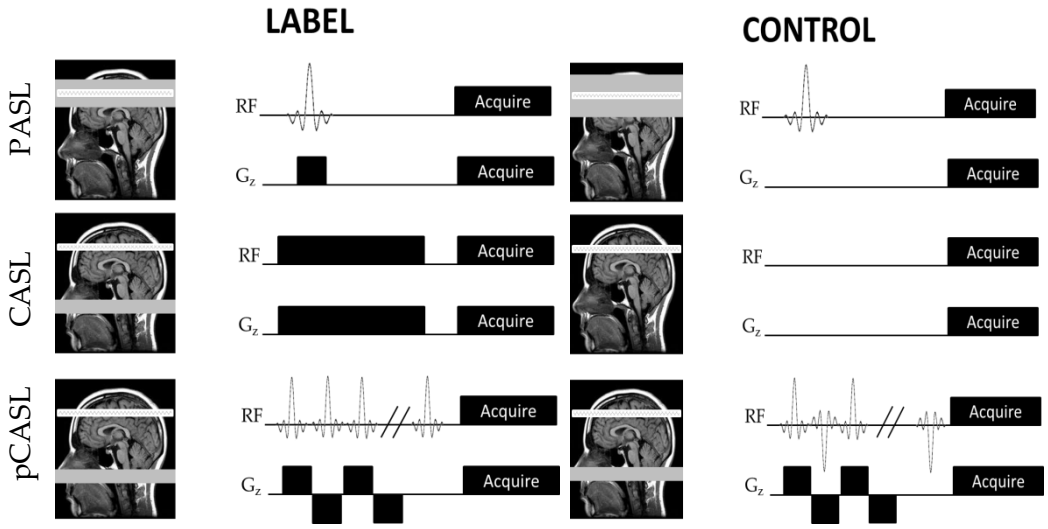

Figure 2.6-6: *ASL labelling schemes*

CASL is the original ASL method and uses a continuous flow-driven adiabatic inversion scheme to invert the inflowing blood as it flows through a plane below the imaging volume. This scheme uses a long low powered continuous radiofrequency pulse which is applied concurrent with a magnetic field gradient in the direction of flowing blood, causing moving arterial blood spins to experience a slow variation of the resonance frequency resulting in these spins being inverted. The inversion efficiency of CASL is dependent on the mean velocity of the blood, angulation of the vessels to the plane, the amplitude of the RF pulse and the strength of the gradient. CASL provides a high SNR ASL image, but high SAR and magnetisation transfer effects associated with CASL can limit its use.

In pulsed arterial spin labelling (PASL), a large spatial slab of arterial blood is labelled typically by a single spatially selective adiabatic inversion RF pulse. There are a number of variants of PASL; the most commonly used are echo planar imaging and signal targeting with alternative radiofrequency (EPISTAR) (9) and flow-sensitive alternating inversion recovery (FAIR) (10) (Figure 2.6-7). In the FAIR approach, the label condition is created using a global (or non-selective) inversion pulse to invert inflowing blood. The control state is achieved using a slice selective inversion centred on the imaging slice, so inflowing blood is unlabelled. The work described in this thesis uses the FAIR technique. In EPISTAR, a single 180° RF pulse is applied with a magnetic field gradient to invert a slab of inflowing blood below the image slice. A control image is then acquired, created using two 180° pulses which sum to give a nominal 360° pulse. For the label and control conditions, the RF power is matched to match magnetisation transfer effects.

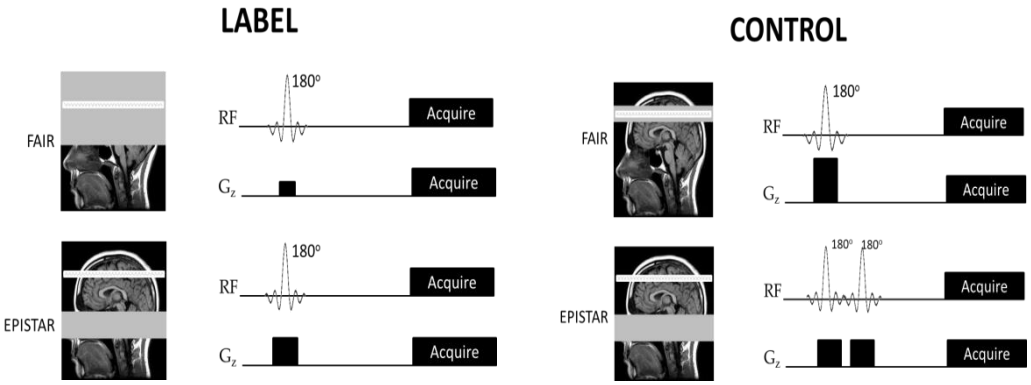

Figure 2.6-7: *FAIR and EPISTAR PASL labelling schemes*

pCASL uses a train of discrete radio frequency pulses to mimic continuous tagging, typically 1500 pulses with a flip angle of 18°. The control image is acquired by alternating the sign of the pulses in the RF train to result in an average $\boldsymbol{B_1}$ of zero whilst maintaining MT effects between label and control images.

2.6.6 Quantification of Pulsed ASL

PASL data can be quantified using the modified Bloch equation (12). $M_{diff}(t)$, the total magnetisation in a tissue voxel in the difference image can be calculated by solving the single compartment model;

$$\frac{dM_{diff}(t)}{dt} = -\frac{M_{diff}(t)}{T_1} + f\left(M_b(t) - \frac{M_{diff}(t)}{\lambda}\right) \quad 2\text{-}57$$

where λ is the blood tissue partition coefficient which describes the freedom of exchange between the tissue and blood supply and $M_b(t)$ is the magnetisation of inflowing arterial blood. The amount of blood entering the imaging slice is given by $fM_b(t)$ and the amount leaving the slice is $fM(t)/\lambda$. By assuming that no perfusing blood leaves the tissue voxel during the imaging time then $fM(t)/\lambda = 0$, the differential equation can be written

$$\frac{dM_{diff}(t)}{dt} = -\frac{M_{diff}(t)}{T_{1b}} + fM_b(t) \quad 2\text{-}58$$

This equation can then be solved using the integrating factor method to give

$$M_{diff}(t) = \frac{1}{e^{t/T_{1b}}} \int e^{t/T_{1b}} fM_b(t)dt \quad 2\text{-}59$$

At a time $t > 0$, $M_b = 2M_0 e^{-t/T_{1b}}$ where M_0 is the equilibrium magnetization of the arterial blood and so

$$M_{diff}(t) = \frac{1}{e^{t/T_{1b}}} \int_0^t 2fM_0 e^{-\frac{t}{T_{1b}}} e^{\frac{t}{T_{1b}}} dt, \quad 2\text{-}60$$

which when integrated between the limits gives,

$$M_{diff}(t) = 2fM_0(t)e^{-\frac{t}{T_{1b}}} \quad 2\text{-}61$$

This describes the signal difference between the FAIR selective and non-selective acquisitions ignoring the transit time for the labelled blood to arrive in the imaging plane. For a more complex analysis, the equation can be solved iteratively assuming a transit delay.

2.6.7 Single time point ASL

Initial ASL experiments were performed at a single post-label delay (PLD) time, and the perfusion signal fit from a single time point. This single TI approach is easy to implement, but can introduce an error in quantification as it does not take account of the arrival time of the blood to the imaging plane. Single TI measurements can be repeated multiple times at a range of PLDs to sample the ASL signal curve, and provide information on arrival time for the fit, however this leads to an increased total scan time.

2.6.8 Look-Locker or Multiphase ASL

Alternatively, a Look-Locker or multiphase ASL scheme can be used to collect multiple low flip angle readouts at different inversion times after a single labelling pulse (13–15) . Acquiring ASL with a Look-Locker readout provides temporal information on the ASL signal curve in a much shorter time than repeating the single TI approach. However, the use of multiple readout pulses perturbs the recovery of the magnetisation resulting in a lower signal and more complex modelling being required for quantification. The Look-Locker recovery curve can be described using the Bloch equation (15), with the magnetisation of the tissue signal ($M(t)$) at time t following a Look-Locker recovery being given by:

$$\frac{dM(t)}{dt} = \frac{M_0 - M(t)}{T_1} + \frac{f}{\lambda}\left[S_{ri}e^{-(k+t)/T_{1blood}} - M_0\left(1 - e^{-\frac{k+t}{T_{1blood}}}\right)\right] - \frac{f}{\lambda}M(t)$$

where S_{ri} is the initial magnetisation of blood, k is the time from the label/control to the previous pulse over which the magnetisation is being evaluated; t is the time since the previous readout pulse, as shown in Figure 2.6-8.

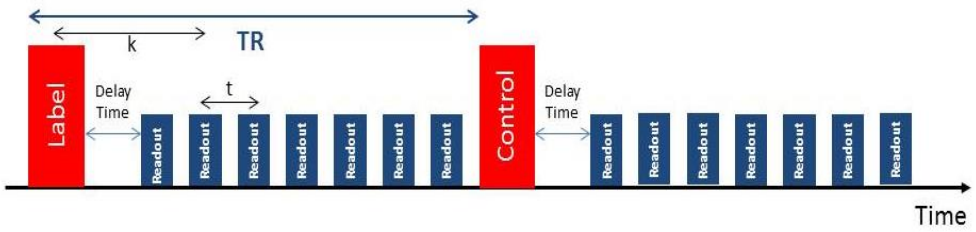

Figure 2.6-8: *Schematic of the ASL pulse sequence with the timing of k and t shown for the third readout.*

From this equation, a general solution to a Look-Locker recovery can be computed. Rearranging 2.61 gives

$$\frac{dM(t)}{dt} + \frac{M(t)}{T_{1app}} = \frac{M_0}{T_1} + \frac{f}{\lambda}\left[S_{ri}e^{-(k+t)/T_{1blood}} - M_0(1 - e^{-(k+t)/T_{1blood}}\right] \quad 2\text{-}63$$

where

$$\frac{1}{T_{1app}} = \frac{1}{T_1} + \frac{f}{\lambda}. \quad 2\text{-}64$$

Solving this differential equation using an integrating factor of $e^{t/T_{1app}}$ gives:

$$M(t) = \frac{1}{e^{t/T_{1app}}}\int e^{t/T_{1app}}\left[\frac{M_0}{T_1} + \frac{f}{\lambda}\left[S_{ri}e^{-(k+t)/T_{1blood}} - M_0(1 - e^{-(k+t)/T_{1blood}}\right]\right]dt \quad 2\text{-}65$$

which can be rearranged to

$$M(t) = \frac{1}{e^{t/T_{1app}}} \int \frac{e^{t/T_{1app}} M_0}{T_1} + \frac{f}{\lambda} \left[S_{ri} e^{t\left(\frac{1}{T_{1app}} - \frac{1}{T_{1blood}}\right)} e^{-k/T_{1blood}} + M_0 e^{t/T_{1app}} - M_0 e^{t\left(\frac{1}{T_{1app}} - \frac{1}{T_{1blood}}\right)} e^{-k/T_{1blood}} \right] dt$$

2-66

Solving this expression yields:

$$M(t) = \frac{1}{e^{t/T_{1app}}} \left[\frac{e^{t/T_{1app}} M_0 T_{1app}}{T_1} + \frac{f}{\lambda} S_{ri} \frac{e^{t\left(\frac{1}{T_{1app}} - \frac{1}{T_{1blood}}\right)} e^{-k/T_{1blood}}}{\frac{1}{T_{1app}} - \frac{1}{T_{1blood}}} + \frac{f}{\lambda} M_0 e^{\frac{t}{T_{1app}}} T_{1app} - \frac{f}{\lambda} M_0 \frac{e^{t\left(\frac{1}{T_{1app}} - \frac{1}{T_{1blood}}\right)} e^{-\frac{k}{T_{1blood}}}}{\frac{1}{T_{1app}} - \frac{1}{T_{1blood}}} + C \right]$$

2-67

where C is a constant of integration. Substituting in T_{1app} (equation 2-64) gives:

$$M(t) = M_0 \left(1 - \frac{f}{\lambda} \frac{e^{-\frac{k}{T_{1blood}}} e^{-\frac{t}{T_{1blood}}}}{\frac{1}{T_{1app}} - \frac{1}{T_{1blood}}} \right) + S_{ri} \left(\frac{f}{\lambda} \frac{e^{-\frac{k}{T_{1blood}}} e^{-\frac{t}{T_{1blood}}}}{\frac{1}{T_{1app}} - \frac{1}{T_{1blood}}} \right) + C e^{-\frac{t}{T_{1app}}}$$

2-68

If at time $t = 0s$ the initial tissue signal $M(t) = M_d$ the constant, C, is

$$C = -M_0 \left(1 - \frac{f}{\lambda} \frac{e^{-\frac{k}{T_{1blood}}}}{\frac{1}{T_{1app}} - \frac{1}{T_{1blood}}} \right) - S_{ri} \left(\frac{f}{\lambda} \frac{e^{-\frac{k}{T_{1blood}}}}{\frac{1}{T_{1app}} - \frac{1}{T_{1blood}}} \right) + M_d$$

2-69

This results in the final solution:

$$M(t) = M_0\left(1 - \frac{f}{\lambda}\frac{e^{-\frac{k}{T_{1blood}}}e^{-\frac{t}{T_{1blood}}}}{\frac{1}{T_{1app}}-\frac{1}{T_{1blood}}} + \frac{f}{\lambda}\frac{e^{-\frac{k}{T_{1blood}}}e^{-\frac{t}{T_{1app}}}}{\frac{1}{T_{1app}}-\frac{1}{T_{1blood}}}\right) + S_{ri}\left(\frac{f}{\lambda}\frac{e^{-\frac{k}{T_{1blood}}}e^{-\frac{t}{T_{1blood}}}}{\frac{1}{T_{1app}}-\frac{1}{T_{1blood}}} - \frac{f}{\lambda}\frac{e^{-\frac{k}{T_{1blood}}}e^{-\frac{t}{T_{1app}}}}{\frac{1}{T_{1app}}-\frac{1}{T_{1blood}}}\right) - M_0 e^{-\frac{t}{T_{1app}}} + M_d e^{-\frac{t}{T_{1app}}} \quad 2\text{-}70$$

where $S_{ri} = -M_0$ for the non-selective signal and $S_{ri} = +M_0$ for the selective signal. $M_d = -M_0$ when no pre-saturation pulses are used and $M_d = 0$ with pre-saturation. Chapter 3 uses this iterative modelling for cardiac ASL data.

2.7 Myocardial Tagging

Myocardial tagging creates visible markers or tags on an image by applying slice selective RF pulses perpendicular to the imaging plane to saturate the longitudinal magnetisation. These tags can then be used to follow the movement of the myocardium to show the deformation of the tissue. Tagging is typically applied at end-diastole imaging with performed at end-systole. Figure 2.7-1 shows an example of a tagging image of the short axis of the heart.

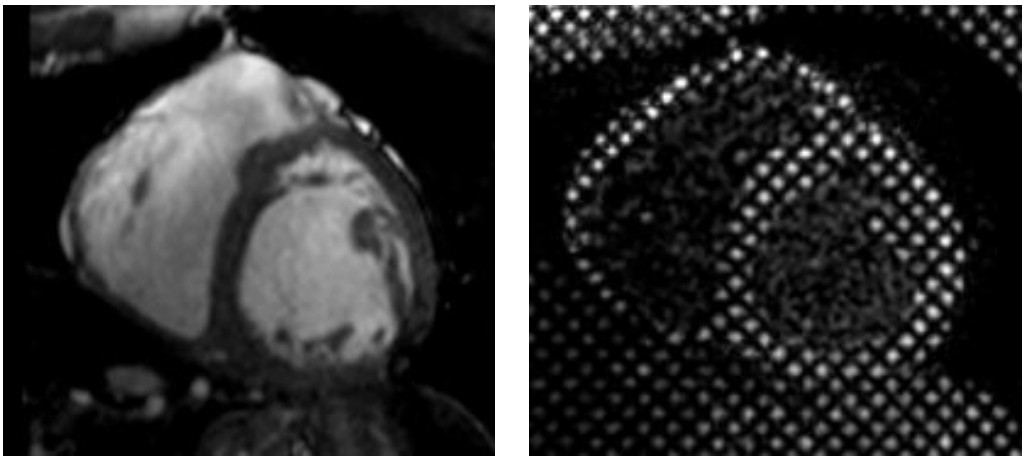

Figure 2.7-1: *Short axis slice acquired from a cine scan and corresponding myocardial tagging of the short axis using SPAMM.*

There are a number of tagging techniques available the most common are spatial modulation of magnetisation (SPAMM) (16) and complementary spatial modulation of magnetisation (CSPAMM) (17). SPAMM is used in

Chapter 4 of this thesis. A schematic of the SPAMM pulse sequence is shown in Figure 2.7-2.

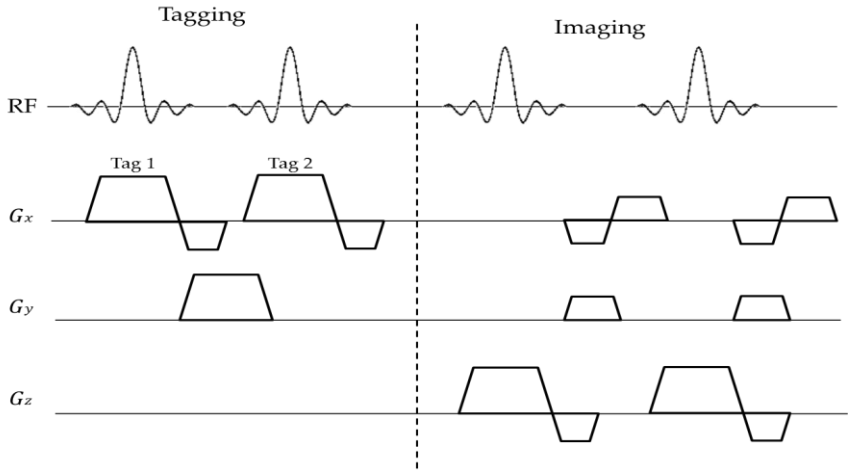

Figure 2.7-2: *Pulse sequence for a SPAMM tagging scheme. The first RF pulse moves the magnetisation into the transverse plane. This is followed by a gradient pulse to modulate the transverse magnetisation sinusoidally along the gradient direction. Subsequently, another RF pulse moves the magnetisation back to the longitudinal plane and a spoiler gradient is used to eliminate any residual transverse magnetisation.*

SPAMM involves applying two equal-strength, non-selective RF pulses separated by a wrapping gradient. The first RF pulse tilts the magnetisation into the transverse plane. This is followed by a gradient pulse along the desired tagging direction which modulates the transverse magnetisation sinusoidally along the gradient direction through incremental phase shifting of the spins in this direction. The second RF pulse is used to restore the modulated magnetisation back to its longitudinal position. After the second RF pulse a spoiler or crusher gradient is applied to eliminate any residual transverse magnetisation before image acquisition. For grid tagging, this process is repeated with the modulating gradient placed at 90^{o} to the first tag. The grid pattern is then imaged to measure any deformation.

2.8 Discussion

This chapter has introduced the basic NMR and MRI principles needed to understand the work in this thesis. The includes the basic principles of NMR and MRI, and the techniques of phase contrast MRI (PC-MRI), arterial spin labelling (ASL) and myocardial tagging. These latter techniques are then applied to the heart and kidney in experimental Chapters 3 – 5 of this thesis for assessment of blood flow, perfusion and myocardial strain.

2.9 References

1. Jellis CL, Kwon DH. Myocardial T1 mapping: modalities and clinical applications. Cardiovasc. Diagn. Ther. 2014;4:126–37. doi: 10.3978/j.issn.2223-3652.2013.09.03.

2. Look DC, Locker DR. Time saving in measurement of NMR and EPR relaxation times. Rev. Sci. Instrum. 1970;41:250–251. doi: 10.1063/1.1684482.

3. Messroghli DR, Radjenovic A, Kozerke S, Higgins DM, Sivananthan MU, Ridgway JP. Modified look-locker inversion recovery (MOLLI) for high-resolution T 1 mapping of the heart. Magn. Reson. Med. 2004;52:141–146. doi: 10.1002/mrm.20110.

4. Pruessmann KP, Weiger M, Scheidegger MB, Boesiger P. SENSE: Sensitivity encoding for fast MRI. Magn. Reson. Med. 1999;42:952–962. doi: 10.1002/(SICI)1522-2594(199911)42:5<952::AID-MRM16>3.0.CO;2-S.

5. Williams DS, Detre J a, Leigh JS, Koretsky a P. Magnetic resonance imaging of perfusion using spin inversion of arterial water. Proc. Natl. Acad. Sci. U. S. A. 1992;89:212–216. doi: 10.1073/pnas.89.9.4220e.

6. Wong EC, Buxton RB, Frank LR. A theoretical and experimental comparison of continuous and pulsed arterial spin labeling techniques for quantitative perfusion imaging. Magn. Reson. Med. 1998;40:348–55.

7. Kwong KK, Chesler DA, Weisskoff RM, Donahue KM, Davis TL, Ostergaard L, Campbell TA, Rosen BR. MR perfusion studies with T1-weighted echo planar imaging. Magn. Reson. Med. 1995;34:878–887.

8. Schwarzbauer C, Morrissey SP, Haase A. Quantitative magnetic resonance imaging of perfusion using magnetic labeling of water proton spins within the

detection slice. Magn. Reson. Med. 1996;35:540–546. doi: 10.1002/mrm.1910350413.

9. Edelman RR, Siewert B, Adamis M, Gaa J, Laub G, Wielopolski P. Signal targeting with alternating radiofrequency (STAR) sequences: application to MR angiography. Magn. Reson. Med. 1994;31:233–238. doi: fmri_Mary M-Converted #86; Used to be #2193.

10. Kim SG. Quantification of relative cerebral blood flow change by flow-sensitive alternating inversion recovery (FAIR) technique: Application to functional mapping. Magn. Reson. Med. 1995;34:293–301. doi: 10.1002/mrm.1910340303.

11. Dai W, Garcia D, De Bazelaire C, Alsop DC. Continuous flow-driven inversion for arterial spin labeling using pulsed radio frequency and gradient fields. Magn. Reson. Med. 2008;60:1488–1497. doi: 10.1002/mrm.21790.

12. Detre JA, Zhang W, Roberts DA, Silva AC, Williams DS, Grandis DJ, Koretsky AP, Leigh JS. Tissue specific perfusion imaging using arterial spin labeling. NMR Biomed. 1994;7:75–82. doi: 10.1002/nbm.1940070112.

13. Gunther M, Bock M, Schad LR. Arterial spin labeling in combination with a look-locker sampling strategy: Inflow turbo-sampling EPI-FAIR (ITS-FAIR). Magn. Reson. Med. 2001;46:974–984. doi: 10.1002/mrm.1284.

14. Brookes MJ, Morris PG, Gowland PA, Francis ST. Noninvasive measurement of arterial cerebral blood volume using Look-Locker EPI and arterial spin labeling. Magn. Reson. Med. 2007;58:41–54. doi: 10.1002/mrm.21199.

15. Francis ST, Bowtell R, Gowland PA. Modeling and optimization of look-locker spin labeling for measuring perfusion and transit time changes in

activation studies taking into account arterial blood volume. Magn. Reson. Med. 2008;59:316–325. doi: 10.1002/mrm.21442.

16. Axel L, Dougherty L. MR imaging of motion with spatial modulation of magnetization. 1989 pp. 841–845. doi: 10.1148/radiology.171.3.2717762.

17. Fischer SE, McKinnon GC, Maier SE, Boesiger P. Improved myocardial tagging contrast. Magn. Reson. Med. 1993;30:191–200. doi: 10.1002/mrm.1910300207.

3. Development of Cardiac Arterial Spin Labelling and application to patients with Chronic Kidney Disease (CKD)

Cardiovascular disease is the leading cause of mortality for patients with Chronic Kidney Disease (CKD). Currently, there are limited methods to assess cardiac function using Magnetic Resonance Imaging (MRI), particularly in CKD patients where the use of MR contrast agents is contraindicated.

This chapter aims to develop a cardiac Arterial Spin Labelling method for application in the human heart to non-invasively quantify myocardial perfusion.

Firstly, previous studies using ASL to measure myocardial perfusion are discussed and the use of a modified Look-Locker inversion recover (MOLLI) scheme for T_1 mapping is introduced. A method is then developed to assess myocardial perfusion using MOLLI-ASL and optimised first in a phantom study and then in healthy volunteers. This method is then applied in a study of cardiac function in CKD Stage 3 patients in comparison to age-matched healthy volunteers, with a hand grip challenge used to modulate cardiac stress.

The work in this chapter has been presented as an oral presentation (p0538) and a poster (p2749) at the annual conference of the International Society of Magnetic Resonance in Medicine (ISMRM), Toronto, 2015.

3.1 Introduction

ASL techniques are widely used in the brain (1–5). More recently these techniques have been adapted for use in the body, including the heart (6–19). However, there are unique challenges to cardiac ASL that are not present in cerebral ASL. Firstly, due to the motion of the heart during the cardiac cycle, the image readouts of the ASL scheme need to be synchronised to the same time point in the cardiac cycle, which is typically chosen to be end-diastole. As a consequence, the spacing between the ASL label and subsequent readouts is limited to an integer number of RR-intervals and so acquiring multiple inversion times can be limited. Secondly, respiratory motion can also influence cardiac imaging, and so data is often acquired during a breath hold, with synchronized breathing or retrospective motion correction performed. There have been a small number of studies to date that have used cardiac ASL for the measurement of myocardial perfusion. This has been done both in the human heart and in an animal model in the rat or mouse.

In the work by Do *et al* (10), myocardial ASL was performed at 3 T in 7 healthy human subjects using FAIR labelling combined with a bFFE readout scheme to collect data from a single slice through the centre of the short axis of the left ventricle. SENSE was used in an attempt to reduce physiological noise by decreasing the scan acquisition time. This work found that the signal to noise ratio (SNR) was greatly improved with the use of SENSE and this was particularly beneficial in subjects with higher heart rates (and so shorter RR intervals) and for imaging the myocardium during systole. To remove respiratory motion, breath holds were used, with the data acquired in 7 breath holds, which resulted in between 2 – 3 minutes to acquire the cardiac ASL protocol.

Zun *et al* (20) measured myocardial blood flow (MBF) in healthy volunteers at 3 T using a cardiac gated FAIR labelling scheme with a bFFE readout scheme.

The labelling and readout pulses were positioned at the same point in the cardiac cycle (end-diastole) in successive RR intervals. To decrease the noise from respiratory motion, one pair of label and control images was acquired in a breath hold and six seconds were left between each image acquisition for near complete recovery of the longitudinal relaxation. This study assessed the sensitivity of myocardial ASL using a stress challenge of either passive leg elevation or a handgrip exercise. This work also assessed the effect of physiological noise and it was shown that for myocardial ASL, the physiological noise is 6.5 times higher than the thermal noise, suggesting the main contributing factor to the low signal-to-noise ratio (SNR) associated with cardiac ASL is due to motion from the subject's respiratory or cardiac cycle. The study concluded that MBF measurements using ASL was feasible and sensitive to changes such as a challenge. However, it was determined that the SNR was only high enough for region of interest (ROI) rather than voxel-wise analysis.

The study by Wacker *et al* (15) assessed the use of ASL for use in patients with coronary artery disease (CAD) in which there was hypothesised to be variations in myocardial perfusion between the anterior and posterior myocardium. 12 healthy volunteers and 16 patients were scanned using a 2 T scanner and perfusion was measured using a comparison of T_1 selective and non-selective values. T_1 measurements were implemented using a fast ECG-gated saturation recovery FLASH sequence with 9 inversion times between 100 ms and 1400 ms. This study determined that as a non-invasive and repeatable measure, ASL could become a useful tool for the assessment of myocardial perfusion which was capable of assessing differences between areas of hyper- and hypo-perfusion.

Wang *et al* (16) used ASL for the estimation of myocardial perfusion and tissue transit time whilst free breathing using a navigator-echo. In this work, a single TI technique was repeated multiple times between 200 and 1700 ms. 11

healthy volunteers were scanned using a 1.5 Tesla scanner. FAIR labelling was used and a navigator echo was acquired immediately prior to the bFFE readout. To assess the sensitivity and reproducibility of the technique, the scan at a single time point (900 ms) was repeated during a stress challenge by asking the subject to squeeze a foam stress ball during the scan. This work also assessed the use of non-rigid motion correction to correct for any residual motion following the free breathing technique. Data was fit to a kinetic model to estimate both perfusion and arterial transit time. This work determined that free-breathing myocardial perfusion imaging with ASL was feasible with use of a navigator echo and with retrospective non-rigid motion correction.

A study by Northrup *et al* (13) compared 1.5 T and 3 T MR measures for myocardial ASL. Eight healthy volunteers were scanned at both field strengths. This study found that 3T is optimal for cardiac ASL, as less variability was seen at 3T and the SNR was higher. The main limitation here was the sensitivity of the scanning to motion as ECG triggering and breath-holding is not entirely effective at the elimination of motion. The repeatability at 3T was found to be 43 % higher than that at 1.5 T although no statistically significant differences were seen.

The work by Zun *et al* (21) sought to determine whether ASL was capable of detecting clinically relevant increases in myocardial blood flow with vasodilator stress induced by use of an adenosine infusion. Sixteen patients who were suspected of having ischemic heart disease were scanned using a 3 T scanner with a double-gated FAIR labelling scheme and a bFFE readout. ASL results were compared to measurements taken with first pass perfusion techniques using a gadolinium based contrast agent. This work showed that ASL was capable of detecting perfusion changes following an adenosine infusion and as such this could be used to identify myocardial ischemia.

It is clear from the previous studies using myocardial ASL that an important consideration is how to eliminate noise from the data. The previous work

indicates that it is feasible to measure myocardial perfusion using cardiac ASL; however there are a few limitations that need to be considered. In the current myocardial ASL studies in humans, there has been work in which single time point ASL has been implemented (10,21,22) (Figure 3.1-1) and studies in which a single time point technique has been repeated across multiple inversion times to build up a full ASL signal curve (13,16). Single time point measures are more susceptible to error when quantifying myocardial perfusion, but a repeated single TI approach can be very time consuming. An alternative to this is to use a Look-Locker scheme in which multiple images at different label delays are acquired after a single inversion using low flip angle excitations. Use of a Look-Locker scheme would decrease the scan time and if a breath hold technique was being used, would necessitate fewer breath holds.

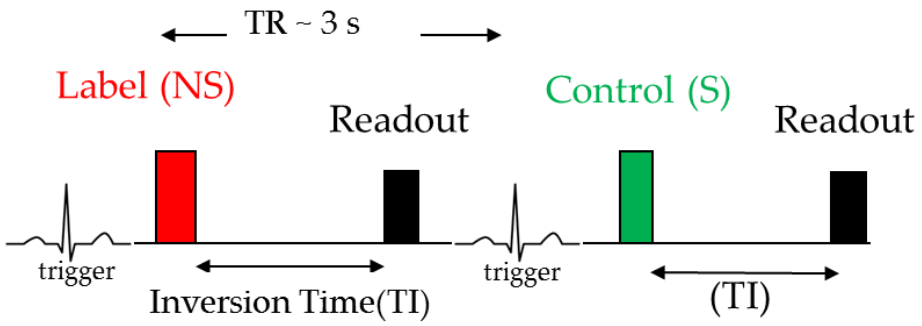

Figure 3.1-1: *Single time point cardiac triggered ASL. The label and control pulses are triggered off the cardiac cycle and then collected after an inversion time (TI).*

Look-Locker schemes have been implemented for cardiac ASL in animal studies. A cardiac triggered Look-Locker technique is highly effective in the rat heart as the RR interval in a rat is approximately 250 ms, there is thus sufficient time to acquire multiple cardiac triggered time points before the ASL signal has recovered. Campbell Washburn *et al* (7) employed an ECG-gated Look-Locker sequence with segmented k-space acquisition with 4 phase encoding lines acquired for each heartbeat. This was implemented to acquire single slice ASL data sets in the mouse heart. A data logger was used to allow automatic rejection of respiration-corrupted images; it also provided

additional prospective gating to improve consistency of acquisition timing and allow uncorrupted lines of k-space from consecutive data sets to be recombined to reduce corruption due to respiration. This study assessed variability and reproducibility of perfusion estimation between-animals, between-session, within-session and between image rejection criteria, by estimating the coefficient of variability (CoV). The results of this work found that the between-animals coefficient of variability was the largest at 24 %, whereas the between-session variability was 17 %, whilst the within-session variability was only 11 %. The magnitude of change in perfusion needed to detect differences was 30% within-session and 55% between-session.

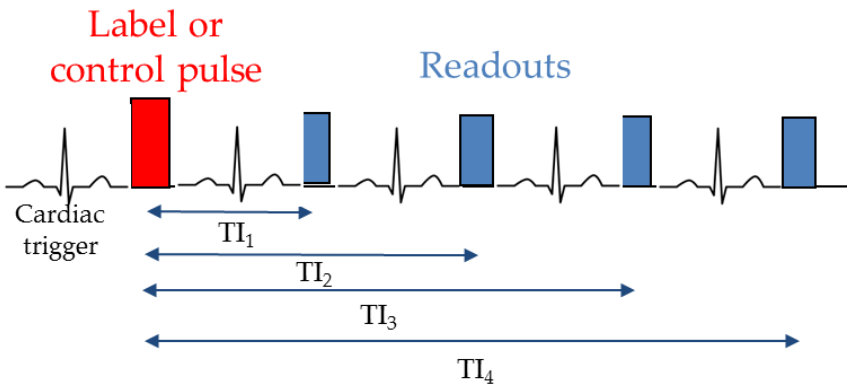

Figure 3.1-2: *A cardiac gated Look-Locker experiment. The label or control pulse is triggered off the cardiac trigger, subsequent Look-Locker readouts are then all triggered from the cardiac cycle to minimise cardiac motion.*

In the work by Kampf *et al* (12), the influence of heart anatomy, cardiopulmonary blood flow and the Look-Locker readout were assessed in the mouse heart. This paper showed that unintentional partial inversion of the inflowing blood occurs during the slice selective inversion, and they assessed this effect, as well as that of the Look-Locker pulse train, on perfusion quantification. This paper concluded that careful consideration of the Look-Locker readout and the non-ideal slice selective inversion is needed as not accounting for the Look-Locker pulses can lead to overestimation of the

perfusion whereas not correcting for the partial inversion of the inflowing blood can cause an underestimation of perfusion.

In humans, the RR interval is much longer than in animals (≈ 1000 ms in humans compared to ≈ 250 ms in the rat), and so a cardiac triggered Look-Locker readout alone will not achieve enough data points for accurate quantification in the time that there is sufficient signal. This is also relevant for T_1 mapping of the myocardium. To overcome this problem, Messroghli *et al* (23) developed a modified Look-Locker inversion recovery (MOLLI) scheme. In this chapter the MOLLI scheme is outlined for T_1 mapping and then adapted for use for ASL. This developed ASL scheme can then be used for assessment of perfusion in a CKD patient group.

3.2 MOLLI T_1 Mapping

Modified Look-Locker inversion recovery (MOLLI) (23–26) is typically used in conjunction with a contrast agent for T_1 mapping. A MOLLI scheme works by repeating a cardiac triggered Look-Locker experiment with different inversion times. In a standard MOLLI scheme for T_1 mapping, three successive Look-Locker experiments are performed with three, three and five single shot cardiac triggered Look-Locker readouts. Each of the readouts is acquired using a low flip angle excitation pulse, generally of 35^o. There is a recovery time of a minimum of four seconds between each Look-Locker experiment to ensure full recovery of the longitudinal relaxation before the next set of Look-Locker data is acquired. A trigger delay (TD) is introduced between the cardiac trigger and the inversion pulse which is changed for each Look-Locker set. By changing the trigger delay, the time between the inversion and first readout is then different for each of the Look-Locker sets. Due to this trigger delay, the scans performed will all have different TIs which will be determined by the initial TI plus the length of the cardiac cycle that has

occurred since the acquisition of the first image. The images are then reordered according to their effective TI as if they had been acquired in one Look-Locker experiment (Figure 3.2-1) each LL set would be fit separately to calculate T_1. Each LL set would be fit iteratively to an inversion recovery with $M_z = M_i \sin\alpha$ for the longitudinal magnetisation and $M_{xy} = M_i \cos\alpha$ for the transverse magnetisation for the first time point and subsequent time points are fit from the magnetisation from the previous time point such that

$$M_i = M_0\left(1 - e^{-\frac{TI(i)-TI(i-1)}{T_1}}\right) + M_z(i-1)e^{\frac{TI(i)-TI(i-1)}{T_1}}$$

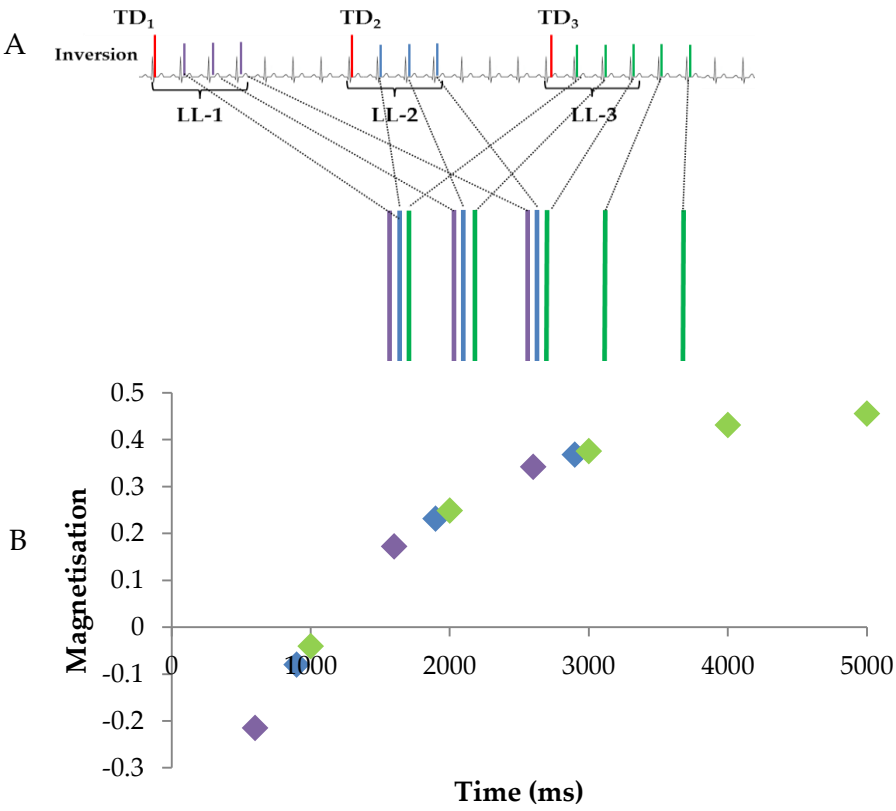

Figure 3.2-1: *A) A Standard MOLLI T1 mapping scheme with three separate Look Locker experiments (LL-1, LL-2, LL-3) with 3, 3 and 5 readouts respectively. B) the resulting recovery curve from these three Look-Locker experiments simulated with T_1 of 1600 ms, RR interval of 1000 ms and trigger delays of 400 ms 100 ms and 0 ms. The colour bars on each of the readouts in A correspond to the points on the graph with the same colours.*

3.3 MOLLI-ASL

MOLLI T_1 mapping can be used as a method to develop a modified Look-Locker ASL scheme (MOLLI-ASL) for the assessment of myocardial perfusion. In this work, a MOLLI-ASL scheme was developed using a similar method to MOLLI T_1 mapping, but using selective or non-selective inversion labelling pulses in place of the non-selective inversion, and placing pre- and post-saturation pulses around the selective and non-selective labelling pulses. In the MOLLI-ASL scheme, FAIR selective/non-selective inversions are triggered from the cardiac trigger and followed by multiple cardiac triggered readouts. In order to minimise motion between scans, all readouts are triggered at the same point in the cardiac cycle which was chosen to be at end diastole (Figure 3.3-1). A trigger delay (TD) is introduced which changes the time between the cardiac trigger and the label pulse and so changes the readout times (TIs) of the LL readout pulses. An increase in the trigger delay will decrease the inversion time (TI) as the time between the cardiac trigger and the inversion is increased so the time between the inversion and first readout decreases (assuming the RR-interval stays constant). In each separate Look-Locker experiment, a number of images are collected at end-diastole of consecutive heart beats to sample the recovery of longitudinal magnetization after the inversion pulse. At the end of each experiment an end delay of 3 seconds was applied to ensure full recovery of the longitudinal magnetisation between selective and non-selective pairs.

As for T_1 mapping, the scans all have different TIs or post-label delays which will be determined by the initial TI plus the length of the cardiac cycles that have occurred since the acquisition of the first image. The images can then be reordered according to their effective TI as if they had been acquired in one Look-Locker experiment, leading to a MOLLI recovery curve. However, data would be fit as separate LL experiments.

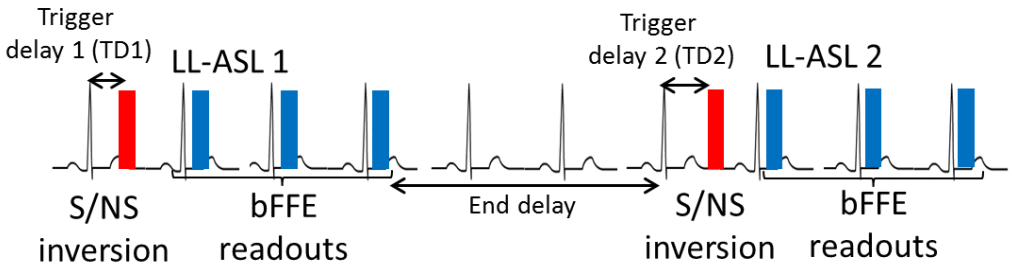

Figure 3.3-1: *MOLLI ASL schematic for two different LL-ASL experiments with different trigger delays (TD1 and TD2) and three Look Locker readouts for each experiment. The sequence starts with a cardiac triggered selective or non-selective inversion which occurs after a trigger delay following the cardiac trigger. This is followed by three readouts which are all cardiac triggered to be at the same point in the cardiac cycle.*

3.3.1 Pulse programming

A MOLLI ASL scheme was coded on a Philips Achieva 3T scanner using the pulse programming environment (PPE). This was performed by enabling cardiac trigging for the FAIR arterial spin labelling module and the subsequent bFFE image readouts. A 'Trigger-delay' (TD) was added prior to the label module to allow data to be collected at a range of post-label delay (PLD) times. An 'End-delay' period was added following the LL readout pulses to ensure full recovery of longitudinal magnetisation between each selective (S) and non-selective (NS) inversion (Figure 3.3-1). Optional pre- (WET scheme) and post-saturation pulses were placed around the S/NS inversion pulse to minimize inversion efficiency differences in the imaging plane between the slice-selective and non-selective conditions.

3.3.2 Techniques to model cardiac ASL data

There are two different methods that have generally been proposed in the literature to model the ASL signal; the Belle model (27) and an approach using iterative Bloch equations (8). These two techniques are described here.

3.3.3 Belle Model

Previously, Belle *et al* (27) developed a model for the quantification of myocardial perfusion using a FAIR ASL scheme. This model considers two compartments; one compartment of intravascular capillary blood and the second of extravascular tissue. The contribution of magnetisation inside the venous and arterial system is assumed to be negligible which is a valid assumption as the arterial and venous volume are less than 3 % of the myocardium. In this model, myocardial perfusion is calculated from the difference between the longitudinal relaxation (T_1) computed following the selective and non-selective inversions. After the selective pulse, it is assumed that all blood flowing into the imaging slice is fully relaxed and this results in a shorter T_1 than for the non-selective case which has been influenced by blood following a non-selective inversion recovery.

The longitudinal relaxation for the selective inversion (T_{1SEL}) is described by

$$\frac{1}{T_{1SEL}} = \frac{1}{T_1} + \frac{P}{\lambda} \qquad 3\text{-}1$$

where T_1 is the T_1 of the tissue, P is the tissue perfusion and λ is the blood-tissue partition coefficient of water (0.92 in the heart). The T_1 for the non-selective condition (T_{1NS}) is given by

$$\frac{1}{T_{1NS}} = \frac{{}^{1}/_{T_1} + {}^{P}/_{\lambda}}{1 + {}^{PT_{1b}}/_{\lambda}} \qquad 3\text{-}2$$

where T_{1b} is the T_1 of blood. These equations can be combined to give an expression for myocardial perfusion (P):

$$P = \frac{\lambda}{T_{1b}}\left(\frac{T_{1NS}}{T_{1SEL}} - 1\right) \qquad 3\text{-}3$$

The assumption that selective blood is always fully relaxed is not strictly correct as when a slice selective inversion is applied, a volume of blood in the right ventricle, left ventricle, capillary bed of the lung and vessels will also be inverted (Figure 3.3-2). This blood is then recirculated through the left ventricle and then perfuses the myocardial tissue and so may still be labelled as it reaches the tissue. Also, as the ejection fraction of the left ventricle is < 100 %, some of the blood delivered to the myocardium will still be inverted for many heartbeats following inversion. However if the slice selective inversion is narrow, as used in this thesis, this volume of blood will be small. This issue is particularly problematic in multi-slice ASL where a larger volume is labelled in the slice selective condition.

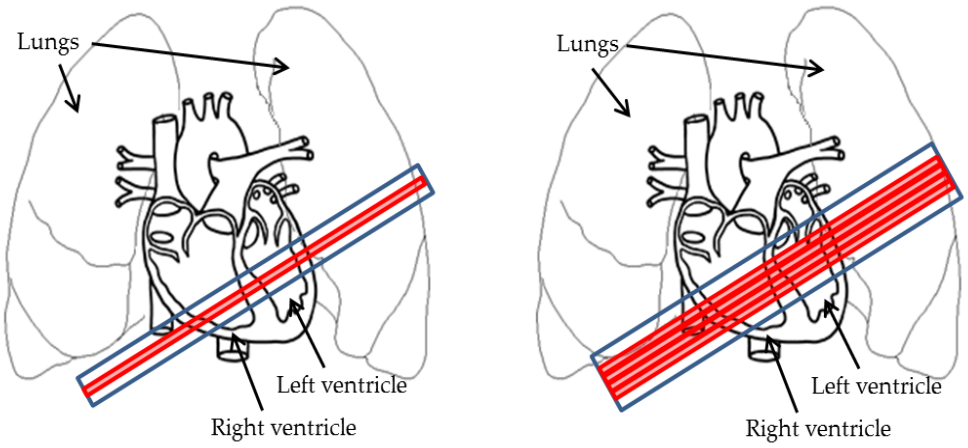

Figure 3.3-2: *Schematic showing the placement of single and multiple slices (red) across the heart. In the multi-slice case, the right ventricle and lungs are also labelled by the slice selective inversion (blue).*

3.3.3.1 Iterative Bloch equations

Campbell-Washburn *et al* (8), proposed an alternative to the Belle model for use with multi-slice FAIR ASL in the mouse model, where this is a greater issue due to the large volume of blood that is inverted following slice selective inversion in the multi-slice case. Thus in this case it is likely that a simple Belle model is not sufficient for precise quantification of perfusion and also due to

the short RR wave of the rat. The model that was derived in this work is known as the blood pool MBF (bpMBF) quantification model. This bpMBF model involves using the measurement of the blood magnetisation from the blood pool as the input signal and fitting the signal iteratively to a modified Bloch equation (3) which describes the longitudinal magnetisation and the effect of perfusion. This model assumes that there is sufficiently fast exchange of spins between the intravascular and extravascular compartments. This has been demonstrated to be a valid assumption in both animals (28) and humans (29). The modified Bloch equation is given by

$$\frac{dM_{tissue}(t)}{dt} = \frac{M_{0,tissue}(t)}{T_{1,tissue}} - \left(\frac{1}{T_{1,tissue}} + \frac{MBF}{\lambda}\right) M_{tissue}(t) + MBF.M_{blood}(t) \quad 3\text{-}4$$

which can be simplified to

$$M_{tissue}(t) = M_{0,tissue}\frac{T_{1,app}}{T_{1,tissue}}\left(1 - e^{-t/T_{1,app}}\right) + M_{tissue}(0)e^{-t/T_{1,app}} + MBF\int_0^t M_{blood}(\tau)\, e^{\tau - t/T_{1,app}} d\tau \quad 3\text{-}5$$

Where $\frac{1}{T_{1,app}} = \frac{1}{T_{1,tissue}} + \frac{MBF}{\lambda}$

A thorough derivation of this model is given in Chapter 2.

This work also showed that in the mouse heart it takes approximately 3 seconds for the blood pool magnetisation to return to equilibrium following slice selective inversion, highlighting the need for an end-delay to ensure all data has returned to equilibrium before acquiring the next LL data set.

3.3.4 Simulations

To assess the sensitivity of the LL-ASL technique, and to understand the source of potential errors in perfusion quantification, Monte Carlo simulations

were performed in MATLAB (Matlab version 8.1, The MathWorks, Inc., Natick, MA, USA). The Monte Carlo simulation was performed by adding random Gaussian noise to simulated 'perfect' data to achieve simulated data with asymptotic SNR up to an SNR of 70:1.

Simulations were first performed to determine how the signal-to-noise ratio (SNR) and flip angle of Look-Locker readout pulses affects the measured signal, the quantified T_1 measurements and calculated perfusion values for a standard Look-Locker readout as shown in Figure 3.3-3.

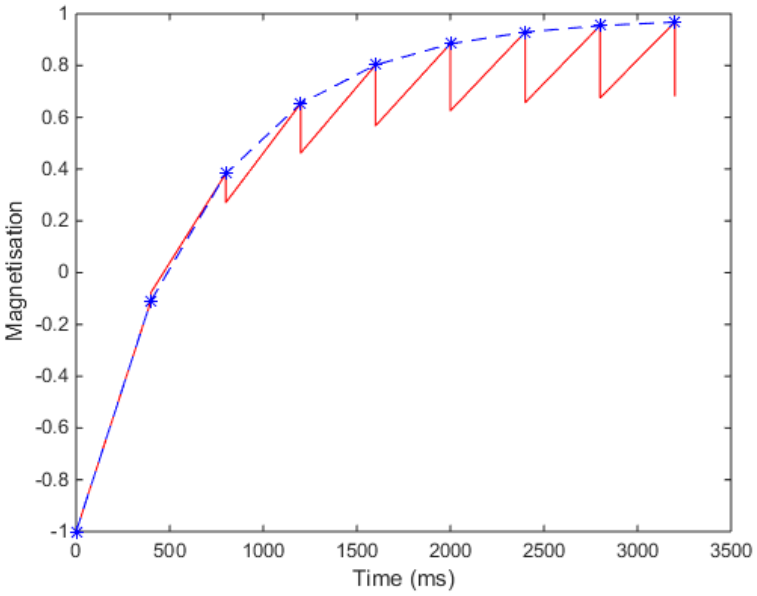

Figure 3.3-3: *A Look-Locker recovery curve simulated for a T_1 of tissue of 1600ms, flip angle of 45° and readout spacing of 400ms.*

The optimal flip angle for different Look-Locker readout spacings (defined by the RR-wave) was then assessed. From the literature (7,8), the optimal flip angle for a Look-Locker scheme to study the mouse heart, where the RR-wave interval and hence readout spacing is small at approximately 100 ms, has been shown to be approximately 20°. In humans, the RR-wave and hence readout spacing is approximately 1000 ms, suggesting a larger readout flip angle is required.

Data was simulated for a Look-Locker readout of 1000 ms (as typically found in the human heart), T_1 non-selective (T_{1NS}) of 1300 ms, T_1 slice-selective (T_{1SEL}) of 1250 ms and T_1 of blood (T_{1blood}) of 1870 ms which gave a MBF of 1 ml/g/min using the Belle model. 1000 repeats were performed for each Monte Carlo simulation.

i) Choice of flip angle for LL-scheme

Firstly, the effect of choice of flip angle on the accuracy and error in the fitted value of T_{1SEL}, T_{1NS} and calculated value of perfusion was investigated, performing a Monte Carlo simulation, simulating data using the Belle model, with 1000 repeats. This was first assessed for an RR interval of 100 ms similar to that of a mouse and thus a LL spacing of 100 ms.

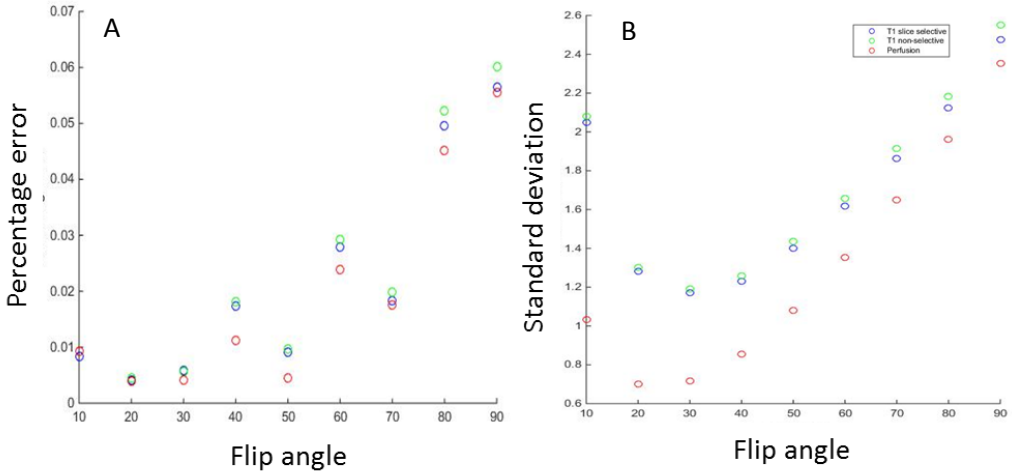

Figure 3.3-4: *Graph to show A) the percentage error and B) the standard deviation in T_{1SEL} (blue), T_{1NS} (green) and perfusion (red) values for increasing flip angle for a Look-Locker ASL scheme with LL readout spacing of 100 ms.*

Figure 3.3-4 shows that the optimal flip angle for the mouse heart would be 20° which is the same as was found in the literature (7) thus providing confidence that the technique used is correct.

This was repeated for a LL readout spacing of 1000 ms (similar to the RR-interval for a human heart). From Figure 3.3-5 it can be seen that for a spacing of 1000 ms, the optimal flip angle is ~ 70° when ignoring any SAR constraints.

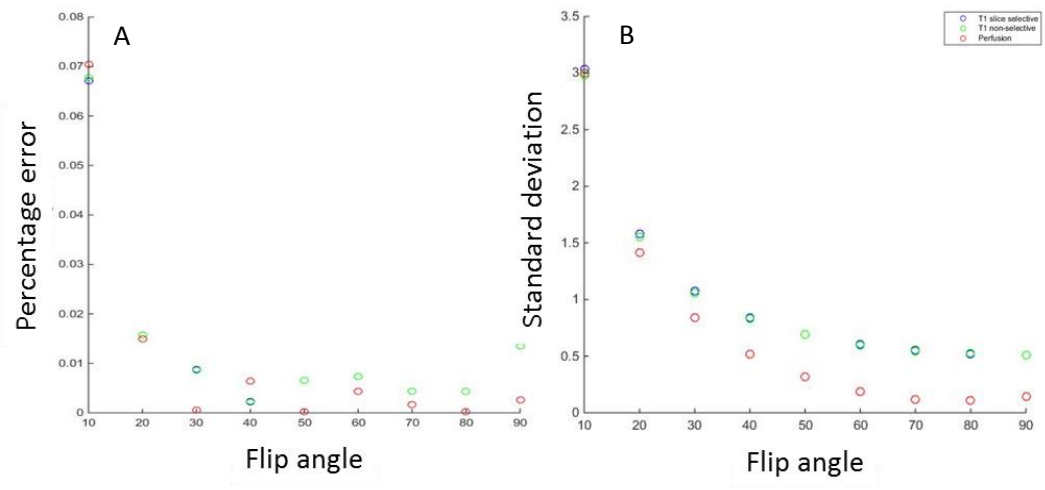

Figure 3.3-5: *A) Percentage error (%) and B) Standard deviation (%) in T_{1SEL} (blue), T_{1NS} (green) and perfusion (red) values for increasing flip angle for a Look-Locker ASL scheme with LL readout spacing of 1000 ms.*

Although the optimal flip angle for a LL acquisition with readout spacing of 1000 ms is around 70°, in practice the flip angle is restricted to 35° due to SAR constraints.

ii) Effect of SNR for LL scheme

Secondly, the effect of the SNR on the error and standard deviation of fitted T_{1SEL}, T_{1NS} and resulting myocardial perfusion values was assessed. This was again performed by Monte Carlo simulation, simulating data using the Belle equation, with 1000 repeats, assuming a LL readout spacing of 1000 ms with 11 readouts, a flip angle of 35°. The SNR was varied from 10:1 to 100:1 in steps of 10.

Figure 3.3-6 shows that, as expected, increasing the SNR decreases the standard deviation and the percentage error in all fitted variables, and for a SNR 50:1 the error becomes approximately constant.

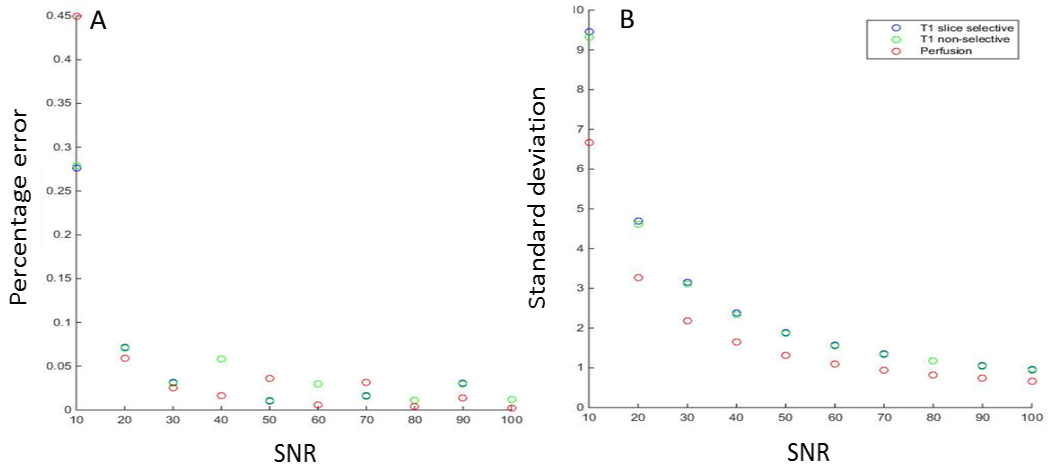

Figure 3.3-6: *A) Percentage error (%) and B) Standard deviation (%) in T_{1SEL} (blue), T_{1NS} (green) and perfusion (red) values for increasing SNR. T_1 selective and non-selective give a similar result and so are overlapping.*

iii) MOLLI-ASL simulations

Having simulated a standard Look-Locker ASL scheme, simulations were performed for a MOLLI-ASL scheme to assess the effect of changing (a) the number of readouts following each selective and non-selective inversion and (b) increasing the number of Look-Locker sets that were performed, thus increasing the number of trigger delays and increasing the maximum trigger delay. All simulations were performed with a Look-Locker spacing of 1000 ms and a flip angle of 35°, as this was the maximum flip angle achievable when scanning patients due to SAR constraints. 1000 iterations of the simulation were performed. Perfusion measures were calculated from the selective and non-selective T_1 values using the Belle model. The number of readouts for each Look-Locker experiment was assessed from between 3 and 5, and the number of separate Look-Locker sets was varied from 1 to 11 each having trigger delays increasing by 50 ms (8 LL sets would give a maximum trigger

delay of 350 ms whereas 11 LL sets would have a maximum trigger delay of 550 ms).

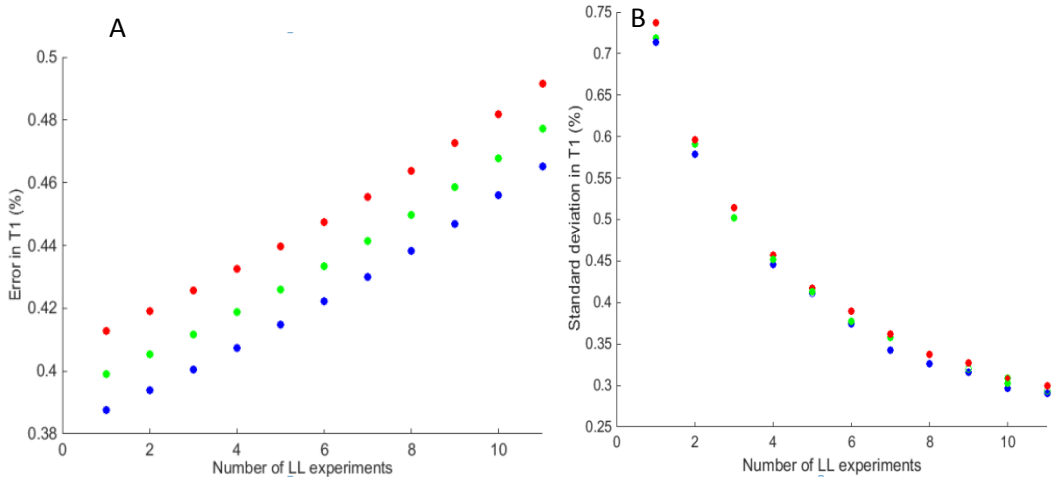

Figure 3.3-7: *A) Percentage error and B) Standard deviation in fitted T_1 values with increasing maximum trigger delay times (corresponding to 1 – 11 different Look-Locker sets) for 3 (red), 4 (green) and 5 (blue) Look-Locker readouts.*

Figure 3.3-7 shows the standard deviation and percentage error in T_1 for increasing number of readouts and increasing number of Look-Locker sets with increasing maximum trigger delay. The same result was seen for both T_{1SEL} and T_{1NS} and so only one result for T_1 is shown here. It can be seen from this graph that the standard deviation decreases as the number of readouts increases and as the number of LL experiments increases. These results are as expected, as more data points are used for the fit as the number of readouts increases. The error in the fit is small (< 1%) which shows that the fit is accurate and errors come from the standard deviation and thus the error will come from lower precision rather than low accuracy.

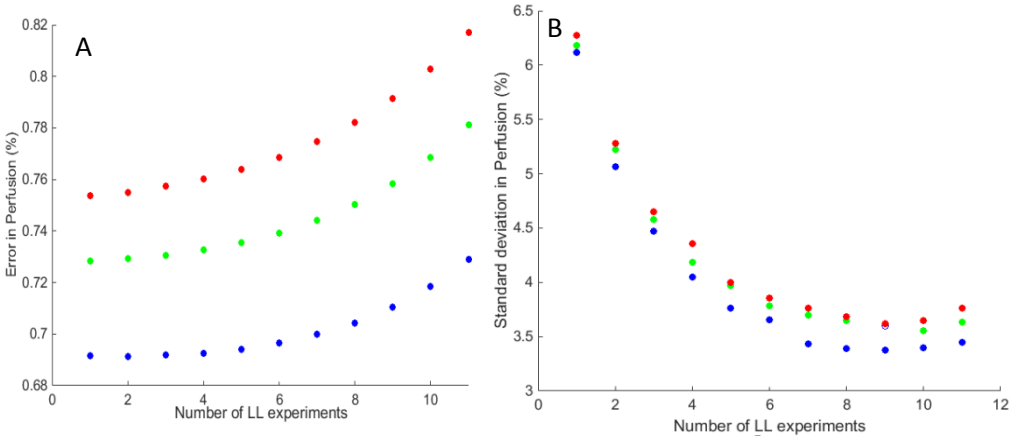

Figure 3.3-8: *Standard deviation in fitted myocardial perfusion values with increasing maximum trigger delay times (corresponding to 1 – 11 different Look-Locker sets) for 3 (red), 4 (green) and 5 (blue) Look-Locker readouts.*

shows results for the standard deviation in perfusion. Similar to the T_1 results, as the number of LL sets and the number of readouts increases, the standard deviation in the calculated perfusion value decreases. It should be noted that for only 3 readouts with a maximum pre-label delay of 350 ms the standard deviations is less than 1.5 % for T_1 and 4 % for perfusion and so accurate results can be measured whilst using only 3 readouts for each trigger delay. Again, similar to T_1 the error in the fit is small (< 1%). The small errors in T_1 fits should also be noted as when the Belle model is used for fitting the ASL data, accurate T_1 values are required. Using less Look-Locker sets and less readouts following each selective or non-selective pulse also decreases the total scan time and so makes the sequence more tolerable for patients. If it was decided that a breath hold was needed then a shorter scan time would be desirable to acquire data within a tolerable breath hold time. All simulations here assume only thermal noise and so the error would increase if any physiological noise was present.

3.3.5 T_1 validation

To assess whether the pulse programming had successfully provided an accurate MOLLI scheme on the Philips system, T_1 data was collected on an agar four quadrant phantom using a simulated RR-interval of 1000 ms. The MOLLI-ASL scheme was performed using a bFFE readout scheme without any pre- and post- saturation pulses. For this quantification, data was acquired using a non-selective label with an inversion slab of 300 mm. This then leads to a standard T_1 inversion recovery technique repeated multiple times with a MOLLI readout. The MOLLI scheme was validated using a phantom with 3 readouts per Look-Locker experiment and 9 trigger delay times starting at 0 ms and increasing to 400 ms in increments of 50 ms. Data was also collected for a standard inversion recovery scheme (TI values of 0 - 5000 ms with 14 steps) for comparison. Data was acquired in the short axis which was defined using bTFE localiser scans. All imaging was performed using a bFFE readout with FOV 288 x 288 mm^2, spatial resolution 3 x 3 mm^2, slice thickness 5 mm, SENSE 2, TE/TR 1.5/3.1 ms, FA 35°, centric half Fourier acquisition with 12 start-up echoes.

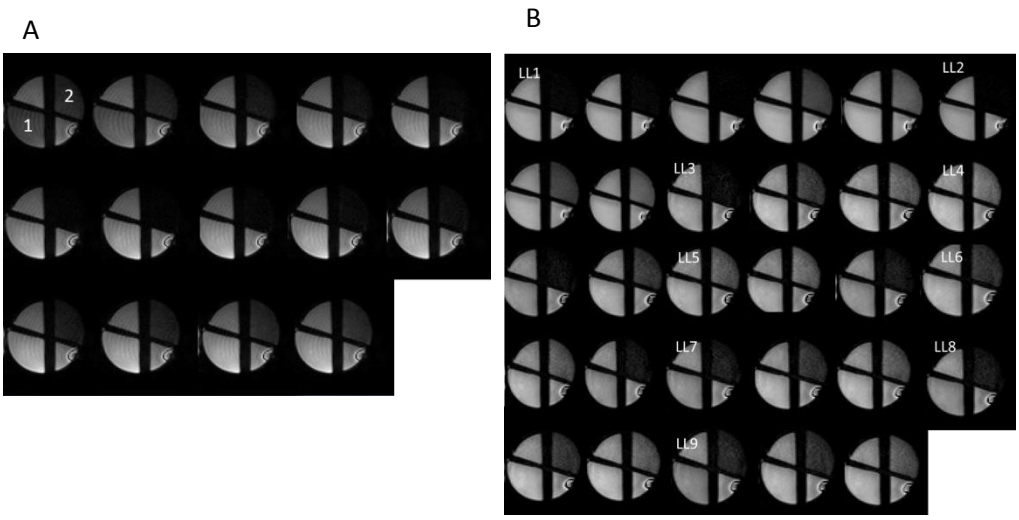

Figure 3.3-9: *A) Inversion recovery phantom data acquired at 17 TIs between 0 and 5000 ms and B) MOLLI data acquired at 9 trigger delay times starting at 0 ms and increasing to 400 ms in increments of 50 ms. The maximum number of readouts was acquired at each TD dependent on SAR restrictions.*

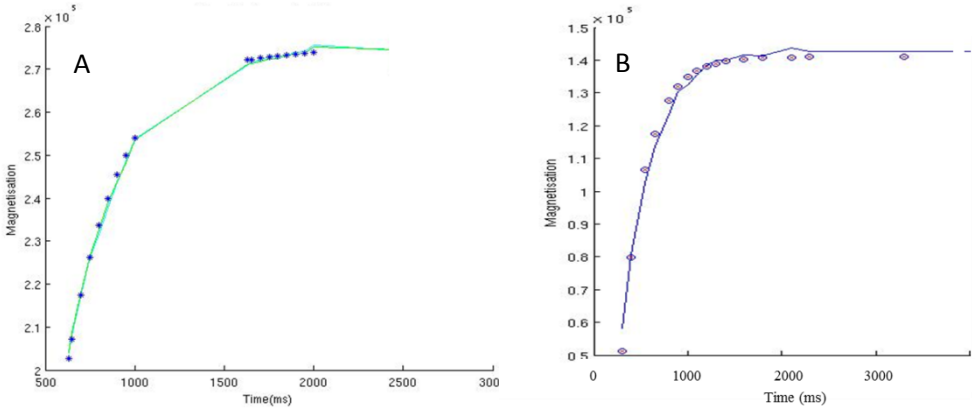

Figure 3.3-10: *Recovery curves for A) MOLLI T1 data and B) inversion recovery data for the upper right quadrant. The fit is shown by the solid line.*

Using a least squares fitting algorithm in MATLAB (Matlab version 8.1, The MathWorks, Inc., Natick, MA, USA), T_1 and M_0 values were fit for all quadrants. The MOLLI data was fitted iteratively to an inversion recovery with $M_z = M_i \sin\alpha$ for the longitudinal magnetisation and $M_{xy} = M_i \cos\alpha$ for the transverse magnetisation for the first time point and subsequent time points were fitted from the magnetisation from the previous time point such that

$$M_i = M_0\left(1 - e^{-\frac{TI(i)-TI(i-1)}{T_1}}\right) + M_z(i-1)e^{\frac{TI(i)-TI(i-1)}{T_1}}$$

The inversion recovery data was fit to the equation

$$M_z(t) = M_0(1 - 2e^{-TI/T_1})$$

When fitting the data to these models, the MOLLI data gave similar results to the inversion recovery scan with approximately 10 % difference between the measures from the two techniques for T_1.

Recovery curves for MOLLI T_1 data and inversion recovery data is shown in

Figure **3.3-10**. T_1 values were fitted to all quadrants. The fitted T_1 values from this data for the two quadrants (shown as 1 and 2 in Figure 3.3-9 A) are shown in Table 3.3-1.

	MOLLI scheme	**Inversion Recovery scheme**
Quadrant 1		
T1 (s)	1.3265	1.2845
Quadrant 2		
T1 (s)	0.313	0.26

Table 3.3-1: *Calculated T1 values from the MOLLI acquisition and inversion recovery curves.*

Good agreement is shown in the T1 values between the two schemes. The other two quadrants had a similar T_1 to quadrant 1 and so were omitted from the results.

3.4 Testing MOLLI-ASL on healthy volunteers

Having validated T_1 measures in a phantom, this section now assesses the application of MOLLI-ASL to the human heart. In this work, a total of 6 subjects were scanned (21-24 years) on a 3T Phillips Achieva scanner with a 16-channel XL Torso coil with multi-transmit. A FAIR labelling scheme was used with selective thickness of 35 mm and non-selective thickness of 350 mm. Imaging was performed using a bFFE readout with FOV 288 x 288 mm^2, spatial resolution 3 x 3 mm^2, slice thickness 5 mm, SENSE 2, TE/TR 1.5/3.1 ms, FA 35^o, centric half Fourier acquisition with 12 start-up echoes. bTFE localiser scans were used to define the short axis of the left ventricle and all ASL images were acquired in this plane. In order to know the correct timings of each readout in the LL set, the MR scanner physiological logs were saved from the scanner and timings were calculated using a MATLAB script (Matlab version 8.1, The MathWorks, Inc., Natick, MA, USA). This script identified the

timing of selective and non-selective inversion pulses and subsequent readouts, allowing the spacing between each of these to then be calculated. In this work 9 LL sets were acquired with trigger delays of 0 ms to 400 ms in steps of 50 ms. Up to 5 readouts were acquired in each LL set dependent on SAR restrictions.

3.4.1 Motion correction

To minimise movement due to the respiratory cycle, breath holds are used in a number of studies using cardiac imaging. However, in a patient population, breath holds are not always tolerable, require patients to hold their breath at the same point in the respiratory cycle, and may not be practical if subjects are also performing a task. An alternative to a breath hold technique would be to retrospectively discard images where there is motion. This would be beneficial as it would remove the necessity for a breath hold which some patients would struggle to tolerate.

3.4.2 Need for an in-plane saturation scheme

For assessment of ASL measures, the MOLLI-ASL data was acquired both with and without in plane saturation to determine the necessity of an in-plane saturation scheme to the quality of the ASL data. An in-plane saturation scheme ensures that the signal in the imaging plane is in the same state at the beginning of each TR period, by nulling the signal in the imaging plane. Pre–saturation pulses using the WET scheme (30) were applied prior to the labelling pulse and post-saturation pulses were applied following the labelling pulse. These pre and post saturations ensure there is no offset between the inversion efficiency of label and control conditions (selective and non-selective inversion) which could cause an artificial ASL signal. However, the use of additional in-plane saturation RF pulses leads to increased SAR, and so limits the number of readouts that can be acquired. Figure 3.4-1 shows MOLLI

selective and non-selective signal curves for both the myocardium and left ventricular blood with and without in-plane saturation.

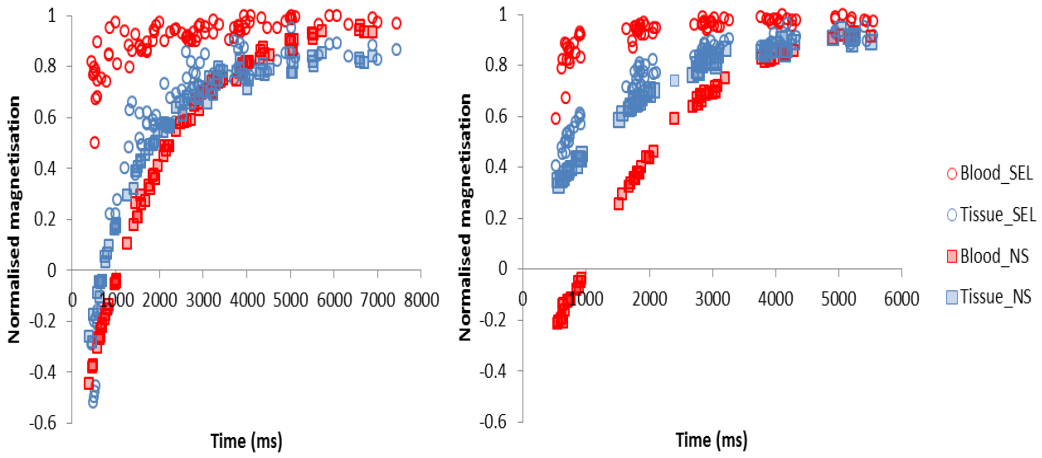

Figure 3.4-1: *MOLLI signal for the myocardium and left ventricular blood pool A) without and B) with in-plane saturation. The blood signal is shown in red and tissue signal in blue for the selective (SEL) and non-selective (NS) case.*

The data follows the trends that are expected for blood and tissue data, with the blood signal (red) being fully recovered for the selective case and following an inversion recovery for the non-selective case. The tissue signal (blue) can be seen to follow an inversion recovery in A) and a saturation recovery in B). It was found that the results were overestimated when an in-plane saturation pulse was not used and there was more variance in the values calculated. Perfusion was fit to the Belle model to be 1.98 ± 0.5 ml/g/min when no in-plane saturation was used versus 0.71 ± 0.1 ml/g/min when an in-plane saturation was used.

3.4.3 Modelling schemes

In order to assess the optimal model for fitting this single slice data, the data for all six patients was fitted to both the Belle model (Section 3.3.3) and the iterative Bloch equations (Section 3.3.3.1) using a least squares regression algorithm in MATLAB (Matlab version 8.1, The MathWorks, Inc., Natick, MA, USA). The fitted values of perfusion and T_1 and the associated sum of square errors were recorded. Using the Belle model, the average perfusion value (± standard error) was found to be 0.71 ± 0.1 ml/g/min and from the iterative Bloch equation, the average perfusion value was found to be 1.45 ± 0.22 ml/g/min. In the literature, a perfusion value of approximately 1 ml/g/min is found and so both models provide a perfusion value consistent with this however the Belle model provides a value with less variance. As this technique is a single slice acquisition, there is less of an issue with unintentional labelling during the selective inversion and so the assumption made in the Belle model that all inflowing blood in the selective case is fully recovered is likely to be valid.

3.4.4 Exercise challenges

In a number of papers, the ability of techniques to measure perfusion and assess changes in cardiac function is validated via an exercise challenge (22,31–33) or by use of a drug such as adenosine (18) to modulate myocardial perfusion. Alternatively, in the work by Capron *et al* (9), a cold pressor test (CPT) was performed on healthy volunteers in which the subjects' hand was immersed in cold water for a short amount of time during scanning. In the work by Zun *et al* (20) a simple leg raise challenge was performed and compared to the use of isometric hand grips as a stress test to measure myocardial perfusion. Another alternative is use of an MR compatible ergometer (34,35), where subjects are asked to exercise on supine bicycle whilst in the scanner. In this work, the choice of two methods available in the

SPMIC of either an MR compatible bicycle (Ergospect Medical Technology, Austria) or hand grips using a Grip Force Bimanual Optic Response Pad (Current Designs, Philadelphia) was assessed to determine which method had the minimal effect from motion and could be well tolerated by a patient group, whilst also inducing a noticeable change in perfusion.

A number of previous exercise studies have been performed using a MR compatible bike to look at the effect of exercise on cardiac function (18). For example, in the work of Hjortdal *et al* (35), real time MRI was used to measure blood flow in the inferior vena cava, superior vena cava and ascending aorta under inspiration and expiration during supine lower limb exercise using an MR compatible ergometer bicycle. Heart rate was monitored by an ECG and by pulse oximetry. The study concluded that aortic and inferior vena cava blood flow increases with exercise but the superior vena cava blood flow does not change.

For a CKD patient group who were the group of interest in this thesis, the use of a bicycle challenge was considered to be too demanding. Thus the alternative use of a cardiac stress challenge using a handgrip challenge (20,31,33) was considered most suitable. In the work by Zun *et al* (20), myocardial blood flow was assessed using a single TI ASL approach and perfusion was modulated using a handgrip challenge. Subjects were asked to maintain an isometric handgrip challenge at 40 % of their maximum voluntary contraction. This exercise was initiated 1-2 minutes before the ASL scan was started and then maintained and monitored throughout the ASL scan. They showed that in a healthy population, the average increase in myocardial blood was 29 % with a handgrip challenge.

3.5 Assessment of cardiac function in CKD patients

Patients with chronic kidney disease (CKD) have significantly higher rates of cardiovascular mortality compared to the normal healthy population. The link

between end-stage CKD and heart disease is known, but it has not been established at what stage of CKD cardiovascular function begins to decline. This study evaluates cardiac function in CKD Stage 3 patients by assessing cardiac function at baseline and in response to a handgrip challenge (33). The assessment of the dynamic change in cardiac function may be more effective at discriminating normal from abnormal cardiovascular function. The aim was to compare the cardiac response in patients with CKD with age-matched controls. A grip force challenge using bimanual handgrips was chosen for this study as an exercise technique that would be tolerated by the entire patient group. This study is used as a validation of the MOLLI-ASL scheme to assess its sensitivity to changes in perfusion following an exercise challenge, and in addition phase contrast MRI blood flow data is also collected for comparison.

3.5.1 Methods

10 Stage 3 chronic kidney disease (CKD) patients and 10 healthy age-matched controls (HC) took part in the study. All patients gave written informed consent and the study was approved by Derbyshire Research Ethics Committee. Clinical measures and patient recruitment was performed by Dr Claire Grant at the Royal Derby Hospital. Blood tests were performed on all subjects to confirm the stage of kidney disease for patients and to confirm that the healthy controls had normal kidney function. All scanning was performed on a 3 Tesla Phillips Achieva scanner using MultiTransmit and a 16-channel SENSE torso receive coil. Localiser scans were acquired in 3 orthogonal planes to define the short axis of the left ventricle and the aorta.

3.5.1.1 Patient cohort and healthy volunteer recruitment

CKD patients (male or female) were identified by the clinical care team at the Royal Derby Hospital following the inclusion and exclusion criteria in Table 3.5-1.

Inclusion	Exclusion
Age 18-65	Known cardiac disease
Able to give informed consent	Taking rate/rhythm controlling medication
CKD Stage 3b	Unstable CKD
	Unable to give consent or understand information
	NYHA Stage IV heart failure
	Contraindications to MRI
	Unable to sustain 20 mins of light exercise
	Diabetes

Table 3.5-1: *Inclusion and exclusion criteria for CKD Stage 3 patients.*

Healthy controls were recruited following the criteria listed in Table 3.5-2

Inclusion	Exclusion
Age 18-65	CKD of any stage
Able to give informed consent	Known cardiac disease
	Taking beta blockers, calcium channel blockers or other rate/rhythm controlling medication
	Major organ pathology, active infection or malignancy
	Smokers
	Pregnant, breastfeeding or intending pregnancy
	Contraindications to MRI
	Unable to sustain 20 mins of light exercise
	Diabetes

Table 3.5-2: *Inclusion and exclusion criteria for healthy control subjects.*

3.5.1.2 Phase Contrast MRI (PC-MRI) of aortic flow

Phase contrast (PC-MRI) data was acquired using a single slice TFE sequence with the imaging slice placed perpendicular to the aorta in all three directions. Scanning was performed whilst free breathing and 30 phases were acquired across the cardiac cycle. Scan parameters were FOV 280 x 264 mm^2, spatial resolution = 0.97 x 0.97 mm^2, slice thickness 10 mm, no SENSE, TE/TR = 2.3/3.7ms, FA = 15^o, TFE factor = 5, TFE shots 25, V_{ENC} = 300 cms^{-1}, NSA = 3. The scan was performed whilst free breathing and triggered on the cardiac cycle from the VCG data, scan time was approximately 1 minute dependent on the patient's heart rate.

3.5.1.3 Data Analysis of Phase Contrast data

PC-MRI data was analysed using ViewForum software (Philips Medical Systems, Best, NL) which was used to draw a region of interest over the aorta. This region of interest was then applied to all phases of the PC-MRI data. This ROI was then to calculate the mean velocity (cm/s) and vessel area (mm^2) across the cardiac cycle. From this the stroke volume was calculated, which defines the amount of blood pumped out of the heart per heart beat (in units of ml), and the cardiac output, which describes the volume of blood pumped out of the heart in a minute (in units of L/min). In addition to this, stroke volume index and cardiac index was calculated by dividing the stroke volume and cardiac output by the body surface area BSA respectively. Aortic strain was also measured, which is the percentage change in aortic area between diastole and systole across the cardiac cycle. The heart rate over the exercise paradigm was calculated from the MR scanner physiological logs. Note that heart rate and stroke volume interact to determine cardiac output. All comparisons of measures between groups were made using a student t-test in SPSS v22.

3.5.1.4 Arterial Spin Labelling

Having defined the short axis of the left ventricle using TFE localiser scans in three orthogonal planes, a free breathing cardiac triggered MOLLI ASL scheme (Figure 3.5-1) was performed using a FAIR labelling scheme with a selective slab with width 35 mm and non-selective slab of width 350 mm. In-plane WET pre-saturation pulses were placed before the FAIR selective and non-selective inversions, and these inversions were followed by sinc post saturation. Images were acquired using a bFFE readout with FOV 288 x 288 mm^2, spatial resolution 3 x 3 mm^2, slice thickness 5 mm, SENSE 2, TE/TR 1.5/3.1 ms, FA 35^o, centric half Fourier acquisition with 12 start-up echoes.

For the MOLLI ASL timings, trigger delays from 0 – 350 ms in 50 ms steps were collected with three readout pulses for each trigger delay and an end delay of 3000 ms following each LL set of three readouts. Three readouts were used as it was seen from the previous data that the signal had fully recovered after three readouts. The maximum trigger delay was set to 350 ms due to SAR restraints. This resulted in a MOLLI-ASL recovery curve with 24 time points with the minimum time point being the length of the subjects RR-wave minus 350 ms and the maximum being three times the length of the subjects RR-wave. Following each set of three Look-Locker readouts, an end delay period of 3000 ms was applied to ensure that the longitudinal magnetisation had fully recovered before the next selective/non-selective pulse. In order to determine the readout times for each of the scans, physiological logs were recorded from the scanner throughout. A schematic of the MOLLI-ASL scheme used is shown in Figure 3.5-1.

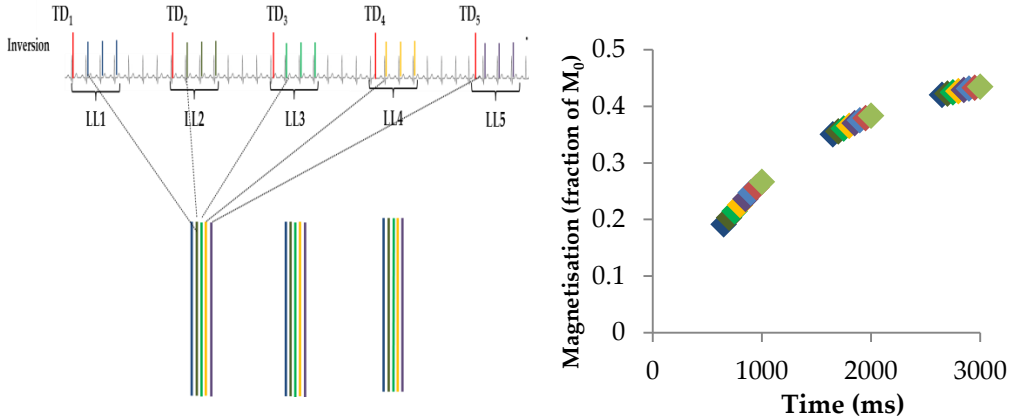

Figure 3.5-1: *A) Schematic of MOLLI-ASL scheme showing 5 of the 8 different Look-Locker sets (LL1 to LL5) each with a different trigger delay (TD). B) Resulting ASL recovery curve with from 8 LL sets with trigger delays from 0 – 350 ms, with each LL set comprising three readouts.*

When the data is collected this way, the data can be reordered according to the TI of the image in order to view the data as the contrast changes. Figure 3.5-2 shows the data in order of acquisition and then reordered according to TI of the image. This data is reordered using the physiological logs from the scanner to know the timings of the images.

A B

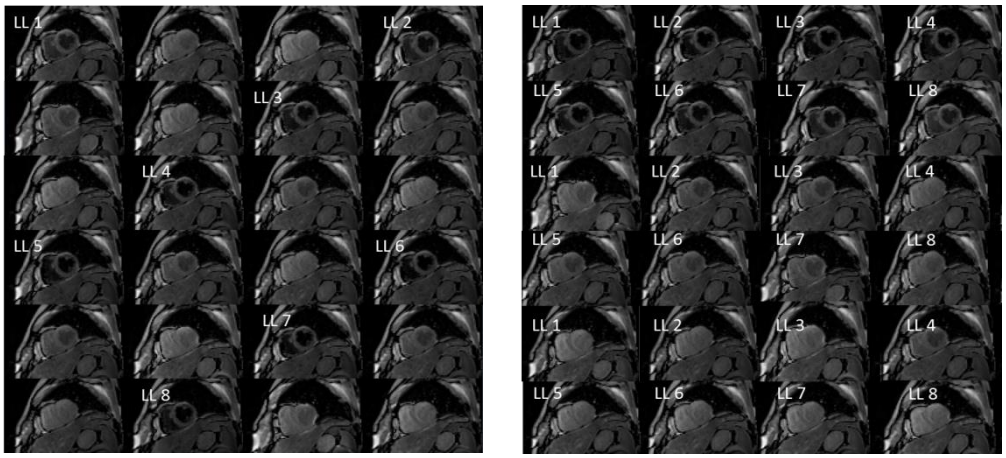

Figure 3.5-2: *A) Data in the order it is acquired in the scheme for 3 readouts for each LL set. B) Reordered data according to the readout time which show the change in contrast as the post label delay increases.*

3.5.1.5 Data analysis of ASL data

ASL data was analysed using custom written MATLAB software (Matlab version 8.1, The MathWorks, Inc., Natick, MA, USA). Data was loaded into the programme and inspected for motion and image volumes with motion were discarded when necessary. Regions of interest were drawn in the myocardium and left ventricular blood pool using the ROI function within MATLAB. The non-selective data from the left ventricular blood pool was fitted to estimate the T_1 of blood (T_{1b}). It was assumed that all blood flowing into the left ventricle was fully recovered for the selective case. The timings of each readout was calculated using the physiological logs recorded from the scanner and using these timings, the selective and non-selective curves were fitted separately to a saturation recovery using a least squares regression algorithm to calculate T_{1S} and T_{1NS} respectively. The fitted values for T_{1NS}, T_{1S} and T_{1b} were then used in the Belle Model to calculate perfusion.

3.5.1.6 Handgrip Challenge

A handgrip exercise paradigm (Figure 3.5-3) was performed using a Grip Force Bimanual Fibre Optic Response Pad (Current Designs, Philadelphia). During the 'Exercise' blocks, subjects were visually cued to squeeze against the resistance in the hand grips until they reached a target maximum force level of 100 N and to remain still during the 'Rest' blocks. The paradigm comprised two 'Rest' and two 'Exercise' blocks to assess both recovery and response to a second exercise session. Visual feedback was given to subjects and the scanner operator throughout the exercise challenge; this was visible in the scan room and in the control room. This programme was written in Presentation software (Neuro Behavioural Systems) to allow the subjects to gauge the force they were using and to ensure this paradigm was linked to the MR scanner triggers.

Subjects were asked to maintain the force level for 8 minutes whilst both PC-MRI and ASL scans were acquired. Before scanning patients and age-matched controls, healthy volunteers were scanned to assess the feasibility of using the handgrips, to determine what the maximum force level that could be set and the amount of time that was tolerable to maintain the handgrip.

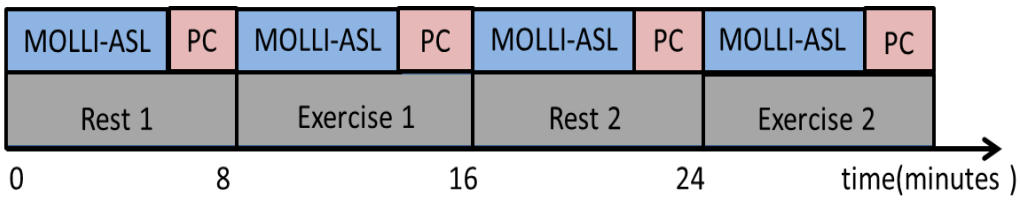

Figure 3.5-3: *Schematic of the exercise paradigm showing a block of 'Rest' period of approximately 8 minutes followed by a block of 'Exercise' period of 8 minutes, this was repeated twice. During each block, MOLLI-ASL and PC-MRI data was acquired. This was then repeated a second time to acquire an additional set of 'Rest' and 'Exercise' data.*

3.5.2 Results

There was no significant difference in age, gender or BMI between the healthy age-matched control subjects and CKD Stage 3 patients. The average age for both the groups was 54 ± 9 yrs with BMI 25 ± 3 kg/m^2. Baseline markers of cardiac function for CKD Stage 3 patients and healthy age-matched controls are summarised in Table 3.5-3.

There were no baseline differences in diastolic or systolic blood pressure, cardiac index or stroke volume index. Heart rate (HR) measured from the MRI physiological logs was significantly higher in CKD Stage 3 patients in comparison with healthy age-matched controls ($p = 0.02$). CKD Stage 3 patients had a significantly lower aortic strain than healthy controls.

Cardiac function in response to the handgrip exercise challenge is shown in the figures below for heart rate, aortic velocity, aortic strain, aortic area, stroke volume index (SVI) and cardiac index (CI). In all figures, healthy age-matched

subjects (HC) are shown in blue and CKD patients in red. The percentage change graphs show the change from baseline, defined as the first 'Rest' measurement. Significance is defined as a $p < 0.05$ using a two tailed students t-test or repeated measures ANOVA.

	Healthy Controls (HC)	Chronic Kidney Disease (CKD)	p- value
Age (years)	49 ± 9.6	55 ± 10.5	0.18
BMI	25.1 ± 2.1	26.4 ± 3.0	0.27
Diastolic Blood pressure (mmHg)	75.6 ± 10.31	79 ± 9.53	0.47
Systolic Blood pressure (mmHg)	124.7± 15.98	124.4 ± 10.84	0.96
Heart rate (bpm)	62.16 ± 12.74	72.49 ± 7.45	***0.02***
Aortic strain (%)	41.36 ± 8.59	22.6 ± 3.01	***0.03***
Stroke volume (ml)	85.53 ± 5.27	79.59 ± 4.34	0.19
Cardiac Output (L/min)	2.96 ± 0.23	3.02 ± 0.18	0.42

Table 3.5-3: *Baseline markers of cardiac function for CKD Stage 3 patients and* healthy age-matched control subjects. Values given as mean ± standard deviation.

CKD patients had a significantly higher HR at rest compared to HC group ($p = 0.02$), Figure 3.5-4. Both groups showed a significant increase in HR between 'Rest' and 'Exercise' ($p = 0.002$ for HC and $p = 0.000$ for CKD patients), with the CKD patients returning to a significantly lower HR during the second rest period compared to the first ($p = 0.04$). This heart rate is measured as an average over each 8 minute scan session however it was seen that there was an initial increase in heart rate much greater than what is seen when averaging the results.

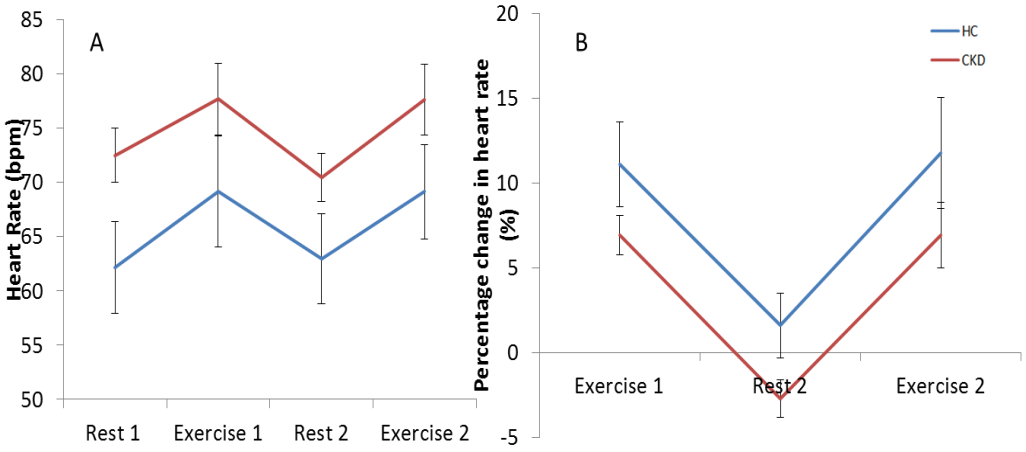

Figure 3.5-4: *A) Heart rate at four time points of the exercise paradigm for CKD and healthy controls. B) Percentage change in heart rate from the first 'Rest' scan to the points given on the x-axis.*

On exercise, there was a significant increase in aortic velocity (Figure 3.5-5) between 'Rest' and the first 'Exercise' period for both healthy controls and CKD patients ($p = 0.02$ and 0.01 for healthy controls and CKD patients respectively).

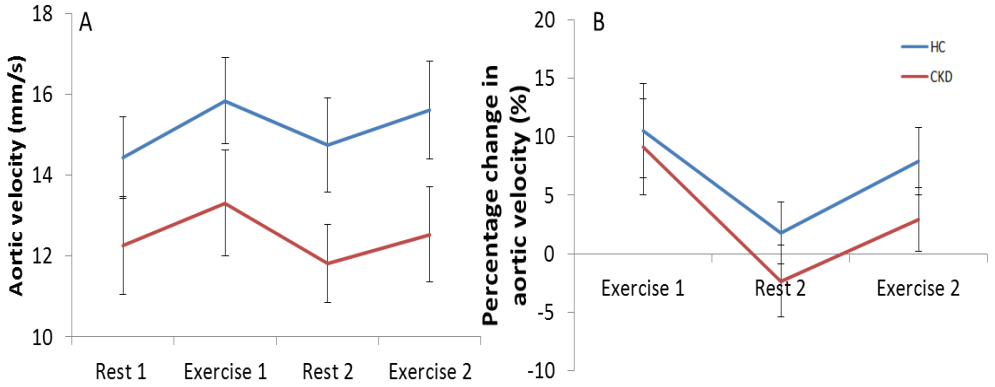

Figure 3.5-5: *A) Mean aortic velocity at four time points across the exercise paradigm for CKD and healthy controls. B) Percentage change in mean velocity from the first rest scan to the points given on the x-axis.*

Between the second 'Rest' period and the second 'Exercise' period, the mean aortic velocity increases again, however this increase on the second exercise block was only significant for the healthy controls (p = 0.04).

When compared to healthy controls, there was a trend for a lower baseline aortic velocity for CKD patients, although the percentage change from baseline were similar for both groups at approximately 10 %. Both groups returned to baseline during the second 'Rest' period.

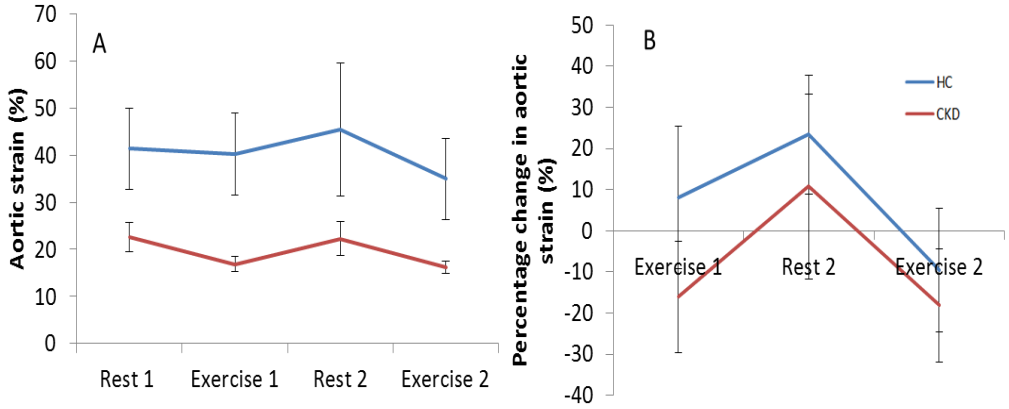

Figure 3.5-6: A) *Aortic strain at four time points of the exercise paradigm for CKD and healthy controls. B) Percentage change in aortic strain from the first rest scan to the points given on the x-axis.*

CKD patients had a significantly lower aortic strain (Figure 3.5-6) compared to healthy at rest (p = 0.02 for the first block). Aortic strain reduced on exercise for both CKD and healthy age-matched control subjects but not significantly, but was significantly lower on exercise for CKD patients compared to healthy age-matched control subjects (p = 0.009 for first exercise block and p = 0.02 for the second exercise block). CKD patients had a trend for a larger aortic area (Figure 3.5-7) in comparison with healthy controls, however this was not statistically significant (p = 0.06).

In both groups aortic area increased on exercise (Figure 3.5-7) and this was determined to be a significant increase for CKD patients (p = 0.02) and

returned to baseline following the first exercise block and then increased significantly again for the second exercise block.

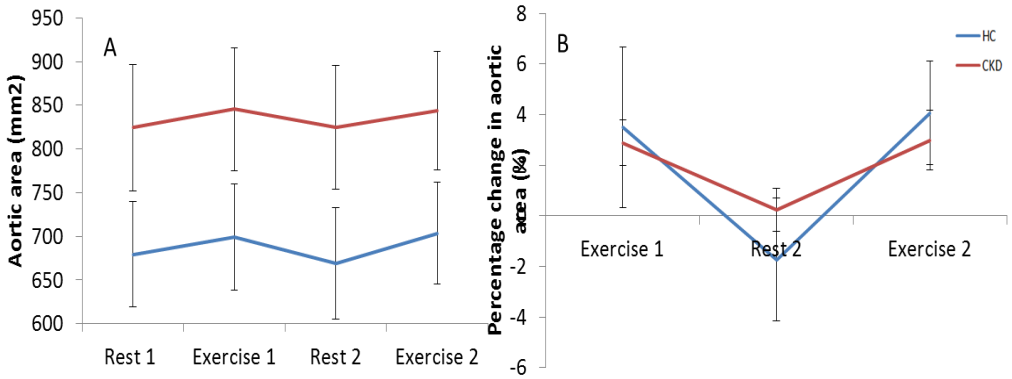

Figure 3.5-7: *A) Aortic area at four time points of the exercise paradigm for CKD and healthy controls. B) Percentage change in aortic area from the first rest scan to the points given on the x-axis.*

When assessing stroke volume index (SVI) (Figure 3.3-14), there were no significant differences at baseline between both groups (p = 0.2). SVI increased slightly for both CKD and healthy controls on exercise however this was not found to be significant. Both groups returned to baseline in the second rest block.

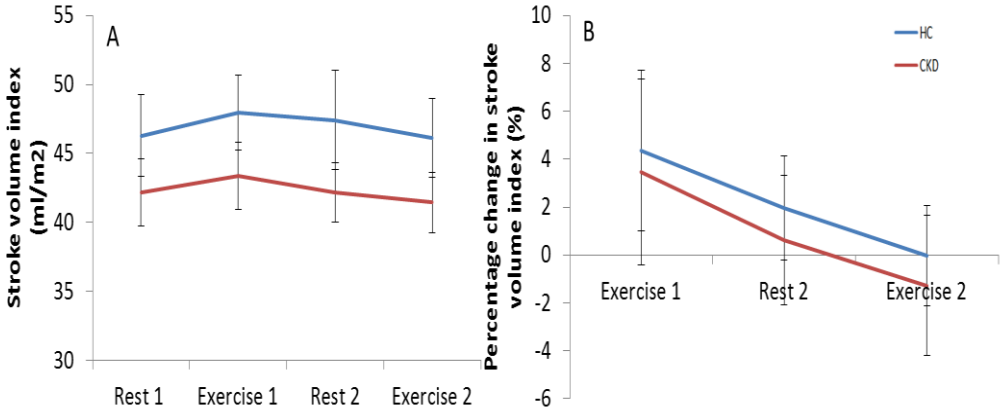

Figure 3.5-8: *A) Stroke volume index at four time points of the exercise paradigm for CKD and healthy controls. B) Percentage change in stroke volume index from the first rest scan to the points given on the x-axis.*

No significant difference was seen in cardiac index (CI) (Figure 3.5-9) between healthy controls and CKD patients at rest (p = 0.421). Cardiac index significantly increased on exercise, with the largest change being seen in the healthy controls. Healthy controls increased by 15 + 0.3 % from baseline to first exercise (p = 0.002) whereas CKD patients' cardiac output increased by 11 + 0.4% (p = 0.01). Both groups returned to baseline in the second rest period (p >0.3) and during the second exercise period, cardiac output increased again although this was only seen to be significant for healthy controls (p = 0.02). As cardiac index is the product of stroke volume and heart rate, it can be seen that as there were no changes in stroke volume on exercise, this difference is driven by the change in heart rate.

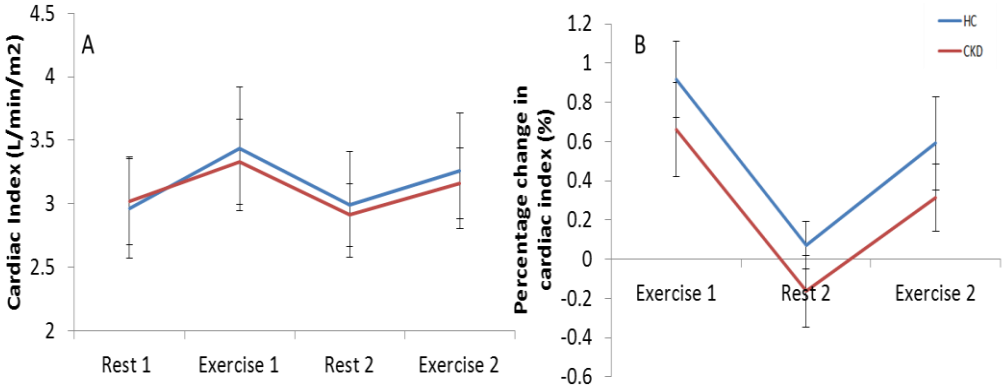

Figure 3.5-9: A) *Cardiac index at four time points across the exercise paradigm for CKD and healthy controls. B) Percentage change in cardiac index from the first rest scan to the points given on the x-axis.*

Example images of selective and non-selective MOLLI-ASL data for 2 different trigger delays are shown in Figure 3.5-10.

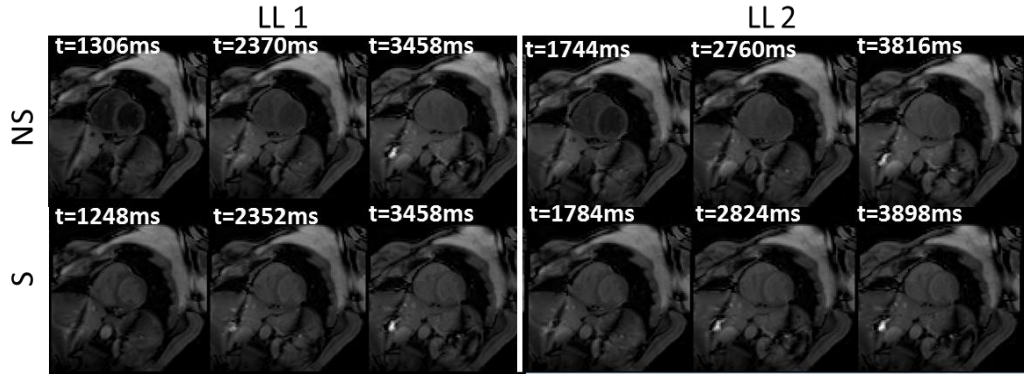

Figure 3.5-10: *Example images of selective and non-selective data for 2 different trigger delays, LL 1 and LL 2. Readout times are given for each image.*

Figure 3.5-11 shows an example of non-selective and selective data from a region of interest in the myocardium and the fitted results. In these plots, the true data is shown by the red crosses and the fitted curve is shown by the blue circles.

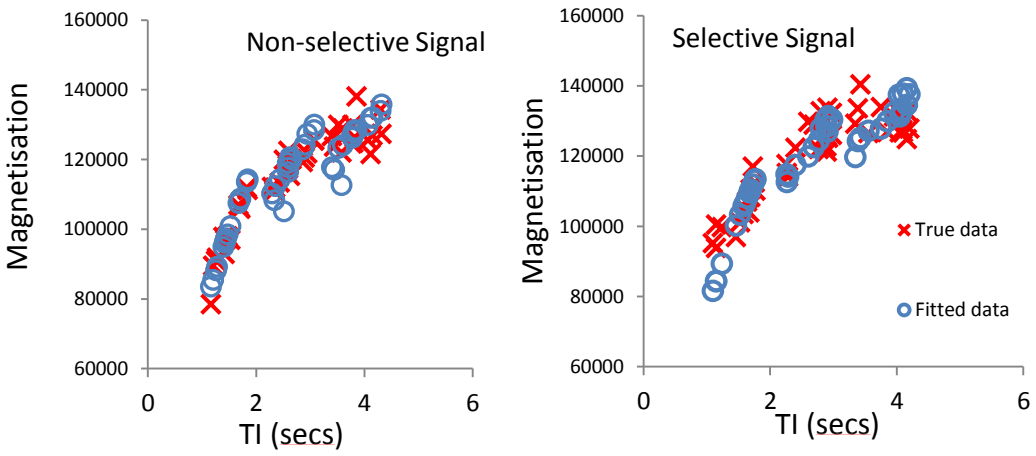

Figure 3.5-11: *Example selective and non-selective data and the fitted curves. The randomness that is seen in the timings in the plot is expected due to the changing heart rate in the subjects.*

Figure 3.5-12 shows that the average increase in perfusion between rest and exercise for healthy controls was 163 ± 44 % whereas for CKD patients it was found to be 268 ± 68%.

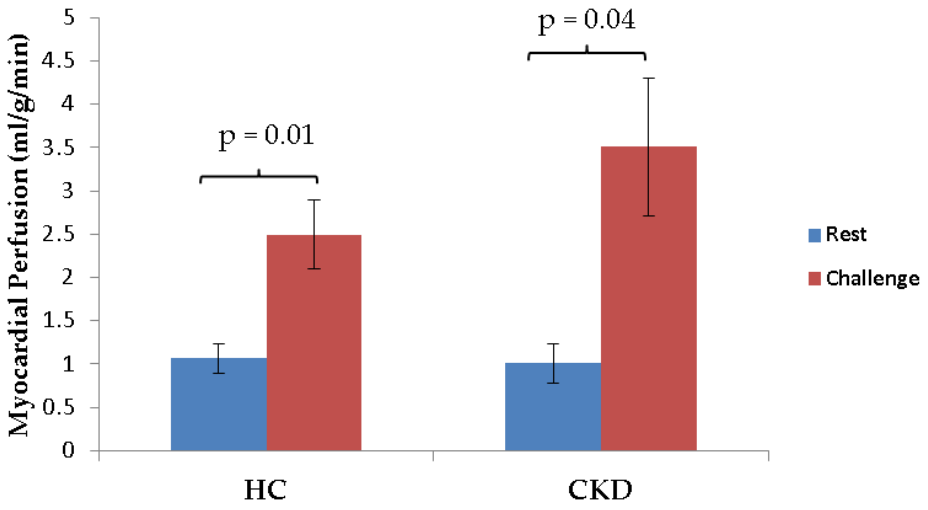

Figure 3.5-12: Myocardial *Perfusion in healthy age-matched control subjects and CKD Stage 3 patients at 'Rest' and during 'Exercise'.*

Perfusion increases were found to be significant with a p-value of 0.01 for healthy controls and 0.04 for CKD patients. This result also shows the sensitivity of the MOLLI-ASL technique to be able to detect differences in perfusion when a modulation in the perfusion is provided by use of a handgrip challenge.

3.6 Discussion

For patients with compromised kidney function, a technique to measure perfusion without the use of contrast agents is necessary due to the risk of nephrogenic systemic fibrosis when a contrast agent is injected. As kidney patients are more susceptible to cardiac problems, a technique to measure myocardial perfusion is needed. In this work, a non-invasive cardiac triggered

modified Look-Locker (MOLLI) ASL technique has been developed to quantify myocardial perfusion within a scan time of less than five minutes. In order to optimise this technique, simulations were first performed to determine the optimal flip angle for an average heart rate of 1000 ms and to assess the effect of SNR on the accuracy and precision of the fit for T_1 and perfusion values. The optimal flip angle was simulated to be 70^o however due to SAR restraints, the flip angle had to be set to 35^o. When simulating the effect of an increased number of LL readouts and LL set, it was shown that with 3 repeats for each LL set and with 8 sets, the theoretical standard deviation was less than 4 % for perfusion and less than 1.5 % for T_1.

Pulse programming was performed to enable a MOLLI-ASL scheme to be implemented. This was tested for T_1 mapping in an agar phantom, by performing a MOLLI-ASL scheme without in-plane saturation and with a non-selective inversion; this was compared to the results of a standard inversion recovery scheme. This data showed there to be good agreement between the results of the MOLLI scheme and the inversion recovery scheme, giving confidence that the pulse programming had been successful.

Two different modelling schemes were considered for fitting the ASL data. The Belle model in which myocardial perfusion is calculated from the difference between the longitudinal relaxation (T_1) computed following the selective and non-selective inversions, and an iterative Bloch equation that uses the signal from the left ventricular blood pool and the myocardium as input variables and uses these to calculate tissue T_1, M_0 and perfusion values. When the two models were compared for data acquired in healthy volunteers, it was decided that the Belle model was optimal due to the smaller variance in values measured and the agreement with published values for myocardial perfusion, and the simplicity of the model. If a multi-slice technique was employed, an iterative Bloch equation could be more appropriate as more of the blood pool would be labelled and so the input function from the left

ventricular blood pool would have a greater impact on the fit. However, for single slice data it can be assumed that all inflowing blood is fully recovered before the slice selective inversion.

The values of myocardial perfusion that were measured in this study for both chronic kidney disease patients and healthy volunteers were in agreement with those found in the literature and were found to increase when a handgrip challenge was performed, as expected. Mean perfusion at rest for healthy age-matched controls was 1.06 ± 0.17 ml/g/min and for CKD Stage 3 patients was 1.01 ± 0.22 ml/g/min.

Phase contrast measures of the aortic flow were performed at 'Rest' and during 'Exercise; and the group of healthy age-matched control subjects demonstrated a normal physiological response to a short period of exercise with an increase in cardiac output achieved primarily through an increase in heart rate with a smaller proportional increase in stroke volume. The CKD Stage 3 group followed the same response as the healthy control group. Aortic strain was significantly lower for CKD patients than healthy age-matched control subjects. Aortic strain describes the ability for the aorta to contract between diastole and systole and reduced aortic strain is representative of arterial stiffness in the CKD group. This has been strongly correlated with mortality in many disease states (36–38). As observed in the healthy age-matched control subjects, one would expect no change in aortic strain with resistance exercise for a healthy population (39). It can be hypothesised that the increase in perfusion is due to this decrease in aortic strain and thus increased aortic stiffness. Both groups had an increase in aortic velocity and aortic area on exercise.

In future studies using the MOLLI-ASL scheme, an additional MOLLI T_1 scan will be performed from which the T_1 of tissue can be measured. This MOLLI T_1 scan can also be used to segment the myocardium from the blood pool which can be used in the analysis of the ASL perfusion data. This developed

MOLLI-ASL scheme can now be used for further assessment of myocardial perfusion in patients with CKD.

3.7 Conclusion

A MOLLI-ASL technique has been developed and optimised for measurement of myocardial perfusion. This technique was then used in conjunction with PC-MRI to assess the response to exercise in a CKD Stage 3 group in comparison with healthy age-matched control subjects. The values of myocardial perfusion that were measured in this study for both chronic kidney disease patients and healthy volunteers were in agreement with those found in the literature, and myocardial perfusion was found to increase significantly during a handgrip challenge for both healthy age-matched control subjects and CKD stage 3 patients. A greater increase in perfusion was seen for CKD stage 3 patients. Phase contrast measures of the aortic flow performed at rest and during the handgrip task and the group of healthy volunteers demonstrated a normal physiological response to a short period of exercise, with an increase in cardiac index achieved primarily through an increase in heart rate with a smaller proportional increase in stroke volume. The CKD group followed the same response as the healthy control group, but aortic strain was significantly lower for CKD patients than healthy controls.

In this chapter, a novel technique has been developed for non-invasive assessment of myocardial perfusion using an arterial spin labelling technique. A non-invasive means for measuring perfusion is necessary in the CKD population where the use of contrast agents in contraindicated. The ability to measure perfusion in patients with CKD allows assessment of cardiac health in more information than is currently available using standard MRI techniques.

3.8 References

1. Alsop DC, Detre J a., Golay X, et al. Recommended implementation of arterial spin-labeled perfusion MRI for clinical applications: A consensus of the ISMRM perfusion study group and the european consortium for ASL in dementia. Magn. Reson. Med. 2014;00. doi: 10.1002/mrm.25197.

2. Detre JA, Zhang W, Roberts DA, Silva AC, Williams DS, Grandis DJ, Koretsky AP, Leigh JS. Tissue specific perfusion imaging using arterial spin labeling. NMR Biomed. 1994;7:75–82. doi: 10.1002/nbm.1940070112.

3. Detre J. Perfusion Imaging. Magn. Reson. Med. 1992;23:37–45. doi: 10.1002/jmri.24382.

4. Gunther M, Bock M, Schad LR. Arterial spin labeling in combination with a look-locker sampling strategy: Inflow turbo-sampling EPI-FAIR (ITS-FAIR). Magn. Reson. Med. 2001;46:974–984. doi: 10.1002/mrm.1284.

5. Wong EC. Quantifying CBF with pulsed ASL: Technical and pulse sequence factors. In: Journal of Magnetic Resonance Imaging. Vol. 22. ; 2005. pp. 727–731. doi: 10.1002/jmri.20459.

6. Buchanan CE, Cox EF, Francis ST. Measuring myocardial blood flow using modified look locker inversion (MOLLI) recovery arterial spin labelling (ASL). Proc. Intl. Soc. Mag. Reson. Med. 23 0538. 2015;64:2015.

7. Campbell-Washburn AE, Price AN, Wells J a., Thomas DL, Ordidge RJ, Lythgoe MF. Cardiac arterial spin labeling using segmented ECG-gated Look-Locker FAIR: Variability and repeatability in preclinical studies. Magn. Reson. Med. 2013;69:238–247. doi: 10.1002/mrm.24243.

8. Campbell-Washburn AE, Zhang H, Siow BM, Price AN, Lythgoe MF, Ordidge RJ, Thomas DL. Multislice cardiac arterial spin labeling using

improved myocardial perfusion quantification with simultaneously measured blood pool input function. Magn. Reson. Med. 2013;70:1125–1136. doi: 10.1002/mrm.24545.

9. Capron T, Troalen T, Robert B, Jacquier A, Bernard M, Kober F. Myocardial perfusion assessment in humans using steady-pulsed arterial spin labeling. Magn. Reson. Med. 2015;74:990–998. doi: 10.1002/mrm.25479.

10. Do HP, Jao TR, Nayak KS. Myocardial arterial spin labeling perfusion imaging with improved sensitivity. J. Cardiovasc. Magn. Reson. 2014;16:15. doi: 10.1186/1532-429X-16-15.

11. Epstein FH, Meyer CH. Myocardial perfusion using arterial spin labeling CMR: Promise and challenges. JACC Cardiovasc. Imaging 2011;4:1262–1264. doi: 10.1016/j.jcmg.2011.08.015.

12. Kampf T, Helluy X, Gutjahr FT, Winter P, Meyer CB, Jakob PM, Bauer WR, Ziener CH. Myocardial perfusion quantification using the T1-based FAIR-ASL method: The influence of heart anatomy, cardiopulmonary blood flow and look-locker readout. Magn. Reson. Med. 2014;71:1784–1797. doi: 10.1002/mrm.24843.

13. Northrup BE, McCommis KS, Zhang H, Ray S, Woodard PK, Gropler RJ, Zheng J. Resting myocardial perfusion quantification with CMR arterial spin labeling at 1.5 T and 3.0 T. J. Cardiovasc. Magn. Reson. 2008;10:53. doi: 10.1186/1532-429X-10-53.

14. Poncelet BP, Koelling TM, Schmidt CJ, Kwong KK, Reese TG, Ledden P, Kantor HL, Brady TJ, Weisskoff RM. Measurement of human myocardial perfusion by double-gated flow alternating inversion recovery EPI. Magn. Reson. Med. 1999;41:510–519. doi: 10.1002/(SICI)1522-2594(199903)41:3<510::AID-MRM13>3.0.CO;2-G.

15. Wacker CM, Fidler F, Dueren C, Hirn S, Jakob PM, Ertl G, Haase A, Bauer WR. Quantitative assessment of myocardial perfusion with a spin-labeling technique: preliminary results in patients with coronary artery disease. J Magn Reson Imaging 2003;18:555–560. doi: 10.1002/jmri.10386.

16. Wang DJJ, Bi X, Avants BB, Meng T, Zuehlsdorff S, Detre JA. Estimation of perfusion and arterial transit time in myocardium using free-breathing myocardial arterial spin labeling with navigator-echo. Magn. Reson. Med. 2010;64:1289–1295. doi: 10.1002/mrm.22630.

17. Zun Z, Wong E, Nayak KS. Assessment of myocardial blood flow (MBF) in humans using arterial spin labeling (ASL): Feasibility and noise analysis. Magn. Reson. Med. 2009;62:975–983.

18. Zun Z, Varadarajan P, Pai RG, Wong EC, Nayak KS. Arterial spin labeled CMR detects clinically relevant increase in myocardial blood flow with vasodilation. JACC Cardiovasc. Imaging 2011;4:1253–1261. doi: 10.1016/j.jcmg.2011.06.023.

19. Zun Z, Wong E.C., Nayak K.S. Assessment of myocardial blood flow {(MBF)} in humans using arterial spin labeling {(ASL):} feasibility and noise analysis. Magn. Reson. Med. 2009;62:975–83. doi: 10.1002/mrm.22088.

20. Zungho Zun, Wong EC, Nayak KS. Assessment of myocardial blood flow (MBF) in humans using arterial spin labeling (ASL): feasibility and noise analysis. Magn. Reson. Med. 2009;62:975–83.

21. Zun Z, Varadarajan P, Pai RG, Wong EC, Nayak KS. Arterial spin labeled CMR detects clinically relevant increase in myocardial blood flow with vasodilation. JACC Cardiovasc. Imaging 2011;4:1253–1261. doi: 10.1016/j.jcmg.2011.06.023.

22. Zun Z, Wong EC, Nayak KS. Assessment of myocardial blood flow (MBF) in humans using arterial spin labeling (ASL): feasibility and noise analysis. Magn. Reson. Med. 2009;62:975–983. doi: 10.1002/mrm.22088.

23. Messroghli DR, Radjenovic A, Kozerke S, Higgins DM, Sivananthan MU, Ridgway JP. Modified look-locker inversion recovery (MOLLI) for high-resolution T 1 mapping of the heart. Magn. Reson. Med. 2004;52:141–146. doi: 10.1002/mrm.20110.

24. Messroghli DR, Greiser A, Fröhlich M, Dietz R, Schulz-Menger J. Optimization and validation of a fully-integrated pulse sequence for modified look-locker inversion-recovery (MOLLI) T1 mapping of the heart. J. Magn. Reson. Imaging 2007;26:1081–1086. doi: 10.1002/jmri.21119.

25. Messroghli DR, Walters K, Plein S, Sparrow P, Friedrich MG, Ridgway JP, Sivananthan MU. Myocardial T1 mapping: Application to patients with acute and chronic myocardial infarction. Magn. Reson. Med. 2007;58:34–40. doi: 10.1002/mrm.21272.

26. Messroghli DR, Plein S, Higgins DM, Walters K, Jones TR, Ridgway JP, Sivananthan MU. Human myocardium: single-breath-hold MR T1 mapping with high spatial resolution--reproducibility study. Radiology 2006;238:1004–1012. doi: 10.1148/radiol.2382041903.

27. Belle V, Kahler E, Waller C, Rommel E, Voll S, Hiller KH, Bauer WR, Haase a. In vivo quantitative mapping of cardiac perfusion in rats using a noninvasive MR spin-labeling method. J. Magn. Reson. Imaging 8:1240–1245. doi: 10.1002/jmri.1880080610.

28. Bauer WR, Roder F, Hiller KH, Han H, Fröhlich S, Rommel E, Haase a, Ertl G. The effect of perfusion on T1 after slice-selective spin inversion in the isolated cardioplegic rat heart: measurement of a lower bound of

intracapillary-extravascular water proton exchange rate. Magn. Reson. Med. 1997;38:917–23.

29. Wacker CM, Wiesmann F, Bock M, Jakob P, Sandstede JJW, Lehning A, Ertl G, Schad LR, Haase A, Bauer WR. Determination of regional blood volume and intra-extracapillary water exchange in human myocardium using Feruglose: First clinical results in patients with coronary artery disease. Magn. Reson. Med. 2002;47:1013–6. doi: 10.1002/mrm.10125.

30. Ogg RJ, Kingsley PB, Taylor JS. WET, a T1- and B1-insensitive water-suppression method for in vivo localized 1H NMR spectroscopy. J. Magn. Reson. B 1994;104:1–10. doi: 10.1006/jmrb.1994.1048.

31. Globits S, Sakuma H, Shimakawa a, Foo TK, Higgins CB. Measurement of coronary blood flow velocity during handgrip exercise using breath-hold velocity encoded cine magnetic resonance imaging. Am. J. Cardiol. 1997;79:234–237. doi: 10.1016/S0002-9149(97)89291-0.

32. Jeneson J a L, Schmitz JPJ, Hilbers P a J, Nicolay K. An MR-compatible bicycle ergometer for in-magnet whole-body human exercise testing. Magn. Reson. Med. 2010;63:257–261. doi: 10.1002/mrm.22179.

33. Von Knobelsdorff-Brenkenhoff F, Dieringer M a., Fuchs K, Hezel F, Niendorf T, Schulz-Menger J. Isometric handgrip exercise during cardiovascular magnetic resonance imaging: Set-up and cardiovascular effects. J. Magn. Reson. Imaging 2013;37:1342–1350. doi: 10.1002/jmri.23924.

34. Weber TF, von Tengg-Kobligk H, Kopp-Schneider A, Ley-Zaporozhan J, Kauczor H-U, Ley S. High-resolution phase-contrast MRI of aortic and pulmonary blood flow during rest and physical exercise using a MRI compatible bicycle ergometer. Eur. J. Radiol. 2011;80:103–108. doi: 10.1016/j.ejrad.2010.06.045.

35. Hjortdal VE. Effects of Exercise and Respiration on Blood Flow in Total Cavopulmonary Connection: A Real-Time Magnetic Resonance Flow Study. Circulation 2003;108:1227–1231. doi: 10.1161/01.CIR.0000087406.27922.6B.

36. Redheuil a., Yu W-C, Wu CO, Mousseaux E, de Cesare a., Yan R, Kachenoura N, Bluemke D, Lima J a. C. Reduced Ascending Aortic Strain and Distensibility: Earliest Manifestations of Vascular Aging in Humans. Hypertension 2010;55:319–326. doi: 10.1161/HYPERTENSIONAHA.109.141275.

37. Vlachopoulos C, Aznaouridis K, Stefanadis C. Prediction of Cardiovascular Events and All-Cause Mortality With Arterial Stiffness. J. Am. Coll. Cardiol. 2010;55:1318–1327. doi: 10.1016/j.jacc.2009.10.061.

38. Benetos A, Gautier S, Labat C, et al. Mortality and cardiovascular events are best predicted by low central/peripheral pulse pressure amplification but not by high blood pressure levels in elderly nursing home subjects: the PARTAGE (Predictive Values of Blood Pressure and Arterial Stiffness i. J. Am. Coll. Cardiol. 2012;60:1503–11. doi: 10.1016/j.jacc.2012.04.055.

39. Ashor AW, Lara J, Siervo M, Celis-Morales C, Mathers JC. Effects of Exercise Modalities on Arterial Stiffness and Wave Reflection: A Systematic Review and Meta-Analysis of Randomized Controlled Trials. PLoS One 2014;9:e110034. doi: 10.1371/journal.pone.0110034.

4. Intradialytic MRI to assess changes in cardiovascular function in CKD patients during dialysis

This chapter aims to apply MRI techniques to assess changes in cardiac function in CKD Stage 5 patients during dialysis. The measures are performed in a randomised design in patients undergoing both haemodialysis and haemodiafiltration.

Firstly, the chapter outlines the association between dialysis and cardiac stress and describes the differences between haemodialysis and haemodifiltration. The study design and MRI techniques used to evaluate the effects of dialysis on cardiac function are then described. Myocardial perfusion measures are collected using the MOLLI-ASL technique developed in Chapter 3. The cardiac measures that change during dialysis are discussed; results are correlated with clinical measures, and a comparison of haemodialysis and haemodiafiltration is provided.

This work will be presented as an oral presentation at the annual conference of the International Society of Magnetic Resonance in Medicine (ISMRM), Singapore 2016.

This work was funded by Fresenius Medical Care.

4.1 Introduction

Dialysis is the procedure that is used to perform many of the normal functions of the kidney when the kidneys no longer function adequately in end stage renal disease ESRD, such as the removal of waste products and excess fluid from the blood. Standard dialysis uses haemodialysis (HD), a method which uses diffusive clearance.

In haemodialysis, patients' blood is moved through an extracorporeal system which contains a semi-permeable membrane with blood moving down one side and dialysate flowing along the other side in the opposite direction (Figure 4.1-1A). This counter-current flow maintains a concentration gradient across the membrane at a maximum which increases the efficiency of the dialysis treatment. Waste products are free to move through the membrane but the pores are only large enough to let small molecules through and so proteins and blood cells remain in the blood. By altering the hydrostatic pressure of the dialysate fluid, ultrafiltration (fluid removal) is achieved as excess fluids are removed from the blood when free water and some dissolved solutes move across the membrane along the created pressure gradient.

Haemodiafiltration (HDF) is a modified form of dialysis that increases clearance of larger uraemic toxins via convection (Figure 4.1-1B), ultrafiltration volumes are higher coupled with greater fluid replacement. Water and solutes move from the blood to the dialysate at a much higher rate than for HD and solutes of both large and small molecular weights are removed. Replacement fluid is infused into the patient to ensure that extracellular fluid volume is maintained.

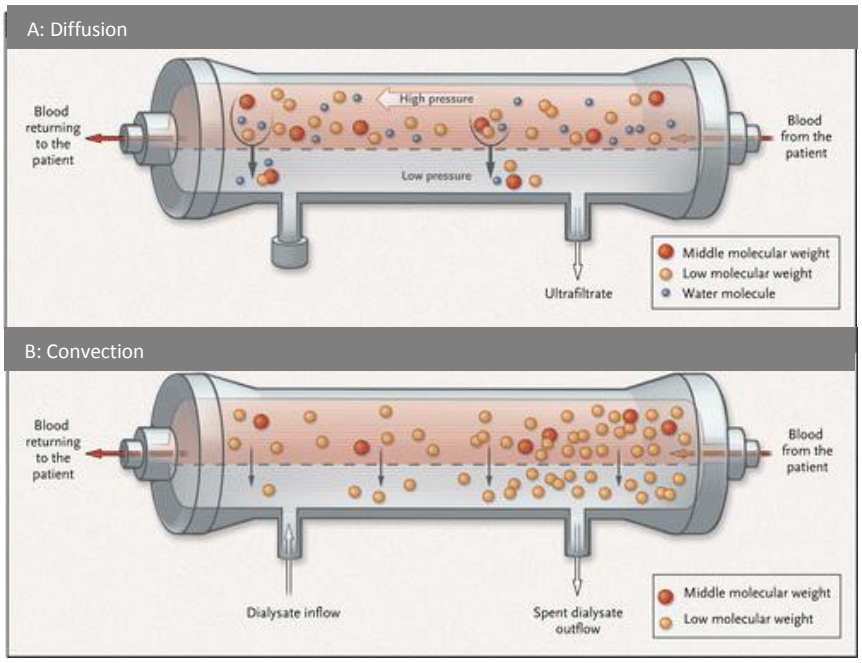

Figure 4.1-1: *(A) Haemodialysis via diffusion. (B) Haemodiafiltration via convection.*

Cardiovascular mortality is grossly elevated in patients with (CKD) (1), and is associated with a wide variety of structural and functional abnormalities. These changes are directed at the cardiovascular system as a whole, from the myocardium to peripheral microcirculation. Peripheral cardiovascular factors are of great importance, with structure and compliance of peripheral conduit arteries increasing the risk of myocardial ischaemia by the alteration of central haemodynamics (2). A substantial body of evidence has developed over the last decade showing that myocardial ischaemia occurs during haemodialysis and this has been summarised in several in-depth reviews (1–4). This is thought to be driven by the circulatory stress that results largely from the ultrafiltration process and changes in blood pressure during dialysis (5). Dialysis induced myocardial ischaemia can be ameliorated by interventions that reduce ultrafiltration rate and/or the degree of haemodynamic instability (6). Such interventions include reducing dialysate temperature (7) and biofeedback dialysis (8). Some, but not all studies have suggested that HDF reduces intradialytic hypotension (IDH) (9,10) compared to HD, with a number of studies suggesting that benefits in this regard are largely driven by thermal effects of patient cooling (11–13).

Dialysis induced hypoperfusion, the reduction in perfusion of the myocardium, has previously been shown in a small numbers of patients using myocardial positron emission tomography (PET) (14). However, this technique is unable to provide contemporaneous measures of cardiac function, such as ventricular function or contractility (14,15). Dialysis stress induced reductions in myocardial perfusion are central to the observed cycle of recurrent injury leading to fixed contractile defects in the heart (5). This has been demonstrated using cardiac PET scanning under the real time stress of conventional HD (6). However, the use of PET to study such effects is limited by the complexities and costs related to generating suitable isotopes, access to appropriate PET facilities, technical limitations relating to resolution and quality of data, and patient radiation exposure. Myocardial contractility has traditionally been determined using intradialytic echocardiography, which has allowed longitudinal follow up in large groups of patients, showing that repetitive dialysis-induced myocardial ischaemia results in fixed reductions in systolic function and associated increased risk of mortality (16). However, echocardiography is subject to some limitations in terms of image quality and user dependency. In contrast, magnetic resonance imaging (MRI) provides a gold standard for measurements of cardiac structure. MRI also provides the only current methodology by which cardiac structure and function, and systemic haemodynamics can be assessed in a single session. Furthermore, recent advances in MRI have enabled the measurement of myocardial perfusion using arterial spin labelling (ASL) (17) and fibrosis using longitudinal relaxation time (T_1) mapping of the myocardium (18). There are obvious technical challenges resulting from the high magnetic field to using MRI to study the effects of dialysis on cardiac function. But if these challenges can be surmounted to allow intradialytic MRI acquisition, then unparalleled image quality coupled with comprehensive measurements would be a significant advance.

To date, no studies have used MRI to study the effects of dialysis on cardiac function. Secondly, HDF has not been studied as an intervention to reduce intra-dialytic cardiac injury. This has relevance as there remains a degree of uncertainty as to whether HDF benefits patient outcomes, despite several large randomised controlled trials. For example, the Turkish Online HDF Study (19) and the CONTRAST Study (20) both compared online HDF against low flux HD and found no difference in primary outcome of mortality or cardiovascular events. Both studies did however report an association between HDF with higher substitution volumes and improved survival. Conversely, the ESHOL Study (21) randomised patients to high efficiency HDF or standard (mainly high flux) dialysis and reported a large (30 %) reduction in mortality (with reductions in both stroke and infection related deaths). A number of observational studies have also shown associations between HDF, higher convection volumes and improved outcomes (22,23); for example the Dialysis Outcomes and Practice Patterns Study (DOPPS) suggested that higher convection volumes (>55 L/week) were associated with reductions in risk of mortality (23). There is a need for mechanistic studies to delineate the biological mechanisms by which HDF may impact on patient outcomes.

The purpose of this study is to use MRI to characterise cardiac structure and function in dialysis patients during dialysis treatment. The effects of haemodialysis and haemodiafiltration are compared to establish whether haemodiafiltration is relatively cardio-protective compared to conventional haemodialysis. This is the first study ever to perform MRI scans during dialysis.

4.2 Challenges to delivering dialysis treatment in an MR environment

There were challenges associated with delivering dialysis treatment in a 3 Tesla MRI environment with a number of modifications needed in order to

ensure that dialysis treatment was performed correctly. Non-ferrous needles were sourced to attach the patients fistula to the dialysis system. The dialysis machine was located outside of the scan room with extension lines added to the circuit resulting in the distance between the dialysis machine and the patient being increased by approximately 3 m and the dialysis system being at the 5 Gauss line. In using extension lines, the blood flow rate (BFR) dropped by 50 ml/min and so to ensure that an adequate BFR of >300 ml/min was achieved, higher gauge blunt needles were used and patients who had a good baseline blood flow rate were carefully selected. In order to keep the blood in the extension lines at the correct temperature, insulation was applied around the lines. A photo of the setup is shown in Figure 4.2-1 showing the dialysis machine and its position outside the MR scan room.

Figure 4.2-1: *Photo of the setup showing the dialysis machine outside of the MR scan room and the patient inside the scanner. To the left of the scanner, the extension lines with insulation can be seen.*

4.3 Patient Cohort

Twelve patients, ten male and two female, with CKD Stage 5 on haemodialysis, took part in this study. Subjects were recruited from the renal unit at the Royal Derby Hospital. Potential participants were identified by the clinical care team with reference to the inclusion and exclusion criteria (Table 4.3-1). Patients were excluded if they fulfilled the criteria for Class 4 New York Heart Association (NYHA) functional assessment of cardiac failure. All patients gave written informed consent and the study was approved by Derbyshire Research Ethics Committee. Clinical measures and patient recruitment was performed by Dr Azharuddin Mohammed at the Royal Derby Hospital.

Inclusion	**Exclusion**
Age 18-70	Change in ideal dry weight in 4 weeks prior to recruitment
Able to give informed consent	Instability on dialysis in 4 weeks prior to recruitment
CKD Stage 5 on chronic haemodialysis	Dialysed via a synthetic line or graft
Receiving dialysis via an arteriovenous fistula	Q_a < 500 ml/min
Able to understand simple instruction in English	NYHA Stage IV heart failure
	Active infection or malignancy
	Contraindication to MRI scanning including claustrophobia
	Incapacity to consent

Table 4.3-1: *List of inclusion and exclusion criteria for patients.*

All patients were stable and undergoing dialysis with haemodialysis for 3 sessions a week, with each session lasting four hours. The mean age of the

patients was 53 ± 12 years (range 32 – 73 years) with average dialysis vintage of 56 ± 6 months (range 3.3 to 263.8 months). The underlying primary aetiologies of the patients' end stage renal disease were diabetic nephropathy (2), autosomal dominant polycystic kidney disease (3), renal amyloidosis (1), light chain deposition disease (1), anti-neutrophil cytoplasmic antibody-associated systemic vasculitis (1), focal segmental glomerulosclerosis (1), and in three patients the cause was undetermined. Median Charlson co-morbidity score was 4 (IQR 3-5). Patients had previously had an electrocardiogram (ECG) and echocardiogram at Royal Derby hospital to assess their cardiac function. Eight patients had normal LV ejection fraction (> 55 %), two patients had mild impairment of systolic function (EF 44-55 %), one patient had moderate LV impairment (EF 36-44 %) and on one patient an echocardiogram was not performed.

Established arteriovenous fistulas, to connect the artery to the dialysis machine, were used to achieve vascular access in all patients with a mean fistula flow rate (Q_a) of 1051 ml/min and baseline between 380-450 ml/min. The substitution volume during HDF defines how much fluid is removed from the body during the treatment, and the mean substitution volume rate for this study during HDF was 4.4 ± 0.2 ml/kg/hr per treatment, this is classified as high volume online-HDF. Haemodynamic measures including heart rate and blood pressure were recorded every 15 minutes on the scan day except for during the MRI scans where it was not possible to collect the data, though heart rate data was collected from the MR scanner VCG recording.

4.4 Methodology

This study was a crossover design in which patients were randomised to either haemodialysis (HD) or haemodiafiltration (HDF) treatments (Figure 4.4-1). Recruited participants began on their first haemodialysis modality, either HD or HDF, for 2 weeks to receive their maintenance dialysis. During the 2nd week, participants attended a study day at the Sir Peter Mansfield Imaging

Centre (SPMIC) where detailed MRI assessment was performed during a dialysis session. Thereafter, participants switched to the other modality, either HD or HDF depending on their initial treatment, for a further 2 weeks. Cardiac assessment was then again performed during the 2nd week of this arm of the study. Following the second MRI day, participants could either return to their baseline dialysis prescription or choose to stay on the alternative treatment.

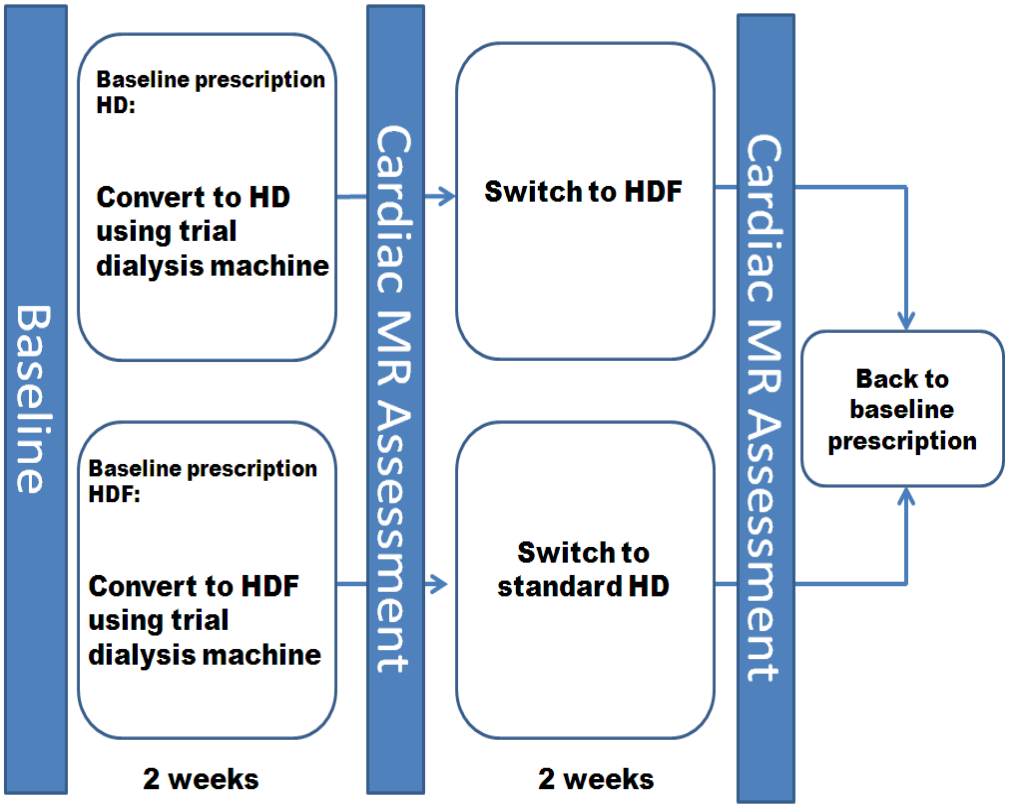

Figure 4.4-1: *Study setup showing crossover design for patients starting with either HD or HDF treatment.*

4.4.1 Scanning Protocol

Patients attended the SPMIC twice, undergoing an identical scan protocol on both visits. Blood samples were taken pre and post dialysis. Five vials of blood were collected in total with blood samples being taken from the dialysis port needle. Blood tests were performed by Dr Azharuddin Mohammed for

standard biochemical and haematological tests including; urea, creatinine, sodium, calcium, magnesium, phosphate, albumin, bicarbonate, glucose, lactate, prothrombin, Troponin T, nTproBNP and full blood count and liver function tests. Troponin T is a protein that is released when damage occurs to the heart muscle thus, a higher level of Troponin indicates an increase in cardiac damage. nTproBNP also informs on the amount of heart damage that occurs.

All data were collected on a 3T Philips Achieva scanner using a 32 channel SENSE XL torso receive coil. MRI scans were performed prior to the dialysis session (Scan 1), to measure the effect of the two week run in period on cardiac function and as a baseline measure to subsequent scans. After the baseline scan, the patients' fistula was connected to the dialysis machine and dialysis was started. There was then a 30 minute wait period to ensure patients were established on dialysis and then a MR scan (Scan 2) was performed. Following this, patients then had up to one hour outside of the scanner before MR Scan 3 was performed. A fourth MR scan during dialysis was then performed 210 minutes into the dialysis treatment; this is the point at which we hypothesised the patients would be at peak stress and the largest effects on cardiac function were expected to be seen. Following this scan and once the four hour dialysis treatment was completed, patients were disconnected from the dialysis machine and a final scan, Scan 5 was performed 30 minutes after the treatment ended to assess recovery. In each of the MRI scans, a series of MR sequences were performed to assess cardiac function, including aortic, coronary artery and inferior vena cava flow, cardiac structure, and myocardial tagging, myocardial perfusion and T_1 measures.

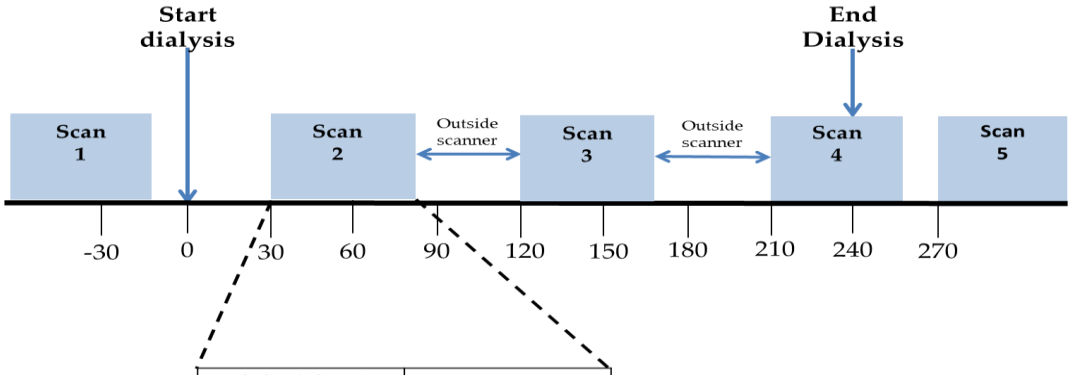

Timing (minutes)	Scan
1 – 20	Set up, survey and localisers
20	Short axis cine
25	MOLLI-ASL
30	MOLLI T_1
36	Coronary artery PCA
38	Aorta PCA
40	Myocardial Tagging
50	Inferior vena cava PCA

Figure 4.4-2: *Summary of scan sessions. This shows MR scans were performed prior to dialysis, at 30, 120 and 210 minutes through dialysis, and 30 minutes post-dialysis. Timings of individual scans are shown in the table.*

The following sections outline each of the MR sequences performed in each MR scan session.

4.4.1.1 Cardiac Function

Left ventricular (LV) function was assessed using a ECG-gated cine MRI to acquire images at multiple time points across the cardiac cycle with a multi-slice TFE sequence with FOV 260 x 209 mm^2, spatial resolution 1.35 x 1.35 mm^2, slice thickness 10 mm, SENSE 2, TE/TR = 2/4 ms, FA (flip angle) 60^o, TFE factor 10, TFE shots 6, 30 heart phases. Cine scans were acquired in 6 breath holds with 2 slices acquired per 15-20 s breath hold, resulting in a total of 12 slices. Slices were positioned along the short axis of the heart. An example of a cine left ventricle images is shown in Figure 4.4-3. From this scan cardiac output (L/min), stroke volume (ml) and ejection fraction (%) were computed.

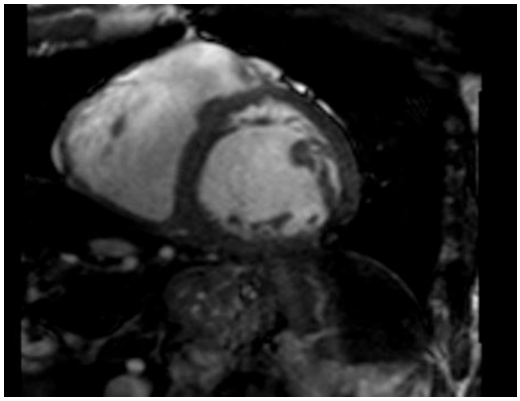

Figure 4.4-3: *Example 2 chamber (2CH) short axis cine image of the left ventricle of the short axis collected using a cine acquisition scheme.*

Aortic function was determined from a phase contrast (PC) MRI sequence placing the imaging place through the aorta, as shown in Figure 4.4-4. Scan parameters were FOV 280 x 264 mm^2, spatial resolution = 0.97 x 0.97 mm^2, slice thickness 10 mm, no SENSE, TE/TR = 2.3/3.7ms, FA = 15^o, TFE factor = 5, TFE shots 25, VENC = 300 cms^{-1}, NSA = 3. The scan was performed whilst free breathing and triggered off the cardiac cycle, scan time was approximately 1 minute dependent on the patient's heart rate.

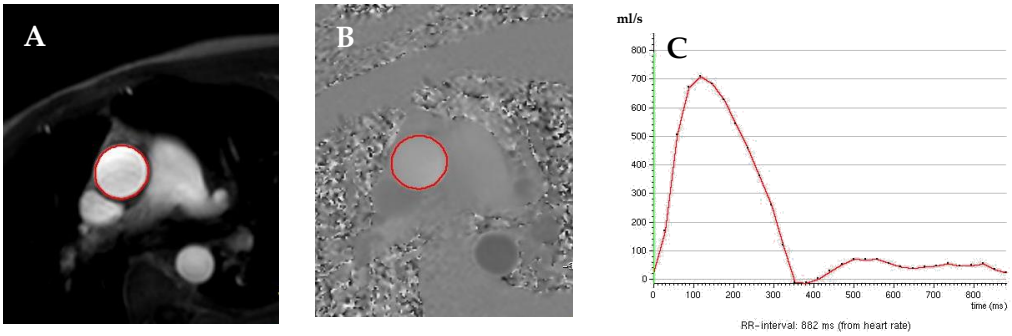

Figure 4.4-4: *Example of phase contrast measures from the aorta showing A) magnitude image, B) phase image, and C) corresponding waveform of flux across the cardiac cycle, created using Philips ViewForum software.*

From these PC-MRI scans, aortic blood velocity (in units of mm/s), cross sectional area of the aorta (mm^2) and aortic strain (%) were measured. Aortic

strain is defined as the percentage change in aortic cross section between diastole and systole. A second independent measure of cardiac output and stroke volume could also be estimated from the flux of blood as it moves through the aorta.

PC-MRI scans were also performed on the inferior vena cava (IVC), the vessel which returns blood from the body to the heart via the right atrium. Scan parameters were: FOV 280 x 140 mm^2, spatial resolution 1.2 x 1.2 mm^2, slice thickness 6 mm, SENSE 2, TE/TR = 3.1/5.6 ms, FA = 25°, TFE factor = 4, TFE shots 13, VENC = 200 cms^{-1}, NSA= 3. Scan acquisition was performed in a 15-20 s breath hold. From these PC-MRI scans, IVC velocity (mm/s), flux (L/min) and cross sectional area (mm^2) were calculated.

4.4.1.2 Cardiac structure

Cardiac structure was assessed from (i) the longitudinal relaxation time (T_1) of the myocardial tissue, and (ii) the contractility of the left ventricle using cardiac tagging.

T_1 measures of the myocardial tissue were performed using a modified Look-Locker inversion recovery (MOLLI) T_1 mapping technique (18) with a balanced fast field echo (bFFE) readout. A MOLLI T1 schematic and resulting recovery curve is shown in Figure 4.4-5.

Imaging was performed with a non-selective slice thickness of 350 mm, FOV 288 x 288 mm^2, spatial resolution 3 x 3 mm^2, slice thickness 5 mm, SENSE 2, TE/TR 1.5/3.1 ms, FA 35°, centric half Fourier acquisition with 12 start-up echoes. For the MOLLI timings, eight trigger delays from 0 – 350 ms in 50 ms steps with three readout pulses for each trigger delay were collected with an end delay of 3000 ms following each set of three readouts pulses. By increasing the trigger delay, the timing between the inversion and first readout decreases, resulting in a shorter inversion time. The maximum trigger delay was set to 350 ms due to SAR restraints.

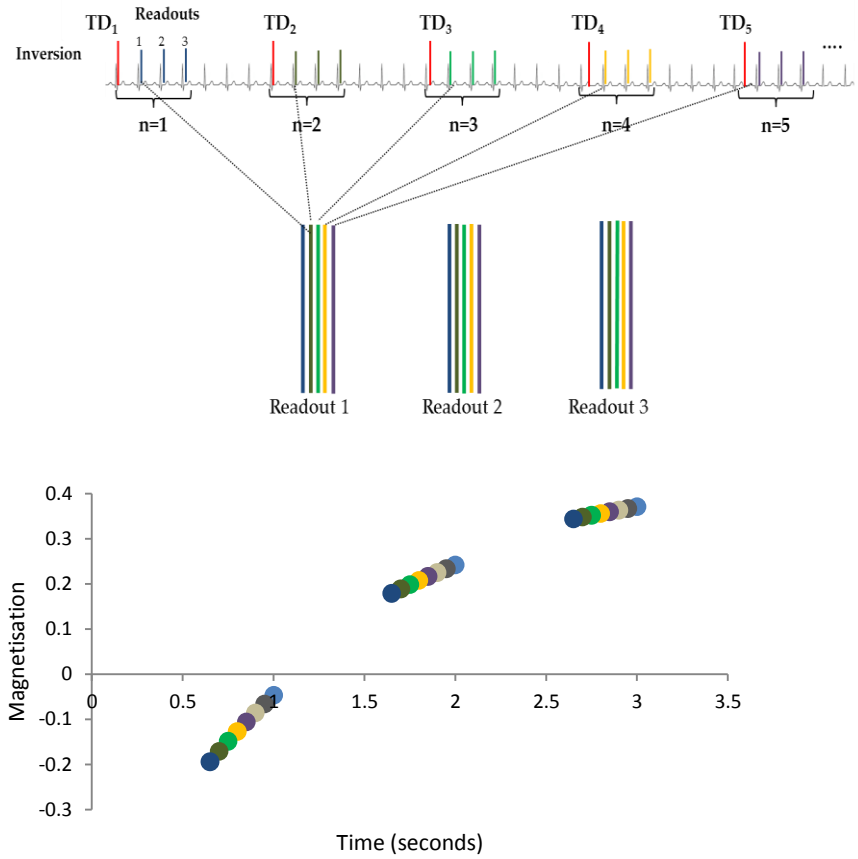

Figure 4.4-5: A) *Schematic of MOLLI scheme showing the first 5 trigger delay times (0-200 ms) with three readouts at each. The inversion pulse is shown in red followed by the three readouts. The spacing between the cardiac trigger and the inversion pulse is given by the trigger delay (TD). B) Graph showing simulated data for a set of MOLLI T1 data with 8 trigger delays from 0 to 350 ms in 50 ms steps, for a tissue T_1 of 1.6 s.*

Comparison of myocardium T_1 measures in dialysis patients to healthy volunteers provides an indication of the degree of fibrosis in the myocardium. Comparison of the T_1 measures during and between dialysis treatment allows the assessment of whether there is increased water content of the myocardial tissue on dialysis.

Contractility and myocardial strain was assessed using a SPAMM tagging technique to inform on how the heart contracts and twists between diastole and systole. Strain data was acquired with a multi-shot TFE sequence during

an end-expiration breath-hold. Imaging parameters were: FOV 320 × 320 mm^2, spatial resolution 1.33 x 1.33 mm^2, slice thickness 8 mm, SENSE 2, TE/TR = 3.5/5.8 ms, FA 10°, 14–16 cardiac phases and 7 mm tag separation using a grid-tag pattern. Strain was estimated in a single slice in both the long and short axis (Figure 4.4-6), with the short axis slice being the same short axis slice to that acquired for T_1 mapping and ASL perfusion measures.

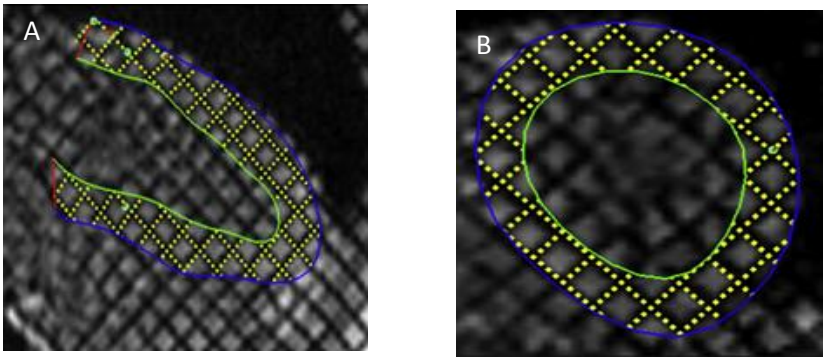

Figure 4.4-6: *A) Long and B) short axis views of myocardial tagging.*

4.4.1.3 Perfusion and coronary artery flow

Myocardial perfusion was assessed using a MOLLI-ASL technique (24) as described in Chapter 3. Data were collected using a FAIR ASL scheme with slice selective thickness of 35 mm and non-selective thickness of 350 mm, in-plane pre- and post- saturation pulses were applied. Imaging was performed using a bFFE readout with FOV 288 x 288 mm^2, spatial resolution 3 x 3 mm^2, slice thickness 5 mm, SENSE 2, TE/TR 1.5/3.1 ms, FA 35°, centric half Fourier acquisition with 12 start-up echoes. For the ASL timings, trigger delays from 0 – 350 ms in 50 ms steps with three readout pulses for each trigger delay and an end delay of 3000 ms following each set of the three readouts. The maximum trigger delay was set to 350 ms due to SAR restraints. Single slice short axis measures of perfusion were acquired in the same spatial location as corresponding T_1 maps for quantification purposes.

Flow in the right coronary artery was assessed using PC-MRI to determine the delivery of blood to the myocardial tissue, a surrogate to inform on changes in myocardial perfusion. The coronary artery was identified by acquiring cine images in each of the three orthogonal planes in order to plan perpendicular to the vessel in all directions and to visualise the movement of the coronary artery throughout the cardiac cycle. Data was collected using FOV 280 x 140 mm^2, spatial resolution 1.2 x 1.2 mm^2, slice thickness 6 mm, SENSE 2, TE/TR = 3.8/7.5 ms, FA = 25°, TFE factor = 2, TFE shots 16, VENC = 50 cms^{-1}, NSA= 3. The scan was collected in a 15-20 s breath hold. Figure 4.4-7 shows an exemplar PC MRI of the coronary artery and its corresponding wave form.

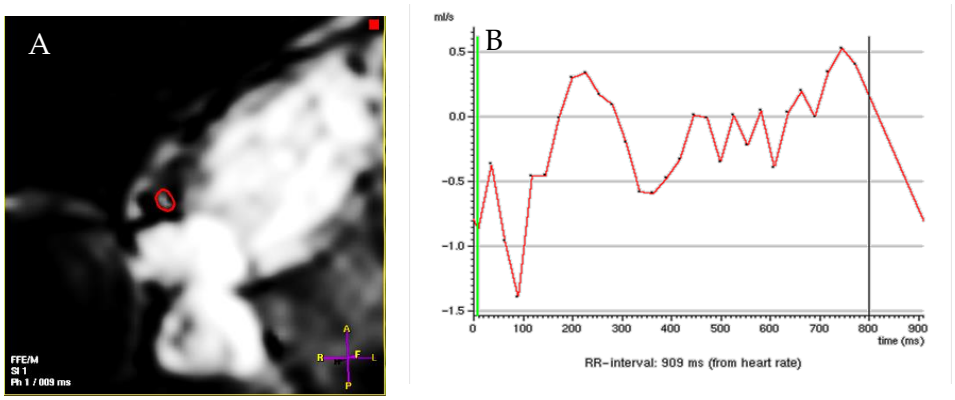

Figure 4.4-7: *A) Example right coronary artery PC-MRI modulus image and B) corresponding coronary artery flux waveform analysed using Philips ViewForum software.*

From this PC scan, coronary artery blood velocity (in units of mm/s), the cross sectional area (mm^2), and flux of blood through the coronary artery (in units of ml/min) and stroke volume (in mL) were computed.

4.4.2 Data Analysis

4.4.2.1 Cardiac Function

Cine MRI data was analysed using the ViewForum software (Philips Medical Systems, Best, NL). The epicardium and the endocardium were first identified

by the user, the software then propagates these contours throughout the other time points in the image. This was repeated for each slice through the myocardium. For this analysis, the basal slice was chosen for end-diastole and end-systole for the left ventricle when all of the blood volume was surrounded by myocardium. The apical slice was defined as the last slice showing an intra-cavity blood pool (Figure 4.4-8).

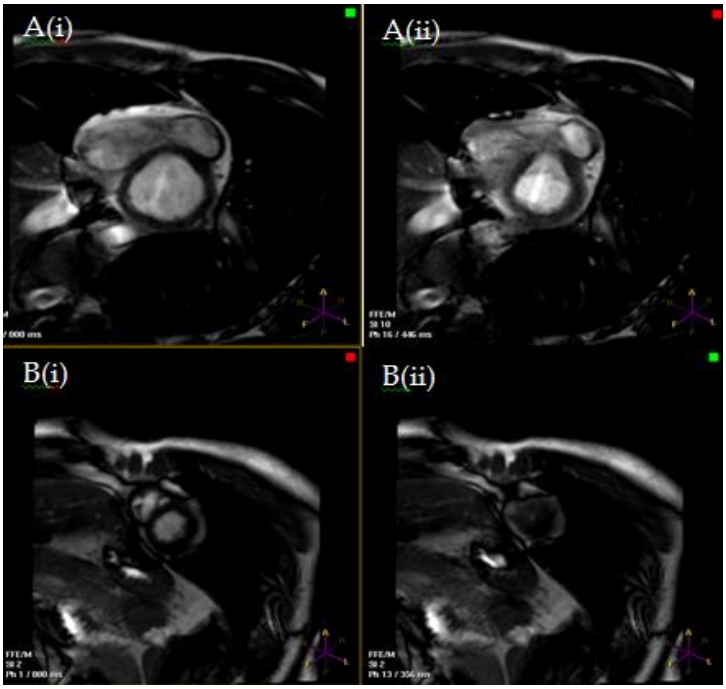

Figure 4.4-8: *Example image of basal slice showing A) i) a slice surrounded by myocardium and i) a slice that would not be included in the analysis* and B *i) a slice that would be included in analysis as there is an intra-cavity blood pool and ii) a slice that would be removed from analysis as there is no intra-cavity blood pool.*

Left ventricular (LV) End Diastolic Volume (EDV) and End Systolic Volume (ESV), stroke volume, cardiac output, wall mass, and ejection fraction were then determined. LV stroke volume (SV) is the volume of blood ejected from the LV with each contraction, given by SV = EDV – ESV. The ejection fraction measures the fraction of volume of blood pumped out of the left ventricle in each heart beat (E_f = (EDV-ESV)/EDV). Stroke volume and cardiac index were

corrected for body surface area (BSA) to give stroke volume index (SVI) and cardiac index (CI) respectively.

PC-MRI data from the aorta and inferior vena cava were also analysed using ViewForum software. An ROI was drawn around the walls of the vessel and this ROI was propagated through all time points across the cardiac cycle. From this, waveforms of the flux and velocity of blood flow over the cardiac cycle were derived, and stroke volume of the blood and cross sectional area of the vessel was calculated. Stroke volume, vessel cross sectional area and flux were BSA corrected.

4.4.2.2 Cardiac Structure

Analysis of MOLLI T_1 data was performed using dedicated software to form short axis T_1 maps (in ms) of the myocardium (Matlab version 8.1, The MathWorks, Inc., Natick, MA, USA). Images were first assessed for motion, discarded if the myocardium was seen to be in a different position and then fit to a Look-Locker inversion recovery (as described in Chapter 2). This process was performed both on a region of interest within the myocardium, and also a T_1 map of the myocardium was formed. To calculate the T_1 of blood in the left ventricular blood pool, the blood signal was fit to an inversion recovery assuming that fresh blood entered the left ventricle for each readout. T_1 maps were then masked to the myocardium by drawing an ROI along the epicardium wall. This T_1 map was also used in the perfusion quantification and to segment the myocardium.

Myocardial SPAMM tagging data was analysed using CIM2D software (Auckland Uni Services). In this programme, the myocardium was defined in the long axis by placing markers on the apex, and on points at the top of the endocardial and epicardial walls. The short axis was defined by placing markers around the epicardium and endocardium. These markers were then propagated for both orientations throughout all the time points. The software then automatically separated the myocardium into six segments, as illustrated

in Figure 4.4-9. In the short axis, segments were anterior septum, anterior, anterior lateral, posterior lateral, inferior and inferior septum. In the short axis, strain was defined as circumferential strain (%) which describes the strain of the short axis as the myocardial wall is contracting inwards. In the long axis, segments were base, middle and apex with two segments defined in each region (i.e. base 1 and base 2). Long axis strain was defined as longitudinal strain (%) which defines how the myocardium is compressed or stretched in the direction of the long axis. From this segmentation, the number of stunned segments in both the long and short axis was assessed by calculating the number of segments that had a reduced strain of greater than 20% on dialysis. Since the short axis slice for the tagging slice was in the same space as the ASL perfusion and T_1 maps the number of stunned segments could be correlated with these measures. A decrease in the measured value of strain reflects a decrease in the contractility of the myocardium, and so would be expected to lead to a decrease in stroke volume, cardiac output and ejection fraction.

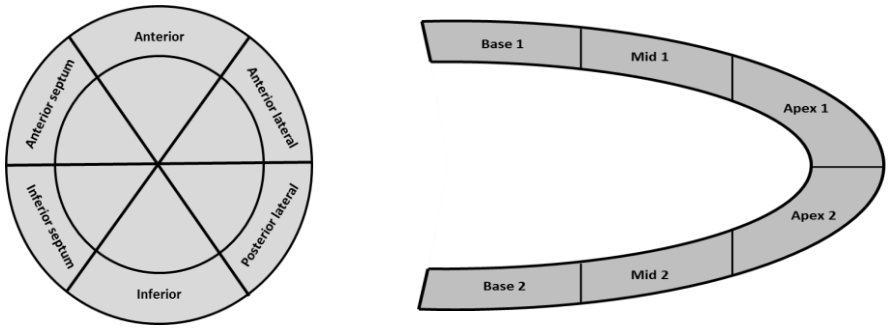

Figure 4.4-9: *Schematic of A) the short and B) the long axes of the left ventricle shown split into the six segments used for the tagging analysis.*

4.4.2.3 Perfusion and Coronary Artery Flow

Myocardial perfusion data acquired using MOLLI ASL was analysed using dedicated in-house MATLAB code (Matlab version 8.1, The MathWorks, Inc., Natick, MA, USA). In this program, images were first assessed for motion and then discarded if necessary, as described in Chapter 3. Non-selective and

selective data were each fit to a saturation recovery curve to estimate selective and non-selective T_1 values. This process was performed both on a region of interest within the myocardium, and also to map the myocardium. These T_1 values were then used to calculate the myocardial perfusion by fitting to the Belle model (25) with the T_1 of blood calculated from an ROI within the left ventricular blood pool of the T_1 maps. The Belle model equation is given as:

$$P = \frac{\lambda}{T_{1b}}\left(\frac{T_{1NS}}{T_{1SEL}} - 1\right)$$

The T_1 maps were masked to only contain the myocardium and limited to voxels with 0.8 s < T_1 < 1.5 s which eliminated signal from outside of the heart. Histograms were produced for the non-selective and selective T_1 values and the median T_1 for each was calculated. These T_1 values were then used in the Belle model to calculate perfusion, assuming a blood tissue partition coefficient of 0.92 ml/g. The standard deviation in the perfusion values was calculated by propagation of errors from the standard deviations of T_1 measures.

4.4.3 Statistical Analysis

Statistical assessment of results was performed in SPSS v22. To assess the significance of the change in a variable during the dialysis treatment, and for comparison between time points for the HD and HDF treatments, a repeated measure ANOVA was performed. To measure the correlation between MR measures and clinical data, paired Pearson correlation tests were performed. For assessment of the significance in the change from baseline to peak stress (defined as 210 minutes into treatment), a paired student T-Test was performed and considered at a p-value > 0.05.

4.5 Results

The ultrafiltration volume defines the amount of fluid that is removed from the body during dialysis treatment. Overall, UF volumes were small, and did not differ between HD and HDF treatment (median UF volume 1.7 l during HD (IQR 0.9-2.1 l) versus 1.7 l (IQR 1.2-2.2 l) during HDF, p=0.3). Mean UF rate during HD was 3.3 ± 0.2 ml/kg/hr and was 4.4 ± 0.2 ml/kg/hr for HDF (p=0.028). Table 4.5-1 shows blood test results.

	HD	**HDF**	**p**
Hemoglobin (g/l)	119.5 ± 7	120.8 ± 3	0.5987
URR (%)	74.6 ± 9	75.6 ± 9	0.2843
Bicarbonate (mmol/l)	24 (IQR 21 to 25)	23.5 (IQR 22 to 24.7)	0.8330
Adj.Calcium (mmol/l)	2.38 ± 0.13	2.48 ± 0.11	0.0848
Phosphate (mmol/l)	1.43 ± 0.38	1.47 ± 0.31	0.6855
PTH (ng/l)	191. (IQR 146.8 to 49.3)	200 (IQR 139 to 307.8)	0.5186
Magnesium (mmol/l)	0.98 ± 0.14	1.03 ± 0.15	0.0995
Lactate	0.34 ± 0.96	1.03 ± 0.44	0.4152
nT-proBNP (ng/l)	2145 (1102 to 3379)	1512 (1026 to 2261)	0.0522
Pre dialysis cTnT (ng/l)	64.7 ± 70	62.4 ± 58	0.65
Post dialysis cTnT	53.8 ± 57	37.3 ± 32	**0.043**
Delta cTnT (ng/l)	-18.09 ± 8.9	-37.68 ± 10.1	**0.0003**
Serum Na+ (Pre)	140.5 ± 0.7	140.6 ± 0.5	0.6844
Serum Na+ (Post)	139.0 ± 0.5	138.8 ± 0.4	0.7401

Table 4.5-1: *Biochemical results for HD and HDF. All results are pre-dialysis unless specified. Comparison of pre to post dialysis cTnT values for HD p=0.02 and for HDF p=0.007.*

The majority of pre-dialysis blood tests were similar in the two treatment arms; this included pre-dialysis high sensitivity troponin T levels. cTnT levels fell following both HD and HDF with the magnitude of decrease being greater

with HDF than HD. There was a trend for pre-dialysis NT-proBNP to be lower in the HDF arm, but this did not attain statistical significance. Body temperature fell significantly during the MR study sessions (from baseline to all time points) in both arms by 1 ± 0.4 ^{0}C during HD and HDF but was not significantly different between the treatments (p = 0.98).

Blood pressure did not significantly differ between treatments (Figure 4.5-1). Mean systolic blood pressure (SBP) was 141 ± 6 mmHg during HD and 142 ± 5.1 mmHg during HDF (p = 0.46). Mean diastolic blood pressure (DBP) was 79 ± 12 mmHg during HD and 77 ± 12 mmHg during HDF, p = 0.28.

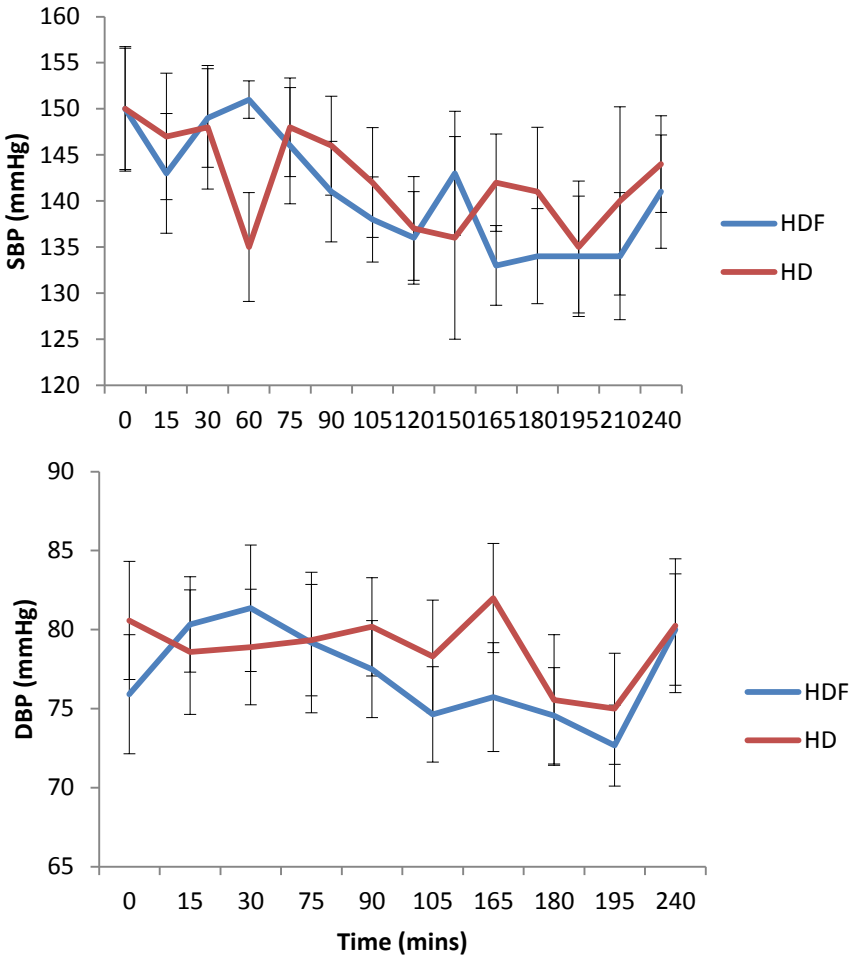

Figure 4.5-1: *Mean blood pressure during HD and HDF measured using a blood pressure cuff. A) Systolic blood pressure (SBP) and B) Diastolic blood pressure (DBP). There were no significant differences between blood pressures for HD and HDF at any timepoint.*

There was no significant difference between blood pressure values at any time point during dialysis. Five patients in each group had at least one systolic blood pressure value that fell by > 20 % from baseline pre-dialysis values, but there was only one episode of symptomatic hypotension which was in the HDF arm.

4.5.1.1 Heart Rate

Heart rate was monitored throughout the scans via the MRI VCG recording.

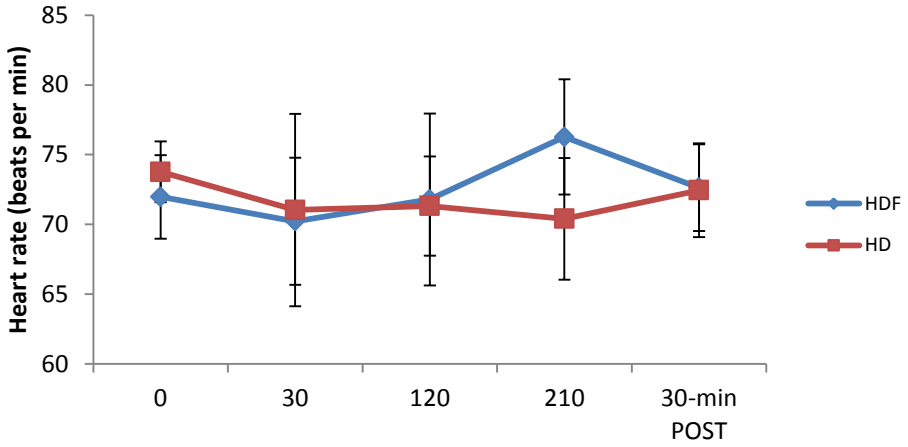

Figure 4.5-2: *Heart rate measured from the VCG data before (-30 mins), during and 30 mins post dialysis showing that heart rate stays fairly constant during the dialysis treatment. Timings are given for the start of each MR scan session.*

Heart rate was seen to remain fairly stable throughout treatment (Figure 4.5-2) with a significant increase in heart rate being seen at the 210 minute scan compared to the baseline scan for HDF but not HD ($p = 0.04$). The difference between heart rates for HD and HDF at each scan point was not found to be significant apart from the scan at 210 minutes ($p = 0.01$).

4.5.2 MR Measures

Results from the MRI measures are provided below. All figures show the time from the start of the dialysis treatment to the start of each MRI scan on the x-axis, from baseline (-30 mins before dialysis has begun), during dialysis and 30 mins post treatment. Graphs shown are mean values ± standard error.

Figure 4.4-2 shows the actual time each MR sequence was collected in the MR scan.

4.5.2.1 Cardiac Function

Results of cardiac function are shown in Figure 4.5-3 for aortic PC-MRI measures. A reduction in cardiac index (CI) ($p = 0.001$ for both HD and HDF for change from baseline to peak stress) and stroke volume index (SVI) ($p < 0.0001$ for both HD and HDF for change from baseline to peak stress) was observed during dialysis, with the minimal values observed at 210 minutes. No significant difference in CV or SVI was found between HDF and HD ($p > 0.1$ for all time points and percentage change from baseline to peak stress).

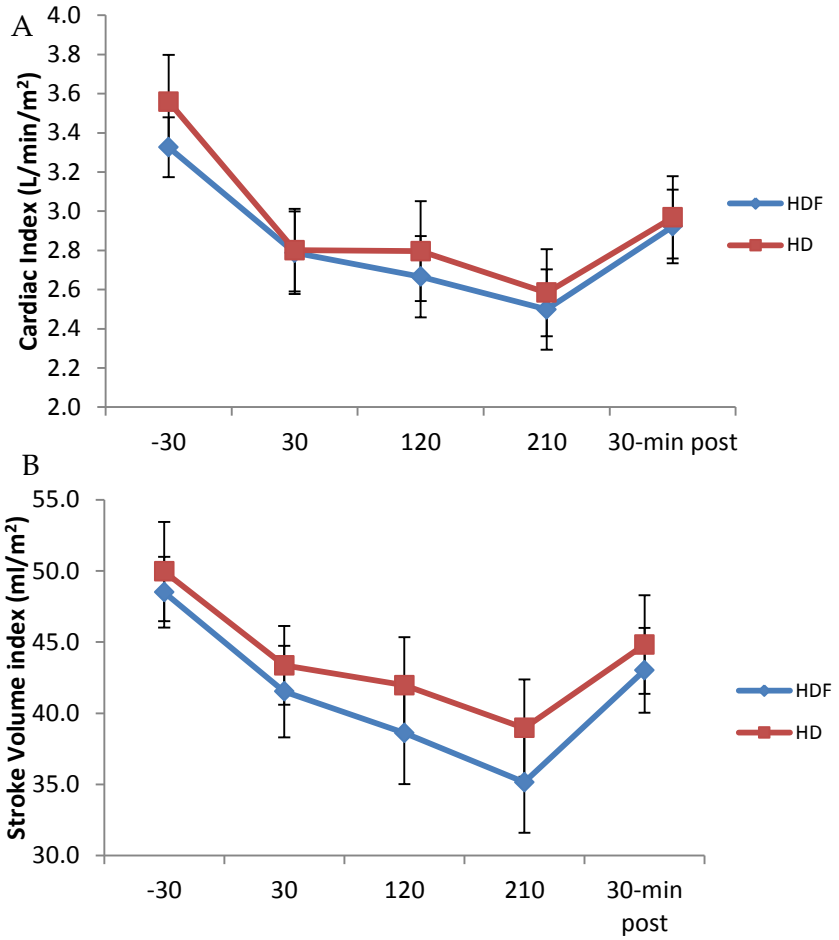

Figure 4.5-3: *A) Cardiac index B) Aortic stroke volume index measured from the PC-MRI aorta data before (-30 mins), during and 30 mins post dialysis showing that aortic SVI and CI both decrease during dialysis, and subsequently increase at 30 minutes recovery time. Timings are given for the start of each MR scan session.*

Analysis of cine MRI data also showed a significant reduction in LV SVI during dialysis ($p < 0.002$ for both HD and HDF for change from baseline to peak stress), as shown in Figure 4.5-4 which is in agreement with results from the PC-MRI aorta measures.

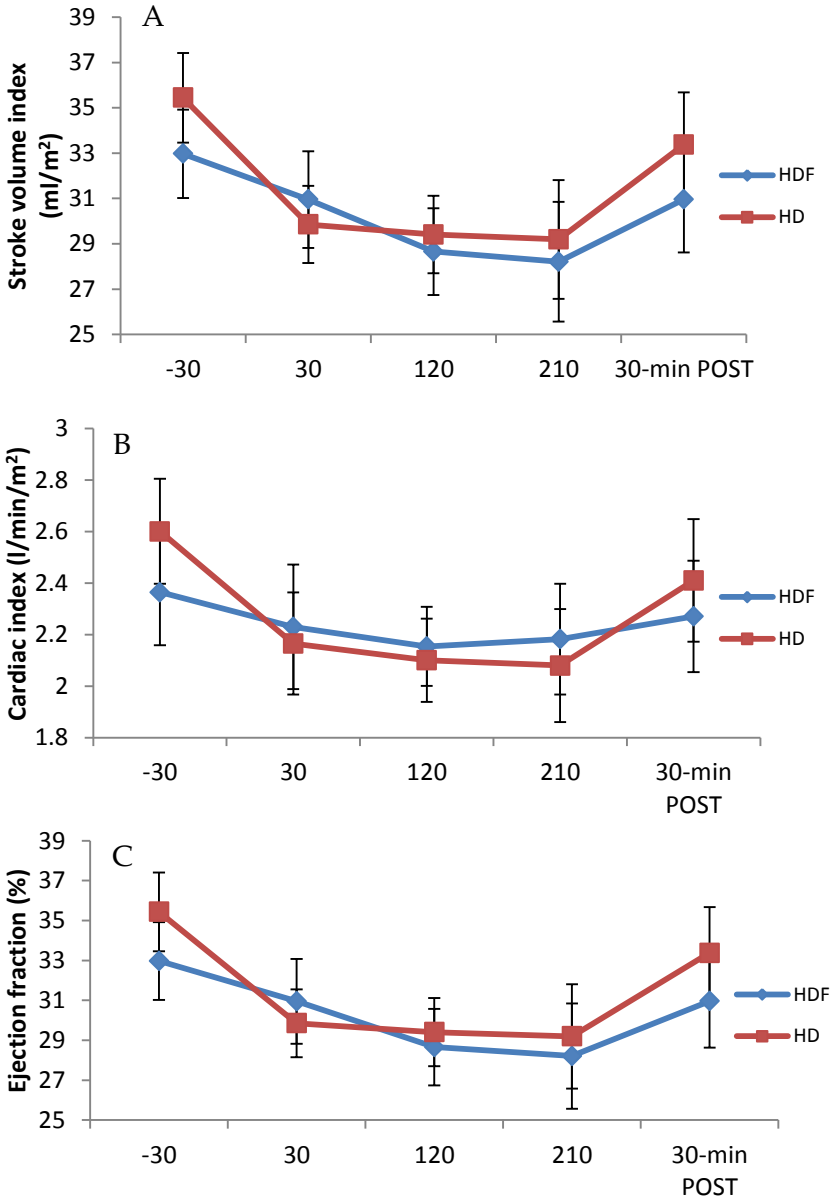

Figure 4.5-4: *Cine MRI results: A) Left ventricular stroke volume index (ml/mm²), B) Left ventricular ejection fraction (%) and C) Left ventricular cardiac index (L/min/m²) for the time points pre, during and post dialysis. Data shows that left ventricular stroke volume index, cardiac index and ejection fraction all decrease during dialysis treatment. Timings are given for the start of each MR scan session.*

There was a significant decrease in ejection fraction during dialysis for HDF. However, no significant difference in ejection fraction was found during HD as a result of a corresponding decrease in both EDV and ESV, though there was a clear trend for a decrease in ejection fraction during HD. As expected, a significant reduction in LV CI ($p < 0.001$ for HD and $p = 0.04$ for HDF) was also measured during dialysis for both HD and HDF modalities, in agreement with the changes shown in the PC-MRI aortic CI. Measures from PC-MRI data and MR cine data were significantly correlated ($r = 0.609$, $p = 0.000$ for SVI and $r = 0.49$, $p = 0.000$ for CI).

IVC flux reflects the flow of blood back into the right atrium, defined as the venous return. This was shown to significantly decrease for HD ($p = 0.02$) during dialysis treatment and subsequently return to baseline post dialysis, a reduction was also seen for HDF but this did not reach significance ($p = 0.07$). There were no significant differences in the response for HD and HDF treatment ($p = 0.45$).

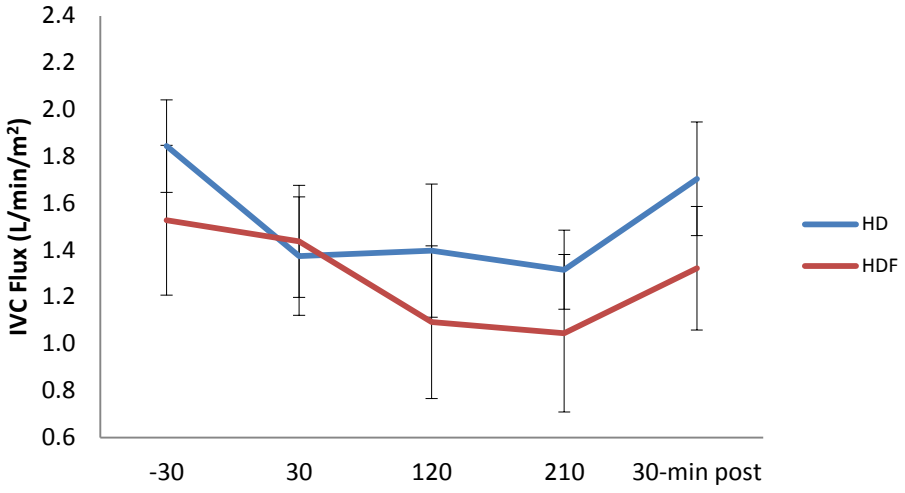

Figure 4.5-5: *Venous return estimated from BSA corrected IVC flux (L/min/m²) prior, during and post dialysis treatment showing a decrease in IVC flux during dialysis. Timings are given for the start of each MR scan session.*

4.5.2.2 Myocardial Strain

Whole wall and segmental myocardial strain was calculated in both the short and long axis. Figure 4.5-6 shows the calculated whole wall strain for a single short axis slice across the dialysis treatment for both HD and HDF.

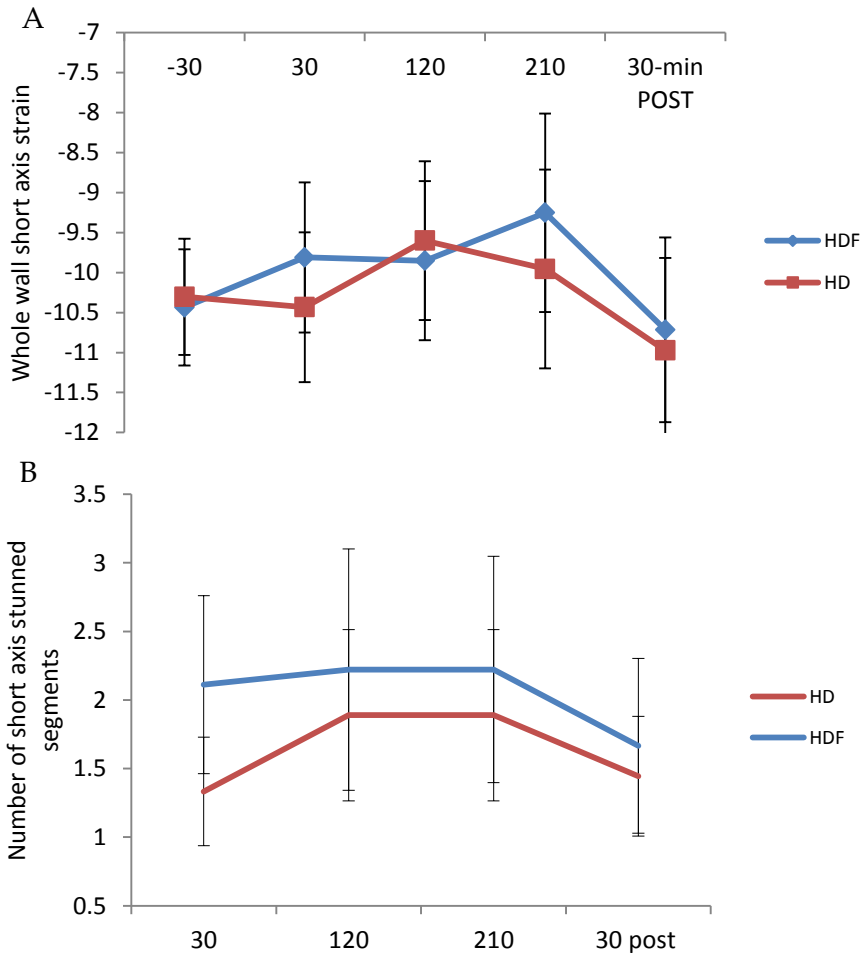

Figure 4.5-6: *A) Global whole wall short axis strain. Strain is seen to decrease (less negative therefore less strain) during dialysis and then return to baseline 30 minutes post dialysis. B) Number of stunned short axis segments. Stunned segments are evident from 30 minutes and then decrease, but do not return to baseline following treatment. Timings are given for the start of each MR scan session.*

A reduction in global whole wall strain is seen across both HD and HDF treatments (i.e. less negative strain values reflecting less strain). The baseline measures of short axis circumferential strain are identical for HD and HDF

treatments, and following dialysis the strain values return to the baseline value for both treatments. Figure 4.5-6B shows the average number of short axis stunned segments for HD and HDF treatment with evidence of myocardial stunning during the 30 minute scan. The myocardial strain scan was performed approximately 1 hour into the dialysis treatment, suggesting that cardiac stunning occurs early during dialysis and not only at the anticipated time of peak stress at 210 minutes. For scans at 30 minutes post dialysis, the number of stunned segments has decreased, but there are still stunned segments apparent for both HD and HDF treatments, suggesting that stunning has not fully recovered even after one hour.

Figure 4.4-16A shows the global whole wall longitudinal strain during HD and HDF treatment. There is a significant reduction in whole wall longitudinal strain (i.e. less negative strain values indicating less strain) throughout the dialysis treatment, with a similar response seen for both HD and HDF ($p < 0.03$ between baseline and all time points during dialysis treatment for both HD and HDF). Baseline measures of longitudinal strain were similar between HD and HDF ($p = 0.3$, no significant difference). Following dialysis, strain values increase towards baseline for both HD and HDF. There were no significant differences seen between the baseline and recovery scans for either HD or HDF treatment. On performing a repeated measure ANOVA between longitudinal strain values for each dialysis treatment across the five time points, no significant differences were found between treatments.

Figure 4.4-16B shows the number stunned segments in the long axis for HD and HDF. As for the short axis measures, it can again be seen that there is evidence of myocardial stunning at approximately an hour into treatment (during the 30 minute scan), with this being the time of greatest increase in number of stunned segments, stunning occurs following this at 120 and 210 minutes into treatment. At 30 minutes post dialysis there are still stunned

segments apparent for both treatments, with the number of stunned segments being less for HD than for HDF (p = 0.007).

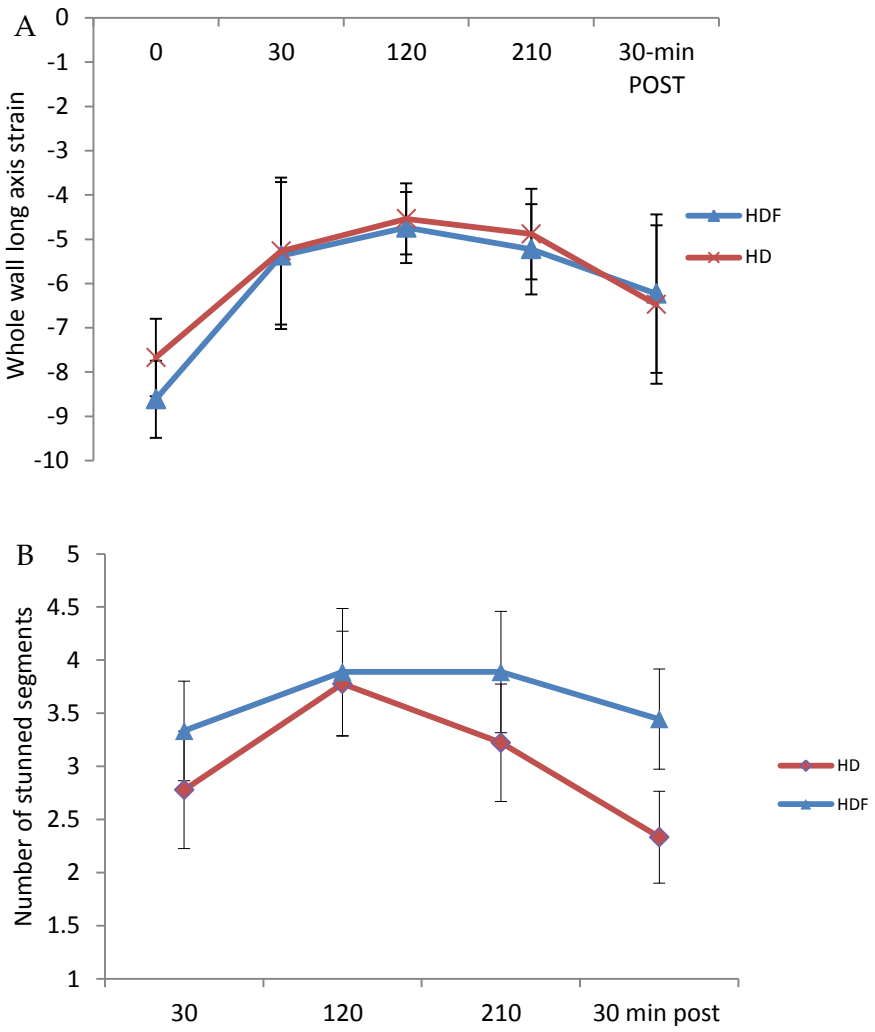

Figure 4.5-7: *A) Whole wall longitudinal strain. Strain is seen to decrease (become less negative) during dialysis and then return towards baseline in the MR scan at 30 minutes post dialysis. B) Number of stunned segments in the long axis at different time points during HD or HDF. Stunned segments are evident in the 30 minutes scan session during dialysis and decrease towards baseline following treatment, though some stunned segments remain. Timings are given for the start of each MR scan session.*

4.5.2.3 Perfusion and Coronary Artery Flow

Right coronary artery flow during dialysis as assessed using PC-MRI is shown in Figure 4.5-8 for both HD and HDF.

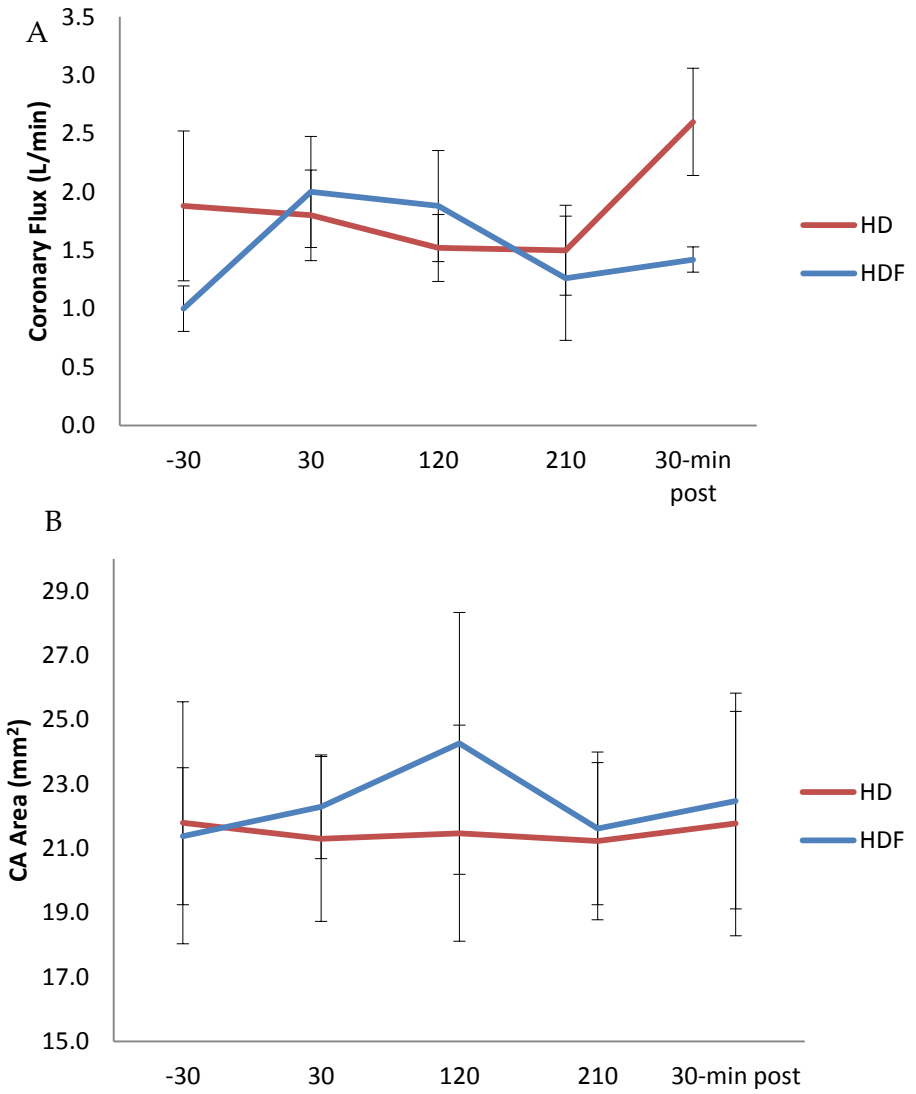

Figure 4.5-8: *A) Right coronary artery flux pre, during and post dialysis. Data shows no clear differences in flux during dialysis treatment. B) Right Coronary artery pre, during and post dialysis showing no clear differences in area during treatment. Timings are given for the start of each MR scan session.*

There were also no clear changes in coronary artery flux, stroke volume, or cross sectional area during dialysis at any time point for either HD or HDF. At

-30 minutes, the coronary artery areas are very similar for both treatments and these values return to baseline at 30 minutes post treatment.

It is hypothesised that the cardiac injury apparent during dialysis is due to areas of hypo-perfusion and so it is predicted that in areas where stunning occurs, there will also be a reduction in myocardial perfusion. Figure 4.5-9 shows global perfusion for the single short axis slice.

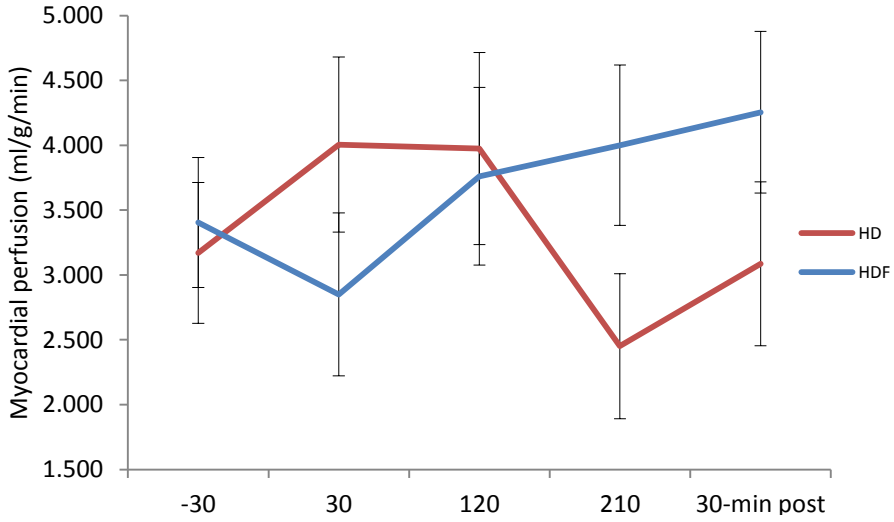

Figure 4.5-9: *Single short axis slice myocardial perfusion at different time points through dialysis treatment. Timings are given for the start of each MR scan session.*

Perfusion values were obtained on 10 of the 12 patients. There was no clear trend in the changes in mean myocardial perfusion during dialysis at any time point, and no differences between HD and HDF treatments. However, population averaged values masked significant individual variation in perfusion during dialysis. Some patients did not demonstrate reductions in perfusion; some had an early fall in perfusion with subsequent recovery and some had a late or progressive fall in perfusion. To examine this further, nadir (minimum) perfusion during treatment was compared with baseline pre-dialysis values. During both HD and HDF this was significantly lower, for HD baseline perfusion was 3.34 ± 1.7 ml/min/100g versus intra-dialytic nadir of 1.93 ± 1.4 ml/min/100g, $p = 0.050$; for HDF baseline perfusion was 3.40 ± 1.5

ml/min/100g versus intradialytic nadir of 1.99 ± 1.3 ml/min/100g, p = 0.019. This is shown in Figure 4.5-10.

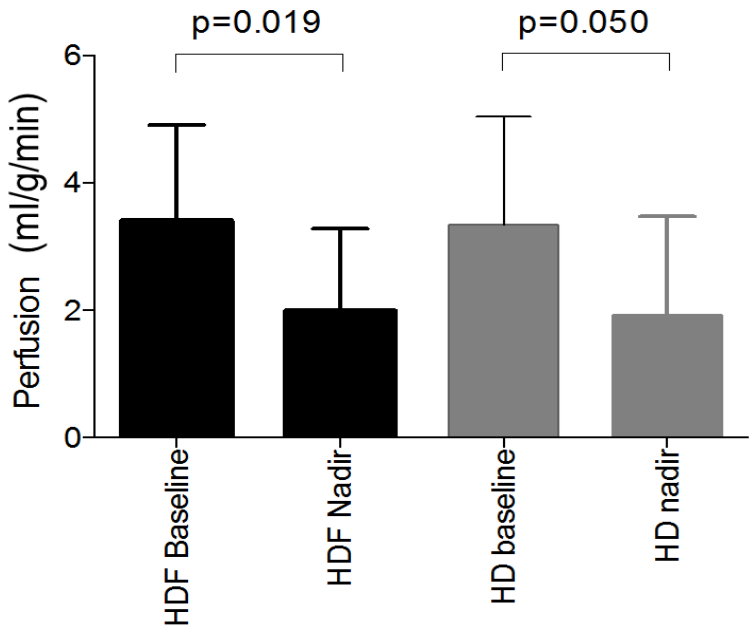

Figure 4.5-10: *Baseline perfusion and nadir perfusion during dialysis for both HD and HDF. A significant decrease in perfusion is seen for both treatment modalities.*

The nadir perfusion values did not differ when comparing HD and HDF treatments (p=0.9). There were no significant correlations found between perfusion and either number of stunned segments in the short axis or whole wall strain at any time point. A significant correlation was found between the percentage decrease in perfusion from baseline to the scan at 30 minutes (the time point when the most newly stunned segments were seen) and the number of stunned segments for HD (r = 0.71, p = 0.03), however this result was not significant for HDF (r = 0.21, p = 0.59).

To determine other associations with a fall in perfusion during treatment, both HD and HDF treatments were grouped together. There were no differences in nadir systolic blood pressure (SBP), percentage change in SBP or maximal numerical fall in SBP between those patients who did and did not experience a 20 % or greater fall in perfusion during dialysis. However, there was a trend

towards greater UF volume in patients with a 20 % or greater fall in perfusion (0.91 ± 0.7 l versus 1.5 ± 0.5 l, p = 0.06). Baseline perfusion was 2.7 ± 1.6 ml/g/min in those without a 20 % fall, compared to 3.9 ± 1.3 in those patients with a 20 % reduction in perfusion (p = 0.16).

4.5.2.4 Myocardial T1

Measurements of T_1 in the myocardium can inform of changes in tissue content such as fibrosis or inflammation. Figure 4.5-11 shows an example T_1 map of the myocardium in the short axis.

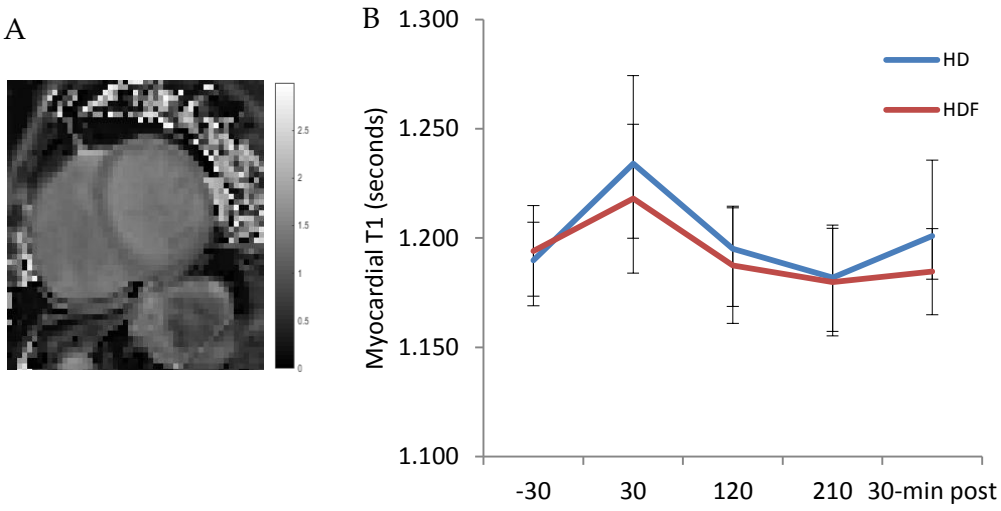

Figure 4.5-11: *A) Example myocardial T_1 map and scalebar of T_1 values in s. B) T_1 of the myocardium before, during and post dialysis showing no changes in the T_1 during dialysis treatment are apparent. Timings are given for the start of each MR scan session.*

Figure 4.5-11B shows the average T_1 value in the myocardium across the five time points during dialysis for HD and HDF. There is no difference in the T_1 value at baseline. There is a slight increase seen in T_1 values between baseline and the 30 minute scan, however this was not statistically significant and the increase was low at less than 3% for both HD and HDF.

4.5.2.5 Correlations between MRI results and Clinical Measures

Figure 4.5-12 shows changes in cardiac index (CI) and stroke volume index (SVI) correlated with the ultrafiltration volume for HD and HDF treatments.

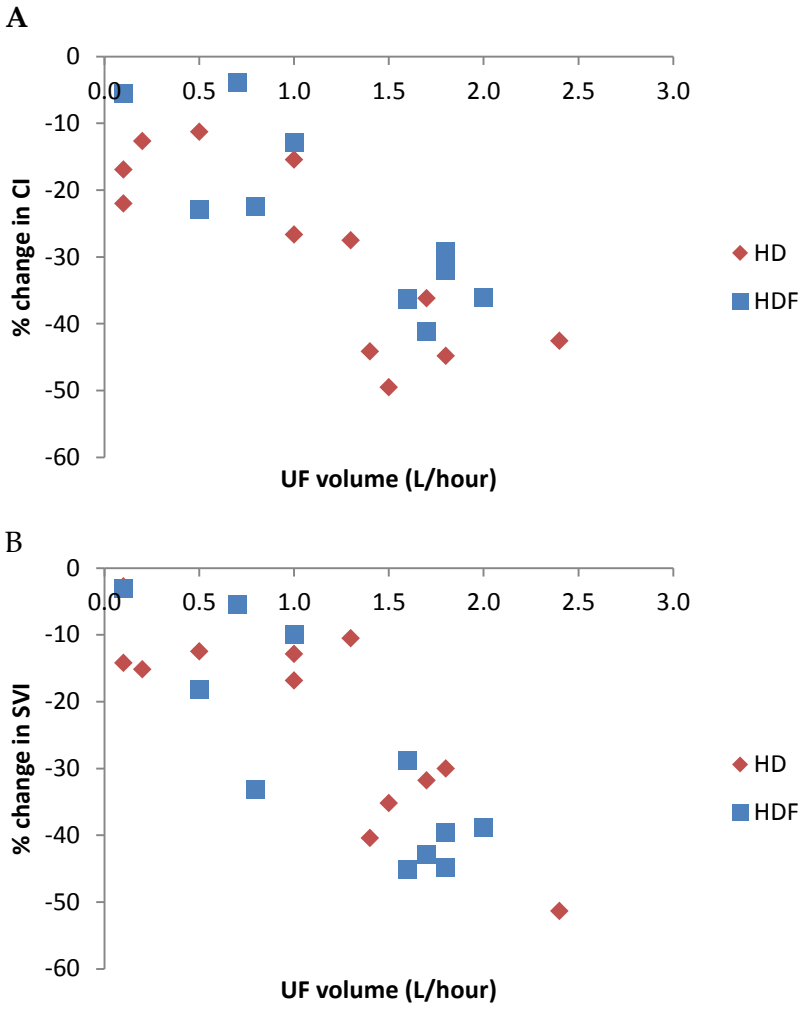

Figure 4.5-12: *A) Correlation between UF volume and cardiac index (CI) showing a negative correlation (r = -0.831, p= 0.000 for HD and r = -0.845, p = 0.001 for HDF) and B) Correlation between UF volume and stroke volume index (SVI)showing a negative correlation (r = -0.813, p= 0.001 and r = -0.838, p = 0.001 for HD and HDF respectively).*

A negative correlation between percentage change in CI from baseline to 210 mins and ultrafiltration volume was seen for both HD and HDF (r = -0.813, p= 0.001 and r = -0.838, p = 0.001 respectively). A similar trend was seen for SVI, (r

= -0.831, p= 0.000 and r = -0.845, p = 0.001 respectively). This demonstrates that an increase in the ultrafiltration volume is associated with a decrease in the cardiac function. No significant correlations were found between ultrafiltration volume and ejection fraction, heart rate or IVC flux.

Figure 4.5-13 shows the number of stunned segments in the long axis correlated with ultrafiltration volume for HD and HDF. A positive correlation was seen for both treatments (r = 0.707, p= 0.017 for HD, r = 0.594, p = 0.046 for HDF) suggesting that an increase in the ultrafiltration volume leads to an increase in the number of stunned segments during dialysis treatment. When correlating the number of stunned segments in the short axis with ultrafiltration volume, a positive correlation (r = 0.661, p = 0.026) was seen for HDF whereas no correlation was seen for HD (r = 0.156, p = 0.344). Note however that fewer stunned segments were identified in the short axis slice compared to the long axis slice.

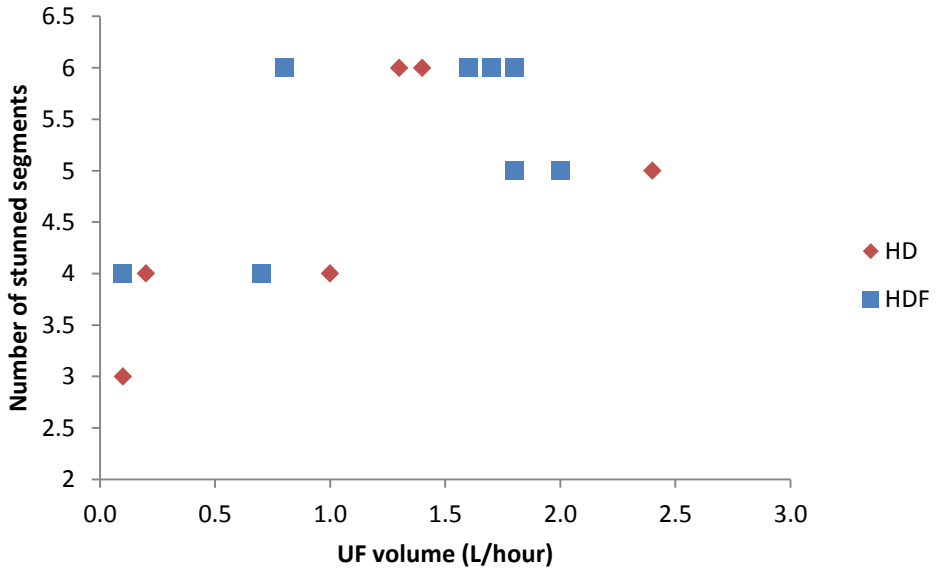

Figure 4.5-13: *Correlation between UF volume and number of stunned segments in long axis showing a positive correlation for HDF (r = 0.661, p = 0.026) but no significant correlation for HD.*

On correlating the number of stunned segments in the long axis with percentage change in stroke volume index, a negative correlation was seen (Figure 4.5-14 A) although this was not found to be a significant correlation for HD ($r = -0.502$, $p > 0.1$ for HD and $r = -0.716$, $p = 0.015$ for HDF) a similar trend was seen for cardiac output index (Figure 4.5-14 B) ($r = -0.720$, $p = 0.014$ for HD and $r = -0.698$, $p = 0.018$ for HDF). This suggests that an increase in the number of stunned segments reduces cardiac output and stroke volume.

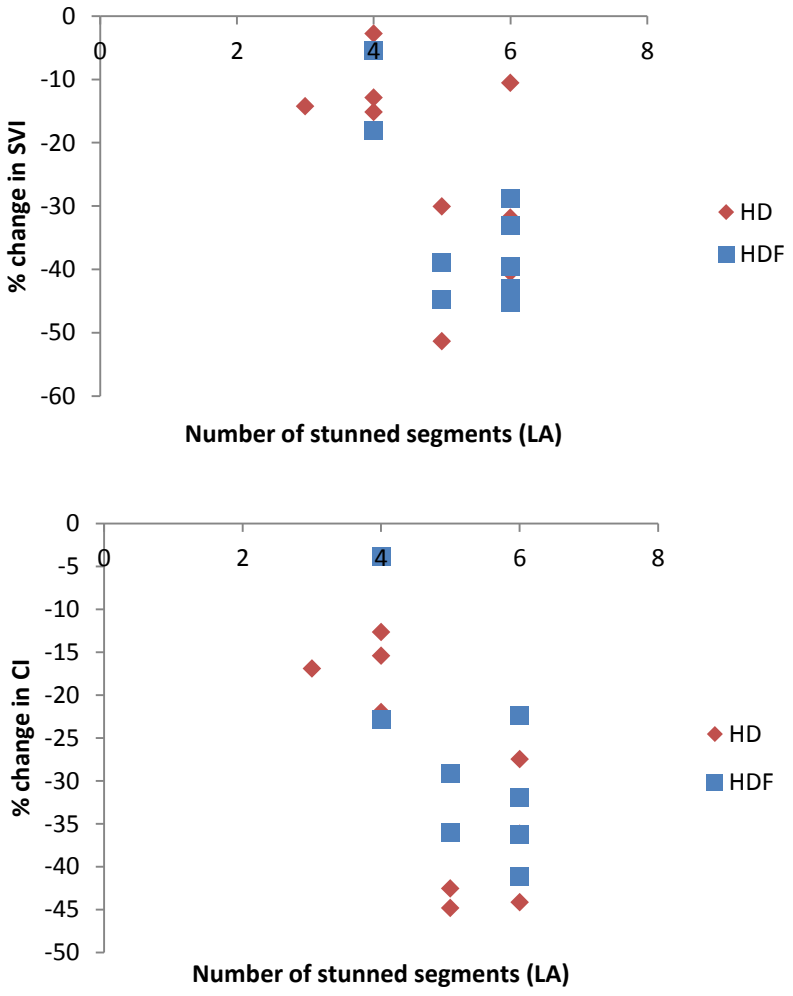

Figure 4.5-14: *A) Correlation between number of stunned segments and the change in stroke volume index (SVI) showing a negative correlation ($r = -0.502$, $p > 0.1$ for HD and $r = -0.716$, $p = 0.015$ for HDF). B) Correlation between number of stunned segments and the percentage change in cardiac index (CI) showing a negative correlation ($r = -0.720$, $p = 0.014$ for HD and $r = -0.698$, $p = 0.018$ for HDF).*

On correlating systolic blood pressure with the number of stunned segments, Figure 4.5-14, a negative correlation between the minimum systolic blood pressure during the treatment and number of stunned segments in the short axis was found for HD (r = -0.8, p = 0.004) (i.e. lower SBP associated with more stunning), this effect was not seen for HDF.

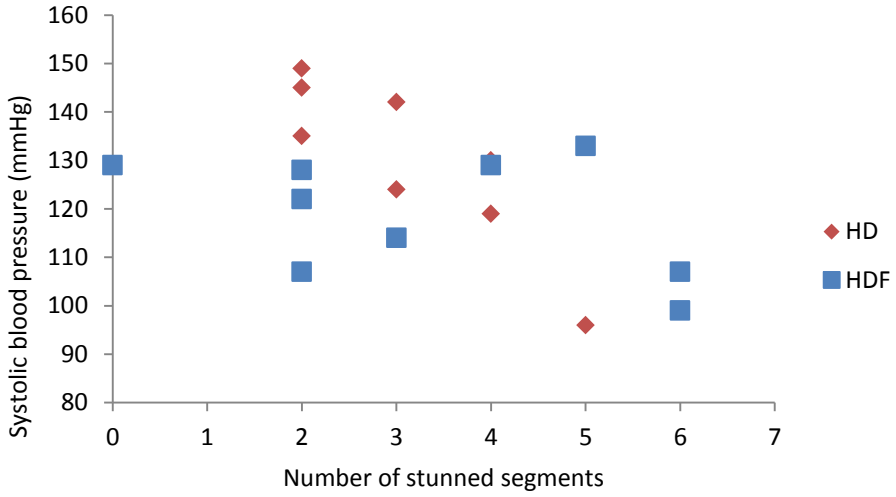

Figure 4.5-15: *Correlation between number of stunned segments in the short axis and systolic blood pressure (SBP). A negative correlation between number of stunned segments and SBP was found for HD (r = -0.8, p = 0.004) but not HDF.*

4.6 Discussion

Having overcome technical barriers associated with performing dialysis in a MRI scanner, this study has, for the first time, used intra-dialytic MRI with novel scanning techniques to provide a comprehensive assessment of cardiac function. In addition, differences in response to haemodialysis (HD) and haemodifiltration (HDF) were assessed. This set-up now provides a model in which other dialysis-based interventions can be characterised in detail to study mechanistic effects directly.

We have demonstrated a clear reduction in stroke volume index and cardiac index during HD and HDF. These data confirm previous observations in other

studies that used less robust imaging techniques (16), and also show that a decline in cardiac index is evident as early as 50 minutes from the start of treatment. The lowest values in cardiac index were observed at 210 minutes and cardiac index recovered after treatment, as previously reported.

A fall in stroke volume index and cardiac index was found to correspond to a reduction in myocardial contractility (less negative strain values) which was more evident on the long axis than the short axis. Similarly we observed the presence of stunning in segments of the myocardium as early as 1 hour from the start of treatment. Interestingly, recovery from stunning was incomplete at approximated one hour after treatment. These data describe regional changes in contractility with much greater precision that has previously been possible with echocardiography.

Myocardial perfusion was assessed in only a single short-axis view, due to technical reasons associated with arterial spin labelling. There was wide inter- and intra-individual variation in perfusion, a feature not evident in previous studies of healthy controls. Analysis of baseline to nadir values did show a significant decline in myocardial perfusion during HD and HDF, as shown in previous studies employing positon emission tomography (14). Crucially, no reduction in right coronary artery blood flow was observed during HD or HDF, suggesting that the observed decrease in myocardial perfusion was not due to a reduction in blood flow in the main coronary arteries; this strengthens the hypothesis that it is changes in microcirculatory blood flow that underpin dialysis induced stunning. A correlation was observed between reduction in myocardial perfusion at the 30 minutes scan and the number of stunned segments in the short axis view, but only for HD.

Ultrafiltration volume was strongly correlated with several adverse changes in cardiac function, including percentage decrease in stroke volume index and cardiac index as well as number of stunned myocardial segments. This confirms previous observations that ultrafiltration volume is one of the main

determinants of intradialytic myocardial stunning as assessed by echocardiography (26). Interestingly, these correlations were observed in a group of patients with relatively low ultrafiltration volumes (median 1.7 litres), suggesting that even relatively small ultrafiltration volumes may provoke adverse cardiac effects. Whilst blood pressure (BP) was generally stable during both treatments, there remained a correlation between number of stunned ventricular segments and fall in systolic blood pressure during dialysis; again reinforcing previous findings that a change in blood pressure is a second key clinical driver of dialysis induced myocardial stunning. This work did not demonstrate a clear association between blood pressure changes and myocardial perfusion, although it remains to be seen whether this was due to technical aspects of image acquisition preventing measurement of perfusion over the entire ventricle or lack of clinical effect.

Overall there were no significant differences in any of the cardiac function variables measured from blood tests studied between HD and HDF. Lower troponin-T concentrations post HDF (but not pre-treatment) likely reflect greater clearance of troponin-T by HDF. These observations do not, however, exclude the possibility that HDF may offer haemodynamic benefits over HD in some patients. It should be noted that because of the physically challenging nature of this first ever intra-dialytic MRI study, relatively healthy patients who had well preserved cardiac function were selected. In addition, due to the low ambient temperature in the MR scanner room, all patients experienced a significant fall in body temperature, an intervention that has been shown to improve intradialytic haemodynamic stability (27). Finally, the participants required relatively low ultrafiltration volumes to maintain fluid balance and did not suffer from high rates of intradialytic hypotension. Thus it remains possible that HDF may be associated with improved intradialytic stability in more frail patient groups, in the presence of higher ultrafiltration volumes and in the absence of cooling, as suggested by some (but not all) published studies.

Here, cardiac index was measured using two MR techniques, PC-MRI and cine MRI scans. Measures collected using these methods were shown to be highly correlated ($r = 0.49$, $p = 0.000$) but to have a systematic error, in agreement with previous studies (28–31). The values measured for cardiac index using PC-MRI are in agreement with previous studies (29) validated using flow phantoms. One of the potential errors between the two methods is caused by partial volume effects and choice of ROI selection. PC-MRI flow measurement has a potential to slightly underestimate actual flow volume due to averaged phase-velocity near vessel wall (28). However, a major advantage of PC-MRI is that it only needs semiautomatic segmentation on a single slice, whereas cine MRI scans require segmentation on multiple short axis slices, and is critical on the choice of the basal and apical slice chosen for end-diastole and end-systole, as shown in Figure 4.4-8 and partial voluming. Further, the number of patient's breath holds is significantly reduced for a single-slice PC-MRI acquisition compared to cine MRI. Previous studies have assessed MR measures against both non-contrast enhanced and contrast enhanced (CE) two-dimensional echocardiography (2DE) and three-dimensional echocardiography (3DE) using MR cine data (30) and PC-MRI (31).

4.7 Conclusion

In summary, this chapter has shown novel intradialytic MRI assessments which provide further support for the hypothesis that haemodialysis treatment provokes a reduction in myocardial perfusion that in turn causes stunning of the myocardium and a fall in cardiac index (32). Ultrafiltration volume and change in blood pressure were confirmed as important determinants of myocardial stunning. This phenomenon was observed even in relatively well patients with preserved cardiac function at baseline and in the presence of intradialytic cooling. Novel results include the demonstration in tandem of significant changes in perfusion, contractility and haemodynamics that occur as early as 1 hour into dialysis, and also that the reduction in

contractility observed during dialysis contributes to the fall in cardiac index (i.e. changes in stroke volume index and cardiac index are not due solely to a reduction in circulating volume). There remains therefore an urgent need to better understand the factors that contribute to intradialytic myocardial stunning and develop more effective strategies to ameliorate it.

In future studies we will collect baseline echocardiogram measures for comparison with MR measures of cardiac function. Future studies will also aim to study the association between intradialytic changes in myocardial perfusion and contractility in greater detail by employing higher spatial resolution acquisitions and multi-slice coverage of ASL perfusion measures. In addition, as well as the effect of reductions in cardiac index on the perfusion and function of other organs will be studied, including the effect of dialysis on residual renal function by monitoring perfusion and T_1 in the kidney. As the kidneys of dialysis patients will be more challenging to image in comparison to healthy patients due to the likelihood of lower blood flow, areas of fibrosis and multiple renal cysts, a robust imaging scheme is needed for the assessment of kidney health. Chapter 5 of this thesis aims to optimise arterial spin labelling and T_1 measures in the kidneys of healthy subjects to ensure such reproducibility and accuracy of the techniques for future assessments in chronic kidney disease.

4.8 References

1. McIntyre CW. Effects of hemodialysis on cardiac function. Kidney Int. 2009;76:371–5. doi: 10.1038/ki.2009.207.

2. McIntyre CW. Haemodialysis-induced myocardial stunning in chronic kidney disease - a new aspect of cardiovascular disease. Blood Purif. 2010;29:105–10. doi: 10.1159/000245634.

3. Mcintyre CW. Recurrent Circulatory Stress: The Dark Side of Dialysis. Semin. Dial. 2010;23:449–451. doi: 10.1111/j.1525-139X.2010.00782.x.

4. Selby NM, McIntyre CW. The acute cardiac effects of dialysis. Semin. Dial. 2007;20:220–228. doi: 10.1111/j.1525-139X.2007.00281.x.

5. Burton JO, Jefferies HJ, Selby NM, McIntyre CW. Hemodialysis-induced cardiac injury: Determinants and associated outcomes. Clin. J. Am. Soc. Nephrol. 2009;4:914–920. doi: 10.2215/CJN.03900808.

6. Selby NM, Mcintyre CW. Protecting the heart in dialysis patients - intra-dialytic issues. Semin. Dial. 2014;27:332–335. doi: 10.1111/sdi.12180.

7. Selby NM, McIntyre CW. A systematic review of the clinical effects of reducing dialysate fluid temperature. Nephrol. Dial. Transplant. 2006;21:1883–1898. doi: 10.1093/ndt/gfl126.

8. Selby NM, Lambie SH, Camici PG, Baker CS, McIntyre CW. Occurrence of regional left ventricular dysfunction in patients undergoing standard and biofeedback dialysis. Am. J. Kidney Dis. 2006;47:830–841. doi: 10.1053/j.ajkd.2006.01.012.

9. Wizemann V, Lotz C, Techert F, Uthoff S. On-line haemodiafiltration versus low-flux haemodialysis. A prospective randomized study. Nephrol. Dial. Transplant. 2000;15 Suppl 1:43–48.

10. Locatelli F, Altieri P, Andrulli S, et al. Hemofiltration and hemodiafiltration reduce intradialytic hypotension in ESRD. J. Am. Soc. Nephrol. 2010;21:1798–1807. doi: 10.1681/ASN.2010030280.

11. Donauer J, Schweiger C, Rumberger B, Krumme B, Böhler J. Reduction of hypotensive side effects during online-haemodiafiltration and low temperature haemodialysis. Nephrol Dial Transplant. 2003;18:1616–22. doi: 10.1093/ndt/gfg206.

12. Karamperis N, Sloth E, Jensen JD. Predilution hemodiafiltration displays no hemodynamic advantage over low-flux hemodialysis under matched conditions. Kidney Int. 2005;67:1601–8. doi: 10.1111/j.1523-1755.2005.00242.x.

13. Van der Sande FM, Kooman JP, Konings CJ, Leunissen KM. Thermal effects and blood pressure response during postdilution hemodiafiltration and hemodialysis: the effect of amount of replacement fluid and dialysate temperature. J. Am. Soc. Nephrol. 2001;12:1916–20.

14. McIntyre CW, Burton JO, Selby NM, Leccisotti L, Korsheed S, Baker CSR, Camici PG. Hemodialysis-induced cardiac dysfunction is associated with an acute reduction in global and segmental myocardial blood flow. Clin. J. Am. Soc. Nephrol. 2008;3:19–26. doi: 10.2215/CJN.03170707.

15. Dasselaar JJ, Slart RHJ a, Knip M, Pruim J, Tio R a, McIntyre CW, de Jong PE, Franssen CFM. Haemodialysis is associated with a pronounced fall in myocardial perfusion. Nephrol. Dial. Transplant 2009;24:604–10. doi: 10.1093/ndt/gfn501.

16. Burton JO, Jefferies HJ, Selby NM, McIntyre CW. Hemodialysis-induced repetitive myocardial injury results in global and segmental reduction in systolic cardiac function. Clin. J. Am. Soc. Nephrol. 2009;4:1925–1931. doi: 10.2215/CJN.04470709.

17. Zun Z, Wong {E.C.}, Nayak {K.S.}. Assessment of myocardial blood flow {(MBF)} in humans using arterial spin labeling {(ASL):} feasibility and noise analysis. Magn. Reson. Med. 2009;62:975–83. doi: 10.1002/mrm.22088.

18. Messroghli DR, Radjenovic A, Kozerke S, Higgins DM, Sivananthan MU, Ridgway JP. Modified look-locker inversion recovery (MOLLI) for high-resolution T 1 mapping of the heart. Magn. Reson. Med. 2004;52:141–146. doi: 10.1002/mrm.20110.

19. Ok E, Asci G, Toz H, et al. Mortality and cardiovascular events in online haemodiafiltration (OL-HDF) compared with high-flux dialysis: Results from the Turkish OL-HDF Study. Nephrol. Dial. Transplant. 2013;28:192–202. doi: 10.1093/ndt/gfs407.

20. Grooteman MPC, van den Dorpel M a., Bots ML, et al. Effect of Online Hemodiafiltration on All-Cause Mortality and Cardiovascular Outcomes. J. Am. Soc. Nephrol. 2012;23:1087–1096. doi: 10.1681/ASN.2011121140.

21. Maduell F, Moreso F, Pons M, Ramos R, Mora-Macià J, Carreras J, Soler J, Torres F, Campistol JM, Martinez-Castelao A. High-efficiency postdilution online hemodiafiltration reduces all-cause mortality in hemodialysis patients. J. Am. Soc. Nephrol. 2013;24:487–497. doi: 10.1681/ASN.2012080875.

22. Vilar E, Fry AC, Wellsted D, Tattersall JE, Greenwood RN, Farrington K. Long-term outcomes in online hemodiafiltration and high-flux hemodialysis: a comparative analysis. Clin. J. Am. Soc. Nephrol. 2009;4:1944–1953. doi: 10.2215/CJN.05560809.

23. Canaud B, Barbieri C, Marcelli D, Bellocchio F, Bowry S, Mari F, Amato C, Gatti E. Optimal convection volume for improving patient outcomes in an international incident dialysis cohort treated with online hemodiafiltration. Kidney Int. 2015:1–9. doi: 10.1038/ki.2015.139.

24. Buchanan CE, Cox EF, Francis ST. Measuring myocardial blood flow using modified look locker inversion (MOLLI) recovery arterial spin labelling (ASL). Proc. Intl. Soc. Mag. Reson. Med. 23 0538. 2015;64:2015.

25. Belle V, Kahler E, Waller C, Rommel E, Voll S, Hiller KH, Bauer WR, Haase a. In vivo quantitative mapping of cardiac perfusion in rats using a noninvasive MR spin-labeling method. J. Magn. Reson. Imaging 8:1240–1245. doi: 10.1002/jmri.1880080610.

26. Burton JO, Jefferies HJ, Selby NM, McIntyre CW. Hemodialysis-Induced Cardiac Injury: Determinants and Associated Outcomes. Clin. J. Am. Soc. Nephrol. 2009;4:914–920. doi: 10.2215/CJN.03900808.

27. Jefferies HJ, Burton JO, McIntyre CW. Individualised dialysate temperature improves intradialytic haemodynamics and abrogates haemodialysis-induced myocardial stunning, without compromising tolerability. Blood Purif. 2011;32:63–8. doi: 10.1159/000324199.

28. Lin HY, Freed D, Lee TWR, et al. Quantitative assessment of cardiac output and left ventricular function by noninvasive phase-contrast and cine MRI: Validation study with invasive pressure-volume loop analysis in a swine model. J. Magn. Reson. Imaging 2011;34:203–210. doi: 10.1002/jmri.22587.

29. Carlsson M, Andersson R, Bloch K, Steding-Ehrenborg K, Mosén H, Stahlberg F, Ekmehag B, Arheden H. Cardiac output and cardiac index measured with cardiovascular magnetic resonance in healthy subjects, elite athletes and patients with congestive heart failure. J. Cardiovasc. Magn. Reson. 2012;14:51. doi: 10.1186/1532-429X-14-51.

30. Jenkins C, Moir S, Chan J, Rakhit D, Haluska B, Marwick TH. Left ventricular volume measurement with echocardiography: a comparison of left ventricular opacification, three-dimensional echocardiography, or both with

magnetic resonance imaging. Eur. Heart J. 2009;30:98–106. doi: 10.1093/eurheartj/ehn484.

31. Chuang ML, Hibberd MG, Salton CJ, Beaudin R a., Riley MF, Parker R a., Douglas PS, Manning WJ. Importance of imaging method over imaging modality in noninvasive determination of left ventricular volumes and ejection fraction: Assessment by two- and three-dimensional echocardiography and magnetic resonance imaging. J. Am. Coll. Cardiol. 2000;35:477–484. doi: 10.1016/S0735-1097(99)00551-3.

32. McIntyre CW, Odudu A. Hemodialysis-Associated Cardiomyopathy: A Newly Defined Disease Entity. Semin. Dial. 2014;27:87–97. doi: 10.1111/sdi.12197.

5 Optimisation of Readout Schemes for Renal Arterial Spin Labelling

This chapter describes the optimisation of renal perfusion measures using a flow alternating inversion recovery (FAIR) ASL scheme. Previously, a number of 2D readout schemes have been proposed for renal ASL, these include gradient echo based methods of balanced fast field echo (bFFE) and gradient echo echo-planar imaging (GE-EPI) or spin echo based schemes of spin echo EPI (SE-EPI) and turbo spin echo (TSE). Alternative 3D methods include 3D gradient and spin echo (GRASE) and 3D TSE. However, to date there is no general consensus on the optimum readout scheme for renal ASL. This chapter aims to compare four 2D readout schemes to determine the optimal readout scheme for pulsed ASL (PASL) for use in future studies in Chronic Kidney Disease.

The work in this chapter has been presented as an oral presentation at the annual conference of the International Society of Magnetic Resonance in Medicine (ISMRM), Toronto, 2015 (p0256).

5.1 Introduction

Tissue perfusion is a potentially important measure of kidney health. Perfusion measures inform on the delivery of nutrients and oxygen to the tissue. Typically, renal function is determined via serum creatinine measurements to estimate glomerular filtration rate (GFR), however these methods are not highly sensitive and changes in GFR may develop relatively late in the progression of Chronic Kidney Disease (CKD). Renal perfusion is an alternative parameter which can be used to monitor renal function. A method to provide reliable and reproducible perfusion assessment of the kidney, in conjunction with precise morphological information, would significantly improve the assessment and monitoring of CKD. Arterial spin labelling (ASL) provides a MRI technique for the non-invasive quantitative assessment of tissue perfusion.

Renal ASL methods were summarized in Chapter 1. The majority of renal ASL studies in the literature have employed the pulsed ASL technique of flow-sensitive alternating inversion recovery (FAIR) scheme (1–9). A pubmed search of renal ASL using the keywords of 'renal ASL' and 'kidney ASL' shows that of renal ASL publications to date, 19 renal ASL publications employ a FAIR scheme with 3 using a pCASL technique.

In the FAIR scheme, two images are collected: a selective image which contains non-inverted arterial blood and a non-selective image in which inflowing blood is magnetically inverted (Figure 5.1-1). By subtracting the non-selective (label) image from the selective (control) image a perfusion weighted difference image is formed. Often in the ASL scheme, pre-saturation and post-saturation pulses are applied immediately prior to and following the labelling pulse, this ensures that the perfusion weighted difference signal is zero over the imaging plane at post label delay of $t = 0\,\mathrm{s}$, and is not dominated by differences in the inversion efficiency between the selective and non-selective slab.

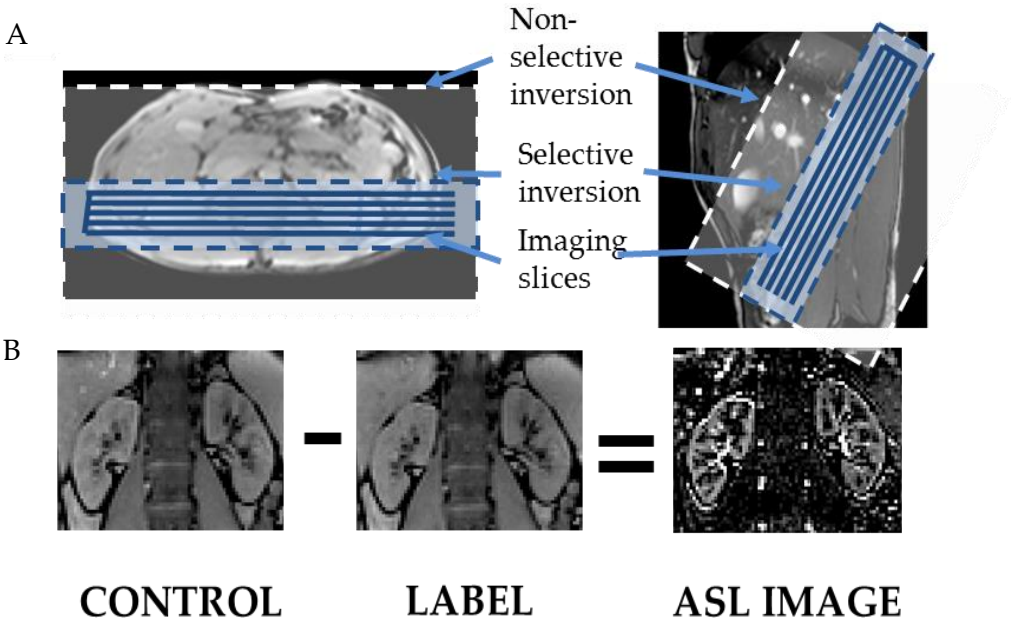

Figure 5.1-1: A) *Position of selective (control, shown in light blue) and non-selective (label, shown in white) slabs in FAIR ASL scheme and imaging slices and B) Subtraction of label image from control image yields a perfusion weighted (PW) difference image.*

T_1 maps are necessary for the quantification of renal perfusion; however T_1 values can also be used as an imaging based marker to provide information on the health of the kidney. It has been demonstrated in animal models that renal T_1 mapping techniques can be used to differentiate between severities of acute kidney injury (AKI) (10), and for the measurement of renal fibrosis and inflammation (11). Importantly, it has been shown that T_1 measures can detect changes to the tissue before they are apparent from renal histology. In the work of Hueper *et al.* (10), it was shown that renal T_1 relaxation times were increased after inducing acute kidney injury (AKI) in the mouse kidney, and that T_1 correlates with subsequent kidney volume loss at 28 days post AKI. In the work by Breidthardt *et al* (12), the association between renal perfusion and T_1 relaxation times was assessed. This work demonstrated that renal cortical perfusion values positively correlated with estimated GFR and that T_1 negatively correlated with estimated GFR. This work highlights the need for robust imaging schemes for measurement of perfusion and T_1 relaxation times

in the kidney as these parameters can be translated to important markers of renal health.

5.2 Readout Schemes

A number of different readout schemes have been implemented in the literature for renal ASL studies (Table 5.2-1). This overview will first describe 2D readout schemes, and then introduce 3D readout schemes. To determine the optimal readout scheme for renal ASL, a number of variables must be considered. The optimal readout scheme is one that should have a short echo time (TE) in order to provide the highest image SNR and reduce the amount of signal dephasing and distortion. The short intrinsic T_2 and T_2^* in the abdomen (T_2 ~70 ms, T_2^* ~ 40 ms at 3T) leads to rapid signal dropout and loss of perfusion signal at longer echo times.

2D Readout scheme	**Number of published studies**	**Example published papers**
bFFE/TrueFISP	*10* (4–6,13–19)	*Martirosian et al. MRM 51:353-361, 2004, Heusch et al., JMRI 40:84–89, 2014, Gillis et al., BMC Nephrology 15:23, 2014*
GE-EPI	*1* (9)	*Sokolska et al, ESR, 1594:1–13, 2014*
SE-EPI	*1* (4)	*Gardener et al., MRM 63:1627-1636, 2010*
TSE	*4* (2,7,8,20)	*Robson et al., MRM 61:1374-1387, 2009*

Table 5.2-1: *List of 2D readout schemes with number of current published studies of each and example papers.*

The ideal readout scheme should also be collected in a short shot length to enable multiple slices through the kidney to be acquired prior to the recovery

of the ASL signal. Secondly, if the acquisition is respiratory triggered, then it is important to acquire all the images within a respiratory cycle, and ideally all within the flat component of the respiratory cycle where there is minimum motion, as illustrated in Figure 5.2-1. Finally, a 2D readout scheme requires a low specific absorption rate (SAR) so that a short temporal spacing can be achieved when collecting data from multiple slices.

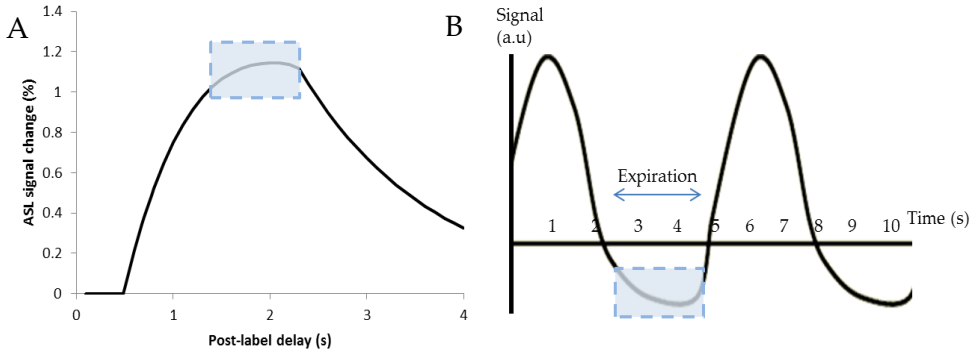

Figure 5.2-1: *A) ASL signal curve showing optimal part of curve to sample for maximum signal (in blue box). B) Respiratory trace showing end expiration where ASL images should be acquired to minimise motion artefacts (in blue box).*

The following section reviews each of the readout schemes used in the literature; each has some optimal qualities. In order to determine the best readout scheme, these parameters need to be assessed and the trade-offs considered.

Echo planar imaging (EPI) is one of the most commonly used techniques for ASL of the brain due to its relatively short scan time (21–29). However, in the body, ASL EPI readouts have echo times of > 10 ms and are susceptible to signal inhomogeneities which may limit their use in regions close to geometrically irregular soft tissue-air or tissue-bone boundaries. Either gradient echo (GE) or spin-echo (SE) based EPI can be used. A GE-EPI pulse sequence diagram is shown in Figure 5.2-2

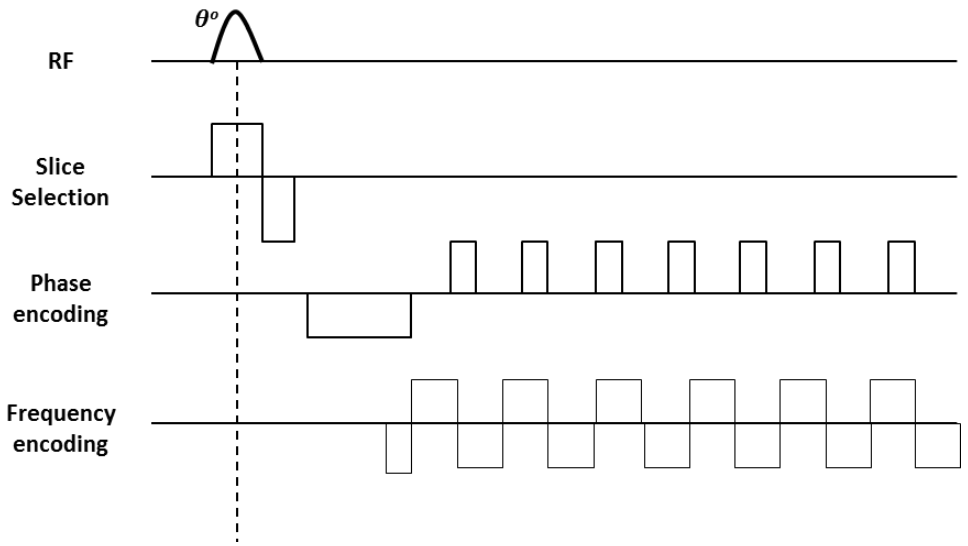

Figure 5.2-2: *Pulse sequence diagram of a GE-EPI scheme.*

A GE-EPI is more dependent on field homogeneity than SE-EPI, and so phase shifts resulting from field inhomogeneities, static tissue susceptibility gradients and chemical shifts are not cancelled. SE-EPI is routinely used for diffusion weighted imaging (DWI) in the body. However since EPI is a single shot technique, the echo time for high spatial resolution acquisitions covering the FOV required of the abdomen (~ 288 x 288 mm) can become very long resulting in poor image quality, especially for GE-EPI.

The major advantage of EPI is that it has a short acquisition time of 20 – 30 ms, leading to the ability to image multiple slices at the peak of the ASL signal curve, thus low variance is expected in the perfusion weighted ASL signal across multiple slices. Secondly, all images can be collected at a given point in the respiratory cycle when using a respiratory triggered acquisition. Finally, the SAR for EPI schemes is also relatively low, especially for GE-EPI. A GE-EPI scheme has been used for renal ASL in the work by Sokolska *et al*. (9) where it was combined with pseudo-continuous ASL (pCASL) labelling to assess feasibility and within subject repeatability of renal perfusion measures. A SE-EPI scheme was employed by Gardener *et al*. (4) to acquire multiple slices across the kidney. In this work, different breathing strategies were also assessed to determine the optimal method to overcome respiratory motion.

A balanced fast field echo scheme (bFFE) is widely used as the image readout for renal ASL (3,5,6,14). This is a gradient echo based scheme which consists of RF pulses that are repeated every TR with no spoiling gradients. The balanced gradients result in longitudinal and transverse magnetisation being maintained, and so T_1 and T_2 contrast are both evident in a bFFE image. The bFFE scheme starts with a RF pulse of less than 90^o (typically around 35^o for body imaging) and all spins are in the steady state in the first TR. Before the next TR, gradients are balanced in the slice, phase and frequency encoding directions so that the net gradient is zero. A bFFE pulse sequence is shown in Figure 5.2-3.

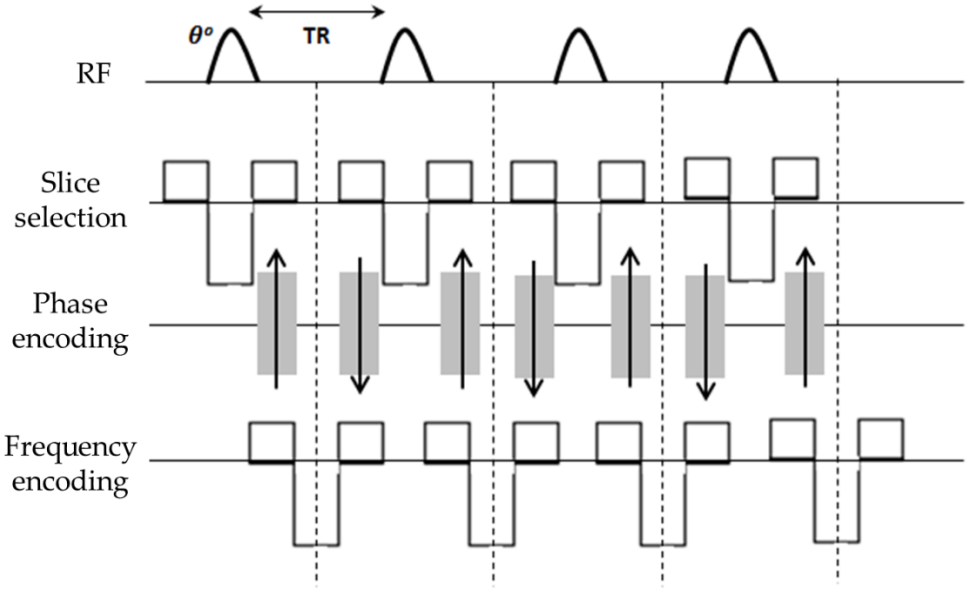

Figure 5.2-3: *A bFFE pulse sequence*

The bFFE scheme is advantageous as it provides a very short TE and high image SNR. However, the shot length of a bFFE scheme is reasonably long at approximately 300 ms for a typical abdominal FOV with 3 mm voxel resolution. This can lead to multiple slices not all being acquired at the peak of the ASL signal curve, and so one would expect there to be a greater variance in the image perfusion weighted signal across slices, particularly in comparison to EPI. Further, the SAR of a bFFE readout scheme is higher than for EPI resulting in longer temporal slice spacing. However, bFFE schemes are limited by their sensitivity to field homogeneity, with banding artefacts

apparent in areas of off-resonance in the image. Martirosian *et al*. (6) was the first to use a bFFE readout scheme with FAIR ASL in the human kidney. In the work by Heusch *et al* (13) a FAIR ASL scheme was applied with a bFFE readout for functional evaluation of transplanted kidneys. Gillis *et al*. (5) measured inter-study reproducibility of ASL MRI at 3T using a FAIR scheme combined with a bFFE readout, and concluded that ASL at 3T provided a repeatable method of measuring renal perfusion.

Another alternative scheme is turbo spin echo (TSE). A TSE pulse sequence is shown in Figure 5.2-4. TSE uses a series of 180° refocusing pulses following a single 90° pulse to generate a train of echoes. By changing the phase encoding gradient for each echo in the TSE sequence, a different line of k-space is acquired for each echo. This results in the acquisition of multiple lines of k-space within a given repetition time (TR).

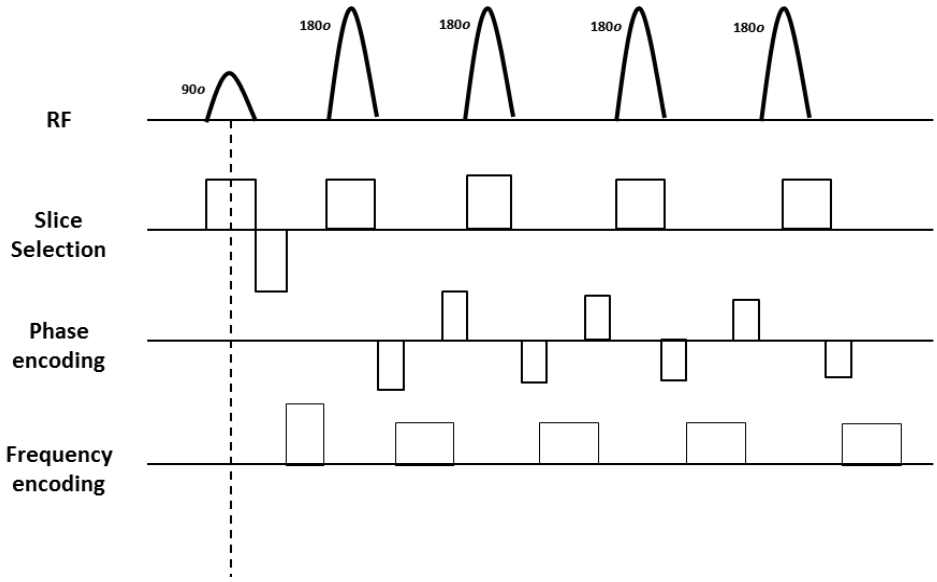

Figure 5.2-4: *TSE pulse sequence diagram*

In the TSE scheme, the time saved by scanning multiple lines of k-space at once means it is possible to lengthen the TR which allows more time for T_1 recovery, resulting in an improved signal-to-noise ratio. A higher number of phase encoding steps can also be used which will allow for an improvement in spatial resolution. Further, susceptibility induced signal losses are low in a TSE scheme. However, the echo time of a TSE scheme is typically 50 ms so

some blurring in the images will occur due to T_2 decay. The shot length of TSE is long at ~160 ms, similar to a bFFE scheme, which can lead to slices being acquired at different points in the ASL signal curve, leading to variance in the perfusion weighted signal across slices. A limitation of the TSE scheme is the high SAR due to the multiple refocussing pulses leading to a long temporal spacing.

Alternatively, 3D schemes of either 3D TSE (30) or 3D GRASE (gradient and spin echo) (1,31) have been implemented. In the white paper for the implementation of ASL in the brain (21), a segmented 3D GRASE technique is recommended due to high SNR and time efficiency. However, for abdominal imaging where breath holds are required, a segmented technique relies on multiple breath holds all being held at the same point in the respiratory cycle for accurate reconstruction of the data, which is limiting. A recent publication by Robson *et al* (30), compared 3D TSE and 2D TSE schemes and no significant differences were found between the SNR of the schemes or the quantitative perfusion measures obtained. This work comments that although it takes more time to acquire a 3D image than a 2D slice, the need for multiple averages of a 2D image for sufficient SNR leads to a 3D approach being faster and providing increased spatial coverage. This work was focussed on the use of ASL for renal tumours, and in one case a renal mass was missed using 2D compared to 3D readout.

5.3 Methods to overcome the respiratory motion

Free breathing, respiratory triggered and breath holding techniques are all used in the literature for renal ASL. A breath hold acquisition increases the total scan time and although it can decrease respiratory motion compared to free breathing, it does not completely eliminate it. Further, breath holding is not tolerable for all subjects, especially patients. Also, data are generally averaged over multiple breath holds for increased SNR, which requires

subjects to hold their breath at the same point in the respiratory cycle, which is unlikely. Alternatively, respiratory triggered data can be acquired in which bellows are placed around the subject's abdomen to monitor respiration and to trigger the readout to a given point in the respiratory cycle (generally end-expiration). Data can also be respiratory triggered using a navigator to measure the position of the acquired slice according to the movement of the diaphragm. In the work by Gardener *et al.* (4) it was determined that a free-breathing, respiratory triggered approach was the optimal technique for acquiring robust data in a short scan time. This work also discussed the use of background suppression, which uses additional non-selective inversion pulses to null the static signal, and has been show to improve ASL sensitivity in the brain (32). However, Gardener *et al*. (4) showed that despite background suppression improving the images visually it can reduce the signal to noise ratio (SNR) of the perfusion data, and thus led to an underestimation of perfusion. It is also difficult to realign data that has been background supressed as there is not sufficient signal in the control/label images.

Techniques for minimising respiratory motion were also assessed in the work by Robson *et al*. (8) where a pCASL labelling scheme was combined with a 2D scheme. It was shown that controlled breathing combined with retrospective image sorting, based on the respiratory position during image acquisition, led to robust data from which perfusion could be estimated.

The remainder of this chapter describes the development of 2D image readout schemes for ASL on the 3T Phillips scanner using Multi Transmit and a SENSE XL Torso receive coil. The optimisation of the schemes is described, and the application of these methods for the assessment of renal perfusion and renal T_1 mapping outlined.

5.4 Development of Renal ASL Readout Schemes Using the Philips Pulse Programming Environment (PPE)

Before scanning could be performed, pulse programming was necessary to allow four 2D image readout schemes (bFFE, GE-EPI, SE-EPI and TSE) to be used with renal ASL. The aim was to match the 2D readout schemes for spatial resolution and the number of slices acquired. Renal ASL is not a standard sequence available on the Phillips platform; however a prior patch was available to provide some renal ASL capability. Here, the code was further modified in the pulse programming environment (PPE) to increase the number of slices for each scheme to 5 (which was initially only achievable with a patch for the bFFE scheme) and provide a respiratory triggered ASL readout for all schemes, this required modification of the code for the TSE and GE-EPI schemes. There was also the need to add an 'end-delay' option to leave a delay period following the readout prior to the next inversion to ensure full recovery of the signal. Finally, an option for a 'pre-label delay' - a delay between the respiratory trigger and the label or control pulse - was also coded. When acquiring pilot data for this study it was noticed that for the SE-EPI scheme, alternate slices were fluctuating in signal intensity. This was determined to arise due to a poor 180^{o} pulse profile. To overcome this, the default 180^{o} pulse was modified in the code to provide a sharp profile which removed this fluctuation due to the much sharper pulse profile.

For all readout schemes, five slices with no slice gap were acquired with the exception of the TSE scheme, for which three slices were collected with a 5 mm gap. It was decided to collect 3 slices for the TSE scheme, although it was possible to achieve 5 slices, since the temporal slice spacing was considerably longer for the TSE scheme compared to other readouts due to SAR restrictions, and so there was not enough time to acquire 5 slices before the ASL signal had recovered. For TSE, 3 slices with a 5mm gap between slices were collected so the same kidney coverage was achieved. The PLD times of the ASL recovery curve that are sampled for the TSE and GE-EPI schemes are

illustrated in Figure 5.4-1, highlighting the time difference between sequential slices for the readout scheme with the largest and shortest temporal spacing (Table 5.4-1).

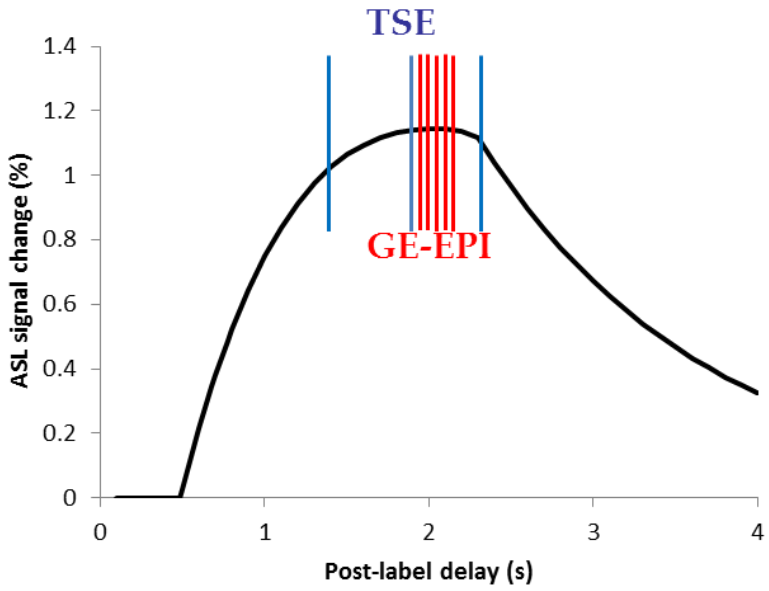

Figure 5.4-1: *Temporal slice positioning on the ASL perfusion weighted signal curve for the GE-EPI (slice spacing ~ 40 ms) and TSE (slice spacing ~ 480ms) schemes.*

A coronal oblique orientation was chosen for all ASL image readouts so any movement was in the plane of the kidney. Also, this orientation ensured that the image volume remains within the selective inversion slab throughout the entire respiratory cycle. Optimised imaging parameters for each 2D readout scheme are summarised in Table 5.4-1.

2D Readout scheme	Post label delay of 1st slice (ms)	TE (ms)	Flip angle (°)	Number of slices (slice gap (mm))	Temporal slice spacing (ms)
bFFE	1300	1.5	45	5 (0)	280
GE-EPI	1800	8	90	5 (0)	40
SE-EPI	1800	18	90	5 (0)	60
TSE	1300	50	90	3 (5)	480

Table 5.4-1: *FAIR ASL imaging parameters for each 2D readout scheme.*

5.5 Methods

Having optimised the 2D GE-EPI, SE-EPI, bFFE and TSE readout schemes for renal ASL, a study was performed in healthy volunteers to determine the optimal scheme. The study was approved by the local ethics committee and all participants gave informed, written consent. Ten healthy volunteers were scanned for approximately one hour on a 3T Philips Achieva scanner with Multi-Transit and a 16-channel XL Torso receive coil. To ensure that all volunteers had healthy kidney function, blood and urine tests were performed and evaluated by a clinician.

Initially, balanced-Turbo-Field-Echo (bTFE) localiser scans were acquired in three orthogonal planes to plan placement of the image and label slabs relative to the kidneys and vessels. Coronal-oblique imaging slices were collected obliquely across the kidney in descending order (lateral – medial) (Figure 5.5-1) whilst taking care that the selective inversion slab avoided the aorta. This geometry of image readout was acquired on each subject for all schemes. All readout schemes were acquired with FOV 288 x 288 mm, in-plane spatial resolution 3 x 3 mm^2; slice thickness 5 mm and SENSE 2. Use of a SENSE factor of 2, allowed the minimum GE-EPI and SE-EPI echo time to be achieved and reduced the readout duration thereby minimising susceptibility related distortions and signal drop out, and allowed multiple slices to be acquired sampling the peak of the ASL signal curve.

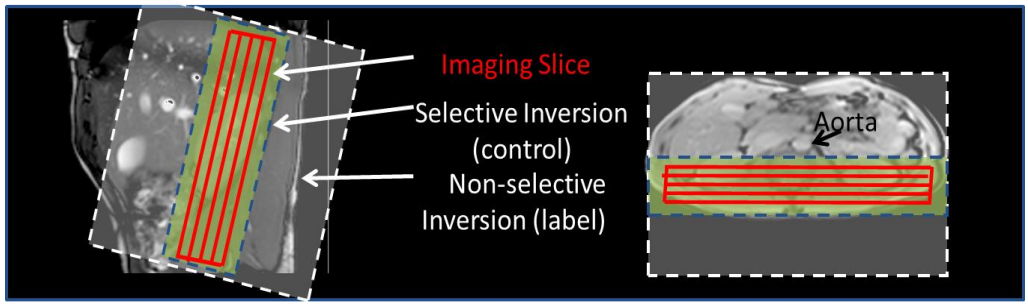

Figure 5.5-1: *Positioning of the FAIR scheme selective and non-selective slabs relative to the kidneys and aorta.*

The FAIR labelling scheme used a selective inversion slab of 45 mm chosen to be 10 mm wider than the imaging volume and a 400 mm non-selective

inversion slab (Figure 5.5-1). A Frequency Offset Corrected Inversion (FOCI) inversion pulse was used for FAIR labelling which provided a sharp inversion profile. To supress any static tissue signal in the perfusion weighted images, in-plane WET (Water suppression Enhanced through T1 effects) saturation pulses were placed immediately before each selective or non-selective pulse and a sinc post-saturation pulse was placed immediately after. In order to achieve the maximum perfusion weighted difference signal, accounting for the different readout durations (see Table 5.4-1) a label delay (time to the centre of k-space for the first slice) was set to 1300 ms for bFFE and TSE and 1800 ms for GE-EPI and SE-EPI schemes. All data sets were acquired respiratory triggered on the inversion pulse. A minimum repetition time (TR) of 3 s was defined; this meant that at least this time or longer was allowed between each selective and non-selective pulse, depending on the subject's respiration rate. For a TR of 3 s, a label/control pair would be acquired every 6 s. In total, 25 label and control pairs were acquired for each renal ASL dataset of each readout scheme.

M_0 scans were also collected respiratory triggered with readouts being acquired at the same point in the respiratory cycle as the ASL data using a trigger delay matched to the PLD. For quantification of perfusion, T_1 weighted images were also acquired for each readout scheme, these matched the geometry of the ASL image.

5.5.1 T_1 Mapping

To map the T_1 relaxation time in the renal cortex, a modified respiratory-triggered inversion-recovery sequence was implemented. Images were acquired at multiple inversion times (TI), with all images collected at the same time in the respiratory cycle as the ASL data by introducing an additional delay (Tv) following the respiratory trigger and prior to the inversion. This sequence is shown in Figure 5.5-2.

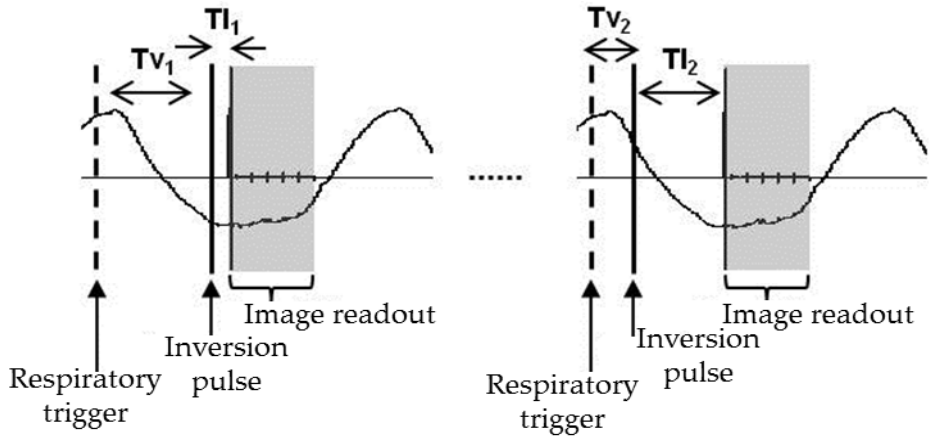

Figure 5.5-2: *Schematic showing the positioning in the respiratory cycle of the inversion and image readout for T_1 mapping. The respiratory trigger is at end inspiration, this is followed by an additional trigger delay (Tv) after which the inversion is applied and images are the acquired after a further delay (TI). This is shown for a short (TI_1 and a long (TI_2) inversion time. All image readouts are acquired at the same point in the respiratory cycle.*

All schemes were collected with a minimum TR of 6 seconds using a non-selective slab thickness of 400 mm. T_1 measures were acquired at inversion times of 200 ms to 1500 ms in 100 ms spacing. For GE-EPI and SE-EPI, slices were acquired in a descend order alone. For the TSE and bFFE readout schemes, slices were acquired using both an ascend and descend ordering to increase the dynamic range (33).

5.5.2 Reproducibility

It is important to assess the reproducibility of each readout scheme to ensure that the same results are achieved. This is important clinically to ensure that any measured changes in the perfusion or T_1 value are due to changes in health and not from fluctuations in scan results. To assess the reproducibility of each readout scheme, all volunteers returned for a second identical scan session within 2 weeks of the first scan session. Reproducibility was assessed for both ASL perfusion and T_1 measures.

5.5.3 Data Analysis

5.5.3.1 Quantification of perfusion and T_1 maps

Analysis was performed using custom written MATLAB programs (Matlab version 8.1, The MathWorks, Inc., Natick, MA, USA). ASL perfusion weighted difference maps were calculated by subtraction of the non-selective image from the selective image. Images were inspected for motion using a home written matlab script in which it was possible to view subtraction images and then discard misaligned pairs. Motion was evident from edge effects around the kidney in the difference image. Example difference images that were discarded and acceptable data are shown in Figure 5.5-3.

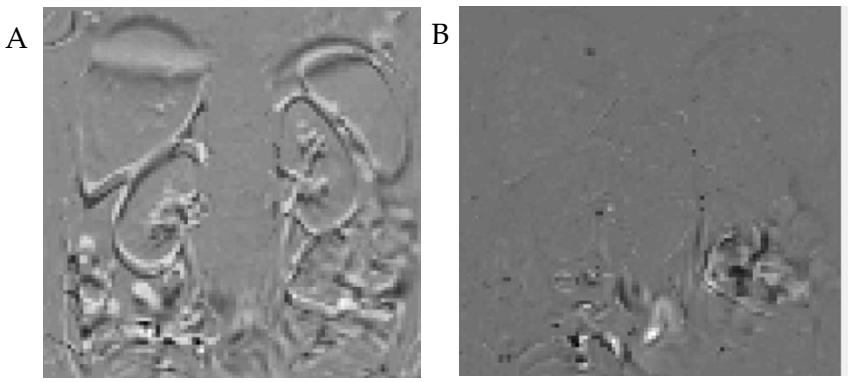

Figure 5.5-3: *Example perfusion weighted difference images showing A) data that would be discarded and B) data considered acceptable.*

The difference images were averaged to form a single perfusion weighted difference image (ΔM) for each slice which were then normalised by the M_0 image. T_1 and M_0 maps were formed by fitting the T_1 data to an inversion recovery curve. These ΔM, T_1, T_{1b}, and M_0 maps were then used together to calculate a renal perfusion (*f*) map, in units of ml/100g/min, by fitting the data to a kinetic model (Equation 5-1) (34) neglecting transit time and exchange time effects.

$$f = \frac{\lambda}{2}\frac{\Delta M}{M_0}\left(\frac{\frac{1}{T_{1b}} - \frac{1}{T_{1t}}}{e^{TI/T_{1t}} - e^{-TI/T_{1b}}}\right) \qquad 5\text{-}1$$

T_{1b} and T_{1t} are the T_1 values of blood and tissue respectively, TI is the inversion time and λ is the blood tissue partition coefficient which is assumed to be 0.8 mL/g for kidneys. To segment the renal cortex, a histogram of the T_1 values in the T_1 map was produced and then a threshold determined to create a cortex mask. These maps were compared across the readout schemes to ensure approximately the same number of voxels were assessed. The average perfusion in the renal cortex was then calculated for each slice.

5.5.3.2 Image Assessment

To assess the quality of each readout scheme, the following quantitative measures were assessed in the renal cortex:

(1) Perfusion weighted image signal-to-noise ratio (PW-SNR). This was calculated as the mean perfusion weighted signal divided by the standard deviation in the background noise of the perfusion image. The background noise was measured by calculating the signal in a region of interest (ROI) outside of the kidneys.
(2) Temporal signal–to-noise ratio of the perfusion weighed image (tSNR): calculated as the mean perfusion weighted signal divided by its standard deviation over the 25 dynamics.
(3) Variance in the perfusion weighted signal across the slices ($var_{\Delta M}$): calculated as the standard deviation in the perfusion weighted difference across the slices divided by the mean perfusion weighted signal.

To illustrate the inter-subject variability in perfusion and T_1 measures, box plots were produced from the first visit data. A repeated measures anova was calculated to determine whether there were any significant differences between readout schemes.

5.5.3.3 Reproducibility of readout schemes

To assess reproducibility of each 2D readout scheme, Bland Altman plots of the mean perfusion value versus the difference between scan sessions were formed, and the 95 % limits of agreement calculated from the mean difference between measures plus or minus 1.96 times the standard deviation of the difference. Reproducibility was assessed from the coefficient of variance (CoV), the ratio of the standard deviation of the differences between visits to the mean perfusion measures. CoV values close to zero suggest good agreement between measurements. A Friedman mean rank test was also performed to inform on whether any readout scheme gave a systematically high or low perfusion value.

Similarly, the reproducibility of T_1 measures was assessed using Bland Altman plots, CoV measures and the Friedman mean rank test.

5.6 Results

M_0 images for each 2D readout scheme are shown in Figure 5.6-1 with high data quality clear for all readout schemes. The longer echo times for the EPI schemes and TSE schemes can be seen to translate to the slight blurring of the M_0 images. In the bFFE image, the vessels appear brighter than in the other schemes due to the high T_2/T_1 contrast in fluids as these are not supressed.

Assessment of specific absorption rate (SAR) showed that the TSE scheme had the highest SAR at approximately 70 % whilst the SE-EPI, GE-EPI and bFFE schemes all had SAR of less than 35 %. A high SAR scheme has a longer temporal spacing between slice acquisitions limiting the number of slices that can be acquired at the peak of the ASL signal curve.

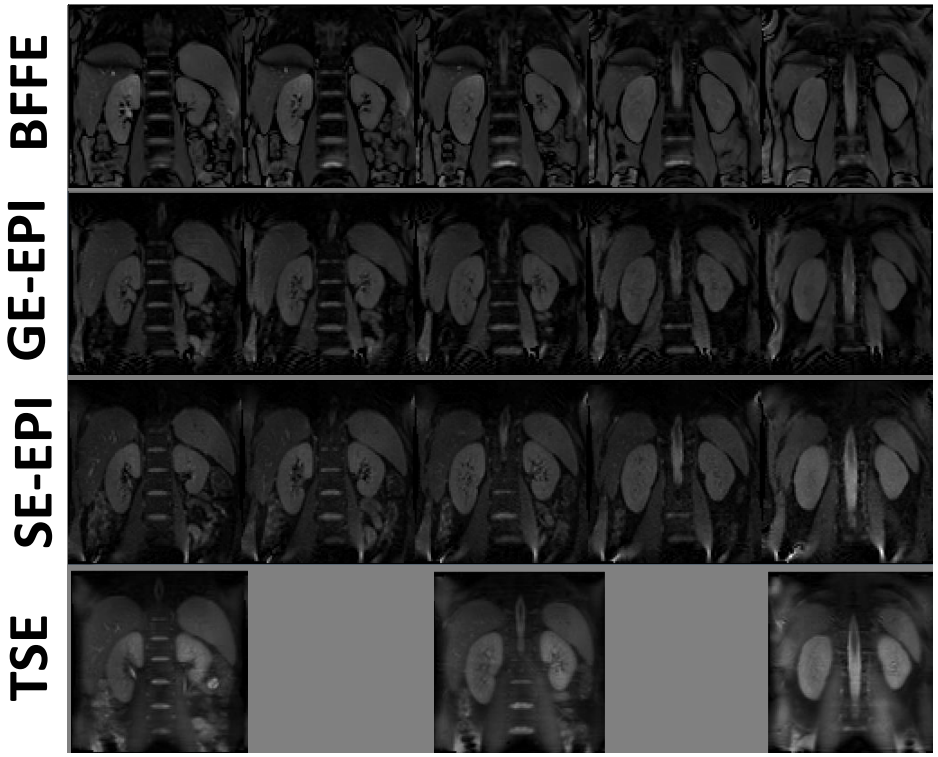

Figure 5.6-1: *Example M_0 images for each of the 4 readout schemes. Each M_0 scan was acquired with identical shim values, slice positioning and a FOV of 288 x 288 mm with a spatial resolution of 3x3x5 mm.*

Table 5.6-1 shows results of the perfusion weighted image SNR (PWI-SNR), temporal SNR (tSNR), and variability of the perfusion signal ($var_{\Delta M}$ (%)) for each readout scheme.

Readout scheme	**PWI-SNR**	**tSNR**	**$var_{\Delta M}$ (%)**
bFFE	6.2	2.4	26 ± 11
GE-EPI	6.3	1.5	20 ± 5
SE-EPI	3.9	2.6	11 ± 3
TSE	8.5	2.4	20 ± 4

Table 5.6-1: *Perfusion weighted SNR (PW-SNR), temporal SNR (tSNR) and variability of the perfusion weighted signal ($var_{\Delta M}$(%)) for each scheme.*

The highest PWI-SNR was for the TSE scheme with the lowest for SE-EPI. tSNR was found to be optimal for the SE-EPI scheme and lowest for the TSE scheme. The $var_{\Delta M}$ was found to be lowest for SE-EPI, with the highest variability found for the bFFE readout. Perfusion weighted images for each scheme are shown in Figure 5.6-2.

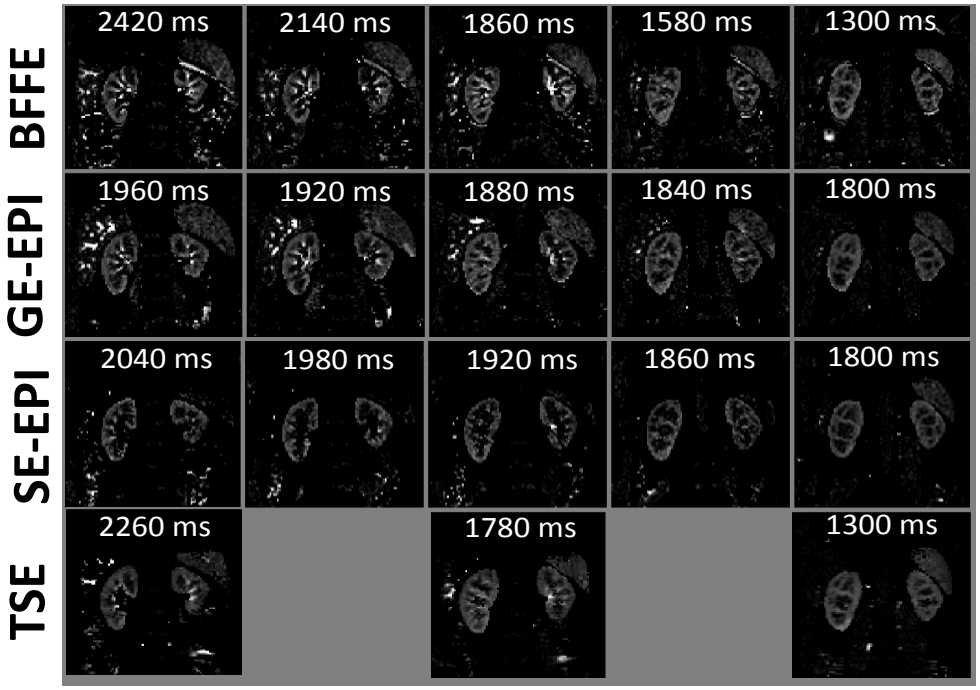

Figure 5.6-2: *Perfusion weighted images (PWI) for each scheme (bFFE, GE-EPI, SE-EPI and TSE) for an example subject. Timings on each of the images indicates the readout time of each. Each scan was acquired with identical shim values, slice positioning and a FOV of 288 x 288 mm with a spatial resolution of 3x3x5 mm.*

The range of perfusion values measured from the first scan session is illustrated in Figure 5.6-3 for each of the four readout schemes.

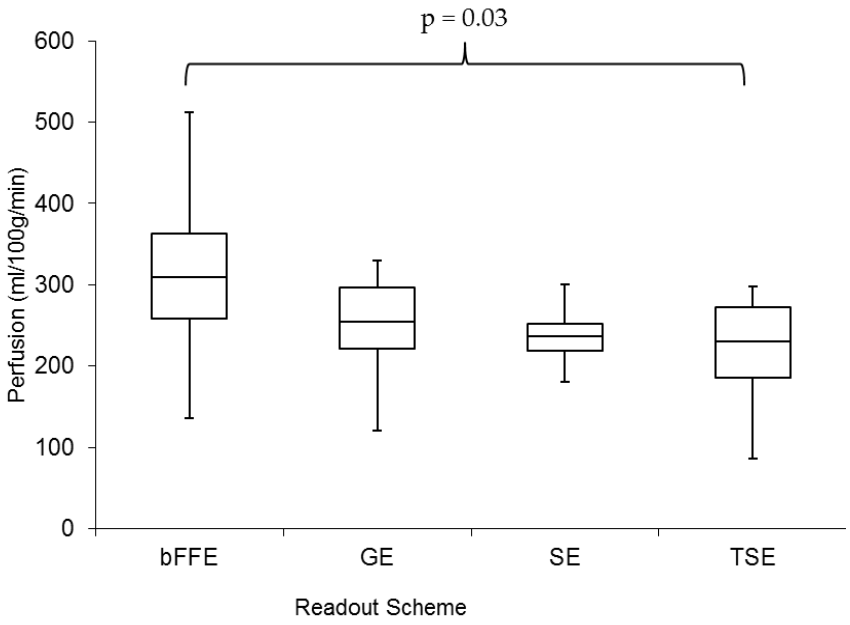

Figure 5.6-3: *Box plot showing renal cortical perfusion values measured from each 2D readout scheme for the first visit.*

Average renal cortical perfusion across all schemes was 238 ± 12 ml/100g/min, the error indicates the standard error of the perfusion values across readout schemes. Perfusion values were calculated to be: bFFE = 317 ± 34 ml/100g/min, GE-EPI = 251 ± 19 ml/100g/min, SE-EPI = 238 ± 12 ml/100g/min, TSE = 221 ± 22 ml/100g/min. On performing a Friedman mean rank test, the bFFE readout yielded consistently higher perfusion values compared to the other three schemes. A repeated measures anova showed that bFFE readouts produced significantly higher perfusion values than TSE ($p = 0.03$). There were no significant differences in measured perfusion between GE-EPI, SE-EPI and TSE schemes. It is likely that the higher perfusion value for the bFFE scheme is due to the presence of vessels in the perfusion weighted image.

The largest inter-subject variability of perfusion values was found for the bFFE scheme and the smallest range for the SE-EPI scheme; this was true of both the first and second scan session.

Bland Altman plots showing the difference in measured perfusion values between visits are shown in Figure 5.6-4. The Bland Altman plots show good agreement between measurements for each readout scheme. The most reproducible readout scheme was SE-EPI, which had a CoV of 8 %, the least reproducible scheme was the TSE scheme with a CoV of 21 %. For each readout scheme, there were no significant differences between results from study days.

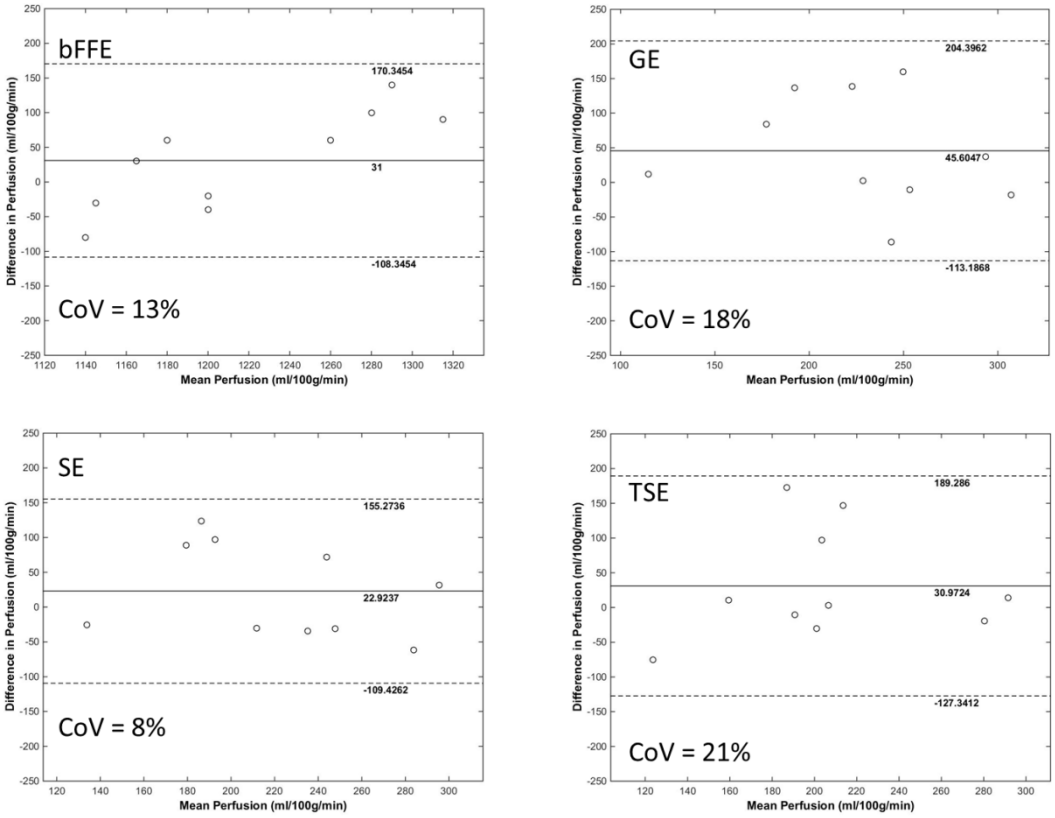

Figure 5.6-4: *Bland Altman plots showing the reproducibility of each readout scheme. The mean perfusion value is shown on the x-axis and the difference between the 2 visits on the y-axis. The lines showing 95% limits of agreement are calculated as the mean difference plus or minus 1.96 times the standard deviation of the differences. The central line shows the mean difference across all subjects.*

The average renal cortex perfusion value, percentage difference between visits and CoV for each readout scheme are listed in Table 5.6-2.

Readout scheme	Perfusion (ml/100g/min)	Average difference (%)	CoV (%)
bFFE	317 ± 34	31	13.14
GE-EPI	251 ± 19	45	18.73
SE-EPI	238 ± 12	22	8.22
TSE	221 ± 22	30	21.33

Table 5.6-2: *Perfusion (ml/100g/min), average perfusion difference between visits (%) and coefficient of variance (CoV) (%) for each readout scheme.*

Figure **5.6-5** shows box plots of T_1 values for each readout scheme.

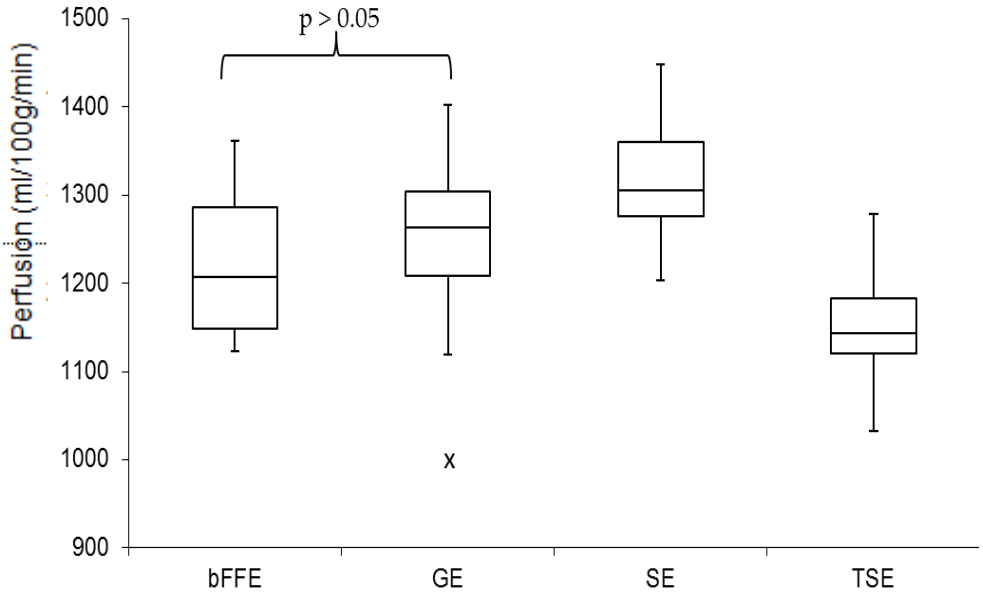

Figure 5.6-5: *Box plot of T_1 values for each readout scheme. Outliers are shown by an x. There were significant differences seen between all schemes other than the bFFE and GE-EPI schemes.*

It can be seen that SE-EPI and GE-EPI schemes yield a higher T_1 value, with the Friedman mean rank test showing that SE-EPI results in a systematically higher T_1 values that the other 3 readout schemes. When looking at the

difference in T_1 values between the different schemes, a significant difference was found ($p < 0.05$) between all schemes except for between bFFE and GE-EPI schemes.

Figure 5.6-6 shows Bland Altman plots of T_1 values for the renal cortex for the four readout schemes. All measures are reproducible with a maximum CoV of 3.8 % for GE-EPI and the smallest CoV of 1.7 % for SE-EPI, making this the most reproducible scheme.

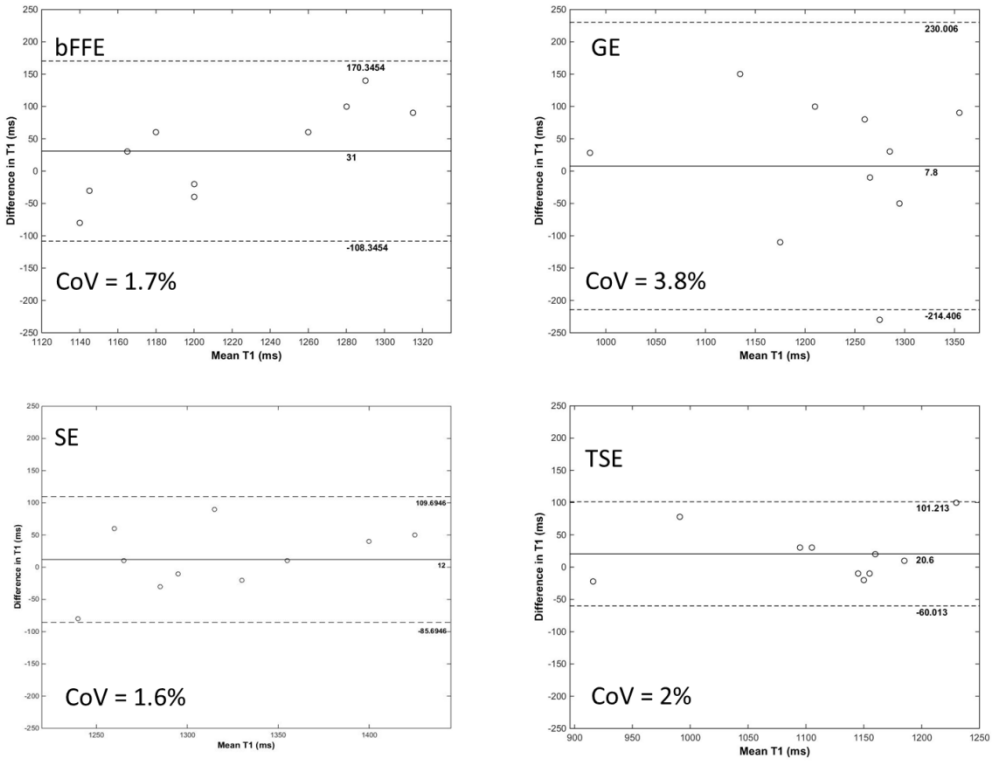

Figure 5.6-6: *Bland Altman plots showing the reproducibility of each 2D readout scheme. Average T_1 values on the x-axis and the % difference between the 2 visits shown on the y-axis. The mean difference and 95% confidence intervals are shown.*

Average renal cortex T_1 values for each readout scheme are given in Table 5.6-3. SE-EPI yielded the highest T_1 values, conversely TSE yielded the shortest T_1 value. The average intra-subject percentage difference between visits was highest for GE-EPI and the lowest for SE-EPI. A student's t-test, showed no significant differences in T_1 values between visit one and visit two for any readout scheme. There was a significant difference when comparing T_1 values

measured across schemes except for between bFFE and GE-EPI which had a p of 0.6 showing there to be no significant differences between these schemes.

Readout scheme	T_1 (ms)	Average difference (%)	CoV (%)
bFFE	1211 ± 36	3.15	1.65
GE-EPI	1225 ± 65	7.30	3.83
SE-EPI	1316 ± 42	3.07	1.56
TSE	1112 ± 44	2.97	1.97

Table 5.6-3: *Average renal cortex T_1 value (ms), average difference between visits (%) and coefficient of variance (CoV) (%) for each of the four schemes.*

5.7 Discussion

Previous renal ASL studies have used a variety of readout schemes in combination with FAIR labelling. In this work, a comparison of balanced fast field echo (bFFE), gradient-echo EPI (GE-EPI), spin-echo EPI (SE-EPI) and turbo spin echo (TSE) schemes is made for renal ASL. For all schemes, multi-slice coverage could be achieved with five contiguous slices collected for bFFE, GE-EPI and SE-EPI and three slices with a 5 mm slice gap for TSE, the higher SAR leading to wider readout spacing for the TSE scheme. GE-EPI and SE-EPI could achieve whole kidney coverage in the shortest amount of time.

A summary of the results from perfusion measures for the four readout schemes is given in Table 5.7-1. The computed renal cortex perfusion was higher for gradient-echo based GE-EPI and bFFE compared to spin echo based SE-EPI and TSE schemes.

Readout scheme	Perfusion (ml/100g/min)	Average perfusion difference (%)	Perfusion Weighed SNR	Temporal SNR	$var_{\Delta M}$ (%)
bFFE	317 ± 34	30.98	6.2	2.4	26 ± 11
GE-EPI	251 ± 19	26.25	6.3	1.5	20 ± 5
SE-EPI	238 ± 12	18.42	3.9	2.6	11 ± 3
TSE	221 ± 22	28.20	8.5	2.4	20 ± 4

Table 5.7-1: *Summary of key results for perfusion*

Perfusion values calculated from the bFFE readout data were significantly higher than all other schemes ($p < 0.05$). This could be attributed to the presence of vascular signal in these images. In future work, the increased perfusion signal from a bFFE scheme could be removed by the use of vascular crushing or by creating a more robust mask from which to exclude vessels. This was assessed by removing the segmental arteries from the chosen ROI. A box plot was then created for the bFFE data to compare the inclusion and exclusion of vessels (Figure 5.7-1).

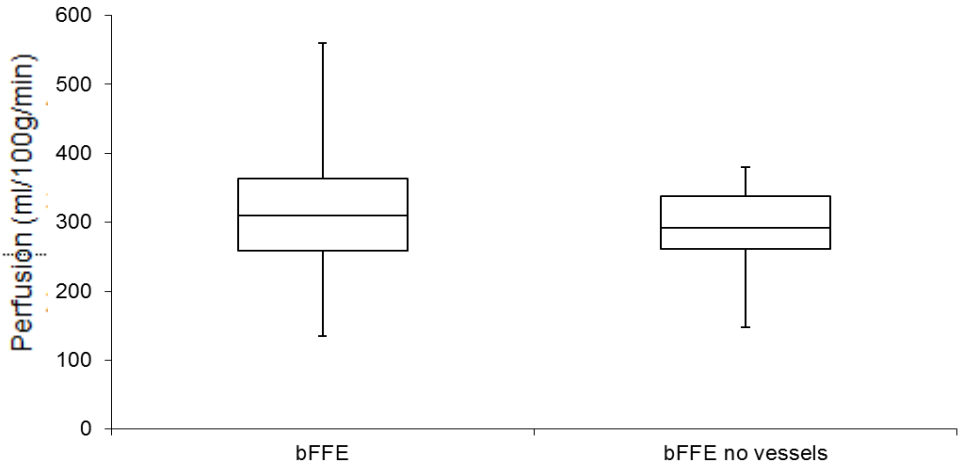

Figure 5.7-1: *Box plot of perfusion values obtained during the first scan session using a bFFE readout scheme. Results are show from a bFFE scheme including vessels and a bFFE readout scheme excluding vessels.*

From this it can be seen that the variance is lower when the vessels are removed, and this will also improve the reproducibility of this method.

When comparing signal-to-noise ratio (SNR), SE-EPI gave a significantly lower PWI-SNR compared to the other schemes, however this could be attributed to the reduction in vascular signal present in the SE-EPI images. This is also supported by the fact that the SE-EPI scheme had the highest temporal SNR, suggesting lowest fluctuations from pulsatile vessels.

SE-EPI was found to display the lowest variance across slices of all the readout schemes. This is unsurprising as the SE-EPI scheme has a short shot length per slice, and so all slices are acquired at almost the same point on both the ASL signal curve and in the respiratory cycle, resulting in a small variance in the signal of each slice. Conversely, TSE readouts have a long shot length; this yielded the highest variance in signal across slices.

All 2D readout schemes were determined to be reproducible with a coefficient of variance of 21% or less. SE-EPI was found to be optimal, CoV of 11%.

Assessing the reproducibility of T_1 measures, it was found that all schemes were reproducible between the two visits. The CoVs were small for all readout schemes, with the largest being 3.8 % for GE-EPI and the smallest at 1.6 % for SE-EPI. There were no significant differences in T_1 measurements between the two visits for any of the readout schemes.

Comparing the T_1 values measured between schemes, showed there were significant differences between the T_1 values measured from all schemes other than between GE-EPI and bFFE. When performing a Monte Carlo simulation (Figure 5.7.1) to estimate perfusion values with increasing T_1 values, it was found that by increasing the T_1 value, the fitted perfusion value decreased.

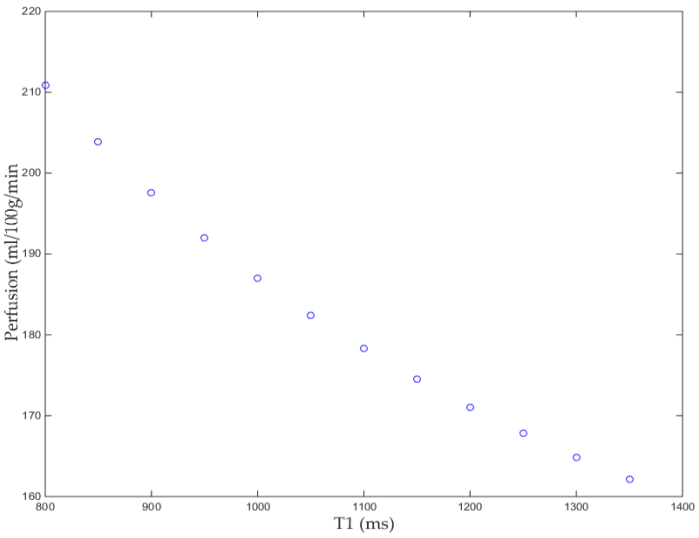

Figure 5.7-2: *An increase in T1 values leads to a decrease in the fitted perfusion values.*

This is important to note, as for situations such as multi-centre studies where different readout schemes could be implemented, it is key to keep the readout schemes the same, or to understand such systematic differences. Also, it is important in patient groups where changes in T_1 are likely to occur due to effects such as fibrosis or inflammation, that individual subject T_1 measures are used in perfusion estimation.

5.8 Conclusion

In summary, this chapter has reviewed and optimised different 2D readout schemes for renal ASL and renal T_1 measures. Balanced fast field echo (bFFE), gradient-echo echo-planar imaging (GE-EPI), spin-echo echo-planar imaging (GE-EPI) and turbo spin-echo (TSE) were assessed for temporal and perfusion weighted image signal-to-noise ratio (t-SNR and PWI-SNR respectively), perfusion values and variance in perfusion signal across multiple slices ($var_{\Delta M}$). The reproducibility of these readout schemes was also assessed by measuring coefficients of variance (CoV) and Bland Altman plots.

All schemes were found to be reproducible for both T_1 and perfusion measures. The most reproducible readout scheme for perfusion measures was SE-EPI, which had a CoV of 8 %; the least reproducible scheme was the TSE scheme with a CoV of 21 %. T_1 measures were highly reproducible with the highest CoV of 3.8 % for GE-EPI and the smallest CoV of 1.7 % for SE-EPI.

When performing a comparison of all four techniques for perfusion measures, it was seen that SE-EPI provides optimal temporal SNR, consistency across slices, reproducibility between sessions and the lowest specific absorption rate (SAR). The measured cortical perfusion was higher for gradient-echo based GE-EPI and bFFE compared to spin echo based SE-EPI and TSE schemes and perfusion values calculated from the bFFE readout data were significantly higher than all other schemes ($p < 0.05$).

A comparison of T_1 values measured from each of the schemes showed there were significant differences between the T_1 values measured from all schemes other than between GE-EPI and bFFE. SE-EPI yielded the highest T_1 values. It is expected that T_1 values are higher for SE-EPI compared to the other schemes as the SE-EPI is governed by only T_1 relaxation whereas the bFFE scheme also has T_2 /T_2* effects (35).

In future work, the techniques optimized in this work for measurement of renal cortex perfusion and T_1 can be extended to also measure perfusion in the medulla and T_1 and can be used to assess residual renal function in patients with chronic kidney disease. As SE-EPI provides optimal temporal SNR, consistency across slices, reproducibility between sessions and the lowest specific absorption rate (SAR), in future work, this technique will be used and so a SE-EPI T_1 mapping technique will be used as this is also needed in the quantification of the perfusion measures.

5.9 References

1. Cutajar M, Thomas DL, Hales PW, Banks T, Clark C a., Gordon I. Comparison of ASL and DCE MRI for the non-invasive measurement of renal blood flow: Quantification and reproducibility. Eur. Radiol. 2014;24:1300–1308. doi: 10.1007/s00330-014-3130-0.

2. Dong J, Yang L, Su T, Yang X, Chen B, Zhang J, Wang X, Jiang X. Quantitative assessment of acute kidney injury by noninvasive arterial spin labeling perfusion MRI: a pilot study. Sci. China. Life Sci. [Internet] 2013;56:745–50. doi: 10.1007/s11427-013-4503-3.

3. Gardener A, Francis S. Multi-slice kidney perfusion using SE-EPI FAIR: Optimised acquisition and analysis strategies. In: Proceedings 17th Scientific Meeting, International Society for Magnetic Resonance in Medicine. Vol. Honolulu. ; 2009. p. 2035.

4. Gardener AG, Francis ST. Multislice perfusion of the kidneys using parallel imaging: Image acquisition and analysis strategies. Magn. Reson. Med. 2010;63:1627–1636. doi: 10.1002/mrm.22387.

5. Gillis K a, McComb C, Foster JE, et al. Inter-study reproducibility of arterial spin labelling magnetic resonance imaging for measurement of renal perfusion in healthy volunteers at 3 Tesla. BMC Nephrol. [Internet] 2014;15:23. doi: 10.1186/1471-2369-15-23.

6. Martirosian P, Klose U, Mader I, Schick F. FAIR True-FISP Perfusion Imaging of the Kidneys. Magn. Reson. Med. 2004;51:353–361. doi: 10.1002/mrm.10709.

7. Pedrosa I, Rafatzand K, Robson P, Wagner A a., Atkins MB, Rofsky NM, Alsop DC. Arterial spin labeling MR imaging for characterisation of renal masses in patients with impaired renal function: Initial experience. Eur. Radiol. 2012;22:484–492. doi: 10.1007/s00330-011-2250-z.

8. Robson PM, Madhuranthakam AJ, Dai W, Pedrosa I, Rofsky NM, Alsop DC. Strategies for reducing respiratory motion artifacts in renal perfusion imaging with arterial spin labeling. Magn. Reson. Med. 2009;61:1374–1387. doi: 10.1002/mrm.21960.

9. Sokolska M, Thomas D, Bainbridge A, Golay X, Taylor S, Punwani S, Pendse D, Uk L. Renal Pseudo-continuous Arterial Spin Labelling (pCASL) MRI : A Repeatability Study . 2014:1–13.

10. Hueper K, Peperhove M, Rong S, et al. T1-mapping for assessment of ischemia-induced acute kidney injury and prediction of chronic kidney

disease in mice. Eur. Radiol. [Internet] 2014;24:2252–60. doi: 10.1007/s00330-014-3250-6.

11. Aisen M, Wiggins C. Technique Renal Scarring. 1994.

12. Breidthardt T, Cox EF, Squire I, Odudu A, Omar NF, Eldehni MT, Francis ST, McIntyre CW. The pathophysiology of the chronic cardiorenal syndrome: a magnetic resonance imaging study. Eur. Radiol. [Internet] 2015;25:1684–1691. doi: 10.1007/s00330-014-3571-5.

13. Heusch P, Wittsack HJ, Blondin D, et al. Functional evaluation of transplanted kidneys using arterial spin labeling MRI. J. Magn. Reson. Imaging 2014;40:84–89. doi: 10.1002/jmri.24336.

14. Park SH, Wang DJJ, Duong TQ. Balanced steady state free precession for arterial spin labeling MRI: Initial experience for blood flow mapping in human brain, retina, and kidney. Magn. Reson. Imaging [Internet] 2013;31:1044–1050. doi: 10.1016/j.mri.2013.03.024.

15. Odudu A, Francis ST, McIntyre CW. MRI for the assessment of organ perfusion in patients with chronic kidney disease. Curr. Opin. Nephrol. Hypertens. 2012;21:647–654. doi: 10.1097/MNH.0b013e328358d582.

16. Kiefer C, Schroth G, Gralla J, Diehm N, Baumgartner I, Husmann M. A Feasibility Study on Model-based Evaluation of Kidney Perfusion Measured by Means of FAIR Prepared True-FISP Arterial Spin Labeling (ASL) on a 3-T MR Scanner. Acad. Radiol. [Internet] 2009;16:79–87. doi: 10.1016/j.acra.2008.04.024.

17. Artz NS, Sadowski E a., Wentland AL, Grist TM, Seo S, Djamali A, Fain SB. Arterial spin labeling MRI for assessment of perfusion in native and transplanted kidneys. Magn. Reson. Imaging 2011;29:74–82. doi: 10.1016/j.mri.2010.07.018.

18. He X, Aghayev A, Gumus S, Ty Bae K. Estimation of single-kidney glomerular filtration rate without exogenous contrast agent. Magn. Reson. Med. 2014;71:257–266. doi: 10.1002/mrm.24668.

19. Boss A, Martirosian P, Graf H, Claussen CD, Schlemmer HP, Schick F. High resolution MR perfusion imaging of the kidneys at 3 Tesla without administration of contrast media. RoFo Fortschritte auf dem Gebiet der Rontgenstrahlen und der Bildgeb. Verfahren 2005;177:1625–1630. doi: 10.1055/s-2005-858761.

20. Lanzman RS, Robson PM, Sun MR, Patel a. D, Mentore K, Wagner a. a., Genega EM, Rofsky NM, Alsop DC, Pedrosa I. Arterial Spin-labeling MR

Imaging of Renal Masses: Correlation with Histopathologic Findings. Radiology 2012;265:799–808. doi: 10.1148/radiol.12112260.

21. Alsop DC, Detre J a., Golay X, et al. Recommended implementation of arterial spin-labeled perfusion MRI for clinical applications: A consensus of the ISMRM perfusion study group and the european consortium for ASL in dementia. Magn. Reson. Med. 2014;00. doi: 10.1002/mrm.25197.

22. Brookes MJ, Morris PG, Gowland PA, Francis ST. Noninvasive measurement of arterial cerebral blood volume using Look-Locker EPI and arterial spin labeling. Magn. Reson. Med. 2007;58:41–54. doi: 10.1002/mrm.21199.

23. Francis ST, Bowtell R, Gowland PA. Modeling and optimization of look-locker spin labeling for measuring perfusion and transit time changes in activation studies taking into account arterial blood volume. Magn. Reson. Med. 2008;59:316–325. doi: 10.1002/mrm.21442.

24. Gunther M, Bock M, Schad LR. Arterial spin labeling in combination with a look-locker sampling strategy: Inflow turbo-sampling EPI-FAIR (ITS-FAIR). Magn. Reson. Med. 2001;46:974–984. doi: 10.1002/mrm.1284.

25. Hall E, Hall E, Wesolowski R, Wesolowski R, Gowland P, Gowland P, Francis S, Francis S. Improved detection and estimation of perfusion using high spatial resolution ASL at 7T. In: Proceedings 17th Scientific Meeting, International Society for Magnetic Resonance in Medicine, Honolulu. ; 2009. p. 1529.

26. Kim SG. Quantification of relative cerebral blood flow change by flow-sensitive alternating inversion recovery (FAIR) technique: Application to functional mapping. Magn. Reson. Med. 1995;34:293–301. doi: 10.1002/mrm.1910340303.

27. Wong EC. Quantifying CBF with pulsed ASL: Technical and pulse sequence factors. In: Journal of Magnetic Resonance Imaging. Vol. 22. ; 2005. pp. 727–731. doi: 10.1002/jmri.20459.

28. Wong EC. An introduction to ASL labeling techniques. J. Magn. Reson. Imaging 2014;40:1–10. doi: 10.1002/jmri.24565.

29. Wong EC, Buxton RB, Frank LR. A theoretical and experimental comparison of continuous and pulsed arterial spin labeling techniques for quantitative perfusion imaging. Magn. Reson. Med. [Internet] 1998;40:348–55.

30. Robson PM, Madhuranthakam AJ, Smith MP, Sun MRM, Dai W, Rofsky NM, Pedrosa I, Alsop DC. Volumetric Arterial Spin-labeled Perfusion Imaging

of the Kidneys with a Three-dimensional Fast Spin Echo Acquisition. Acad. Radiol. [Internet] 2016;23:144–154. doi: 10.1016/j.acra.2015.09.013.

31. Cutajar M, Thomas DL, Banks T, Clark CA, Golay X, Gordon I. Repeatability of renal arterial spin labelling MRI in healthy subjects. Magn. Reson. Mater. Physics, Biol. Med. 2012;25:145–153. doi: 10.1007/s10334-011-0300-9.

32. Garcia DM, Duhamel G, Alsop DC. Efficiency of inversion pulses for background suppressed arterial spin labeling. Magn. Reson. Med. 2005;54:366–372. doi: 10.1002/mrm.20556.

33. Hoad CL, Palaniyappan N, Kaye P, et al. A study of T<inf>1</inf> relaxation time as a measure of liver fibrosis and the influence of confounding histological factors. NMR Biomed. 2015;28:706–714. doi: 10.1002/nbm.3299.

34. Buxton RB, Frank LR, Wong EC, Siewert B, Warach S, Edelman RR. A general kinetic model for quantitative perfusion imaging with arterial spin labeling. Magn. Reson. Med. 1998;40:383–396. doi: 10.1002/mrm.1910400308.

35. Schmitt P, Griswold M a, Jakob PM, Kotas M, Gulani V, Flentje M, Haase A. Inversion recovery TrueFISP: quantification of T(1), T(2), and spin density. Magn. Reson. Med. [Internet] 2004;51:661–7. doi: 10.1002/mrm.20058.

6. Conclusion

The work in this thesis has focused on the development and application of MRI techniques for the study of Chronic Kidney Disease (CKD). In particular, arterial spin labelling (ASL) techniques have been developed for the assessment of perfusion in both the heart and kidneys.

In Chapter 3, a modified Look-Locker inversion recovery (MOLLI) ASL technique was developed to quantify myocardial perfusion. To optimise this technique, simulations were performed for an average heart rate of 1000 ms to determine the effect of flip angle and to assess the effect of SNR on the standard deviations of the fit for T_1 and calculated perfusion values. However due to SAR, the flip angle had to be set to 35^o (lower than the optimal flip angle of 70^o). On simulating a MOLLI-ASL scheme with 3 readouts following each inversion and 8 LL sets, this resulted in a simulated standard deviation of less than 4 % for perfusion quantification and less than 2 % for assessment of T_1 (this assumes thermal rather than physiological noise).

This MOLLI-ASL technique was first validated in phantoms and then in healthy volunteers to assess the need for in-plane saturation and to determine the modelling scheme to quantify perfusion. The MOLLI-ASL technique was then applied together with phase contrast MRI (PC-MRI) measures to assess the changes in perfusion and blood flow in patients with CKD Stage 3 during a handgrip exercise challenge. MOLLI-ASL and PC-MRI measures of aortic flow were performed at rest and during exercise. Their response was compared to that of healthy age-matched controls. The calculated myocardial perfusion measured in this study for CKD patients was 1.01 ± 0.22 ml/g/min and 1.06 ± 0.17 ml/g/min in healthy controls, in agreement with literature. During the handgrip challenge myocardial perfusion was found to increase by

163 ± 44 % in healthy controls and 268 ± 68 % in CKD Stage 3 patients. In PC-MRI data, the healthy control subjects demonstrated a normal physiological response to a short period of exercise with an increase in cardiac index (CI) achieved primarily through an increase in heart rate with a smaller proportional increase in stroke volume index (SVI). The CKD group followed a similar response to the healthy control group, but aortic strain was significantly lower for CKD patients than healthy controls. Both groups had an increase in aortic velocity and aortic area on exercise. This study suggested that differences in the physiology of CKD and the healthy population can be determined using MOLLI-ASL and phase contrast and that a dynamic challenge maximizes sensitivity to changes in the patient group.

In Chapter 4, the first ever intradialytic MRI was performed to provide a thorough assessment of cardiac function, structure and perfusion during haemodialysis (HD) and haemodifiltration (HDF). This study demonstrated a clear reduction in SVI and CI during HD and HDF. Corresponding to the fall in CI, reductions in myocardial contractility were observed (less negative strain values) which were more evident on the long axis than the short axis cardiac views. Myocardial stunning, defined as a greater than 20% decrease in cardiac output, was evident from 1 hour into the dialysis treatment for both HD and HDF. Analysis of myocardial perfusion from baseline to nadir values showed a significant decline in myocardial perfusion during HD and HDF, as shown in previous studies employing PET. When correlating the MRI measures with clinical data, the ultrafiltration volume was strongly correlated with several adverse changes in cardiac function, including percentage decrease in SVI and CI as well as number of stunned myocardial segments. This confirms previous observations that ultrafiltration volume is one of the main determinants of intradialytic myocardial stunning as assessed by echocardiography. Blood pressure was generally stable during both HD and HDF, however a correlation between number of stunned ventricular segments

and fall in systolic blood pressure was seen during dialysis; again reinforcing previous findings that change in BP is a second key clinical driver of dialysis induced myocardial stunning. This study has achieved the first intradialytic MRI measures and provides a model in which other dialysis-based interventions can be characterised in detail during an MRI scan to study mechanistic effects directly.

In Chapter 5, the assessment of the kidney is studied using ASL. 2D readout schemes for renal ASL and T_1 measures are reviewed and optimised. The readout schemes considered were balanced fast field echo (bFFE), gradient-echo EPI (GE-EPI), spin-echo EPI (SE-EPI) and turbo spin echo (TSE) for use in combination with a FAIR ASL labelling scheme. These schemes were assessed for SNR, SAR, perfusion and T_1 quantification, variability in the signal across multiple slices, and reproducibility across two study days. All schemes were found to be reproducible for both T_1 and perfusion measures. The most reproducible readout scheme for perfusion measures was SE-EPI, the least reproducible scheme was the TSE scheme. T_1 measures were highly reproducible with the highest CoV of 3.8 % for GE-EPI and the smallest CoV of 1.7 % for SE-EPI. On performing a comparison of all four readouts for ASL perfusion measures, it was shown that SE-EPI provides the optimal temporal SNR, consistency across slices, reproducibility between sessions and the lowest specific absorption rate (SAR). The measured cortical perfusion was higher for gradient-echo based GE-EPI and bFFE compared to spin echo based SE-EPI and TSE schemes. In future work, the techniques optimised in this work for measurement of renal cortex perfusion and T_1 will be extended to measures of medulla perfusion and T_1 and can be used to assess residual renal function in patients with CKD.

This thesis has developed both cardiac and kidney ASL measures for future application in CKD which is a chronic disease that leads to both heart and

kidney dysfunction. Future work will aim to improve the MOLLI-ASL technique by increasing the spatial resolution of the images and acquiring multi-slice data to cover the entire of the short axis view of the left-ventricle. This will then require comparison of the Belle and iterative model of perfusion quantification. This improved technique will then be used to study the association between intradialytic changes in myocardial perfusion and contractility in myocardial segments to directly correlate with stunning. Future studies will also assess the effect of the reductions in the cardiac index on perfusion of the kidneys by determining residual renal function.

In order to apply the optimised ASL and T_1 techniques developed for renal imaging in Chapter 5 to a patient group, the reproducibility and repeatability of such measures needs to be assessed in patients where T_1 measures may change due to fibrosis or inflammation and other structural changes may occur such as cysts. In future work ASL and T_1 measures will be acquired in patients with CKD Stage 3. Other MR measures such as diffusion weighted imaging (DWI) blood oxygenation dependent imaging (BOLD) and phase contrast of the renal arteries and veins will also be acquired so these multi-parametric measures can be correlated and a thorough MRI assessment of CKD can be performed.

This thesis has developed a novel technique for assessment of myocardial perfusion with MRI that can now be translated to other clinical studies to assess myocardial health in different patient groups and can be used to assess the effects of cardiac interventions. The work in chapter 4 has provided a novel technique for intradialytic assessment that can now be used to evaluate the effect of dialysis treatments intended to improve stability and limit ischaemic injury.